MULTI-BAND SEARCH FOR VOLCANIC OUTGASSING IN THE THARSIS AND SYRTIS MAJOR REGIONS ON MARS

A DISSERTATION SUBMITTED TO THE GRADUATE DIVISION OF THE UNIVERSITY OF HAWAIʻI IN PARTIAL FULFILLMENT OF THE REQUIREMENTS FOR THE DEGREE OF

DOCTOR OF PHILOSOPHY

IN

ASTRONOMY

December, 2015

By
Alain S. J. Khayat

Dissertation Committee:

Alan Tokunaga, Chairperson
Shadia Habbal
Paul Lucey
Karen Meech
Michael Mumma
Norbert Schörghofer
Geronimo Villanueva

We certify that we have read this dissertation and that, in our opinion, it is satisfactory in scope and quality as a dissertation for the degree of Doctor of Philosophy in Astronomy.

DISSERTATION COMMITTEE

_____

Chairperson

_____

_____

_____

_____

_____

_____

© Copyright 2015
by
Alain S. J. Khayat
All Rights Reserved

To Salma and Joseph, my parents.

Acknowledgements

> "Le monde serait peu de chose s'il ne fournissait matière aux recherches du genre humain. Il est des secrets qui ne se révèlent pas en un jour; la nature ne les livre pas tous à la fois. Nous nous croyons initiés, mais nous ne sommes réellement qu'à la porte du temple. Notre âge découvre quelques-uns de ces mystères; l'avenir continuera notre oeuvre."
> *Sénèque. Questions naturelles.*

It is very difficult to sum up in few paragraphs the sense of appreciation I owe to all the amazing individuals that I have met during my Ph.D, and who contributed to this work in one form or another.

I owe a tremendous sense of gratitude and admiration to my thesis advisor Alan Tokunaga for his unconditional and continuous support throughout the years since I first arrived in Hawai'i. I have learned so much from him, beyond what i could have imagined. Alan's virtues combined are hard to find in a thesis advisor. That includes patience, immense knowledge, fairness, compassion, high work ethics, humility, vision and the right guidance. I could not have imagined a better time spent working on my Ph.D.

I would also like to show my immense gratitude to Shadia Habbal for her unconditional support, guidance, wisdom and for treating me like a family member when I am away from my own family. Her tremendous research skills, expertise and advices at very tough moments and dead-end situations I have encountered, were crucial and pivotal in my career and life choices.

I would also like to equally thank Michael Mumma and Geronimo Villanueva of the NASA Goddard Space Flight Center who provided me the opportunity to be part of their research team while working on my thesis at Goddard. Their un-paralleled research skills, guidance, helpfulness, sense of inclusiveness, and never ending research ideas have made me feel very privileged doing world class research in planetary science.

My sincere thanks also go to Karen Meech and Norbert Schörghofer of the NASA Astrobiology Institute. I feel very lucky getting to know them and be able to work with them. Karen's teaching role at the solar system course and her mentoring during my 699 research on comets have truly been inspiring. The scientific discussions with Norbert over coffee for the last 5 years have been helpful and very refreshing, and kept me on going, especially in a place where few people share similar research interests.

Thanks also to Paul Lucey for agreeing to serve on my committee, and for his insightful comments.

I am particularly grateful to Pascale El Hayek (Da couicoui) for having to bear with me throughout my boring work-related conversations. Her advices and recommendations on many aspects have always made a positive impact on my daily life, and have kept me sane.

The list of people is very long, but in alphabetical order, I would like to thank Jamal Bittar, Boncho Bonev, Morgan Bonnet, Bobby Bus, Michael Connelley, Iain Coulson, Thomas Dixon, Doris Daou, Joseph Dagher, Michel Disanti, Corinne Eby, Steve Freeland, Nader Haghighipour, Debra Hew-Harano, Gerald Hamadon, Patrick Henry, Jacqueline Keane, Susan Lemn, Mike Lum, Mike Liu, Shady Matta, Majd Mayyasi, Geoffrey Mathews, Roberto Mendez, Mike Nassir, Robert Novak, Tobias Owen, Timm Riesen, Riad Rifai, Simon Radford, John Rayner, Christina Richey, Kathleen Robertson, Narayan Raja, Gavin Seo, Luis Scuderi, Dave Tholen, Karen Teramura, Bill Unruh, Peter Veres, Jonathan Williams, Po-Feng Wu, Bin Yang, the staff at Sure Shot Café where I have spent hundreds of hours working, the Institute for Astronomy, the NASA Infrared Telescope Facility, Caltech Submillimeter Observatory, James Clerk Maxwell Telescope, NASA Goddard Space Flight Center, the University of Hawai'i, the state of Hawai'i and the US tax payers.

It is amazing how science could bring so many people from all sorts of cultural backgrounds to work together on enhancing the human understanding of our place in the Universe. This journey has been made amazing thanks to all the above-mentioned fascinating individuals. Thanks to everybody, I was able to spend the best years of my life during the Ph.D program.

I would also like to thank my brothers Etienne, Daniel and their families: Nancy, Katia, Joey, Tamara and Clara Khayat.

Last but never least, I would like to thank my mother Salma Faddoul and father Joseph Khayat, to whom I am dedicating this work. I couldn't have imagined being able to accomplish anything in life without their endless love, support, vision and care. Nothing in life makes sense except in the light of their presence.

This work has been supported by NASA, the NASA Planetary Astronomy Program, NASA's Astrobiology Program, and the California Institute of Technology.

Abstract

We carried out the first and most comprehensive to date (2015), ground-based, semi-simultaneous, multi-band and multi-species search for sulphuretted gases (SO_2, H_2S, OCS and SO) above the Tharsis and Syrtis volcanic regions on Mars. The submillimeter search extended between 23 November 2011 and 25 May 2014 which corresponded to Mars' mid Northern Spring and mid Northern Summer seasons (L_s = 34 - 135°). SO_2, SO and H_2S were targeted at their rotational transitions at 346.652 GHz, 304.078 GHz and 300.505 GHz, respectively, using the high-resolution heterodyne receiver Barney on the 10.4 m single-dish antenna of the Caltech Submillimeter Observatory (CSO), and SO_2 at HARP on the 15 m James Clerk Maxwell Telescope (JCMT) at Maunakea, Hawai'i. No sulphuretted gases were detected. We infer 2σ upper limits across the disk of the planet using the CSO of 1.1 ppb, 0.7 ppb and 1.3 ppb for SO_2, SO and H_2S, respectively, and 3.1 ppb on SO_2 using the JCMT. The infrared search covered OCS in its combination band ($\nu_1+\nu_3$) at 3.42 μm (2924 cm^{-1}), during Mars' late Northern Spring and mid Northern Summer seasons, spanning L_s= 43° and L_s= 145°, between 15 Dec. 2011 and 13 June 2014, using the high resolution infrared spectrometer CSHELL on the 3 m NASA Infrared Telescope Facility (IRTF). No absorption of atmospheric OCS has been detected, and we infer a 2σ upper limit of 0.8 ppb on OCS. Our current limit 1.1 ppb for SO_2 yields an outgassing rate of less than 55 tons/day. Compared to two terrestrial analogs, we would have been able to detect any volcanic release that is more than 4% the size of Kilauea (Hawai'i) or one twentieth the size of the Masaya volcano (Nicaragua). The mass rate of magma that is able to degas 55 tons of SO_2 per day is estimated as 37 kilotons of magma per day, or 12,000 m^3 per day (0.14 m^3/s). The non-

detection of any of the sulfur compounds in the atmosphere of Mars provides limits to the level of current volcanic activity in the crust of Mars.

Table of Contents

List of Tables

List of Figures

Chapter 1

Introduction: Volcanism on Mars

This chapter discusses Mars' volcanic history, describes a current technique for dating volcanic activity, and points out the places where the most recent volcanic activity occurred on Mars. The inventory of volcanic outgassing is later described, its relationship to methane, and the prospects of finding active vents releasing volcanic gases on Mars today are discussed. At the end, the state of research in terms of looking for sulphuretted gases in the martian atmosphere is presented, and the goals of this research which include conducting the most comprehensive multi-band search for active release of volcanic gases on Mars, are stated.

1.1 A Brief History of Volcanism on Mars

The study of planetary atmospheres by means of spectroscopy is important for understanding their origin and evolution. The presence of short-lived trace gases in the martian atmosphere would have implications for recent ongoing geologic activity on the planet. For example, volcanism not only helps to reshape the surface of a planet, but it also influences the chemistry and evolution of its atmosphere through outgassing from the planet's interior, and alters the planet's surface composition (Carr 2006).

1.1.1 Types of Volcanoes and Volcanic Activities

Volcanism reflects the thermal evolution of a planet, and it is now known that Mars had a complex history of volcanism that started 3.8 billion years ago (Carr 2006). Even though intermittent, volcanic activity has re-occurred at different geologic times up until a few hundred million years ago (Head 2007).

The geologic history of Mars is divided into 3 main periods, based on the major geologic processes occurring on the planet. The "Noachian" age, occurred during the period of the late heavy bombardment, and is divided into early, middle, and late periods, extending from over 3.95 Gyr to 3.70 Gyr (Hartmann & Neukum 2001). Greeley (1987) estimated a total volume of volcanic material of 21×10^6 km^3 released during that period. The "Hesperian" period followed the late heavy bombardment. It is characterized by lower impact cratering and flood volcanism, between 3.7 Gyr and 3.0 Gyr (Barlow 2008), and during that epoch, a total estimated volume of volcanic material of 12×10^7 km^3 was released. The most recent era, the "Amazonian" epoch, is characterized by volcanic activity present in the Elysium and the Tharsis provinces, the formation of polar caps and channels, occurring during the last 3.0 Gyr to present (Barlow, 2008). Compared to the Hesperian period, a smaller amount of volcanic material, 6×10^7 km^3, was released during the Amazonian epoch. Today, more than half the surface of Mars is covered by volcanoes (Tanaka & Davis 1988).

There are three types of volcanoes on Mars. "Shield" volcanoes, the largest in the solar system, are formed by numerous individual flows. They have shallow slopes, and several calderas at the summit (Cattermole 2001). Calderas are formed by the collapse of the ground at the center of a volcano after the migration of lava from the subsurface channels (Neukum et al. 2004). The shallowness in shield volcano slopes is a result of numerous fluid lava flows that accumulated when forming them, and that travelled for long distances (100s of kilometers) on their flanks (Forget et al. 2008). "Tholi" volcanoes have steeper slopes, probably because of the more viscous lava, and they extend on a smaller scale compared to the shield volcanoes. The third type, the "Paterae", which are older than shield volcanoes,

are located mainly near Tharsis and Elysium. They have calderas at their center, very shallow profiles and lava flow channels on their flanks (Cattermole 2001; Forget et al. 2008).

The type of volcanic eruption depends on the viscosity of the lava, which depends on the temperature, the amount of solid and gas inclusions in the magma, and predominantly the amount of silicate (SiO_2). Higher amounts of SiO_2 lead to a more viscous, thicker magma (Barlow 2008). As viscous magma with high volatile content rises, the volatiles are under less pressure, which leads to explosive, violent, and far-reaching flows. Such type of volcanism is called "explosive" volcanism.

In contrast, magma with low volatile content leads to more fluid flows, called an effusive (flood) type of volcanic eruption. Low-viscosity magma can also lead to explosive eruptions when the lava encounters water. On Mars, even though different regions expressed different transition times from explosive to effusive volcanism, a general transition period from explosive to effusive volcanism occurred $\sim$ 3.5 Gyr in the Hesperian epoch (Robbins et al. 2011).

1.1.2 Major Volcanic Districts of Interest

Tharsis region is the largest volcanic district on Mars, covering 25% of its surface, with a diameter of 3500 km (Robbins et al. 2011). Among the volcanoes present in Tharsis are shield volcanoes of Alba, Arsia, Ascraeus, Olympus and Pavonis Mons, and Tholi volcanoes including Tharsis Tholus and Ceranius Tholus (Figure 1.1). Effusive volcanism shaped the majority of the volcanoes in Tharsis (Robbins et al. 2011).

Another volcanic region, Syrtis Major, has a diameter of 1200 km, and is home of two major volcanoes, Meroe Patera and Nili Patera (Figure 1.1). The highest edifice in Syrtis Major extends up to 2 km above the Mars mean geoid (Robbins et al. 2011). This region is partly characterized by explosive eruptions.

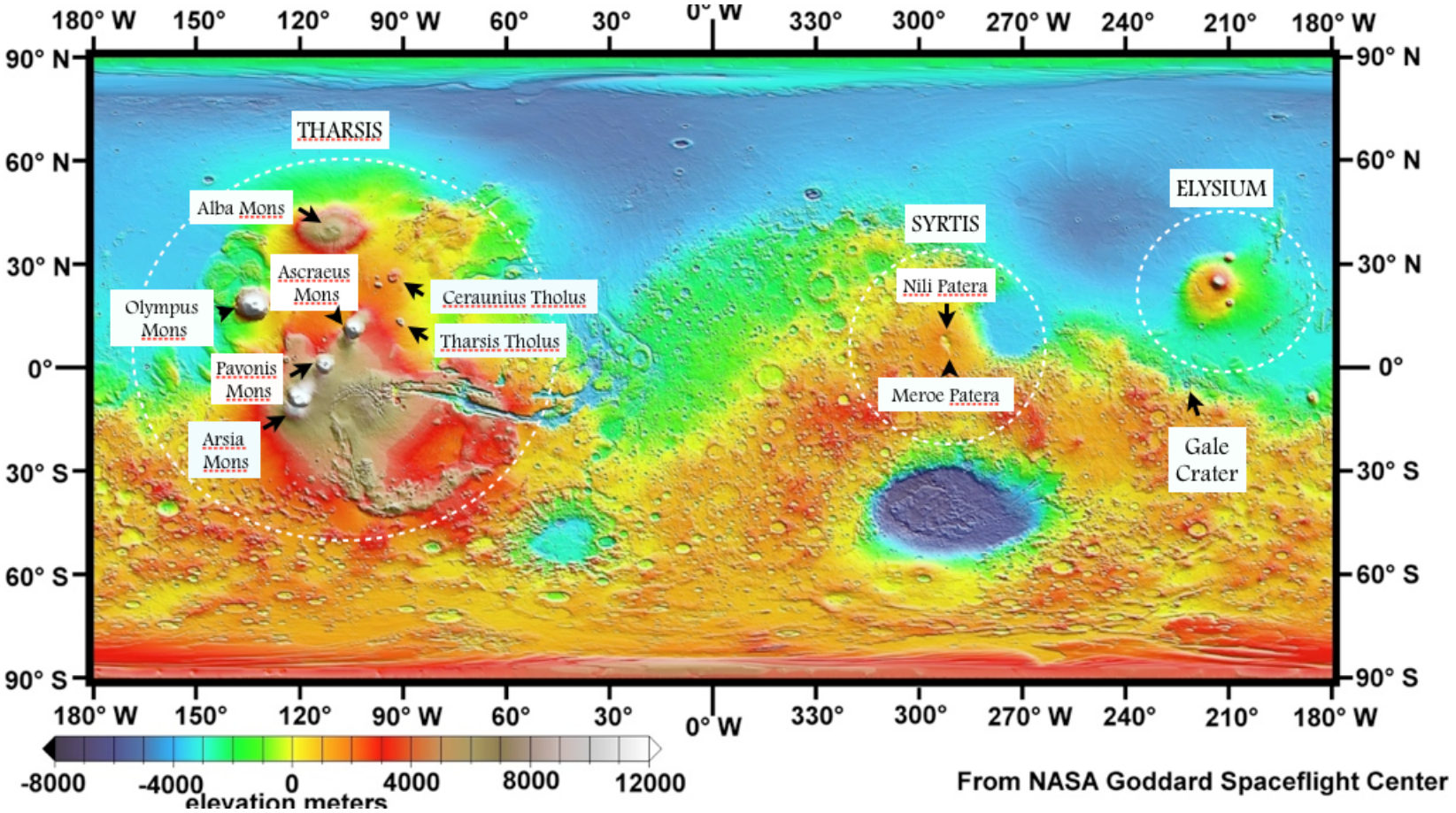

Figure 1.1 : Tharsis and Syrtis volcanic districts on Mars and their major volcanoes, are shown here. The shaded relief and color topographic map is from the Mars Orbiter Laser Altimeter (MOLA), created by the MOLA team at Goddard Space Flight Center, NASA. Image credit: MOLA Science Team. The data from MOLA are in the public domain.

1.1.3 Size-frequency Distribution for Dating Volcanic Activity

The size-frequency distribution of craters on the surface of Mars is an indicator of the relative ages of martian volcanoes. The crater number density on old surfaces is higher compared to new ones, owing to the fact that time allowed more craters to form on old surfaces. However, due to continued deposition processes and the lack of any absolute ages, all ages based on crater counting are uncertain.

Using the High Resolution Stereo Camera (HRSC) onboard Mars Express, Neukum et al. (2004) applied cratering chronology models to investigate the geologic evolution of two focal points of volcanism on Mars: Tharsis province and Elysium area. On the summit of Ascraeus Mons in the Tharsis region, their study of different calderas shows different volcanic activities, ranging from 3.6 Gyr to 100 Myr ago. They identified 5 different calderas on Ascraeus Mons with intermittent volcanic activities that occurred around 100 Myr, 200 Myr, 400 Myr, 800 Myr and 3.6 Gyr ago. As a consequence of prolonged episodic volcanic activity, Neukum et al. (2004) suggested that volcanoes in Tharsis may still be outgassing, even today.

Werner (2009) who also used data from HRSC, was able to confirm the earlier measurements of Neukum et al. (2004), and suggested that the most recent volcanic activity is being localized in Tharsis, with volcanism occurring up until about 200-100 Myr ago. Hauber et al. (2010) investigated plain-style volcanism in Tharsis using Mars Reconnaissance Orbiter's ConTeXt Camera (CTX) and determined the ages of 60 volcanoes and lava flows. They dated clusters of low shield volcanoes to ages < 100 Myr.

Robbins et al. (2011) conducted the largest and most comprehensive research to date (May 2010), constraining the time since volcanoes on Mars were last active. Using high-resolution images from the CTX, down-sampled to 10 m/pixel, they targeted 93 calderas for extensive crater counting within 20 major volcanoes on Mars, and inferred a volcanic activity in Tharsis ending around $\sim$150-100 Myr ago, in Arsia, Olympus and Pavonis Montes.

Robbins et al. (2011) also concluded that for the Tharsis region, the volcanic activity, even-though intermittent, extended between the Noachian and the late Amazonian, and in

general the smallest volcanoes show older caldera age than the large volcanoes in Tharsis, with the exception of Alba Mons that shows different caldera ages between 3.0 Gyr and 300 Myr.

In addition, images from the Mars Global Surveyor helped Hartmann et al. (1999) to refine the results of crater count statistics by studying crater sizes down to 16 m. The wide range of surface ages indicated by their results suggests a continuous process of volcanism that could extend to the current geological time.

In Earth's volcanoes, large quantities of volatiles are released into the atmosphere, and the same undoubtedly applies for Mars. The lower surface gravity and atmospheric pressure on the red planet allow more lava to reach the surface during a volcanic activity, releasing higher amounts of volcanic gases into the atmosphere (Forget et al. 2008). Even between periods of volcanic activity, a slow release of sulfur compounds and carbon dioxide from fractures in magma chambers at shallow depths could still occur (Mouginis-Mark et al. 1992).

1.1.4 Inventory of Volcanic Gases

As lava migrates from subsurface reservoirs to the surface, dissolved gases are released into the atmosphere through the regolith, volcanic vents or hydrothermal systems. By analogy with the Earth (Symonds et al. 1994), volcanic outgassing includes sulfur compounds such as sulfur dioxide (SO_2), hydrogen sulfide (H_2S) and sulfur monoxide (SO), a major photochemical product (Wong et al. 2005, 2004, 2003). Symonds et al. (1994) and Oppenheimer et al. (2011) listed the inventory (mol%) of gases in some terrestrial volcanoes as shown in Table 1.1.

The Momotombo volcano in central America is a result of convergent plate boundaries, where the process of subduction of an oceanic plate introduces water derived from seawater to the deep crust. During the formation of such volcanoes, water vapor and chlorine are emitted at higher rates than in divergent plate volcanoes such as Erta'Ale in Ethiopia, or hot spot volcanoes such as Kilauea in Hawai'i. The higher percentage of HCl released by

Table 1.1 : Representative compositions of volcanic gas-samples (mol%) in some terrestrial volcanoes. Data taken from Symonds et al. (1994) and Oppenheimer et al. (2011).

	H_2O	CO_2	SO_2	H_2	CO	H_2S	HCl	HF	OCS
Erta'Ale	77.2	11.3	8.34	1.32	0.44	0.68	0.42	-	-
Momotombo	97.1	1.44	0.50	0.70	0.01	0.23	2.89	0.26	-
Kilauea	37.1	48.9	11.8	0.49	1.51	0.04	0.08	-	-
Erebus (2004)	57.9	36.4	1.40	-	2.33	-	0.69	1.27	0.01
Nyiragongo (2005)	70.5	23.7	4.55	-	0.86	-	0.26	0.11	0.0023

Momotombo is the result of ocean water, containing chlorine, that gets incorporated as the lava migrates to the surface. In addition to H_2S, SO_2 and SO, the detection of carbonyl sulfide (OCS) has been reported. Infrared spectroscopy enabled quantitative measurements of OCS in the volcanic plumes of a handful of volcanoes including Erebus, Antarctica (Oppenheimer & Kyle 2008; Oppenheimer et al. 2011), Aso, Japan (Mori & Notsu 1997; Mori & Notsu 2008), and Nyiragongo, Democratic Republic of the Congo (Sawyer et al. 2008).

OCS is a byproduct of the chemical reaction involving SO_2 and CO (Hong & Fegley 1997; Oppenheimer et al. 2011):

$$SO_2 + 3CO = OCS + 2CO_2 \tag{1.1}$$

By measuring the compositions of fluxes from 14 volcanoes around the world, Mori & Notsu (1997) were able to demonstrate that the CO/CO_2 ratio is correlated with the equilibrium temperature (T) of the volcanic gases. The relationship is:

$$\log(CO/CO_2) = -4417(\pm 368)/T + 1.76(\pm 0.33) \tag{1.2}$$

In a smiliar equilibrium reaction, just like for CO/CO_2, one would expect to find a correlation between the OCS/SO_2 ratio and the equilibrium temperature. In fact, Sawyer et al. (2008) found remarkably similar proportions of OCS and SO_2 ($OCS/SO_2 = 0.0005$)

between 2005 and 2007, in the regime of the steady-state degassing from Nyiragongo volcano.

Even before these findings, researchers were looking for correlations between the gas temperature and the ratio of different elements involved in the chemical reaction shown in Eq.(1.1). Belviso et al. (1986), for example, using data from previous publications and their own observations, estimated the global contribution of volcanic OCS on Earth. They established a correlation between the OCS/CO_2 ratio and the temperature of the volcanic plume, and concluded that the ratio increases with temperature. Even at temperatures as low as 360 K, they were able to detect OCS in the plume from Vulcano volcano, Italy. By using measurements of the OCS/SO_2 ratio and the SO_2 fluxes from about 520 volcanoes around the globe, they estimated a global release of 6×10^9 - 90×10^9 g/year of volcanic OCS. Average values for the measured OCS outgassing rates and OCS/SO_2 abundance ratios for some Earth volcanoes are shown in Table 1.2.

Table 1.2 : Average values for the measured OCS outgassing rates and OCS/SO_2 abundance ratios for some Earth volcanoes.

Volcano	Average OCS flux (kg/s)	OCS/SO_2	Period over which the measurements were obtained	Reference
Nyiragongo (Congo)	38	5×10^{-4}	May/June 2005	Sawyer et al. (2008)
Nyiragongo (Congo)	23	5×10^{-4}	January 2006	Sawyer et al. (2008)
Aso (Japan)	-	1.5×10^{-3}	July 26, 1996	Mori & Notsu (1997)
Erebus (Antarctica)	5.9×10^{-3}	$\sim 7.5\times10^{-3}$	December 2004	Oppenheimer & Kyle (2008)

1.2 Motivation

1.2.1 Search for Active Release of Volcanic Gases on Mars

Even though more recent active volcanism on Mars has not yet been found (Edgett et al. 2010), the presence of local outgassing vents may be possible. Outgassing from local vents could temporarily alter the composition and disrupt the equilibrium of Mars' atmosphere (Wong et al. 2003). In terms of possible outgassing, for example, methane release on Mars in mid-summer in the northern hemisphere in 2003, may have occurred from subsurface

warming or by connecting subpermafrost regions to the atmosphere by openings or fissures in scarps or crater walls (Mumma et al. 2009).

Models by Gaillard & Scaillet (2009) show that the volcanic gases released from martian volcanoes during formation of the Tharsis region were 10-100 times richer in sulfur compared to the gases released from volcanoes on Earth. Since SO_2 is the main sulphuretted gas released (Andres et al. 1991), its absence places a sensitive limit on the volcanic outgassing on Mars today.

To look for such outgassing, it is necessary to search for H_2S, OCS and SO, along with SO_2. Measuring the chemical composition of the gas flux gives important clues about the magma and its volatile content, its behavior, and the dynamics of degassing under martian conditions. In Earth's volcanoes, the SO_2/H_2S ratio generally varies between 10^{-1} and 3×10^2. Measuring the relative proportions of the sulfur species is essential for understanding local conditions in the magma chambers where these species form, because the SO_2/H_2S ratio is also dictated by the local pressure and temperature (Oppenheimer et al. 2011; Delmelle & Stix 2000).

In case of a one-time outgassing event on Mars, the (photochemical) lifetime of 2 years for SO_2 (Wong et al. 2003, 2004, 2005; Krasnopolsky 2005) requires a search that must span multiple seasons and years in order to constrain episodic or occasional release.

In the case of a steady state outgassing, the number of molecules in the atmosphere above the outgassing source reaches an equilibrium state. Since the lifetime of SO_2 in the martian atmosphere is larger than the global mixing timescale of 0.5 year (Krasnopolsky et al. 2004), one can consider the molecules to be well mixed across the planet, and no major seasonal changes should be observed.

1.2.2 Relationship to Methane

The presence of methane (CH_4) in Earth's atmosphere is for the most part a result of biological activity (Atreya et al. 2007; Mumma et al. 2009; Webster et al. 2015). Non-

biological origins include volcanism, and the abundance ratio of volcanic CH_4/SO_2 released in Earth's volcanoes varies between 10^{-5} and 1 (Delmelle & Stix 2000; Nakagawa et al. 2009).

Using the 3-meter NASA Infrared Telescope Facility, Mumma et al. (2009) reported the presence of methane plumes above Syrtis Major, Nili Fossae and Terra Sabae during Northern summer on Mars in 2003. The total amount of CH_4, when integrated over the size of the plumes, is 42 ktons. When distributed over the entire planet, it corresponds to a mixing ratio (number of moles of a species per 1 mole of atmosphere) of 6 parts per billion (hereafter ppbv). Although production and release mechanisms were explored, no conclusions were drawn regarding the biological or geochemical origins of the methane released.

The presence of the methane plumes did not persist, even-though the estimated photochemical lifetime of CH_4 is $\sim$ 350 years (Krasnopolsky et al. 2004). There should be some destruction mechanism that is more powerful than photochemistry.

Webster et al. (2015) conducted in situ observations also looking for methane on Mars, using the tunable laser spectrometer of the geochemical laboratory Sample Analysis at Mars (SAM) on-board the Mars rover at Gale crater (4.5°S, 137.4°E) for 605 sols (1 sol = 1 day on Mars = 24h 35.3 min), over a 20-month period between 25 October 2012 and 9 July 2014. They confirmed the presence of transient spikes of methane between mid and late Northern spring on the red planet, with a mean abundance value of 7.19 ± 2.06 ppbv over the period where transients were observed between 29 November 2013, and 28 January, 2014. The methane spikes did not persist, and a mean background level of atmospheric methane of 0.69 ± 0.25 ppbv was presented. This number is not larger than what is expected from meteoric infall.

The methane release between 2003 and 2013 occurred at different regions on Mars (Figure 1.1), at two different seasons, and the methane did not persist. Therefore, transient outgassing from the surface of Mars is not something to be considered unusual. The

continuous monitoring of atmospheric CH_4 on Mars is critical for identifying the biotic or abiotic origins, and helps locating the sources of the methane release.

The possibility of ruling out a volcanic origin of methane could be addressed by conducting an observing strategy targeting the release of magmatic volatiles on the red planet, such as SO_2, H_2S, and OCS, and their photochemical product, SO.

1.2.3 Solidification Timescales

Robbins et al. (2011) inferred that volcanic activity in Tharsis ended around ∼150-100 Myr ago, in Arsia, Olympus and Pavonis Montes, and the question remains if this is enough time for the magma reservoirs beneath the volcano summit to solidify fully. The large volume of lava flows on Mars ($>$ 100 km^3 in the case of Tharsis (Wood 1984b; Cattermole 1987)), indicates that the sizes of magma chambers of martian volcanoes are 40-100 times that of their terrestrial counterparts (Wilson et al. 2001), hence a longer solidification timescale.

Calderas are good indicators of the widths of the magma chambers beneath them (Marti et al. 1994). As viewed from the top, the diameter of a magma reservoir is assumed to be roughly the size of the diameter of its corresponding summit caldera (Wood 1984a). The vertical extent (H) and the depth (Z) to the top of magma reservoirs are theoretically expected to vary inversely proportional to the acceleration of gravity, with a factor of ~ 2.5 larger for martian volcanoes compared to Earth (Wilson & Head 1994; Wilson et al. 2001). We adopt H and Z to be 10 km, as suggested by Wilson et al. (2001). We consider the magma chamber for Arsia Mons to be a cylinder, with a diameter of 115 km (Robbins et al. 2011), equal to the caldera's size, and a vertical extent H. The volume of the magma chamber of Arsia is then estimated to be 10^5 km^3. The power output from the magma chamber, or the amount of thermal energy lost to the surface with respect to time, is proportional to the horizontal cross-sectional area of the chamber, and is inversely proportional to the depth of the top of the chamber. For a magma reservoir situated at Z = 10 km below the

surface, the power output is given by the fundamental heat conduction equation:

$$P = dQ/dt = \frac{k \times A \times (T_m - T_s)}{Z} \tag{1.3}$$

where k = 1 W $m^{-1}K^{-1}$ is the thermal conductivity (Robbins et al. 2011), A is the cross sectional area (m^2), T_m is the magma temperature (1300 K), and T_s is the surface temperature (150 K at the top of the volcano). The resulting power output is P $\sim$ 1200 MW.

The mantle magma supply to the magma chamber is considered to be cut off after the major recent volcanic activity ended (ca. 100-150 Myr ago), and the reservoir is left to cool down, while the magma is degassing. The crystals formed in the magma pool stay close to the top of the magma chamber and form a solidification front, or settle down the bottom of the chamber. Martin & Nokes (1988) conducted models describing crystal sedimentation in magma pools, and provided settling timescales, or the time it takes the crystals to settle at the bottom of the magma chamber, as described by the equation:

$$t_{settle} = 9\,H\,\mu/2\,g\,\Delta\rho\,r^2 \tag{1.4}$$

where H is the height of the convective layer of magma, μ is the viscosity of the basalt magma, g is the acceleration of gravity, $\Delta\rho$ is the difference in densities between the crystals and the surrounding magma, and r is the radius of the crystal. We adopt values for the basalt magma as presented in Hawkesworth et al. (2000), with $\mu = 10^2 - 10^4$ Pa s, $\Delta\rho = 500$ kg/m^3 and r = 10^{-3} m. Therefore we estimate t_{settle} = 80 - 80,000 yr.

Hawkesworth et al. (2000) conducted a simple heat balance model for closed cooling magma chambers, and calculated crystallization time scales for the magma it contains. The thermal energy is released from cooling and crystallizing magma. The corresponding cooling timescale is calculated by the following energy balance equation (Hawkesworth et al. 2000):

$$t_{cool} = V\rho\,(c\,\Delta T + \Phi\,L)/P \tag{1.5}$$

where t_{cool} is the cooling time, V is the volume, ρ is the density, c is the specific heat (specific means per unit mass, and is written in lower case), and L is the latent heat of crystallization of the magma. Φ is the crystallization mass fraction, and for full solidification, $\Phi = 1$. P is the power output from the magma chamber, as calculated in equation 1.3. As a comparison, P ranges between 100 and 1000 MW for terrestrial volcanoes (Hochstein 1995). Volcanism on Mars is of basaltic origin (Carr 2006). In order for the basalt magma to solidify, it requires a temperature drop ΔT in the range of 200 K (Hort 1997). The values for the physical properties of such magma are listed in Spera (2000), with $\rho = 2600$ kg/m^3, c = 1500 J/kg/K and L = 4 $\times 10^5$ J/kg. Therefore, we estimate the magma chamber to reach full solidification in 5 Myr.

1.2.4 Is There any Current Volcanic Activity in the Crust of Mars?

The solidification timescale is smaller than the estimated time since the last volcanic activity on Mars has occurred, if the mantle magma supply to the magma chamber is considered to be cut off since then, and the reservoir is left to cool down. In contrast, the possible lifetime of volcanoes on Mars, extending to 2-3 billion years in the case of Olympus Mons, although intermittent, makes such longevity exceptional among other volcanoes in the solar system (Frankel 1996). Such longevity increases the probability of finding long-term active vents, that might be present on Mars today. In addition, several lines of evidence show that the volcanic activity in the Tharsis region happened episodically, with periods of activity lasting for < 1 Myr, and "quiet" periods extending for ~ 100 Myr. The study of complex flows around the edges of the large volcanic structures in Tharsis, show that vents and fissures are quite present throughout much of Tharsis (Schaber et al. 1978; Mouginis-Mark et al. 1982, 1992). In the case of current active volcanism with no extrusion, the magma does not reach the surface. The SO_2 that is originating from the magma in the reservoir underneath the volcano is therefore released into the atmosphere through the vents and scarps in the surface of Mars.

This work is motivated by the possibility of detecting further substantial outgassing, and attempting to constrain the current volcanic activity on Mars. We searched for volcanic outgassing from the surface of the planet, and improved the abundance of sulfur species in its atmosphere. Looking for the sulfur-bearing species is extremely helpful as an indicator that such outgassing did occur.

Two of the best candidate places to look for such outgassing on Mars are Tharsis, where the most recent volcanic activity is believed to have occurred, and the Syrtis volcanic region where methane release has been reported (Fig. 1.1).

1.3 State of Research

Prior to this work, ground-based attempts to detect gaseous sulfur species in the atmosphere of Mars placed upper limits on the abundance. SO_2 was looked for by Encrenaz et al. (2011) during October 2009, and Krasnopolsky (2012) during June 2003, at 7.4 μm using the Texas Echelon Cross Echelle Spectrograph (TEXES) at the NASA Infrared Telescope Facility (IRTF). In order to compensate for the low signal-to-noise ratio caused by the opacity of Earth's atmosphere near this wavelength, Encrenaz et al. (2011) and Krasnopolsky (2012) co-added the spectra spatially and spectrally at several selected transitions, and obtained a similar stringent upper limit of 0.3 ppbv at 2σ. In the submillimeter, SO_2 at the $J_{n,k} = 16_{4,12} - 16_{3,13}$ transition at 346.524 GHz was searched for during December 2007 Nakagawa et al. (2009), and a stringent upper limit of 2.0 ppbv was achieved. Encrenaz et al. (1991) looked for H_2S in the millimeter at the $J_{n,k} = 2_{2,0} - 2_{2,1}$ transition at 216.71 GHz, and found an upper limit of 20 ppbv for the mixing ratio. Using the Mariner 9 Infrared spectrometer (IRIS), Maguire (1977) targeted minor constituents in the atmosphere of Mars between 200 and 2000 cm^{-1}, including OCS at its fundamental band ν_1 centered at 859 cm^{-1}. After combining 1747 spectra spanning almost one Mars year beginning later 1971, no OCS was detected, and an upper limit of 14 ppbv (at 2σ) was established. Using the OCS (12-11) transition at 145.95 GHz in the radio, Encrenaz et al.

(1991) were not able to find evidence for carbonyl sulfide, and the resulting upper limit for the mixing ratio is 70 ppbv. SO was searched by Nakagawa et al. (2009), but an upper limit was not reported. Table 1.3 is a summary table listing the previous upper limits for the sulphuretted species in the atmosphere of Mars.

Table 1.3 : Previous abundance limits (2σ) for the sulphuretted species on Mars.

Molecule	Abundance Limit (ppbv)	Reference
SO_2	<0.3 (in the IR)	Encrenaz et al. (2011) and Krasnopolsky (2012)
SO_2	<2.0 (in the submm)	Nakagawa et al. (2009)
OCS	<14 (in the IR)	Maguire (1977)
OCS	<70 (in the millimeter)	Encrenaz et al. (1991)
H_2S	<20 (in the millimeter)	Encrenaz et al. (1991)
SO	-	

1.4 Goal of Research

To summarize the goals of this work:

- Conduct the most comprehensive multi-band, multi-species search for active release of volcanic gases on Mars to date.
- Draw conclusions on the levels of current volcanic activity in the crust of Mars.
- In case of absence of current volcanism, place sensitive limits on volcanic outgassing, and stringent upper limits on the above-mentioned sulphuretted species in the atmosphere of Mars.
- Give more insights on the possibility of a volcanic origin of the methane released on Mars in 2003 and 2013.

References

Andres, R. J., Rose, W. I., Kyle, P. R., de Silva, S., Francis, P., Gardeweg, M., & Moreno Roa, H. 1991, J. Volc. Geotherm. Res., 46, 323

Atreya, S. K., Mahaffy, P. R., & Wong, A.-S. 2007, Planet. Space Sci., 55, 358

Barlow, N. 2008, Mars: An Introduction to its Interior, Surface and Atmosphere (Cambridge University Press)

Belviso, S., Nguyen, B. C., & Allard, P. 1986, Geophys. Res. Lett.

Carr, M. H. 2006, in The Surface of Mars. ISBN-10 0-521-87201-4; ISBN-13 978-0-521-87201-0. (Cambridge University Press), 43–44

Cattermole, P. 1987, J. Geophys. Res., 92, 553

Cattermole, P. J. 2001, Mars: The Mystery Unfolds (Oxford University Press)

Delmelle, P. & Stix, J. 2000, in Encyclopedia of Volcanoes, ed. H. Sigurdsson (Academic Press, San Diego), 803–815

Edgett, K. S., Cantor, B. A., Harrison, T. N., Kennedy, M. R., Lipkaman, L. J., Malin, M. C., Posiolova, L. V., & Shean, D. E. 2010, in Bulletin of the American Astronomical Society, Vol. 42, AAS/Division for Planetary Sciences Meeting Abstracts #42, 1016

Encrenaz, T., Greathouse, T. K., Richter, M. J., Lacy, J. H., Fouchet, T., Bézard, B., Lefèvre, F., Forget, F., & Atreya, S. K. 2011, Astron. & Astrophys., 530, A37

Encrenaz, T., Lellouch, E., Rosenqvist, J., Drossart, P., Combes, M., Billebaud, F., de Pater, I., Gulkis, S., Maillard, J. P., & Paubert, G. 1991, Ann. Geophys., 9, 797

Forget, F., Costard, F., & Lognonné, P. 2008, Planet Mars: Story of Another World (Springer Praxis Books)

Frankel, C. 1996, Volcanoes of the Solar System (Cambridge University Press)

Gaillard, F. & Scaillet, B. 2009, Earth Planet. Sci. Lett., 279, 34

Greeley, R. 1987, Science, 236, 1653

Hartmann, W. K., Malin, M., McEwen, A., Carr, M., Soderblom, L., Thomas, P., Danielson, E., James, P., & Veverka, J. 1999, Nature, 397, 586

Hartmann, W. K. & Neukum, G. 2001, Space Sci. Rev., 96, 165

Hauber, E., Brož, P., & Jagert, F. 2010, in Lunar Planet. Inst. Sci. Conf. Abstr., Vol. 41, 1298

Hawkesworth, C. J., Blake, S., Evans, P., Hughes, R., Macdonald, R., Thomas, L. E., Turner, S. P., & Zellmer, G. 2000, Journal of Petrology, 41, 991

Head, J. W. 2007, The geology of Mars: new insights and outstanding questions (Cambridge University Press), 1

Hochstein, M. P. 1995, J. Volc. Geotherm. Res., 68, 117

Hong, Y. & Fegley, B. 1997, Icarus, 130, 495

Hort, M. 1997, J. Volc. Geotherm. Res., 76, 297

Krasnopolsky, V. A. 2005, Icarus, 178, 487

—. 2012, Icarus, 217, 144

Krasnopolsky, V. A., Maillard, J. P., & Owen, T. C. 2004, Icarus, 172, 537

Maguire, W. C. 1977, Icarus, 32, 85

Marti, J., Ablay, G. J., Redshaw, L. T., & Sparks, R. S. J. 1994, J. Geol. Soc., 151, 919

Martin, D. & Nokes, R. 1988, Nature, 332, 534

Mori, T. & Notsu, K. 1997, Geophys. Res. Lett., 24, 2047

Mori, T. & Notsu, K. 2008, Geochem. J., 42, 133

Mouginis-Mark, P. J., Wilson, L., & Zuber, M. T. 1992, The Physical Volcanology of Mars (Cambridge University Press), 424–452

Mouginis-Mark, P. J., Zisk, S. H., & Downs, G. S. 1982, Nature, 297, 546

Mumma, M. J., Villanueva, G. L., Novak, R. E., Hewagama, T., Bonev, B. P., DiSanti, M. A., Mandell, A. M., & Smith, M. D. 2009, Science, 323, 1041

Nakagawa, H., Kasaba, Y., Maezawa, H., Hashimoto, A., Sagawa, H., Murata, I., Okano, S., Aoki, S., Moribe, N., Mizuno, A., Momose, M., Ohnishi, T., Mizuno, N., & Nagahama, T. 2009, Planet. Space Sci., 57, 2123

Neukum, G., Jaumann, R., Hoffmann, H., Hauber, E., Head, J. W., Basilevsky, A. T., Ivanov, B. A., Werner, S. C., van Gasselt, S., Murray, J. B., McCord, T., & HRSC Co-Investigator Team. 2004, Nature, 432, 971

Oppenheimer, C. & Kyle, P. R. 2008, J. Volc. Geotherm. Res., 177, 743

Oppenheimer, C., Scaillet, B., & Martin, R. S. 2011, Rev. in Min. and Geochem., 73, 363

Robbins, S. J., Achille, G. D., & Hynek, B. M. 2011, Icarus, 211, 1179

Sawyer, G. M., Carn, S. A., Tsanev, V. I., Oppenheimer, C., & Burton, M. 2008, Geochemistry, Geophysics, Geosystems, 9

Schaber, G. G., Horstman, K. C., & Dial, Jr., A. L. 1978, in Lunar and Planetary Science Conference Proceedings, Vol. 9, Lunar and Planetary Science Conference Proceedings, 3433–3458

Spera, F. J. 2000, in Encyclopedia of Volcanoes (Academic Press), 171–190

Symonds, R., Rose, W., Bluth, G., & Gerlach, T. 1994, Volatiles in Magmas: Miner. Soc. Am. Rev. Miner., 30, 1

Tanaka, K. L. & Davis, P. A. 1988, J. Geophys. Res., 93, 14893

Webster, C. R., Mahaffy, P. R., Atreya, S. K., Flesch, G. J., Mischna, M. A., Meslin, P.-Y., Farley, K. A., Conrad, P. G., Christensen, L. E., Pavlov, A. A., Martín-Torres, J., Zorzano, M.-P., McConnochie, T. H., Owen, T., Eigenbrode, J. L., Glavin, D. P., Steele, A., Malespin, C. A., Archer, P. D., Sutter, B., Coll, P., Freissinet, C., McKay, C. P., Moores, J. E., Schwenzer, S. P., Bridges, J. C., Navarro-Gonzalez, R., Gellert, R., Lemmon, M. T., & Team, M. 2015, Science, 347, 415

Werner, S. C. 2009, Icarus, 201, 44

Wilson, L. & Head, J. W. 1994, Reviews of Geophysics, 32, 221

Wilson, L., Scott, E., & Head, J. 2001, J. Geophys. Res., 106, 1423

Wong, A.-S., Atreya, S. K., & Encrenaz, T. 2003, J. Geophys. Res., 108, 5026

—. 2004, J. Geophys. Res., 109, 1007

—. 2005, J. Geophys. Res., 110, 10002

Wood, C. A. 1984a, J. Geophys. Res., 89, 8391

Wood, C. A. 1984b, in Lunar and Planetary Science Conference, Vol. 15, 929–930

Chapter 2

Scientific Approach in Searching for Volcanic Outgassing

This chapter lists the best molecular species for probing volcanic outgassing on Mars, and presents the photochemical products and their corresponding lifetimes when releasing H_2S and SO_2 into the atmosphere. It examines the best spectral windows within which to observe the sulphuretted species, and lists the frequencies of their strongest spectroscopic transitions where one can obtain the best sensitivity limits. At the end, the observing plans and strategies to probe volcanic outgassing on Mars using the NASA Infrared Telescope Facility, the Caltech Submillimeter Observatory, and the James Clerk Maxwell Telescope, are presented.

2.1 Candidates for Probing Volcanic Outgassing on Mars: H_2S, SO_2, OCS and SO

Molecular species, through their vibrational and rotational transitions, exhibit vibrational and rotational spectra spanning the infrared, submillimeter and millimetric wavelength regimes (Encrenaz et al. 1995). High resolution near-infrared spectroscopy (R= $\nu/\Delta\nu \sim$ 40,000), and heterodyne spectroscopy in the submillimeter (R= 10^5-10^6),

are powerful tools for analyzing the vibrational and rotational spectra respectively. They can reveal important clues about the vertical structure and the chemical composition of the atmospheres (Encrenaz 2008), down to mixing ratios in the order of parts-per-billion.

H_2S and SO ro-vibrational transitions in the infrared are generally weak (Rothman et al. 2009). SO_2 has a strong band centered at 7.34 μm, but Earth's atmosphere is almost opaque at this wavelength. However, the strengths of rotational transitions of SO_2, H_2S and SO at submillimeter wavelengths, combined with Earth's high atmospheric transmission at these specific wavelengths, make it possible to achieve a sensitive search for these volcanic molecules. Therefore, one of the best ways to detect the molecules is through their rotational spectra (Encrenaz et al. 2004), including using large single dish antennae such as the Caltech Submillimeter Observatory (CSO) and the James Clerk Maxwell Telescope (JCMT).

OCS exhibits strong ro-vibrational bands, and it is possible to obtain a much more sensitive search for this molecule than reported previously. Figure 2.1 shows the infrared transmission spectrum (olive) of Earth's atmosphere above Maunakea, Hawai'i. The transmittance has been generated using ATRAN software (Lord 1992), and we acknowledge Gemini Observatory for the spectrum[1]. The line strengths of OCS (black), H_2S (purple), SO_2 (blue), and CO_2 (red) are taken from the HITRAN database (Rothman et al. 2009). The H_2S and SO_2 bands are weak compared to ones belonging to OCS. The strongest OCS band is the ν_3 fundamental band centered at 4.85 μm (2062 cm^{-1}). One would rely on such a band to get the best sensitivity on OCS, but spectral lines of CO_2, the most abundant molecule in the martian atmosphere (95 %), abound in this spectral region (see Figure 2.1). The presence of such a complex CO_2 band lowers the sensitivity to OCS, and therefore switching to the OCS at the R branch of its combination band ($\nu_1+\nu_3$) at 3.42 μm (2924 cm^{-1}) could give better sensitivities. More discussion on the sensitivity will follow in section 2.3.1. As mentioned in section 1.3, earlier ground-based attempts to detect carbonyl sulfide in the atmosphere of Mars were unsuccessful.

[1]http://www.gemini.edu/sciops/telescopes-and-sites/observing-condition-constraints/ir-transmission-spectra

Because of the frequency-dependent field of view of a telescope, single-dish antennae like the CSO and the JCMT encompass the entire disk of the planet. In contrast, with IRTF/CSHELL at near infrared wavelengths, a 0.5 arsec slit, one could sample local regions on Mars down to 350 km spatial resolution when the angular size of Mars is 10 arsec. Therefore, infrared spectroscopy presents a major and crucial advantage over the submillimeter, by looking at "specific" regions on Mars where local vents might exist.

In addition to the sulfur-bearing molecules, hydrogen fluoride (HF) and hydrogen chloride (HCl) are among the magmatic gases released from Earth's volcanoes (Table 1.1 in Chapter 1). We will discuss the feasibility of their observations in section 2.3.3.

As part of our multi-band survey of sulfur species on Mars, we searched for H_2S, SO_2 and SO in the millimeter region, and OCS in the infrared. Measurements of the absorption lines of SO_2 ($J_{n,k} = 19_{1,19} - 18_{0,18}$) at 346.652 GHz, H_2S ($J_{n,k} = 3_{3,0} - 3_{2,1}$) at 300.505 GHz and SO ($J_n = 7_8 - 6_7$) at 304.077 GHz (Pickett et al. 1998) were proposed, in order to determine their abundance in the atmosphere of Mars. This is possible by synthesizing the spectral lines of the sulfur species, using a radiative transfer model of the atmosphere of Mars, with a certain mixing ratio for each molecular compound. By measuring the depth (in units of brightness temperature) of the spectral line detected by the CSO, and fitting it to a synthetic line, one can infer the abundance of each molecule in the atmosphere of the planet.

2.2 What happens when H_2S and SO_2 are Released from Localized Vents on Mars?

In an attempt to estimate the abundance of sulfur compounds released into the atmosphere of Mars, Wong et al. (2003, 2004, 2005) developed a photochemical model. They considered outgassing of H_2S and SO_2 from possible hot spots. After being released into the atmosphere, a fraction of the molecules is photo-dissociated, another fraction reacts with other species in the atmosphere, and the remainder gets recycled back into the original

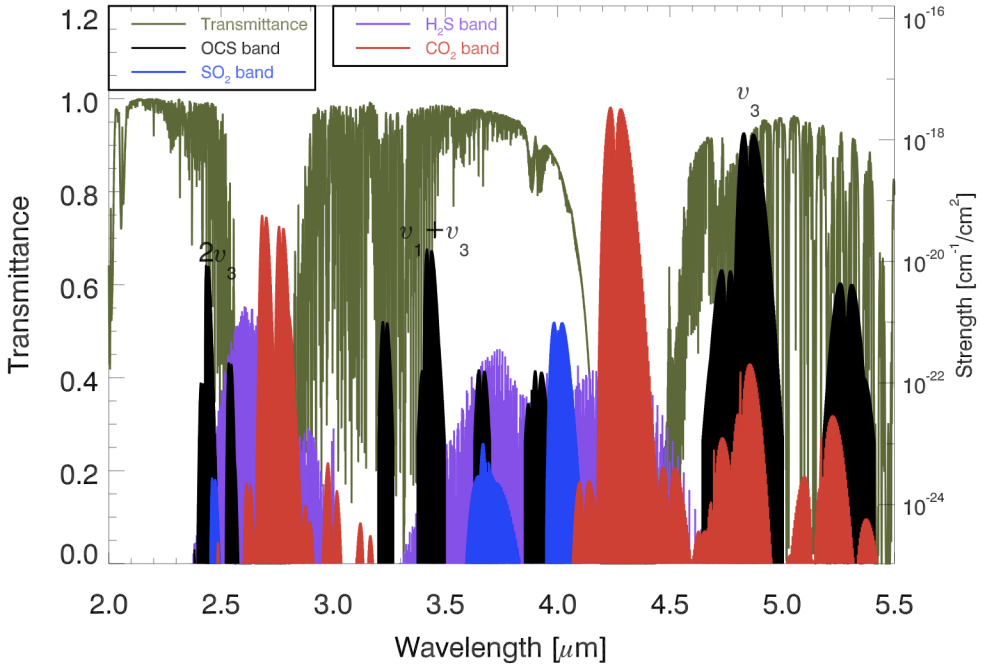

Figure 2.1 : Infrared transmission spectrum (olive) of Earth's atmosphere above Maunakea, Hawai'i. The transmittance has been generated using ATRAN software (Lord 1992), and we acknowledge Gemini Observatory for the spectrum. The legend in the figure identifies the line strengths of the spectroscopic bands and their positions at rest frequencies for each species. The transition strengths have been extracted from the HITRAN database (Rothman et al. 2009). The H_2S and SO_2 bands are weak compared to those of OCS.

molecules. Assuming an initial local abundance ratio at the surface of 100 ppm for the released H_2S and SO_2, the computed lifetime, or time it takes each species to be removed photochemically, is 600 days for SO_2 (Wong et al. 2005), 9 days for H_2S, and 4.6 hours for SO (Wong et al. 2003, 2005). An additional motivation to look for SO and H_2S along with SO_2 is that their relative abundance better constrains the photochemical cycle involving sulfur species during an outgassing event of volcanic origin.

Assuming they are correct, the short lifetimes of H_2S and SO do not allow the molecules to be globally mixed across the planet because they will be destroyed before that. Therefore, one should then assume a release of these molecules from a global distribution of sources on

Mars in order to have a detection in the submillimeter. At these wavelengths, the telescopes cannot resolve localized sources on the planet, and the results are disk-averaged.

2.3 Methodology

2.3.1 Looking for OCS with the NASA Infrared Telescope Facility

The atmosphere of Mars is very tenuous, with an average surface pressure P= 6 mbar. It is mainly composed of carbon dioxide CO_2 (95.32 %), and its other constituents being minor like nitrogen N_2 (2.7 %), argon Ar (1.6%), oxygen O_2 (0.13%) and carbon monoxide CO (0.08%) (Barlow 2008). These abundances are needed to compute the mean molecular weight of the martian atmosphere, $\bar{\mu}$ = 43.2 g/mol. The lower atmosphere is considered in hydrostatic equilibrium, and the pressure decreases exponentially with an average scale height H= 10.8 km. The column density N_j of an atmospheric component, or the number of molecules per cm^2 along the line of sight between the observer and the surface of Mars, is equal to (Sanchez-Lavega 2010):

$$N_j(cm^{-2}) = \frac{N_A\, q(x)}{\bar{\mu}\, g} \times P \tag{2.1}$$

where N_A is the Avogadro number, q(x) is the volume mixing ratio (number of moles of species per 1 mole of the atmosphere), $\bar{\mu}$ is the mean molecular weight of the atmosphere, g and P are the gravitational acceleration and the pressure at the surface of Mars, respectively.

The column density is related to the spectral line strength S (cm^{-1}/cm^{-2}) of the transition, and the equivalent width (EW) of the spectral line. The EW (cm^{-1}) is the area within a spectral line, divided by the continuum level around the line. In the optically thin case where the opacity is very small ($\tau \ll 1$), the EW is related to the column density by the simple formula: EW = $N_j \times S$ (Spitzer 1968). The strengths of the infrared transitions were provided by Rothman et al. (2009).

In case of no detection, we extracted upper limits for the mixing ratio of a trace species. For the purpose of obtaining preliminary limits, one could approximate the EW of a gaussian line normalized to its continuum level, by EW = FWHM $\times$ 3σ, where sigma is the RMS uncertainty in the continuum. The FWHM of the line, is related to the wavenumber at the OCS transition, and the spectrograph's spectral resolving power (R= $\nu/\Delta\nu$) by FWHM= ν/R, where ν is the frequency (cm^{-1}). Once the minimum detectable EW is retrieved, the column density N_j, and therefore the mixing ratio q(x) of OCS are estimated.

Figure 2.2 shows parts of the P and R branches of the OCS (ν_1+ν_3) combination band and the related line strengths (black), in addition to the Earth's atmospheric transmittance (blue). The R(10-23) transitions have the highest line strengths, and therefore should be targeted.

Using equation (2.1), and relating the EW to the column density, the 1σ uncertainty on the mixing ratio is given by the equation:

$$q(x) = \frac{4.43 \times 10^{-24} \times \nu}{R \times SNR \times S} \tag{2.2}$$

where R is the spectral resolving power of the spectrometer, ν is the frequency in wavenumber units, S is the spectral line strength, and SNR is the signal-to-noise ratio achieved on the continuum near the OCS line. Equation (2.2) shows that the highest resolving power (43,000 at CSHELL) gives the best upper limit on the mixing ratio. By choosing the R22 transition at 2926.46 cm^{-1} with $S_{R22} = 1.63 \times 10^{-20}$ cm^{-1}/cm^{-2} and at SNR=1000, an upper limit of 18 ppbv (1σ) for OCS could be obtained, and a corresponding equivalent width of 6.8 $\times 10^{-5}$ cm^{-1}. Improved detection limits are obtained by combining data from multiple lines (Chapter 4).

Using CSHELL's signal-to-noise equation[2], and the fact that at 3.42 μm at the (ν_1+ν_3) band, the photon noise from Mars dominates over the background noise, we find that the SNR is 930 in 4 hours of integration.

[2]http://irtfweb.ifa.hawaii.edu/ cshell/info.html

In contrast, at the ν_3 fundamental band of OCS centered at 4.85 μm (2062 cm^{-1}) where most of the radiation collected from the Mars is thermal emission, the sky (and telescope) emission is 8 times stronger than that of Mars. At this regime, the background noise dominates over the photon noise from Mars, and it degrades the sensitivity of the instrument. For example, for the same integration time of 4 hours, we get a SNR of 440, more than two times weaker than the SNR when observing Mars at 3.42 μm.

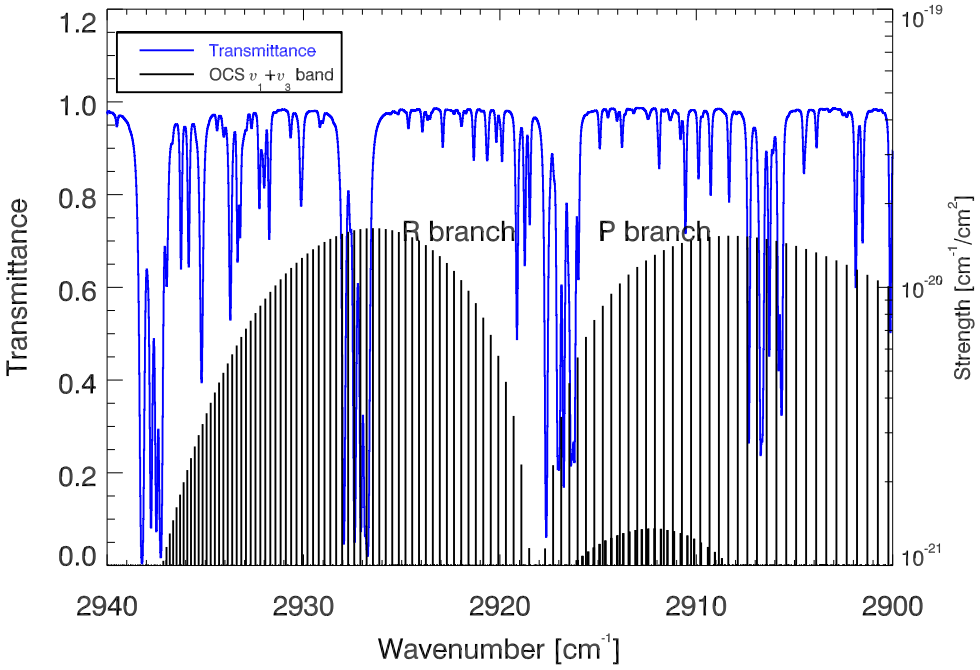

Figure 2.2 : Infrared transmission spectrum (blue) of Earth's atmosphere above Maunakea, Hawai'i at 43,000 spectral resolving power. The transmittance has been generated using ATRAN software (Lord 1992), and we acknowledge Gemini Observatory for the spectrum. The line strengths of the OCS P and R branches of the (ν_1+ν_3) combination band centered at 3.425 μm, and their positions are shown in black. The transition strengths have been extracted from the HITRAN database (Rothman et al. 2009).

The optimum times to observe Mars are at sufficient Doppler shifts between the planet and Earth to separate OCS lines on Mars from those present in the Earth's atmosphere (Δv $\geq$ 10 km/s), while preserving a large angular size for Mars in order to sample regions

on the red planet. A Mars Doppler shift of 10.0 km/s corresponds to 3.6 pixels, with 2.5 pixels/resolution for CSHELL[3] at R=43,000. The observing nights should have the longest coverage of Mars in the sky, combined with an airmass limit of less than 1.5.

The certainly plausible candidates to look for the volcanic outgassing, the Tharsis and Syrtis regions, are to be fully scanned at the sub-Earth point. When observing Mars, the slit will be placed at the central meridian, while the volcanic regions move past the slit when the planet is rotating. Due to limitations on the seeing (1 arcsec), and telescope tracking, the point-spread-function (PSF) corresponds to 5 pixels in the spatial direction. Guiding on CSHELL is done using an optical CCD, operating in the visible.

2.3.2 Looking for H_2S, SO_2 and SO in the Submillimeter

In order to understand the spectral line formation caused by atmospheric species, it is necessary to model the martian atmosphere using radiative transfer equations. At the lower parts of the atmosphere below 50 km where most molecules are present, pressure broadening dominates. The ratio between the pressure and the Doppler broadening depends on pressure, temperature, and frequency. The atmosphere of Mars is approximated to be plane parallel, and is divided into different layers (Fig. 2.3) of pressure ($P_1, P_2..., P_n$) and temperature ($T_1, T_2..., T_n$). When solar radiation reaches the surface of the planet, the latter gets heated and starts emitting as a gray body. The thermal radiation leaving the surface is then attenuated by the layers of the atmosphere on its way into space. The optical depth in every layer τ(z) is given by the equation (Encrenaz et al. 1995):

$$\tau(z) = \int_z^\infty \frac{S\ q(x)\ P_i}{\pi\ \Delta\nu\ k_B\ T_i} dz' \tag{2.3}$$

where S is the line strength, provided by Pickett et al. (1998) for millimeter and submillimeter transitions, q(x) the mixing ratio, P_i the pressure at each layer, $\Delta\nu$ is the line broadening, k_B is the Boltzmann constant and T_i is the layer temperature. When the

[3]http://irtfweb.ifa.hawaii.edu/ cshell/info.html

thermal radiation leaving the surface of Mars gets absorbed by an atmospheric layer, the latter is heated up, and starts emitting radiation depending on its temperature, which later gets absorbed by the atmospheric layers on top of it, as illustrated in Figure 2.3. At the

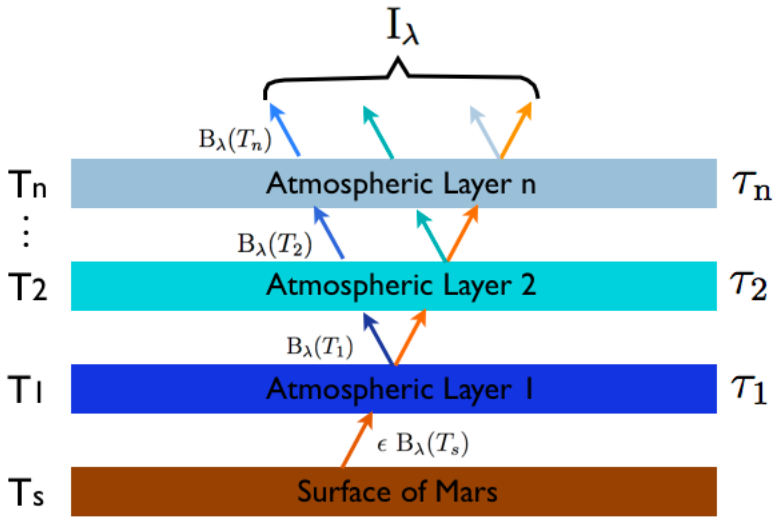

Figure 2.3 : This scheme illustrates how the radiative transfer operates in a planetary atmosphere. The atmosphere of Mars is divided into a number of layers. In each layer of optical depth τ, the radiation from the surface of Mars gets attenuated, and the corresponding atmospheric layer emits radiation depending on its temperature, which later gets absorbed by the atmospheric layers on top of it. The end-product is the emergent intensity. The arrows represent the radiation from the corresponding layer of the same color that is transmitted through the other layers on top. This schematic illustration has been made based on equation 2.4 (Encrenaz et al. 1995).

line center, the outgoing intensity (in units of brightness temperature) from Mars, in the submillimeter region and at the Rayleigh-Jeans regime, is given by Encrenaz et al. (1995):

$$T_c = \epsilon\, T_s\, e^{-\tau_0} + \int_0^{\tau_0} T(z)\, e^{-\tau(z)}\, d\tau(z) \tag{2.4}$$

where ϵ is the surface emissivity of Mars, T_s is the surface temperature, T(z) is the physical temperature of the atmospheric layer at altitude z, τ_0 is the total optical depth at line center, τ(z) is the optical depth of the atmospheric layer at altitude z.

By measuring the temperature contrast ΔT_b between the line center and the continuum around it, one can infer the abundance of each molecule in the atmosphere of the planet. The best transitions to be targeted for SO_2, H_2S and SO are listed in section 2.1. The best sensitivities on the abundance ratios for these molecules could be obtained when combining high transition strengths with a high Earth's atmospheric transmittance, as shown in Figure 2.4. The minimum difference in brightness temperature detected by the receiver (Encrenaz et al. 1995) is $\Delta T_{inst} = \alpha \times T_{sys}/\sqrt{(B \times t)}$, where B is the spectral resolution of 1 MHz for the array Acousto-Optic spectrometer (AOS) at the CSO, t is the total integration time (s), $\alpha = 2$ for beam switching observations, and T_{sys} (K) is the system temperature (equation 1 in chapter 3).

For single-dish antennae like the CSO and the JCMT, the results are disk-averaged because the telescope "sees" the planet as whole. With the planet's disk (10 arcsec) filling the main beam of the CSO (21 arcsec at 345 GHz) and a filling factor f (Equation 3.4 in Chapter 3), for 90 minutes on-source integration time, the following $f \times \Delta T_b/\Delta T_{inst}$ predictions are presented in the following Table 2.1:

Table 2.1 : Expected sensitivities (2σ) for the Mars submillimeter observations at the CSO.

Molecule	Frequency of Transition	Strength (cm^{-1}/cm^{-2})	$f \times \Delta T_b/\Delta T_{inst}$	Minimum Detectable Mixing Ratio
H_2S	300.51 GHz	1.490×10^{-21}	2	1.43 ppbv
SO_2	346.65 GHz	1.100×10^{-21}	2	1.75 ppbv
SO	304.08 GHz	3.844×10^{-21}	2	0.40 ppbv

The volcanic regions are observed at two geocentric Doppler shifts for Mars. The reason is not only to confirm or disprove detections, but also to separate between sulfur isotopes originating in the Earth's atmosphere from Martian ones. An opposite Doppler shift of Mars gives clues about the origins of the spectral lines in the observed spectrum.

Table 2.2 represents the telescope time awarded, and the observing parameters for Mars with the IRTF, CSO and the JCMT.

2.3.3 The Feasibility of Observing HF and HCl

Amounts of HF and HCl in the volcanic plumes of some Earth's volcanoes have been measured (see Table 1.1 in Chapter 1).

HF shows no transitions in the wavelength range of the CSO (200 GHz - 900 GHz). However, HF exhibits ro-vibrational transitions in the infrared. By using the maximum line strength S= 2.36 $\times 10^{-18}$ cm^{-1}/cm^{-2} of the R1 transition at 4038.96 cm^{-1} (2.47588 μm) and R = 40,000 on CSHELL, at SNR= 300, one could get an upper limit of 1.9 ppbv (3σ). There is no existing upper limit known for HF in the atmosphere of Mars. It is tricky to observe HF in the infrared, because the Earth's transmittance around the spectral band at 2.47 μm is very low, and it exhibits drastic fluctuations (see Figure 2.1).

Using the Herschel/HIFI (Hartogh et al. 2010), the existing upper limit for HCl on Mars at 1876 GHz is 0.3 ppbv (3σ). In the case of CSO, the maximum line strength of HCl is S= 2.498 $\times 10^{-20}$ cm^{-1}/cm^{-2} at 625.918 GHz (R0). It is $\sim$ 20 $\times$ weaker than the one targeted by Hartogh et al. (2010). In addition, the transmittance of the Earth's atmosphere is very low at 626 GHz (opacity <0.1)[4], whereas Hartogh et al. (2010) observed Mars from space. Therefore, one will not be able to get a better sensitivity on the mixing ratio of HCl on Mars using the CSO.

In the case of CSHELL in the infrared, the maximum line strength is S= 5.034 $\times 10^{-18}$ cm^{-1}/cm^{-2} of the R2 transition at 2944.91 cm^{-1}. At R= 40,000, SNR= 300, one can obtain an upper limit of 6.5 ppbv (3σ) on HCl. Villanueva et al. (2013) observed Mars using CSHELL on IRTF around 2998 cm^{-1}, and CRIRES (Kaeufl et al. 2004) on the 8-m Very Large Telescope (VLT) around 2981 cm^{-1} and 2998 cm^{-1}, and reported 3σ upper limits on atmospheric HCl of 2.1, 1.5 and 0.6 ppbv, respectively.

On Earth, HCl is released from convergent plate volcanoes at a higher rate than from hot spot volcanoes (Symonds et al. 1994), but this could not occur on current Mars because of the absence of plate tectonics on the planet. In addition, the higher percentage of HCl released by some of Earth's volcanoes is the result of ocean water, containing chlorine, that

[4]http://www.submm.caltech.edu/cso/weather/atplot.shtml

gets dissolved in the lava as it migrates to the surface. None of that happens for Mars, and therefore the probability of detecting volcanic HCl is very low.

Because of what is mentioned above, HCl and HF are unlikely volcanic gases on Mars, in addition to being difficult to detect.

To conclude this chapter, the discovery of active vents would be a breakthrough in terms of active geology on Mars and would profoundly impact our view of this planet, much like the discovery of methane on Mars (Mumma et al. 2003, 2004, 2005, 2009). A successful detection of OCS by IRTF, as well as H_2S, SO_2 and SO by the CSO would be also crucial for understanding the chemical pathways of sulfur compounds, and improve photochemical models on the distribution and interaction between the constituents of the martian atmosphere. Our study of volcanic outgassing will assist planning of future space missions and landers on Mars.

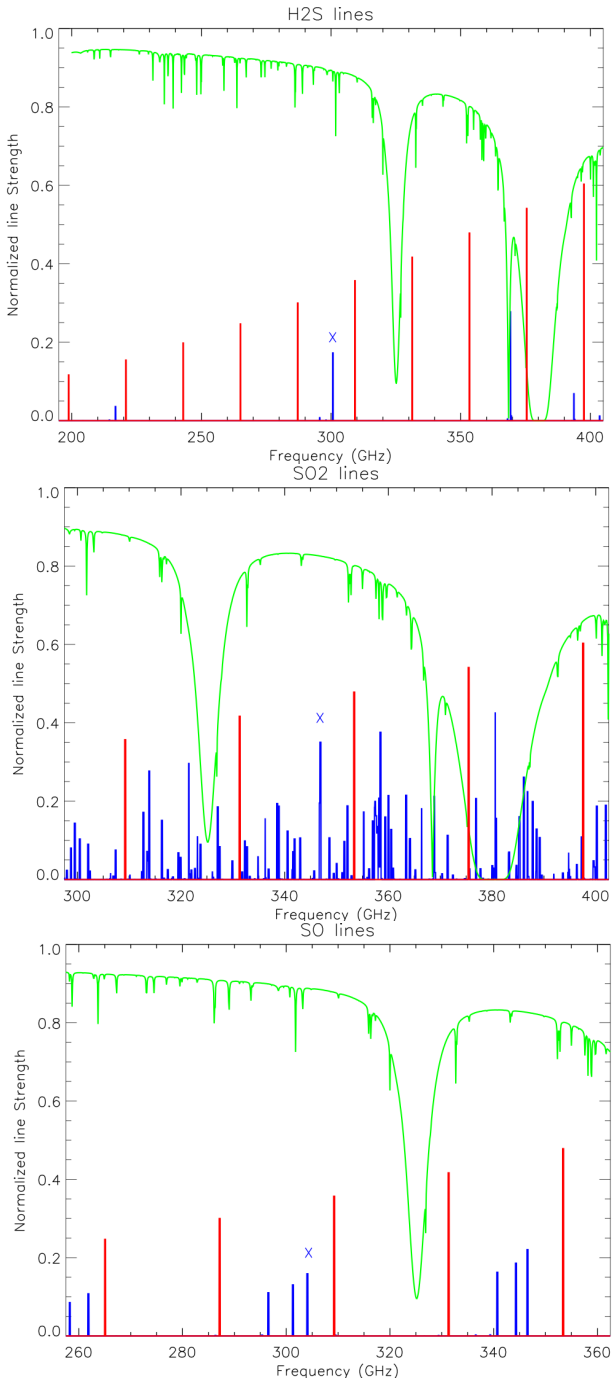

Figure 2.4 : Relative line strength ratios for the transitions of asymmetric isotopologues for H_2S at 300.51 GHz, SO_2 at 346.65 GHz, and SO at 304.08 GHz (blue). "X" marks the candidate lines to be observed. CO_2 (red) present in the Martian atmosphere. The Earth's transmission curve (Lord 1992) (green).

Table 2.2 : Telescope time obtained and parameters for Mars during the observing dates at the CSO, JCMT and IRTF between 2011 and 2014. L_s are the areocentric longitudes, indicating the different seasons on Mars.

Target molecule	Frequency	Date	Volcanic Region	Geocentric velocity (km/s)	Angular size (arcsec)	L_s (°)	Integration time (min)
At the CSO	(GHz)						
SO_2	346.652	28 November 2011	Syrtis	-15.6	6.9	36	67
SO_2	346.652	22 January 2012	Tharsis	-13.1	10.9	60	93
SO_2	346.652	23 January 2012	Tharsis	-13.0	11.0	61	89
SO_2	346.652	21 April 2012	Syrtis	+12.3	10.7	100	71
SO_2	346.652	22 April 2012	Syrtis	+12.4	10.6	101	62
SO_2	346.652	23 April 2012	Syrtis	+12.6	10.6	101	67
SO_2	346.652	08 May 2012	Tharsis	+13.6	9.4	107	53
SO_2	346.652	09 May 2012	Tharsis	+13.6	9.3	108	59
At the JCMT	(GHz)						
SO_2	346.652	23 May 2014	Tharsis	+9.62	12.6	135	60
SO_2	346.652	24 May 2014	Tharsis	+9.75	12.5	135	60
SO_2	346.652	25 May 2014	Tharsis	+9.88	12.4	136	80
At the CSO	(GHz)						
SO	304.078	27 November 2011	Syrtis	-15.6	6.9	34	56
SO	304.078	18 January 2012	Tharsis	-13.7	10.5	59	72
SO	304.078	19 January 2012	Tharsis	-13.6	10.6	59	86
SO	304.078	20 April 2012	Syrtis	+12.2	6.9	99	50
SO	304.078	24 April 2012	Syrtis	+12.7	6.9	101	52
SO	304.078	10 May 2012	Tharsis	+13.7	9.1	108	57
SO	304.078	11 May 2012	Tharsis	+13.7	9.1	108	50
H_2S	300.505	29 November 2011	Syrtis	-15.7	7.0	36	60
H_2S	300.505	20 January 2012	Tharsis	-13.4	10.7	59	96
H_2S	300.505	21 January 2012	Tharsis	-13.3	10.8	60	97
H_2S	300.505	25 April 2012	Syrtis	+12.7	10.4	102	65
H_2S	300.505	26 April 2012	Syrtis	+12.8	10.3	102	61
H_2S	300.505	12 May 2012	Tharsis	+13.7	9.1	109	47
H_2S	300.505	13 May 2012	Tharsis	+13.7	9.0	110	39
At the IRTF	CSHELL setting centered at (cm^{-1})						
OCS	2924	15 December 2011	Tharsis	-15.9	7.9	43	100
OCS	2924	18 December 2011	Tharsis	-15.9	8.0	45	62
OCS	2924	3 January 2012	Syrtis	-15.3	9.2	52	142
OCS	2924	5 January 2012	Syrtis	-15.1	9.3	53	152
OCS	2924	6 January 2012	Syrtis	-15.0	9.5	53	160
OCS	2924	30 May 2014	Tharsis	+10.4	12.0	138	92
OCS	2924	12 June 2014	Syrtis	+11.2	10.8	144	76
OCS	2924	13 June 2014	Syrtis	+11.2	10.7	145	104

References

Barlow, N. 2008, Mars: An Introduction to its Interior, Surface and Atmosphere (Cambridge University Press)

Encrenaz, T. 2008, Space Sci. Rev., 135, 11

Encrenaz, T., Bézard, B., Crovisier, J., Coustenis, A., Lellouch, E., Gulkis, S., & Atreya, S. K. 1995, Planet. Space Sci., 43, 1485

Encrenaz, T., Lellouch, E., Atreya, S. K., & Wong, A. S. 2004, Planet. Space Sci., 52, 1023

Hartogh, P., Jarchow, C., Lellouch, E., de Val-Borro, M., Rengel, M., Moreno, R., Medvedev, A. S., Sagawa, H., Swinyard, B. M., Cavalié, T., Lis, D. C., Błęcka, M. I., Banaszkiewicz, M., Bockelée-Morvan, D., Crovisier, J., Encrenaz, T., Küppers, M., Lara, L.-M., Szutowicz, S., Vandenbussche, B., Bensch, F., Bergin, E. A., Billebaud, F., Biver, N., Blake, G. A., Blommaert, J. A. D. L., Cernicharo, J., Decin, L., Encrenaz, P., Feuchtgruber, H., Fulton, T., de Graauw, T., Jehin, E., Kidger, M., Lorente, R., Naylor, D. A., Portyankina, G., Sánchez-Portal, M., Schieder, R., Sidher, S., Thomas, N., Verdugo, E., Waelkens, C., Whyborn, N., Teyssier, D., Helmich, F., Roelfsema, P., Stutzki, J., Leduc, H. G., & Stern, J. A. 2010, Astron. & Astrophys., 521, L49

Kaeufl, H.-U., Ballester, P., Biereichel, P., Delabre, B., Donaldson, R., Dorn, R., Fedrigo, E., Finger, G., Fischer, G., Franza, F., Gojak, D., Huster, G., Jung, Y., Lizon, J.-L., Mehrgan, L., Meyer, M., Moorwood, A., Pirard, J.-F., Paufique, J., Pozna, E.,

Siebenmorgen, R., Silber, A., Stegmeier, J., & Wegerer, S. 2004, in Society of Photo-Optical Instrumentation Engineers (SPIE) Conference Series, Vol. 5492, Ground-based Instrumentation for Astronomy, ed. A. F. M. Moorwood & M. Iye, 1218–1227

Lord, S. D. 1992, NASA Technical Memor., 103957

Mumma, M. J., Novak, R. E., DiSanti, M. A., & Bonev, B. P. 2003, in Bulletin of the American Astronomical Society, Vol. 35, AAS/Division for Planetary Sciences Meeting Abstracts #35, 937

Mumma, M. J., Novak, R. E., DiSanti, M. A., Bonev, B. P., & Dello Russo, N. 2004, in Bulletin of the American Astronomical Society, Vol. 36, AAS/Division for Planetary Sciences Meeting Abstracts #36, 1127

Mumma, M. J., Novak, R. E., Hewagama, T., Villanueva, G. L., Bonev, B. P., DiSanti, M. A., Smith, M. D., & Dello Russo, N. 2005, in Bulletin of the American Astronomical Society, Vol. 37, AAS/Division for Planetary Sciences Meeting Abstracts #37, 669

Mumma, M. J., Villanueva, G. L., Novak, R. E., Hewagama, T., Bonev, B. P., DiSanti, M. A., Mandell, A. M., & Smith, M. D. 2009, Science, 323, 1041

Pickett, H. M., Poynter, R. L., Cohen, E. A., Delitsky, M. L., Pearson, J. C., & Müller, H. S. P. 1998, J. Quant. Spectrosc. Radiat. Trans., 60, 883

Rothman, L. S., Gordon, I. E., Barbe, A., Benner, D. C., Bernath, P. F., Birk, M., Boudon, V., Brown, L. R., Campargue, A., Champion, J.-P., Chance, K., Coudert, L. H., Dana, V., Devi, V. M., Fally, S., Flaud, J.-M., Gamache, R. R., Goldman, A., Jacquemart, D., Kleiner, I., Lacome, N., Lafferty, W. J., Mandin, J.-Y., Massie, S. T., Mikhailenko, S. N., Miller, C. E., Moazzen-Ahmadi, N., Naumenko, O. V., Nikitin, A. V., Orphal, J., Perevalov, V. I., Perrin, A., Predoi-Cross, A., Rinsland, C. P., Rotger, M., Šimečková, M., Smith, M. A. H., Sung, K., Tashkun, S. A., Tennyson, J., Toth, R. A., Vandaele, A. C., & Vander Auwera, J. 2009, J. Quant. Spectrosc. Radiat. Trans., 110, 533

Sanchez-Lavega, A. 2010, An Introduction to Planetary Atmospheres (Taylor & Francis)

Spitzer, Jr., L. 1968, Diffuse Matter in Space., Vol. 28 (Interscience Tracts on Physics and Astronomy)

Symonds, R., Rose, W., Bluth, G., & Gerlach, T. 1994, Volatiles in Magmas: Miner. Soc. Am. Rev. Miner., 30, 1

Villanueva, G. L., Mumma, M. J., Novak, R. E., Radeva, Y. L., Käufl, H. U., Smette, A., Tokunaga, A., Khayat, A., Encrenaz, T., & Hartogh, P. 2013, Icarus, 223, 11

Wong, A.-S., Atreya, S. K., & Encrenaz, T. 2003, J. Geophys. Res., 108, 5026

—. 2004, J. Geophys. Res., 109, 1007

—. 2005, J. Geophys. Res., 110, 10002

Chapter 3

Submillimeter Observations and Data Processing

This chapter describes new and extensive submillimeter searches for SO_2, H_2S and SO above the Tharsis and Syrtis volcanic regions. This work is motivated by the possibility of detecting current outgassing and improving the limits of sulfur species in the atmosphere of Mars. In section 3.1 observations using the Caltech Submillimeter Observatory are presented. In section 3.2 the methodology in retrieving the thermal structure and brightness temperature of Mars at the times of the observations is explained, a thermal model for the sub-surface of the planet is described, and the radiative transfer model that is used to retrieve the abundances is explained. Disk-averaged (2σ) upper limits for SO_2, SO and H_2S are reported in section 3.3. In section 3.4, new submillimeter searches for SO_2 above Tharsis using the James Clerk Maxwell Telescope, and (2σ) limits are presented. The implications of the results and the conclusions are described in Chapter 5.

3.1 Observations at the Caltech Submillimeter Observatory

We used the double side band high resolution heterodyne receiver "Barney" (Kooi et al. 2007) at the 10.4 m single dish antenna of the CSO on Mauna Kea, Hawaii, to look for several sulphuretted species: SO_2 ($J_{n,k} = 19_{1,19} - 18_{0,18}$) at 346.652 GHz, H_2S ($J_{n,k} = 3_{3,0} - 3_{2,1}$)

at 300.505 GHz and SO ($J_n = 7_8 - 6_7$) at 304.077 GHz (Pickett et al. 1998). The targeted volcanic areas, Tharsis and Syrtis Major, were observed during the interval 23 Nov. 2011 to 13 May 2012 spanning mid Northern Spring and early Northern Summer seasons, between L_s= 34° and L_s= 110° in Mars year 31 (MY 31). L_s represents the areocentric longitude (in degrees) of the Sun. It ranges from L_s= 0° to 360°, where the Northern spring on Mars extends from L_s= 0° to 89°, and the Northern summer extends from L_s= 90° to 179°. MY represents the Mars year number where MY1 begins on the Northern Spring equinox on April 11, 1955 (Clancy et al. 2000).

We observed Syrtis at longitudes on Mars ranging from 222°W to 345°W, and Tharsis from longitude 48°W to 177°W. These longitudes are covered by the sub-Earth point when observing the two volcanic regions. The angular size of Mars changed between 6.7 and 9.0 arcsec on the first and the last run, respectively. The observing parameters are given in Table 3.1.

Table 3.1 : Parameters for Mars during the observing dates with the CSO.

Target line	Frequency (GHz)	Date (UT)	Volcanic Region	Heliocentric velocity (km/s)	Geocentric velocity (km/s)	Angular size (arcsec)	L_s (°)	Integration time (min)
SO_2	346.652	28 November 2011	Syrtis	1.3	-15.6	6.9	36	67
SO_2	346.652	22 January 2012	Tharsis	0.4	-13.1	10.9	60	93
SO_2	346.652	23 January 2012	Tharsis	0.4	-13.0	11.0	61	89
SO_2	346.652	21 April 2012	Syrtis	-1.1	12.3	10.7	100	71
SO_2	346.652	22 April 2012	Syrtis	-1.1	12.4	10.6	101	62
SO_2	346.652	23 April 2012	Syrtis	-1.1	12.6	10.6	101	67
SO_2	346.652	08 May 2012	Tharsis	-1.3	13.6	9.4	107	53
SO_2	346.652	09 May 2012	Tharsis	-1.3	13.6	9.3	108	59
SO	304.078	27 November 2011	Syrtis	1.3	-15.6	6.9	34	56
SO	304.078	18 January 2012	Tharsis	0.5	-13.7	10.5	59	72
SO	304.078	19 January 2012	Tharsis	0.5	-13.6	10.6	59	86
SO	304.078	20 April 2012	Syrtis	-1.1	12.2	6.9	99	50
SO	304.078	24 April 2012	Syrtis	-1.1	12.7	6.9	101	52
SO	304.078	10 May 2012	Tharsis	-1.4	13.7	9.1	108	57
SO	304.078	11 May 2012	Tharsis	-1.4	13.7	9.1	108	50
H_2S	300.505	29 November 2011	Syrtis	1.3	-15.7	7.0	36	60
H_2S	300.505	20 January 2012	Tharsis	0.4	-13.4	10.7	59	96
H_2S	300.505	21 January 2012	Tharsis	0.4	-13.3	10.8	60	97
H_2S	300.505	25 April 2012	Syrtis	-1.1	12.7	10.4	102	65
H_2S	300.505	26 April 2012	Syrtis	-1.2	12.8	10.3	102	61
H_2S	300.505	12 May 2012	Tharsis	-1.4	13.7	9.1	109	47
H_2S	300.505	13 May 2012	Tharsis	-1.4	13.7	9.0	110	39

The tapered beam of the CSO at 346.5 GHz has a FWHM of 24.3 arcsec[a]. The geocentric velocity for Mars ranges between -15.41 km/s and +13.71 km/s. The Earth's atmospheric transmission, $\exp(-\tau)$, at the SO_2 frequency setting is lower than at the SO and H_2S, therefore more signal from Mars is absorbed by Earth's atmosphere, leading to a lower signal-to-noise ratio at the continuum around the SO_2 transition. In order to compensate for that, SO and H_2S were targeted under normal weather conditions at a telluric optical depth at 225 GHz, $\tau_{225\mathrm{GHz}} < 0.14$[b], and SO_2 was searched under excellent submillimeter conditions with $\tau_{225\mathrm{GHz}} < 0.1$. $\tau_{225\mathrm{GHz}}$ refers to opacity as introduced by water vapor, and since there is a significant water absorption at the observed frequencies (300 - 350 GHz), low opacity levels at 225 GHz produce excellent transmission at the SO_2 transition.

The accuracy in the pointing of the telescope was checked on shorter time intervals at the beginning of the night and before sunrise when there are considerable changes in the telescope temperature [c]. During the night, the continuum source pointing using Mars was done every 1.5 to 2 hours by making a five-point map around the planet. Chopping between Mars and the sky at 60 arcsec from the planet was achieved by wobbling the secondary mirror of the telescope [d]. We used the chopper-calibration method (Penzias & Burrus 1973) to calibrate the antenna temperature. The major contributions to the systematic errors in the antenna temperature are the pointing and focussing of the telescope, the double side band ratio, the tuning of the receivers and the variations in the atmospheric transmission (Matthews et al. 2004). As a result, variations in the baseline are expected. The calculated uncertainties resulting from each contributing factor were later added quadratically. The resulting estimated systematic uncertainty for these nights was $\sim 15\%$ of the continuum level. Examples of the observed spectra after baseline removal, at the SO_2, SO and H_2S settings for April, 23, 24 and 25 UT, 2012, respectively are displayed in Figure 3.1. The details about the data handling and baseline removal are explained in section 3.3.

[a] http://www.submm.caltech.edu/cso/receivers/beams.html
[b] http://cso.caltech.edu/tau/
[c] http://cso.caltech.edu/wiki/cso/instruments/heterodyne/pointing
[d] http://cso.caltech.edu/wiki/cso/instruments/heterodyne/chop

The antenna temperature of the Mars continuum depends on the telescope's efficiency, beam width at the frequency setting, the size of Mars and the ratio of contributions from the receiver's lower and upper side bands. For one night, we measured the double-side-band ratio, and found equal contributions from both side bands. The same ratio is considered for the rest of the nights. The slight shifts at the continuum level in Figure 3.1 among the three different settings are within the systematic uncertainty from night to night. The error bars presented in the spectra are the RMS noise level of the continuum.

As a sanity check to see if there is anything blocking the beam, we pointed the telescope to Orion KL and confirmed the presence of the SO_2 and SO emission lines (Schilke et al. 1997), their transition frequency, and antenna temperature. Figure 3.2 shows the double-side-band spectrum at rest frequency of Orion KL on November 26 UT, 2011, after 1 hour on-source integration time. The indicated spectral features belong to SO_2 ($J_{n,k} = 16_{4,12} - 16_{3,13}$) at 346.523 GHz, SO ($J_n = 9_8 - 8_7$) at 346.528 GHz, and SO_2 ($J_{n,k} = 19_{1,19} - 18_{0,18}$) at 346.652 GHz.

In the Mars data, the variations in the baseline were corrected for in the data analysis, by using polynomial fitting. For each night, the expected noise level in the spectra is calculated from the system temperature using the radiometer equation (eq. 3.3), and it is found to be consistent with the measured noise. An example is given in section 3.2.2.

At the SO_2 setting, the spectrometer's 4 GHz bandwidth includes the ^{12}CO (3-2) transition at 345.795 GHz. This ^{12}CO is later used to retrieve the thermal structure and the physical conditions in the Martian atmosphere on the nights when we searched for SO_2. We used the array Acousto-Optic Spectrometer (AOS) to measure the CO line shape. The array is divided into 4 individual sections covering 1 GHz each, with 1600 channels (650 kHz spacing) and a spectral resolution of 1 MHz (spectral resolving power $\sim$ 346,000) (Horn et al. 1999).

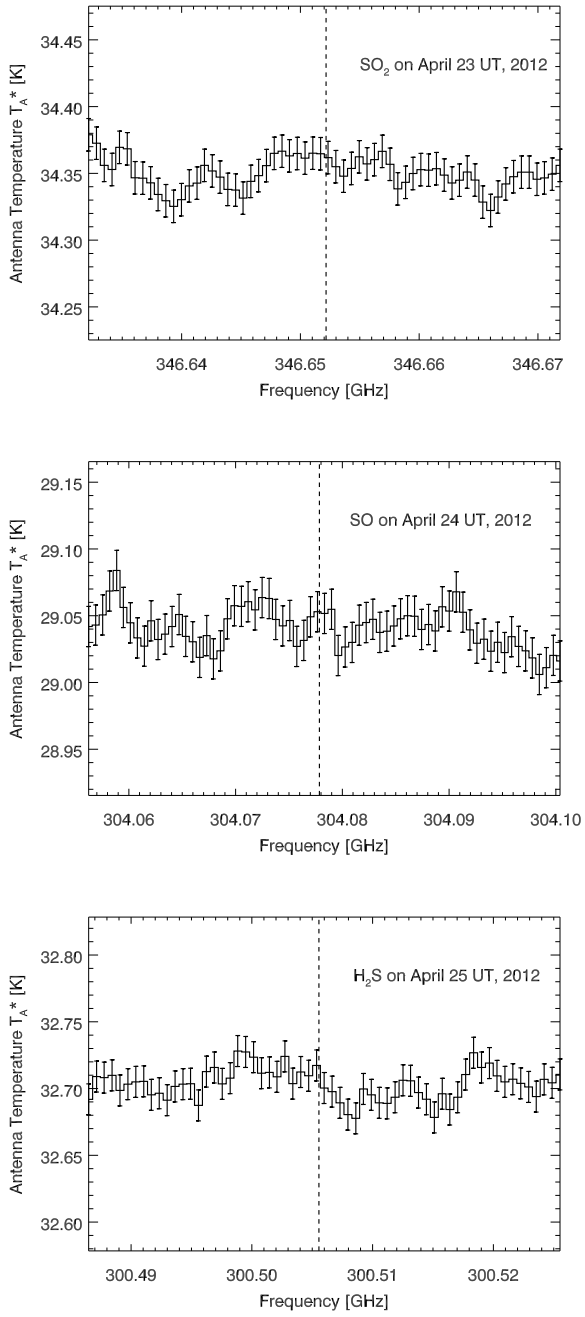

Figure 3.1 : Examples of summed double side band spectra of SO_2, SO and H_2S on April 23, 24 and 25 UT, 2012, respectively. The spectra are presented at rest frequencies (dashed lines) of the lines at 346.652 GHz, 304.078 GHz and 300.505 GHz, respectively. The error bars are the RMS uncertainty of the continuum.

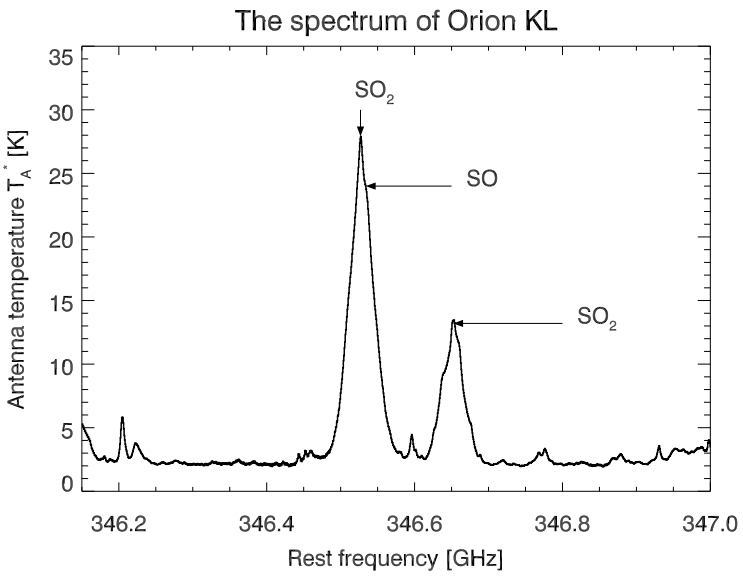

Figure 3.2 : The double-side-band spectrum of Orion KL, at rest frequency on November 26 UT, 2011, after 1 hour on-source integration time. The indicated spectral features belong to SO_2 ($J_{n,k} = 16_{4,12} - 16_{3,13}$) at 346.523 GHz, SO ($J_n = 9_8 - 8_7$) at 346.528 GHz, and SO_2 ($J_{n,k} = 19_{1,19} - 18_{0,18}$) at 346.652 GHz.

3.2 Method

3.2.1 System Temperature

The system temperature above Maunakea is given by the equation (Matthews et al. 2004; Villanueva 2004; Kooi et al. 2007):

$$T_{sys} = \frac{T_{rx} + (1 - \eta_{sky}) T_{sky}^{physical} + (1 - \eta_{mb}) T_{tel}^{physical}}{\eta_{SB} \times \eta_{sky} \times \eta_{mb}} \tag{3.1}$$

where T_{rx} is the receiver noise temperature (about 90 K for Barney at the CSO, at 345 GHz)[e]. We measured the receiver noise temperature at the telescope using the so called "Y" factor described in Ke & Feldman (1993). The method consists of placing a hot (ambient temperature) and cold (liquid nitrogen) loads at the entrance window of the

[e]http://cso.caltech.edu/wiki/cso/science/proposal

receiver, and measure the total receiver intermediate frequency (IF) output powers, P_{hot} and P_{cold}, respectively, and then calculate $Y = P_{hot}/P_{cold}$. We did that at the CSO every night we observed (Figure 3.3). The receiver noise temperature is given by the equation:

$$T_{rx} = \frac{T_{hot} - Y \times T_{cold}}{Y - 1} \tag{3.2}$$

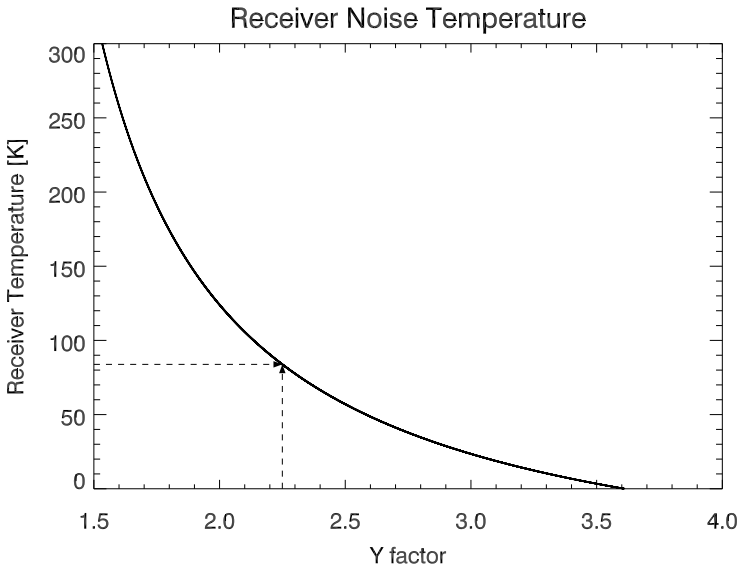

Figure 3.3 : The receiver noise temperature as a function of the measure "Y" factor when the hot and cold loads have temperatures of 278 K and 77 K, respectively. The arrows indicate a receiver temperature of 84 K when Y is 2.25 on April 22 UT, 2012.

For example, on April 22 UT, 2012, we measured a Y factor = 2.25 (P_{hot} = 4.85, P_{cold} = 2.15), and therefore a receiver noise temperature of 84 K (Figure 3.3).

η_{sky} is the transmission of the atmosphere above Mauna Kea and is equal to $e^{-\tau}$ (τ is the opacity). $T_{sky}^{physical}$ is the average physical temperature of the sky at Mauna Kea = 255 K. η_{mb} is the efficiency of the telescope (= 0.65 at 345 GHz)[f], and $\eta_{SB} = 1/SB$. In a double-side-band observation, there is a contribution to the signal from both side-bands, and therefore SB= 2, whereas SB = 1 for single-side-band observations.

[f]http://cso.caltech.edu/wiki/cso/instruments/heterodyne/calibration

Using the input values for the above-mentioned parameters, and the atmospheric opacity at zenith above Maunkea at water vapor level of 1mm (PWV)[g], we display the system temperature as a function of frequency in Figure 3.4.

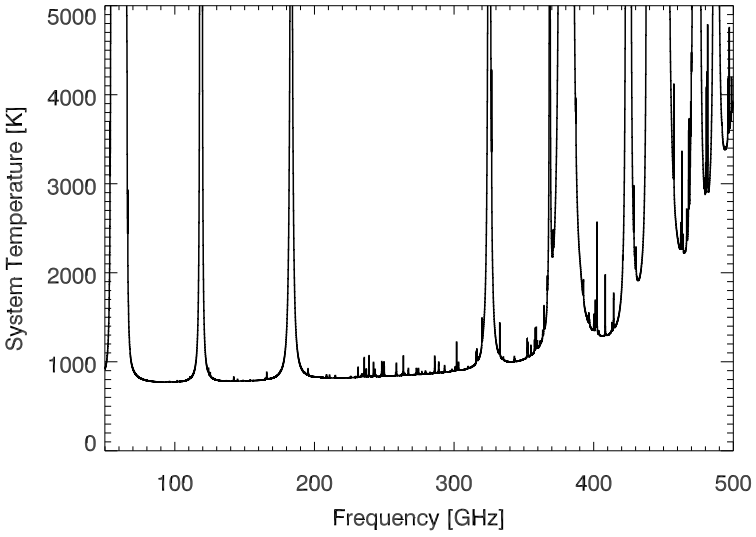

Figure 3.4 : The system temperature above Maunakea as a function of frequency, at zenith and at 1mm PWV. The values for the opacity of Earth's atmosphere have been modeled using the CSO Atmospheric Transmission Interactive Plotter.

3.2.2 Minimum Detectable Difference in Brightness Temperature: The Radiometer Equation

The minimum detectable difference in brightness temperature is given by the radiometer equation (Encrenaz et al. 1995; Villanueva 2004):

$$T_{rms}[K] = \frac{\alpha \times (T_{sys} + SB \times \eta_{mb} \times f \times T_b)}{\sqrt{B \times t}} \tag{3.3}$$

where $\alpha = 2$ for beam-switch observations, T_{sys} is the system temperature (eq. 3.1), η_{mb} is the main-beam efficiency of the telescope, f is the filling factor, $\mathrm{T_b}$ is the brightness

[g]http://www.submm.caltech.edu/cso/weather/atplot.shtml

temperature of Mars, B is the spectral resolution, and t is the total integration time ($\sim$2 times on-source integration time). In our case, SB= 2 because we are conducting double side band observations at the CSO/Barney.

The filling factor depends on the angular size of the planet ($\theta_{\rm Mars}$) and the telescope main-beam FWHM ($\theta_{\rm mb}$). It is given by the equation (Mangum 1993; Encrenaz et al. 1995):

$$f = 1 - 2^{-(\theta_{Mars}/\theta_{mb})^2} \tag{3.4}$$

For example, on January 23 UT, 2012, with a system temperature of 384 K, a spectral resolution of 1 MHz, a total integration time of 2.6 minutes, a Mars brightness temperature of 210.4 K, a filling factor of 0.132, a beam efficiency of 0.65 and a beam-switching observing mode, the measured noise is 69.4 mK, compared to the expected noise of 67.2 mK.

3.2.3 A-priori Mars Brightness Temperature

Local temperatures on Mars respond to insolation and vary according to surface albedo. We estimated the disk-integrated brightness temperature using a simple map based on these two parameters and the surface emissivity. We extracted the albedo map obtained by the Mars Global Surveyor's Thermal Emission Spectrometer (Christensen et al. 2001) and created a two dimensional orthographic projection. The benefit from using such projections is that this method takes into account the sizes of the different projected areas of the surface elements on Mars, as a weighting factor.

The disk is divided into a square grid of 90×90 equal-sized bins. The disk of Mars is normalized to one (R = 1), therefore each bin inside the grid at position (x,y) has the values -1 $\leq$ x $\leq$ +1 and -1 $\leq$ y $\leq$ +1. The surface temperature at the center of each bin is calculated using the Mars Climate Database (MCD) (Lewis et al. 1999; Forget et al. 1999). For $\rho = \sqrt{x^2 + y^2}$ and c = arcsin(ρ/R), one could retrieve the geographic latitudes and longitudes on Mars corresponding to the x and y values on the grid, using the inverse

transformations for the orthographic projection (Snyder 1987):

$$\varphi = arcsin\left[cos(c) \times sin(\varphi_0) + \frac{y \times sin(c) \times cos(\varphi_0)}{\rho}\right] \tag{3.5}$$

$$\lambda = \lambda_0 + arctan\left[\frac{x \times sin(c)}{\rho \times cos(\varphi_0) \times cos(c) - y \times sin(\varphi_0) \times sin(c)}\right] \tag{3.6}$$

where φ and φ_0 are the latitudes on Mars corresponding to the center of each bin on the grid, and the latitude at sub-Earth point, respectively. λ and λ_0 are the longitudes on Mars corresponding to the center of each bin on the grid, and the latitude at sub-Earth point, respectively. Figure 3.5 shows the orthographic projection of Mars created by our own code, compared to the one generated by "Mars24" (Allison 1997; Allison & McEwen 2000), on April 22, 2012, at 08:00 UT.

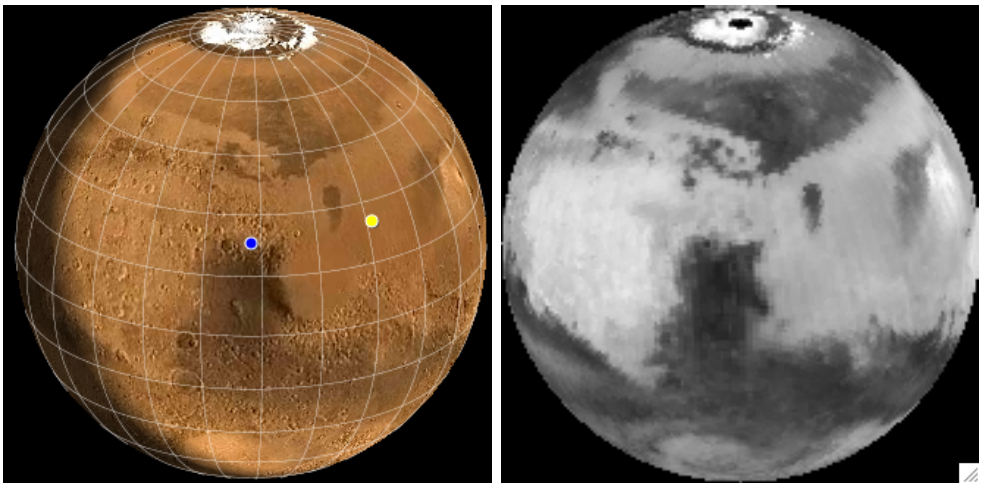

Figure 3.5 : Syrtis region on Mars as it appears on April 22, 2012, at 08:00 UT. Left panel: The map of Mars as rendered using Mars24 (Allison 1997; Allison & McEwen 2000). The yellow dot represents the sub-solar point (noon on Mars), and one would expect the highest surface temperature around this region in the direction of early-afternoon on the planet (near the right limb). Right panel: Using the albedo map obtained by the Mars Global Surveyor's Thermal Emission Spectrometer (Christensen et al. 2001), we were able to create a 2D orthographic projection of Mars, which was later used to extract the representative brightness temperature over the martian disk. Note that the images do not represent the real amount of the residual ice on the Northern polar at the observing season ($L_s = 101°$).

By centering a two dimensional gaussian kernel, the normalized telescope beam, at the disk of Mars (left and middle panels in Figure 3.6), the average brightness temperature for the whole planet at the time of the observations is calculated using the following equation:

$$\overline{T_b} = \epsilon_0 \times \frac{\sum_i Kernel_i \times Mask_i \times T_i}{\sum_i Kernel_i \times Mask_i} \tag{3.7}$$

where ϵ_0, Kernel, Mask and T are the emissivity of Mars at the observing frequency range, the values of the contribution from the CSO gaussian beam, the mask (1 for the bins inside the Martian disk, 0 elsewhere) and the surface temperature at each bin, respectively. For example, on April 22, 2012 at 08:00 UT, the calculated average brightness temperature is $\overline{T_b}$ = 211.75 K.

Main beam temperature: If we remove the mask in the same equation (3.7), we will be calculating the main beam temperature = 26.06 K (right panel in Figure 3.6). The main beam temperature is also calculated using the equation $f \times \overline{T_b}$, where f is the filling factor in equation (3.4). The angular size of Mars is 10.66 arcsec on the same date, so the filling factor is 0.124, and therefore the expected main beam temperature is 26.26 K; which is very close to the one calculated in equation (3.7).

Mangum (1993) has estimated the double-side-band (DSB) antenna temperature from the following equation:

$$T_A{}^* = SB \times \eta_{mb} \times f \times \overline{T_b} \tag{3.8}$$

where η_{mb} is the main beam efficiency in equation 3.1, SB= 2 because the DSB continuum level is the summation of the lower and upper side bands, with equal contributions from each band. The estimated DSB antenna temperature is 34.14 K, and the observed continuum level for the same night is 35.38 K as shown in Figure 3.7.

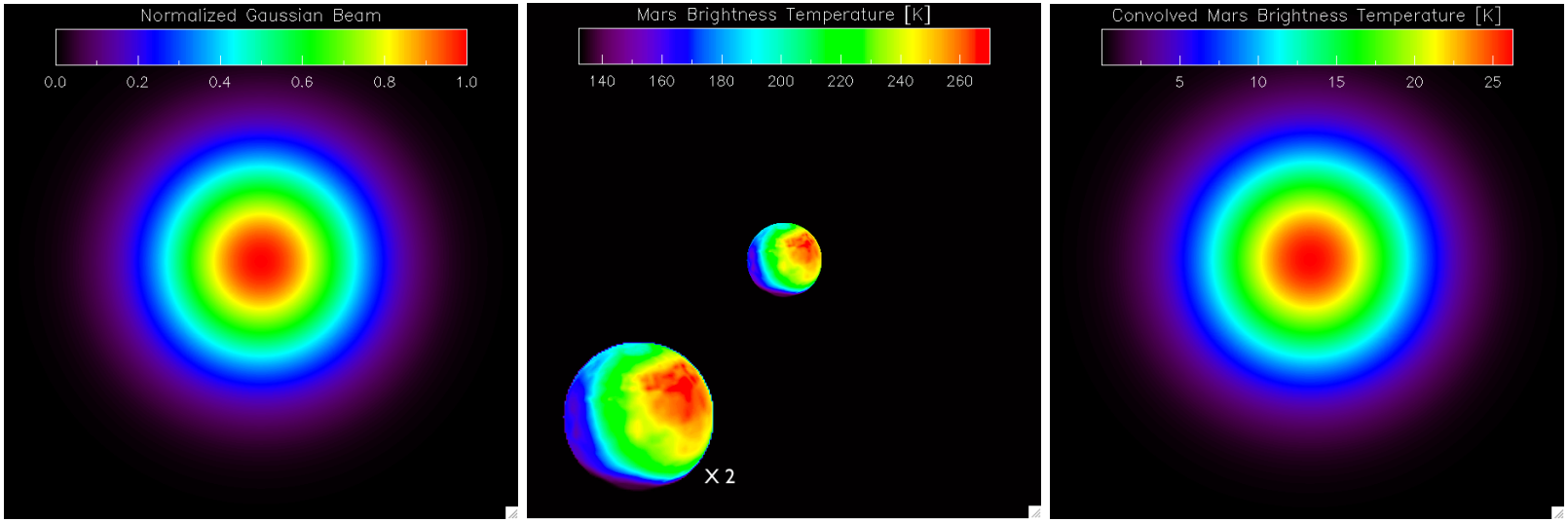

Figure 3.6 : Date: April 22, 2012 at 8:00 UT. Left: The normalized gaussian beam of the CSO at 346 GHz, with FWHM = 24.40 arcsec. Middle: The brightness temperature across the disk of Mars. Mars' angular size is 10.66 arcsec, and the exploded view (2 times) is at the bottom. Right: The result of the convolution of the brightness temperature across Mars, when sliding the 2D gaussian Kernel in the left panel across the disk of the planet. All three panels have the exact angular sizes relative to each other for the CSO beam, the disk of Mars and the convolved disk of Mars.

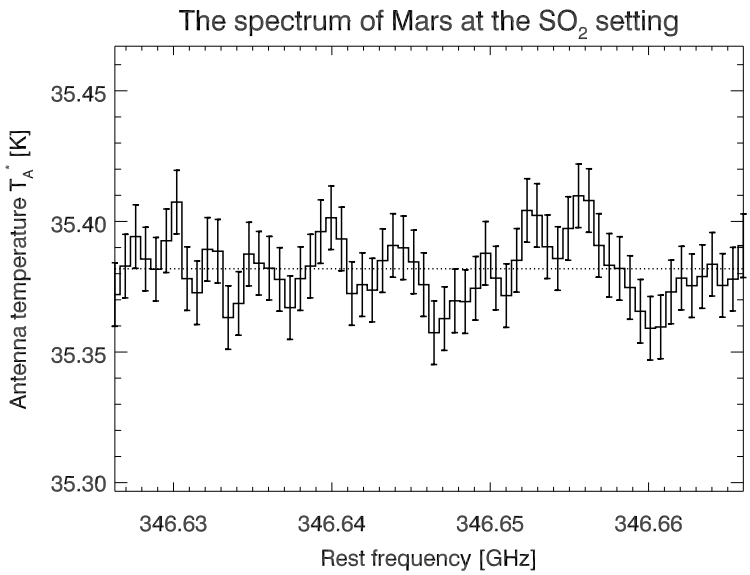

Figure 3.7 : Summed double-side band spectrum of Mars at the SO_2 setting on April 22 UT, 2012. The on-source integration time is 62 minutes, and the continuum level is at 35.38 K. The error bars are the RMS uncertainty of the continuum level. The continuum has been corrected for baseline variations as described later.

Another test that should give similar results for the main beam temperature has been conducted. We convolved the brightness temperature across Mars with a sliding 2D gaussian Kernel, the normalized gaussian beam. In the left panel of Figure 3.6, the normalized gaussian beam of the CSO at 346 GHz is FWHM = 24.40 arcsec, on April 22, 2012 at 8:00 UT. In the middle panel, we show the brightness temperature across the disk of Mars. Mars' angular size is 10.66 arcsec, and the exploded view (2×) is at the bottom. The right panel shows the result of the convolution of the brightness temperature across Mars, when sliding the 2D gaussian Kernel in the left panel over each bin on the disk of Mars. All three panels have the exact sizes compared to each other for the CSO beam, the disk of Mars and the convolved disk of Mars. The resulting convolution shows a main beam temperature of 26.09 K. The result is also very close to the one obtained when centering a 2D gaussian beam on the disk of Mars, and not applying any sort of masking in equation 3.7.

Using this method we have extracted the *a-priori* brightness temperatures for Mars at the time of the observations.

3.2.4 Thermal Modeling of the Sub-surface of Mars

The Mars Climate Database (MCD) provides surface temperatures, but the submillimeter waves penetrate below the surface of Mars, and therefore the "surface" temperature given by the MCD might not be the correct one used to calculate the brightness temperature for Mars. In order to determine the sub-surface temperature profile, we need to perform a thermal model. At the surface (z = 0), the diurnal temperature profile is roughly represented by (Leovy 1966; Clancy et al. 1983):

$$T(z=0,t) = T_m + T_a sin(wt + \phi) \tag{3.9}$$

where T_m[K] is the average temperature, T_a[K] is half the diurnal variation in temperature, w[rad/s] is the angular frequency of the diurnal cycle, and ϕ[rad] is the phase shift.

In the middle of the observing night on April 22, 2012 at UT 08:00 AM, the sub-Earth point is located on Mars at $\lambda = 74.1°$E and $\varphi = 23.02°$N. Using the MCD for this geographic point, we get the values for T_m (= 230.04 K), T_a (= 45.19 K), and ϕ (= -1.82 rad) by fitting a sine function to the data with an angular frequency $w = 7.07 \times 10^{-5}$ rad/s for Mars (Figure 3.8).

The sub-surface temperature profile is a sine function, with smaller amplitude as the one on the surface, eq. 3.9, an exponential decay as a function of depth, and a delay in heat transfer depending on the thermal skin depth λ_{th}. At large depths relative to λ_{th}, the temperature profile takes the value of the average temperature T_m. The sub-surface temperature profile in given by the equation:

$$T(z,t) = T_m + T_a \times e^{-z/\lambda_{th}} \times sin(wt + \phi - \frac{z}{\lambda_{th}}) \tag{3.10}$$

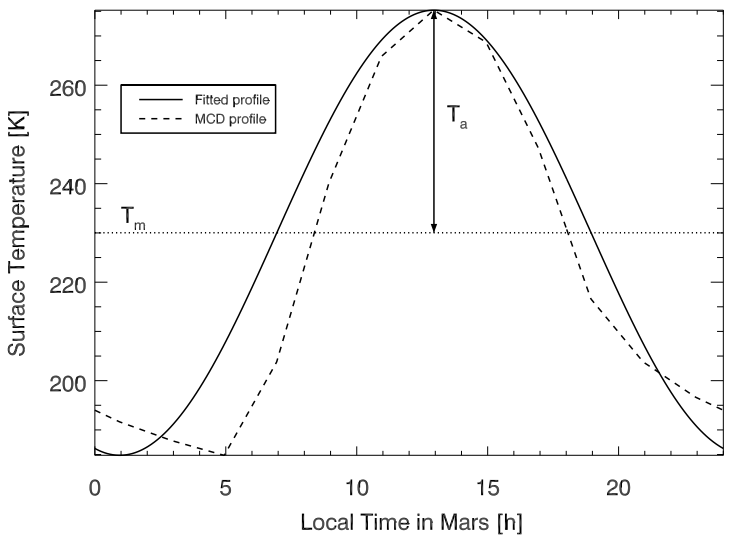

Figure 3.8 : Diurnal profile on the surface of Mars at $\lambda = 74.1°$E and $\varphi = 23.02°$N. These coordinates belong to the sub-Earth point on Mars when observing the planet on April 22, 2012 at UT 08:00 AM. The dashed line indicates the profile on the surface of Mars as extracted from the MCD. The solid line is a fitted profile based on equation (3.9). T_m[K], the average temperature, and T_a[K], half the diurnal variation in temperature, are indicated by the horizontal dotted line and the vertical arrow, respectively.

where z [m] is the geometric depth, λ_{th} [m] is the thermal skin depth, T_m, T_a, w and ϕ are the same as in equation 3.9. The solution for $T(z,t)$ must satisfy the following thermal diffusion equation:

$$\frac{dT}{dt} = \frac{k}{\rho c}\frac{d^2T}{dz^2} \tag{3.11}$$

where k is the typical thermal conductivity for the martian soil (0.122 W/m/ K, (Leovy 1966)), c is the specific heat capacity (800 J/kg/K)[h], and ρ is the density (1600 kg/m^3, Spera (2000)).

In order for T(z,t) to satisfy the diffusion equation (eq. 3.11), we solve for the diurnal thermal skin depth:

$$\lambda_{th} = \sqrt{\frac{k}{\rho c}\frac{P}{\pi}} \tag{3.12}$$

[h]http://lasp.colorado.edu/ bagenal/3750/ClassNotes/Class15.16/Class16.html

where P is the period of the martian sol (= 8.87×10^4 s). After substituting for the values in equation (3.12) we get $\lambda_{th} = 5$ cm. Figure 3.9 shows the sub-surface temperature profiles at each time of the day. The top panel shows, in pink, the envelope of all the temperature profiles plotted on-top of each other. All the profiles are included inside it. The solid red line is the sub-surface profile at 01:00 h when the surface temperature is at its lowest, and the solid black line is the sub-surface profile at 13:00 h when the surface temperature is at its peak. At depths larger than a few thermal skin depths, the temperature converges to the average temperature T_m during the day just like equation (3.10) behaves.

The submillimiter wave penetrates to a depth equal to the "electric skin depth" = 7.7 λ (Clancy et al. 1983), where the wavelength λ = 0.87 mm (at 345 GHz). The electric skin depth = 0.67 cm. The bottom panel of Figure 3.9 is an expanded view of the top panel down to z= -3 cm. At the position (dashed black line) of the electric skin depth, the temperatures at point A and B are ± 5 K from the surface temperature at any one point. The differences are 2.6 % and 1.8 % at points A and B, respectively, smaller than the 15 % systematic uncertainty on the continuum level measured. In conclusion, our retrieval process for the brightness temperature at Mars is not affected by the penetration depth of the submillimeter wave.

3.2.5 The Emissivity of the Surface Mars

The emissivity of Mars is related to the Fresnel coefficient R, $\epsilon_0 = 1 - \mathrm{R}$, which depends on the emission angle θ_i and the properties of the Martian surface: the surface roughness and the dielectric constant ϵ. For a typical soil, the dielectric constant ranges between 2 and 3. Radar observations of the Martian surface give values closer to 2 (Simpson et al. 1992; Golombek et al. 2008), and we adopt $\epsilon = 2.25$ [i]. The Fresnel coefficient of the polarized

[i] http://www.lesia.obspm.fr/perso/emmanuel-lellouch/mars/

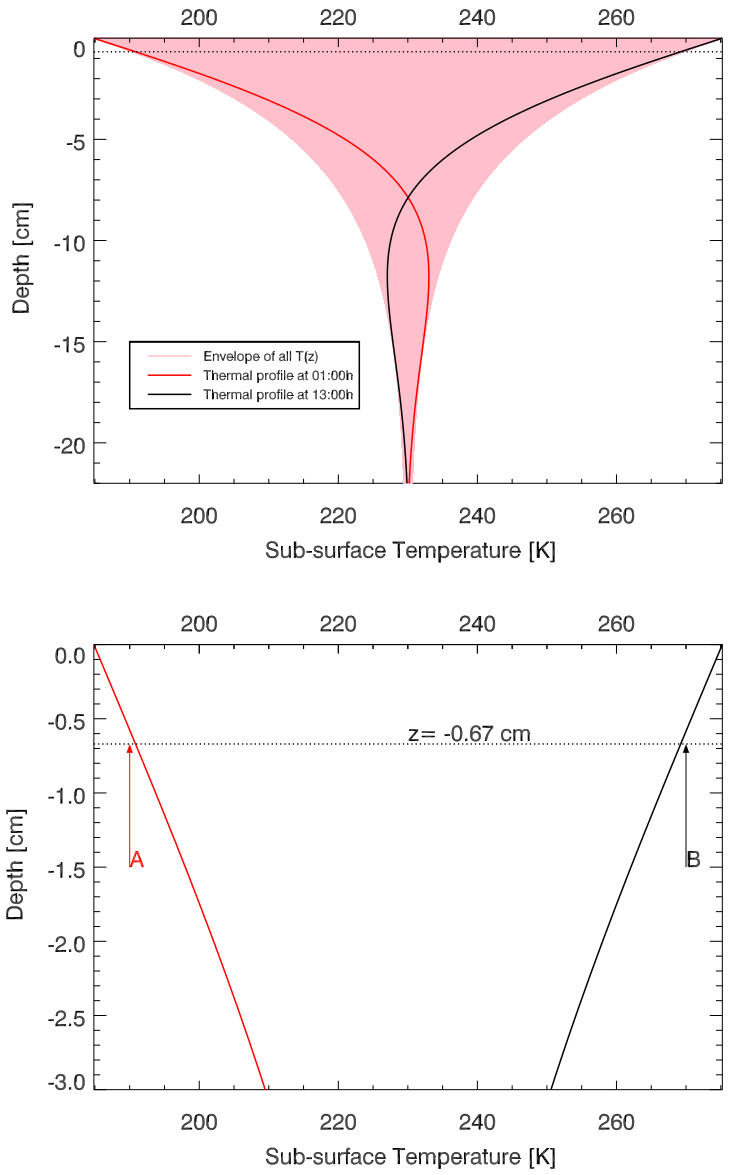

Figure 3.9 : Mars sub-surface temperature at the sub-Earth position on April 22, 2012 (L_s = 100°). The top panel shows the envelope (pink) of all the temperature profiles plotted on-top of each other. All the profiles are included inside it. The solid line (red) is the sub-surface profile at 01:00 h when the surface temperature is at its lowest, and the solid line (black) is the sub-surface profile at 13:00 h when the surface temperature is at its peak. The bottom panel shows the expanded view of the top panel down to z= -3 cm. At the position (dashed black line) of the electric skin depth, the temperatures at point A and B are ± 5 K from the surface temperature at any one point.

light has a parallel and a perpendicular component, $R = (R_s + R_p)/2$, where:

$$R_s = \left| \frac{n_1 cos\theta_i - n_2 \sqrt{1 - (\frac{n_1}{n_2} sin\theta_i)^2}}{n_1 cos\theta_i + n_2 \sqrt{1 - (\frac{n_1}{n_2} sin\theta_i)^2}} \right|^2 \tag{3.13}$$

$$R_p = \left| \frac{n_1 \sqrt{1 - (\frac{n_1}{n_2} sin\theta_i)^2} - n_2 cos\theta_i}{n_1 \sqrt{1 - (\frac{n_1}{n_2} sin\theta_i)^2} + n_2 cos\theta_i} \right|^2 \tag{3.14}$$

n_1 and $n_2 = \sqrt{\epsilon}$ are the indices of refraction for the air on Mars and the Martian regolith, respectively, and θ_i is the incidence angle. The emissivity is flat at emission angles up to 25°, and is ϵ_0=0.96 (Figure 3.10). This number is used in our radiative transfer model.

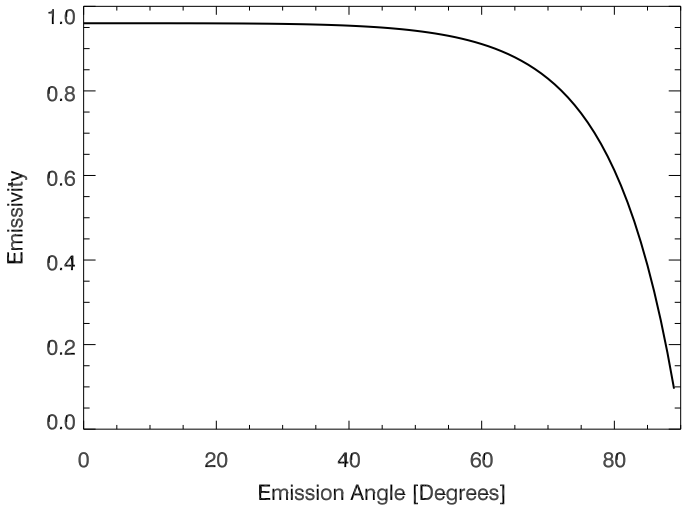

Figure 3.10 : Mars' surface emissivity as a function of emission angle.

3.2.6 Thermal Structure Retrieval

The optically thick martian CO(3-2) rotational transition at 345.795 GHz was detected (Fig. 3.11) each time we used the SO_2 setting. The spectral line shape for each element depends on the line-of-sight atmospheric temperature profile, local topography, surface-atmosphere temperature difference, and so on. The convolved line shape thus depends

on viewing geometry, season, time of day, and related factors, and is used to retrieve a representative temperature profile for Mars at the time of the observations. CO is assumed to be well mixed in the vertical and horizontal directions on Mars (Muhleman & Clancy 1995) and we adopt a constant mixing ratio of 800 ppm (Lellouch et al. 1991). For comparison, Curiosity's Sample Analysis at Mars (SAM) measured atmospheric CO mixing ratio of $< 1.0 \times 10^{-3}$ using repeated measurements from Gale crater (4.5°S, 132°E) between areocentric solar longitudes 133.7° and 211.2° (Mahaffy et al. 2013).

The method of inverting the CO line is as follows: For each night, we adopted Mars' geometry at the mid-point of each observation interval as representative of the entire interval. We then divided the Mars disk into a grid of 36×36 bins and extracted the temperature-pressure profile above the local surface at the center of each bin from the MCD, extending up to 140 km. Six contribution functions (Fig. 3.12), calculated from each of these profiles, chosen to peak at roughly equally spaced altitudes, were later used as *a priori* functions (and parameters) in the retrieval of the thermal structure in the atmosphere of Mars. The functions were carefully chosen, with equal frequency resolution offsets close to the line center, and then equally spaced in units of scale heights away from line center, close to the CO line continuum. A non-linear least square fitting algorithm, the Levenberg-Marquardt (Markwardt 2009), was used to retrieve the temperature profiles by multiplying each of the contribution functions in the *a priori* profiles by a scaling factor, and changing the brightness temperature of Mars.

In order to test the assumption of using the surface geometry at the middle of the observation, we calculated the brightness temperature at the beginning and the end of each night. By comparing these values to the brightness temperature calculated when using the geometry at the middle of the observation, we find the variations to be smaller than 3.5 %.

The estimated brightness temperature of the disk of Mars is an *a priori* input parameter for the fitting algorithm. This initial guess for the brightness temperature and the thermal profiles aims to prevent the Levenberg-Marquardt algorithm from finding a local minimum that is a good mathematical solution, but not a physically plausible one. The extracted

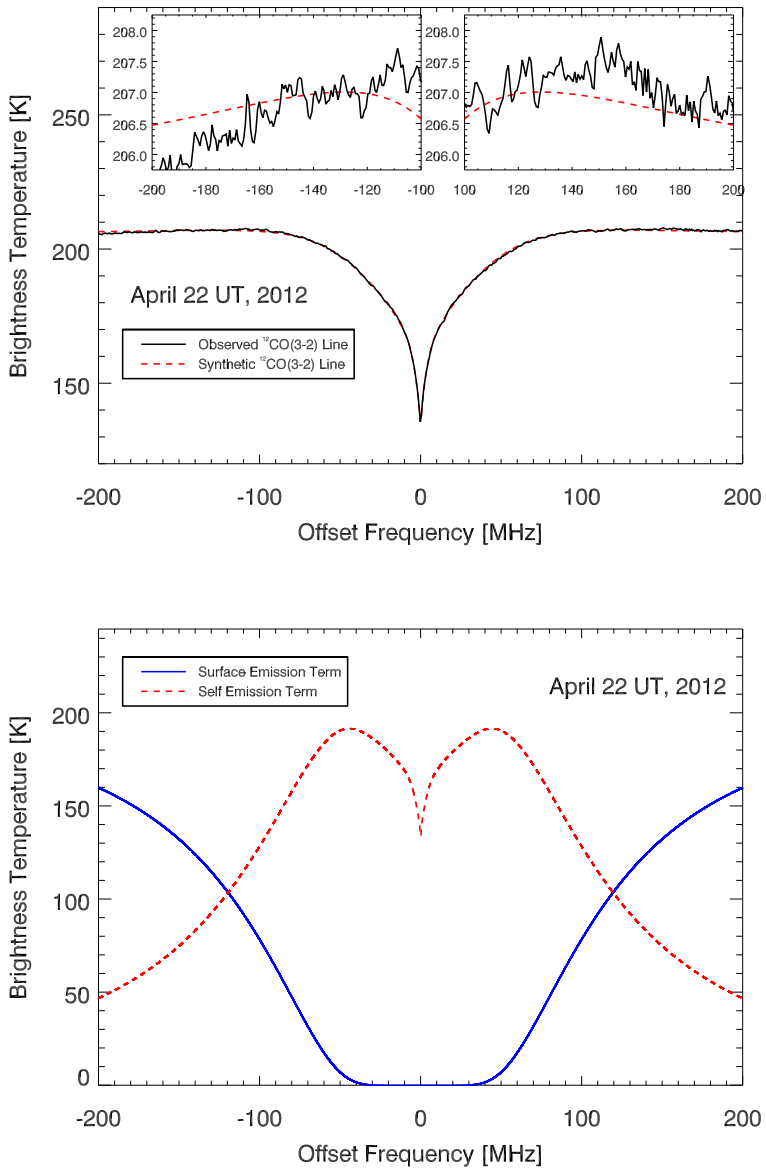

Figure 3.11 Top panel: Observed ^{12}CO (3-2) absorption (solid line), shifted to the rest frequency at 345.796 GHz, in the spectrum of Mars at the retrieved Mars brightness temperature on April 22 UT, 2012. The dashed red lines show the synthetic ^{12}CO(3-2) spectrum using the retrieved temperature profile and brightness temperature for Mars at the time of the observation. The inserts show an expanded view of the fit in the wings of the line. Bottom panel: Atmospheric self (dashed lines) and surface emission (solid line) terms; their sum is the emergent intensity.

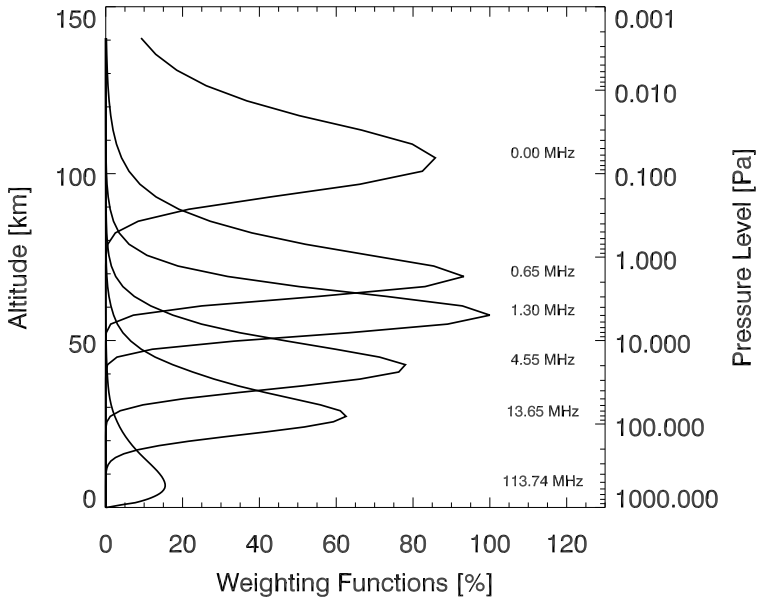

Figure 3.12 Contribution functions for the ^{12}CO (3-2) line on April 22 UT, 2012. The frequency offsets where the contribution functions peak from the highest to lowest altitude level are 0, 0.65, 1.3, 4.55, 13.65 and 113.74 MHz.

thermal profile for Mars that represents the observed disk of the planet (Fig. 3.19) is one of the 36×36 retrieved profiles. It leads to a minimum chi-square between the modeled and observed CO line shape. The residual spectra resulting from subtracting the model from observed CO, deviate within ± 0.7 % around zero (Fig. 3.21). The *a priori* brightness temperatures that we calculated and the retrieved ones from the observations are listed in Table 3.2 (Khayat et al. 2015).

The 3.5% uncertainty is for the *a priori* brightness temperatures, and not for the retrieved temperatures that will later be used to calculate the mixing ratios of the sulfur-bearing species.

The extracted temperature profiles and the brightness temperatures for Mars are later used in synthesizing the targeted lines at the time of the observation (Fig. 3.23). Since the

apparent size of Mars is smaller than the diffraction limited field of view of the CSO, the resulting spectra for the different sulfur molecules are disk-averaged.

Table 3.2 Calculated and retrieved brightness temperatures for the disk-averaged surface of Mars

Date (UT)	T_b (K)	Retrieved T_b (K)	L_s (°)
28 November 2011	217.79	206.51	36.00
22 January 2012	226.33	211.22	60.40
23 January 2012	226.28	208.93	60.85
21 April 2012	213.86	203.60	99.84
22 April 2012	211.75	204.86	100.29
23 April 2012	211.56	210.39	100.75
8 May 2012	214.34	203.83	107.53
9 May 2012	214.45	209.33	107.96

3.2.7 Radiative Transfer Model

We developed a radiative transfer code for computing the expected line absorption. We assume that the sulphuretted species are well mixed, and we consider that the temperature-pressure profile is uniform across Mars. In order to correct for the airmass changes on Mars, we used an approximation to the entire disk of the planet by assuming a diffusivity factor of 1.66 for our calculations (Encrenaz et al. 2004), explained in Equation (3.17). In our model, the mixing ratio for each target species is assumed to be uniform across the disk, as is the total surface pressure. For a multi-layered, plane-parallel atmosphere, at normal incidence, the radiative transfer equation is given by the equation for the emerging intensity:

$$I_\nu = \epsilon_0 B_\nu(T_s) e^{-\tau_{0,\nu}} + \int_0^{\tau_{0,\nu}} B_\nu(T) e^{-\tau_\nu(z)} d\tau_\nu(z) \tag{3.15}$$

where ϵ_0 is the emissivity of the surface of Mars at the observed frequency ($\epsilon_0 = 0.96$), B_ν is the Planck function, T_s is the surface temperature of Mars, $T = T(z)$ is the temperature at each layer at altitude z, $\tau_\nu(z)$ is the frequency-dependent optical depth above each layer at altitude z, and $\tau_{0,\nu}$ is the total optical depth of the atmosphere.

At the Rayleigh-Jeans approximation of Planck's law, the radiative transfer equation becomes:

$$T_\nu = \epsilon_0 T_s e^{-\tau_{0,\nu}} + \int_0^{\tau_{0,\nu}} T(z) e^{-\tau_\nu(z)} d\tau_\nu(z) \tag{3.16}$$

where T_ν is the frequency-dependent flux in units of brightness temperature. The optical path increases with the incidence angle, and therefore the optical depth is multiplied by the factor $1/\mu = \sec(\theta)$. In our calculation, we use the effective zenith angle (θ=53°), leading to an airmass of $1/\bar{\mu}$=1.66. The opacity above each layer at altitude z in the atmosphere is given by:

$$\tau_\nu(z) = \int_z^\infty \alpha_\nu(z') \frac{dz'}{\bar{\mu}} \tag{3.17}$$

where $\alpha_\nu(z')$ is the absorption coefficient at each layer at altitude z ($z > z'$), and $d(z')$ is its corresponding thickness. The atmospheric layers are chosen to have an increasing thickness in the direction of altitude, having comparable optical depths between the atmospheric layers.

The absorption coefficient at each layer of the atmosphere, as a function of frequency is given by:

$$\alpha_\nu(z) = S_{\nu_0}(T) \times N(z) \times f_v(\nu - \nu_0). \tag{3.18}$$

where $S_{\nu_0}(T)$ is the strength of the transition with central frequency ν_0, and is given by:

$$S_{\nu_0}(T) = S_{\nu_0}(T_0) \frac{\exp(-hcE_L/k_BT) Q_T(T_0)[1 - \exp(-hc\nu_0/k_BT)]}{\exp(-hcE_L/k_BT_0) Q_T(T)[1 - \exp(-hc\nu_0/k_BT_0)]} \tag{3.19}$$

where S and Q are the spectral line strength and the partition function, respectively. These two parameters are calculated at temperature T of the atmospheric layer, and the reference temperature $T_0 = 296$ K. E_L is the lower state energy. S, Q and E_L are extracted from the HITRAN 2008 database (Rothman et al. 2009). h, c and k_B are the Planck constant, the speed of light, and Boltzmann constant, respectively.

$N(z)$ is the number density of the analyzed constituent in the atmosphere contained in each layer, and is expressed as:

$$N(z) = \frac{q \times P(z)}{k_B \times T(z)} \tag{3.20}$$

$P(z)$ is the pressure at altitude z of the atmospheric layer, q is the volume mixing ratio of the molecule analyzed. We consider a well mixed atmosphere where the mixing ratio is constant with altitude and k_B is the Boltzmann constant. $f_v(\nu - \nu_0)$ is the frequency-dependent normalized Voigt function. In the pressure-broadened profile, γ, the half width of the Lorentzian should be calculated by:

$$\gamma = \gamma_f \times \frac{P}{P_0} \times (1 - q) \times \left(\frac{T_0}{T}\right)^{n_f} + A \tag{3.21}$$

$$A = \gamma_s \times \frac{P}{P_0} \times q \times \left(\frac{T_0}{T}\right)^{n_s} \tag{3.22}$$

P_0 and T_0 are the pressure and temperature at the reference standard temperature and pressure (STP), P and T are the pressure and temperature at each atmospheric layer, γ_f and γ_s are the foreign and self broadening coefficients, whereas n_f and n_s are the temperature dependent coefficients for the foreign and self broadening coefficients, respectively. In the Martian atmosphere, the molecules are considered under a CO_2 collisional regime. Therefore we used for CO(3-2) the following pressure-broadening constants: γ_{CO-CO_2}=0.116, γ_{CO-CO}=0.079 (Belov et al. 1992), n_{CO-CO_2}=0.75 (Varanasi 1975) and n_{CO-CO}=0.74 (Rothman et al. 2009).

3.3 Results

The data were processed using the Continuum and Line Analysis Single-dish Software (CLASS)[j] and our own data reduction and analysis pipeline, coded in IDL (Exelis Visual Information Solutions, Boulder, Colorado). For each scan during each night, the baseline was corrected using a polynomial fitting (degree 8), then aligned based on the velocity

[j]http://www.iram.fr/IRAMFR/GILDAS

(Doppler) shift. After summing up the spectra for one night, the baseline around line center was corrected using a polynomial fitting of degree 3. The reciprocal square of the corresponding RMS at the continuum was used as a weighting factor, when summing up the spectra over time during one night, and over different nights. The double sided band spectrum was converted into a single side spectrum after removing the continuum contribution from the lower side band. Taking into account the beam efficiency of the telescope, the angular size of Mars and the telescope's beam width at the frequency setting, we then normalized the single side band spectrum to the retrieved continuum of Mars at the time of each observation.

3.3.1 Empirical Mode Decomposition versus Polynomial Fitting

In order to test whether the correction of the baseline and the reduction of the ripple and standing wave appearing in Figure 3.1 are good enough for such a sensitive search for trace gases and also for CO, we checked the polynomial fitting method against the Empirical Mode Decomposition (EMD) used in de Val-Borro et al. (2012). EMD decomposes the signal into different non-periodic oscillatory modes, the Intrinsic Mode Functions (IMF), with the baseline as the lowest frequency mode (residue) and the noise as the highest frequency modes combined. Dealing with non-periodic oscillatory modes is an advantage that EMD presents over FFT. Another advantage is that EMD allows the signal to be reconstructed by simply adding the different IMFs and the residue together (de Val-Borro et al. 2012).

Using the polynomial fitting method, we applied a polynomial fitting of degree 8 (in red) to a single spectrum measured on April 22-23, 2012, shown in figure 3.13. Figure 3.14 shows the data after the baseline removal, and one standard deviation of the noise is 68.9 mK. We zoomed in and plotted the spectrum around the expected line center in Figure 3.15. We fitted a polynomial baseline of degree 3 (in red), and show the residual spectrum around the line center after the baseline had been removed in Figure 3.15.

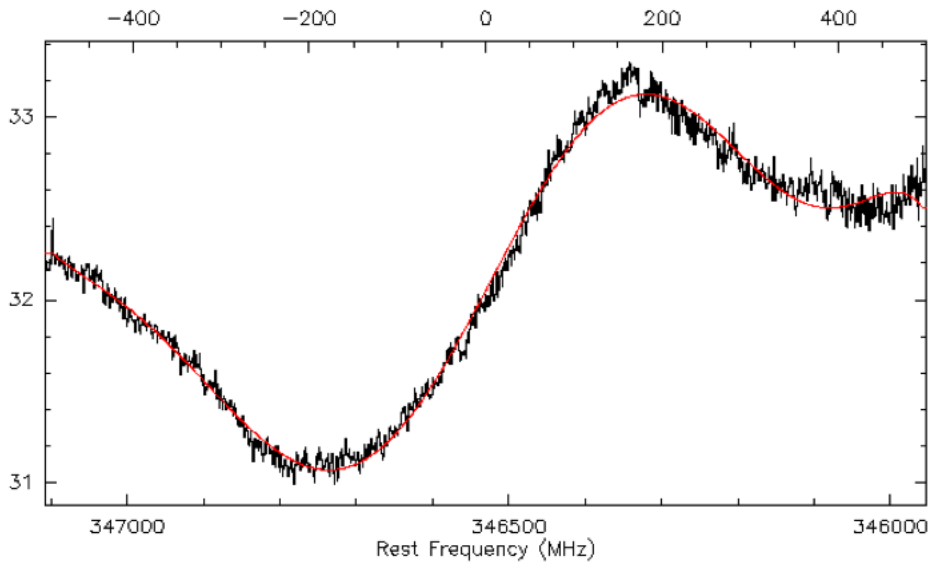

Figure 3.13 : The full spectrum of Mars is in black, and the fitted baseline polynomial of degree 8 is in red.

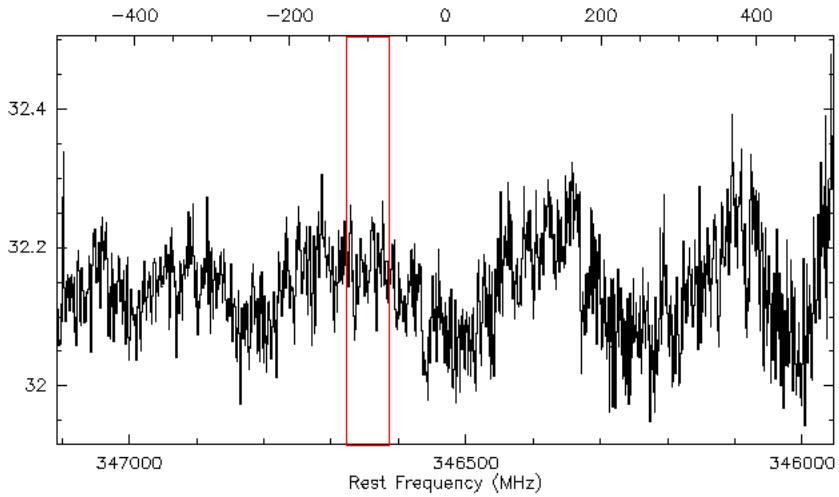

Figure 3.14 : Data after the baseline removal in Figure 3.13. The red box indicates the region around line center to be further analyzed in Figure 3.15.

Using the EMD method, we present the full spectrum of the data in Figure 3.16 (same spectrum as in Figure 3.13), then applied the EMD method and extracted eleven IMFs and the residue. The measured rms noise level in the highest frequency component IMF1

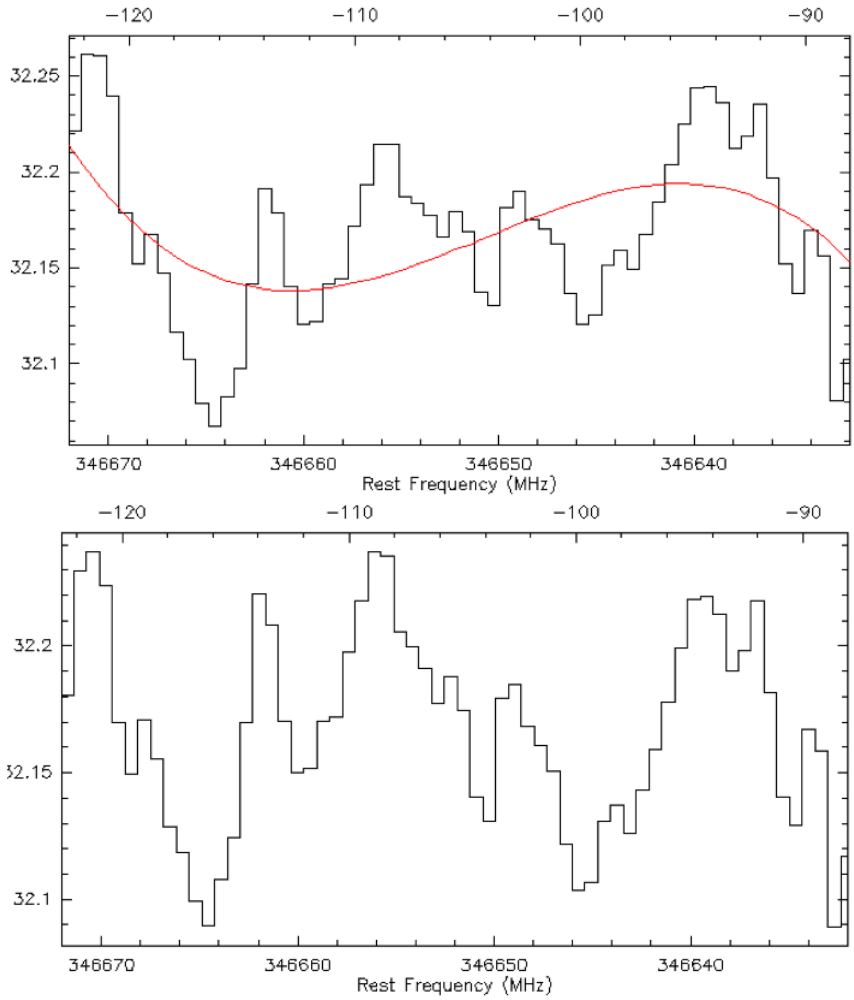

Figure 3.15 : Top panel: The spectrum around the expected line center is in black, and the fitted polynomial baseline of degree 3 is in red. Bottom panel: The spectrum around line center after the baseline had been removed.

is 24.3 mK, 2.3 times smaller than the expected 54.7 mK rms noise level derived from the radiometric equation. When we combine IMF1 with lower frequency components up to IMF5, we obtain an rms noise level in the combined spectrum of 51.7 mK, comparable to the expected noise level. Therefore the best estimate of the noise is the summation of IMF1 to IMF5, and not the IMF1 by itself.

Figure 3.17 shows IMF 1 in red, the summation of IMF1 to IMF5 in black, and the summation of IMF1 to IMF6 in blue. The summation of IMF1 to IMF6 (or higher) shows

structures at the boundaries of the frequency range. This is an additional reason for using the summation of IMF1 to IMF5 as the best estimate of the noise. Figure 3.18 (left panel) shows the summation of IMF1 to IMF5 around the expected line center.

Figure 3.18 shows the best estimate of the noise around the line center, when using the polynomial fitting (left), and when using the EMD method (right). The main features have been preserved in both residual spectra, with slight differences. Therefore applying polynomial fitting or using the EMD with the right combination of IMFs gives comparable results. We selected the polynomial fitting method in our analysis.

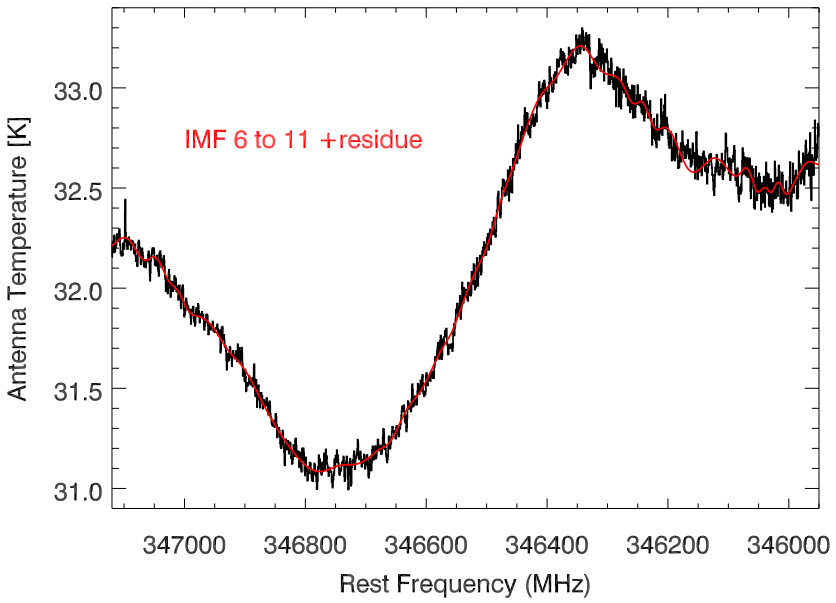

Figure 3.16 : The data is in black, and the summation of IMF 6 to 11 and the residue is in red. The summation of IMF 6 to 11 and the residue serve as the baseline, whereas the summation of IMF1 to IMF5 serve as the best estimate of the noise.

3.3.2 Extracting the Upper Limits on SO_2, H_2S and SO

We applied our radiative transfer model to synthesize each spectral line, with the appropriate line shape parameters in a CO_2 collisional atmosphere (with 95 % CO_2). The foreign broadening coefficients for SO_2 and H_2S are 0.18 cm^{-1}/atm (Suleiman et al. 1996)

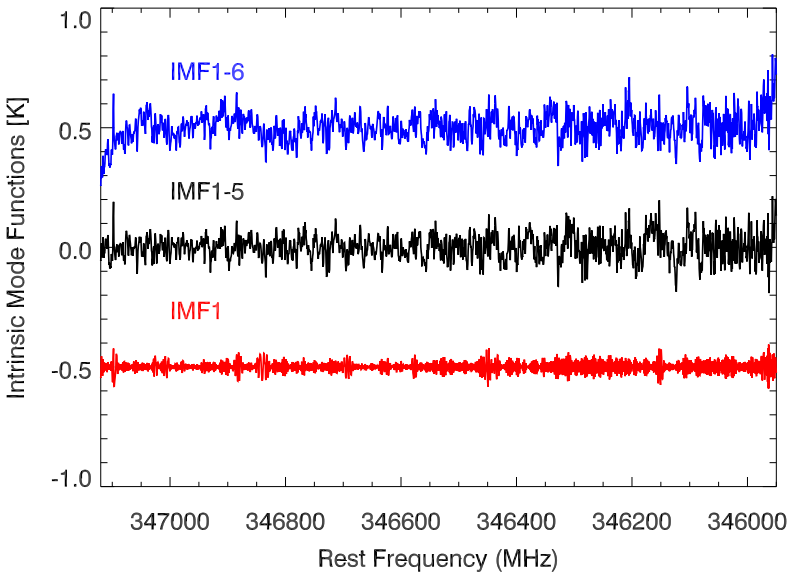

Figure 3.17 : IMF 1 (red) has a measured noise level that is 2.3 times smaller than the expected one by the radiometric equation, and is unrealistically low. The best estimate of the noise is the summation of IMF1 to IMF5, and is presented in black. If we add IMF1 to IMF6 (in blue) or higher, structures at the boundaries of the frequency range start to show up.

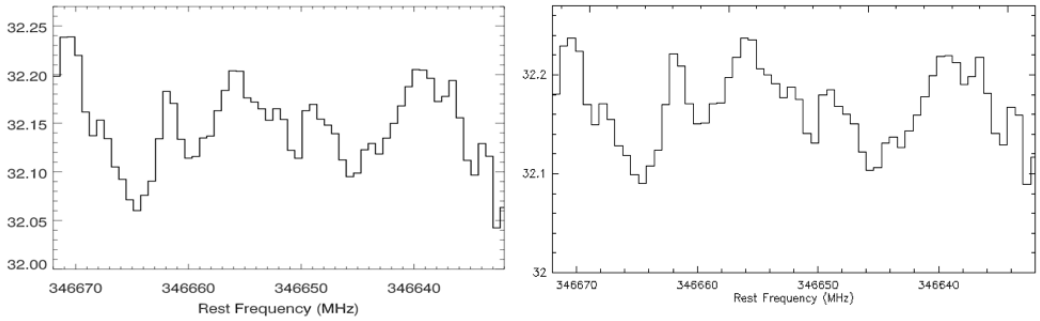

Figure 3.18 : Left: Summation of IMF1 to IMF5 around line center, which is taken to be the best estimate of the noise, added to the residue, using the EMD method. Right: Best estimate of the noise using the polynomial fitting method. The main features of the noise are similar in both spectra.

and 0.13 cm^{-1}/atm (Kissel et al. 2002), respectively. For SO, the broadening coefficient is not measured but we assumed it to be 1.3 times larger than in air, or 4 MHz/torr (0.10

cm^{-1}/atm). The dependence of the transition strength on temperature is taken into account by implementing the appropriate partition functions. The spectral lines are modeled at a spectral resolution of $\sim 7\times10^{-3}$ MHz, then convolved with a boxcar kernel of 1 MHz width, the spectral resolution of the spectrometer. We later interpolated these values with the channel spacing of 0.65 MHz in order to compare our synthetic line shapes with the combined measured spectrum.

In order to calculate the photochemical lifetimes of the targeted molecules in the atmosphere of Mars, a photochemical model is required. Krasnopolsky et al. (2004) noted that it requires 0.5 years for molecules to be well mixed in the atmosphere of Mars. This timescale is shorter than the calculated 2 years lifetime for SO_2 (Krasnopolsky 1995; Nair et al. 1994). Therefore, SO_2 is assumed to be well mixed across the disk of the planet. If we consider a steady state outgassing event for SO_2 we can combine the spectra of this molecule independently for all the observing runs from November 2011 (L_s= 34°) until May 2012 (L_s= 110°). We cannot do the same for H_2S and SO due to the shorter photochemical lifetimes than the timespan between the observing runs, and therefore each observing night is treated individually. None of these sulfur species is condensible at the pressure and temperature conditions present on Mars, even in the polar regions.

When modeling the SO_2 spectral line that we compare against the co-added spectrum, we applied the same weighting factor we used before when co-adding the data. It is the reciprocal square of the corresponding RMS at the continuum of each spectrum at each night. This same weighting factor is used to average the temperature-pressure profile, the surface temperature, and the surface pressure extracted for each night. The weighted-averaged atmospheric parameters are then used to model the long term average SO_2 line.

The co-added spectrum of SO_2, and the spectra of SO and H_2S on the best nights of 11 May and 21 January, 2012, respectively are displayed in Figure 3.28. The spectrum for each species is shown as a solid line with error bars. The spectrum is normalized to the continuum of Mars and shifted to the rest frequency. The red lines are the expected absorption for each molecule at the 2σ level, where an upper limit at the 2σ level corresponds to a line

depth that is two standard deviations from the continuum. We do not see any absorption line for SO_2, SO or H_2S. For total integration time of 9.33 h, the RMS noise level (one standard deviation) in the co-added spectrum is 0.0165 % for SO_2. For the integration times of 50 min and 97 min on 11 May and 21 January, 2012, respectively, the RMS noise levels in the spectra are 0.0495 % for SO and 0.0367 % for H_2S. A summary of our results is presented in Table 3.3 (Khayat et al. 2015).

Although the continuum level is uncertain by $\pm 15\%$, the equivalent width of the spectral lines is conserved, and therefore this 15% uncertainty does not affect the retrieved upper limit on the mixing ratios.

Our upper limit for SO_2 is consistent with previous limits by Krasnopolsky (2012), Encrenaz et al. (2011) and Nakagawa et al. (2009), and is the most sensitive obtained in submillimeter wavelengths (see Table 3.3). Our value for the H_2S upper limit is 15 times smaller than the upper limit retrieved at millimeter wavelengths by Encrenaz et al. (1991), because the transition at 300.505 GHz is 5 times stronger than that at 216.716 GHz, and that longer on-source integration was spent to collect the spectra.

Table 3.3 Abundance limits (2σ) for the sulphuretted species on Mars using the CSO.

Molecule	Date (UT)	RMS at the normalized continuum (K)	This Work (ppbv)	Previous (ppbv)	Reference
SO	11 May 2012	4.95×10^{-4}	<0.7	-	-
H_2S	21 January 2012	3.67×10^{-4}	<1.3	<20 (in the mm)	Encrenaz et al. (1991)
SO_2	co-added over all nights	1.65×10^{-4}	<1.1	<0.3 (in the IR)	Krasnopolsky (2012) and Encrenaz et al. (2011)
		1.65×10^{-4}	<1.1	<2.0 (in the submm)	Nakagawa et al. (2009)
SO_2	28 November 2011	10.4×10^{-4}	<5.7		
SO_2	22 January 2012	4.00×10^{-4}	<2.0		
SO_2	23 January 2012	3.98×10^{-4}	<2.3		
SO_2	21 April 2012	6.60×10^{-4}	<4.3		
SO_2	22 April 2012	8.38×10^{-4}	<5.6		
SO_2	23 April 2012	3.86×10^{-4}	<2.4		
SO_2	08 May 2012	5.00×10^{-4}	<3.2		
SO_2	09 May 2012	7.49×10^{-4}	<5.4		
SO	27 November 2011	13.1×10^{-4}	<1.2		
SO	18 January 2012	20.0×10^{-4}	<1.8		
SO	19 January 2012	9.62×10^{-4}	<0.9		
SO	20 April 2012	14.9×10^{-4}	<1.7		
SO	24 April 2012	7.81×10^{-4}	<0.9		
SO	10 May 2012	6.47×10^{-4}	<0.9		
H_2S	29 November 2011	12.5×10^{-4}	<4.1		
H_2S	20 January 2012	4.10×10^{-4}	<1.5		
H_2S	25 April 2012	7.83×10^{-4}	<3.1		
H_2S	26 April 2012	4.42×10^{-4}	<1.8		
H_2S	12 May 2012	8.05×10^{-4}	<3.7		
H_2S	13 May 2012	6.73×10^{-4}	<3.0		

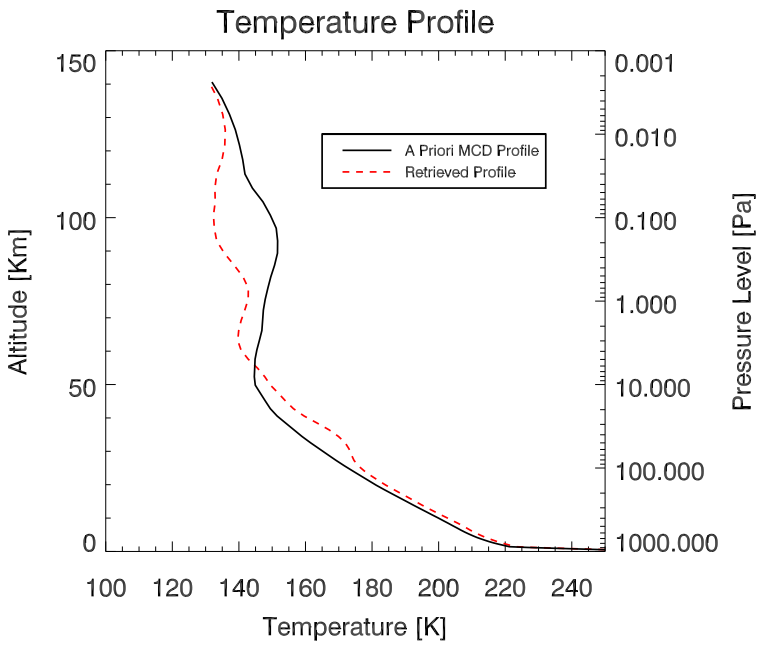

Figure 3.19 One of the 36×36 *a priori* MCD profiles (solid line) that are used to invert the ^{12}CO (3-2) line. The retrieved temperature profile (dashed red lines) leads to the best fit between the observed and synthetic ^{12}CO (3-2) on April 22 UT, 2012, shown in Fig. 3.11.

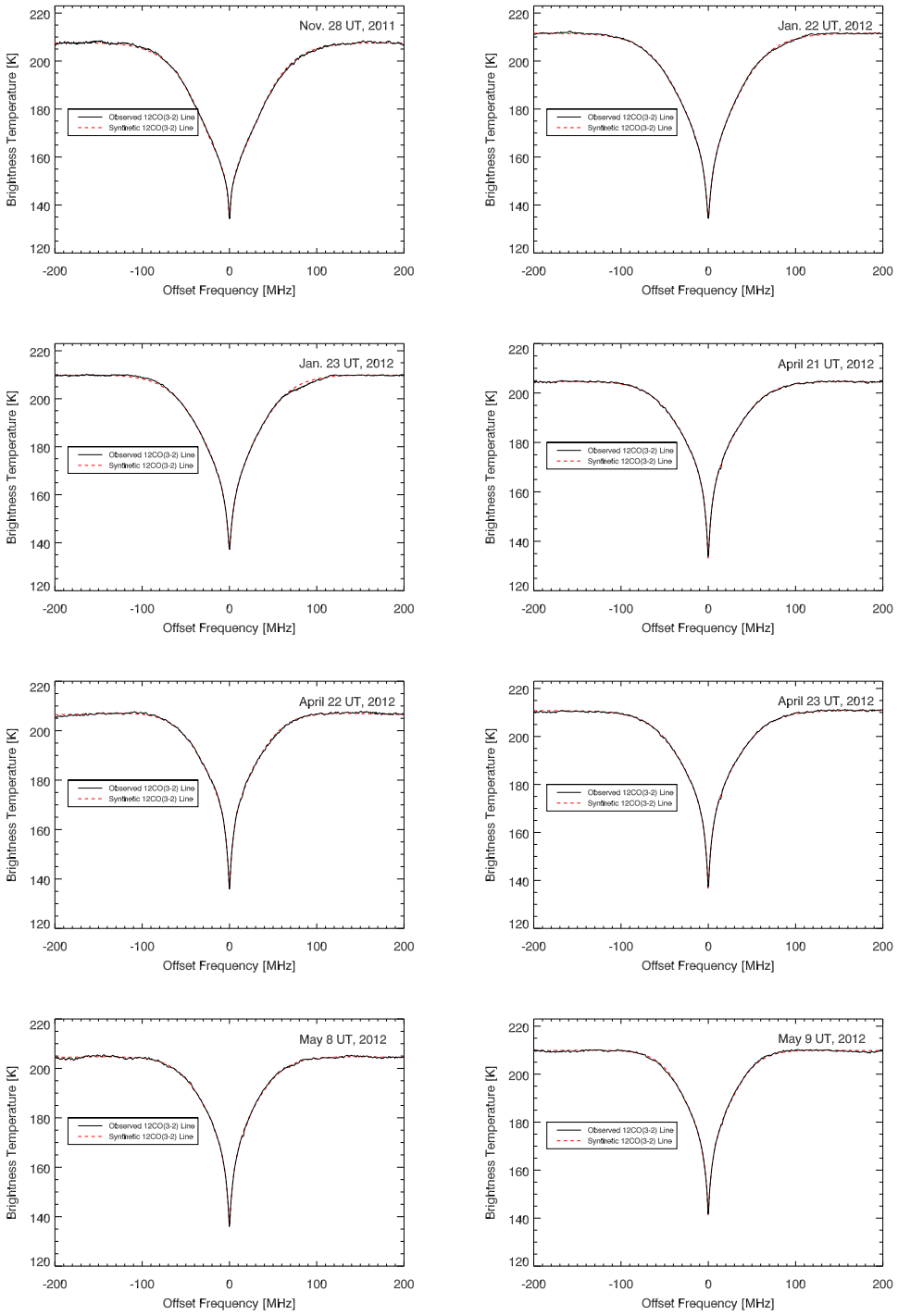

Figure 3.20 : Observed ^{12}CO (3-2) spectrum of Mars shifted to the rest frequency at 345.796 GHz (solid line) at the retrieved Mars brightness temperature on different observing dates. The dashed red lines show the synthetic ^{12}CO(3-2) spectrum using the retrieved temperature profile and brightness temperature for Mars at the time of the observation.

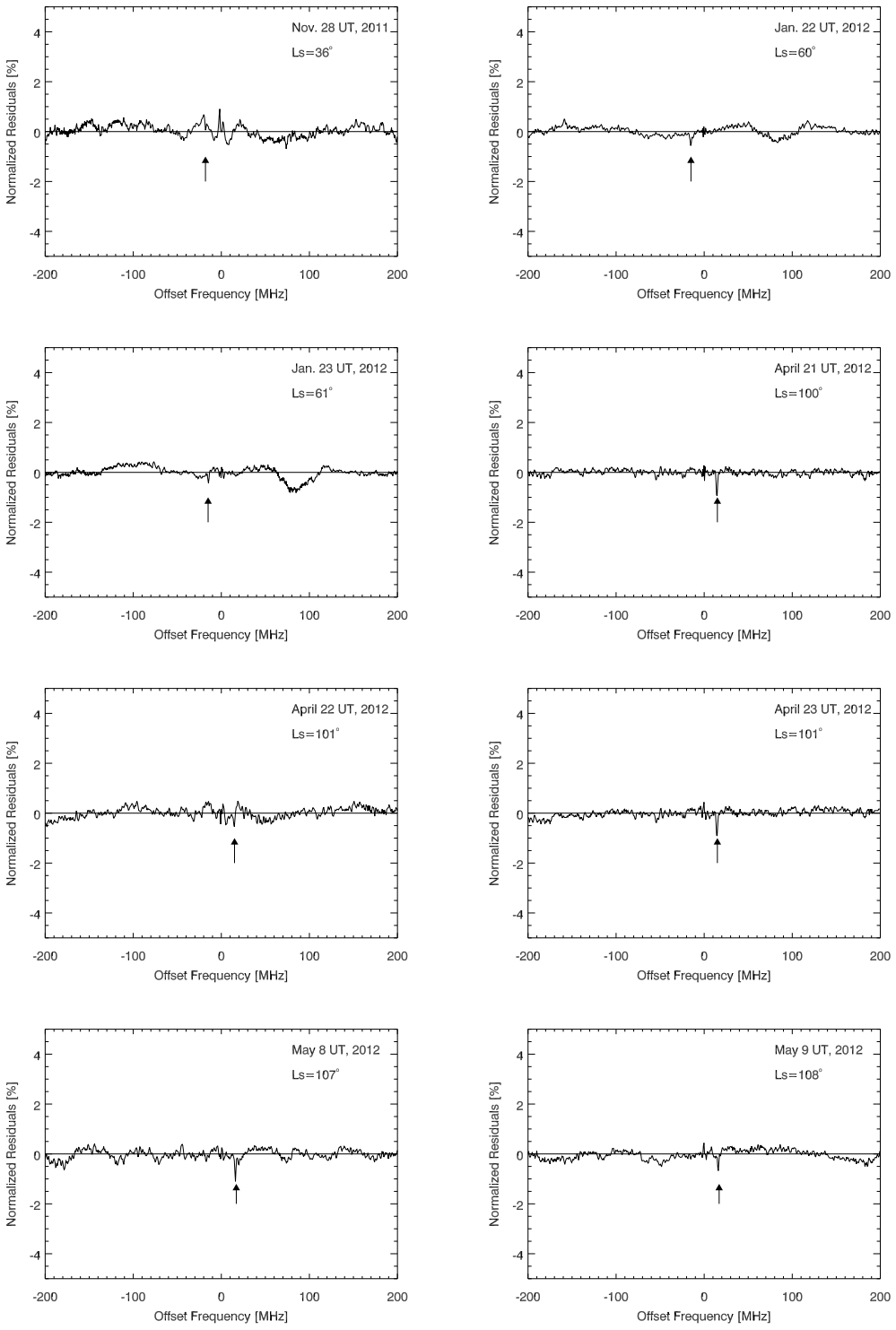

Figure 3.21 : Residual spectra showing the difference between the observed and synthetic ^{12}CO(3-2), normalized to the continuum of Mars at different observing dates. The arrow indicates the position of the telluric ^{12}CO(3-2) line.

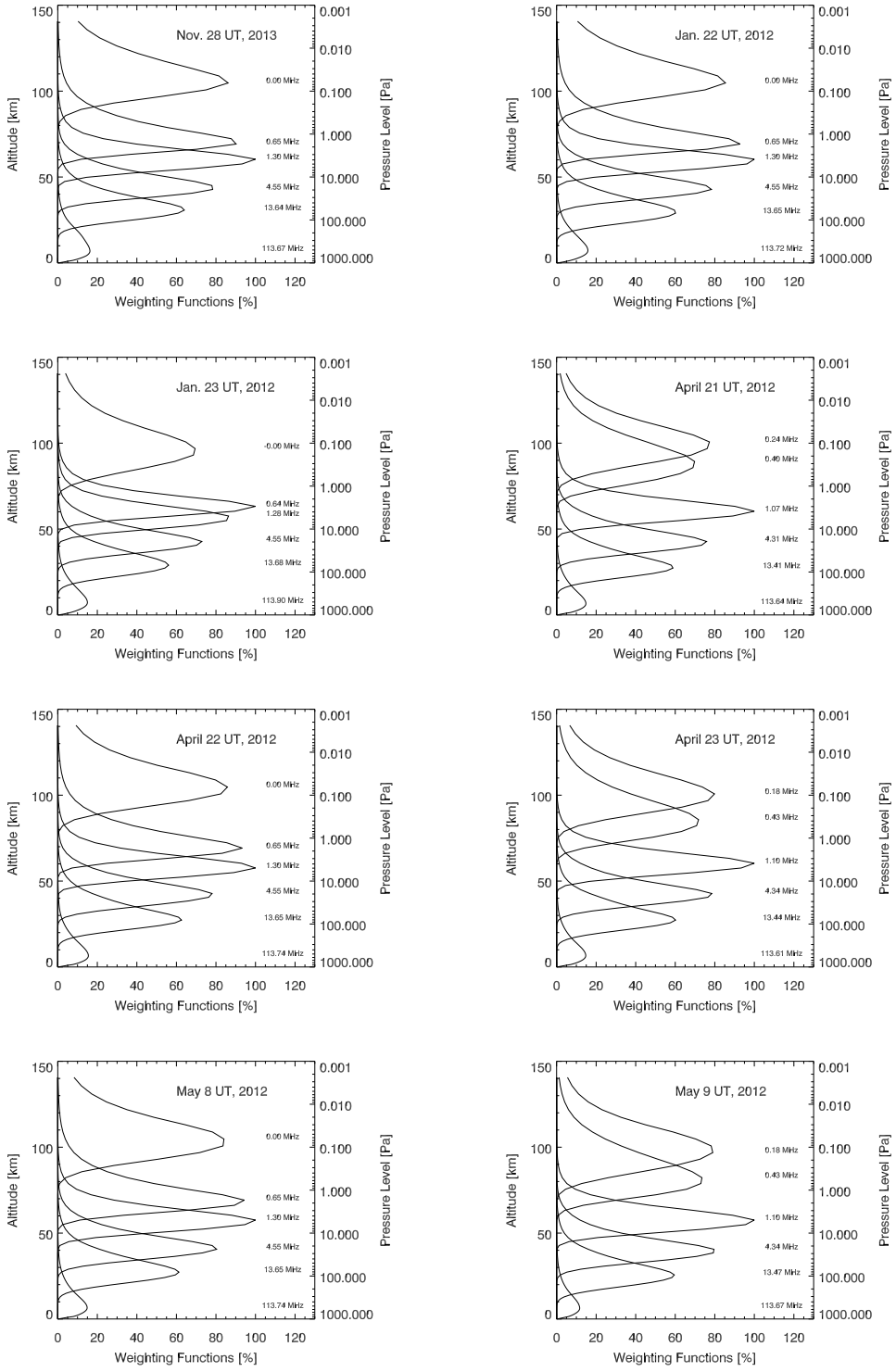

Figure 3.22 : Contribution functions for the ^{12}CO (3-2) line for the different observing date in Figure 3.20. The frequency offsets where the contribution functions peak from the highest to lowest altitude level are 0, 0.65, 1.3, 4.55, 13.65 and 113.74 MHz.

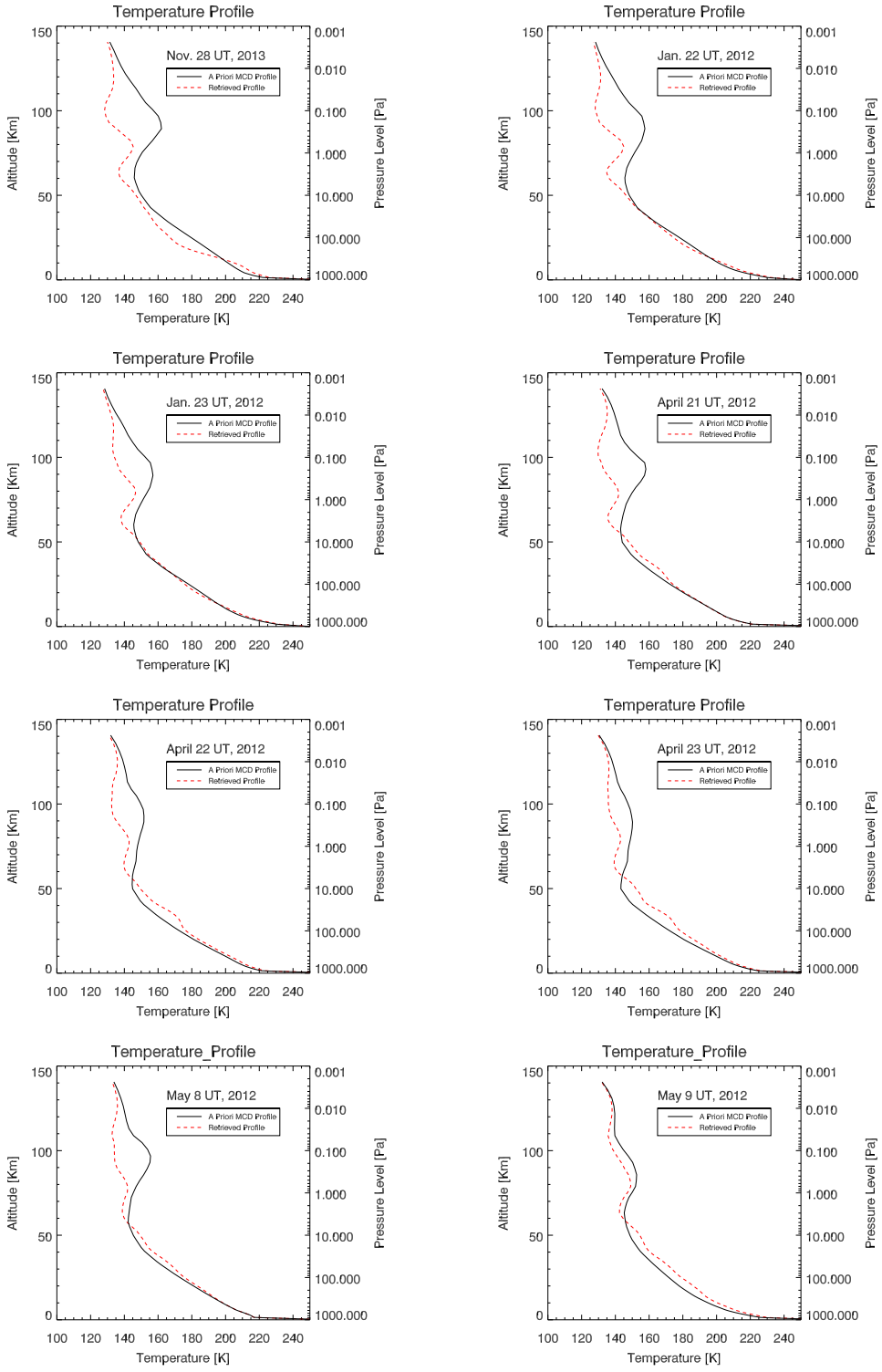

Figure 3.23 : One of the 36×36 *a priori* MCD profiles (solid line) that are used to invert the ^{12}CO (3-2) line. The retrieved temperature profile (dashed red lines) leads to the best fit between the observed and synthetic ^{12}CO (3-2), shown in Fig. 3.20.

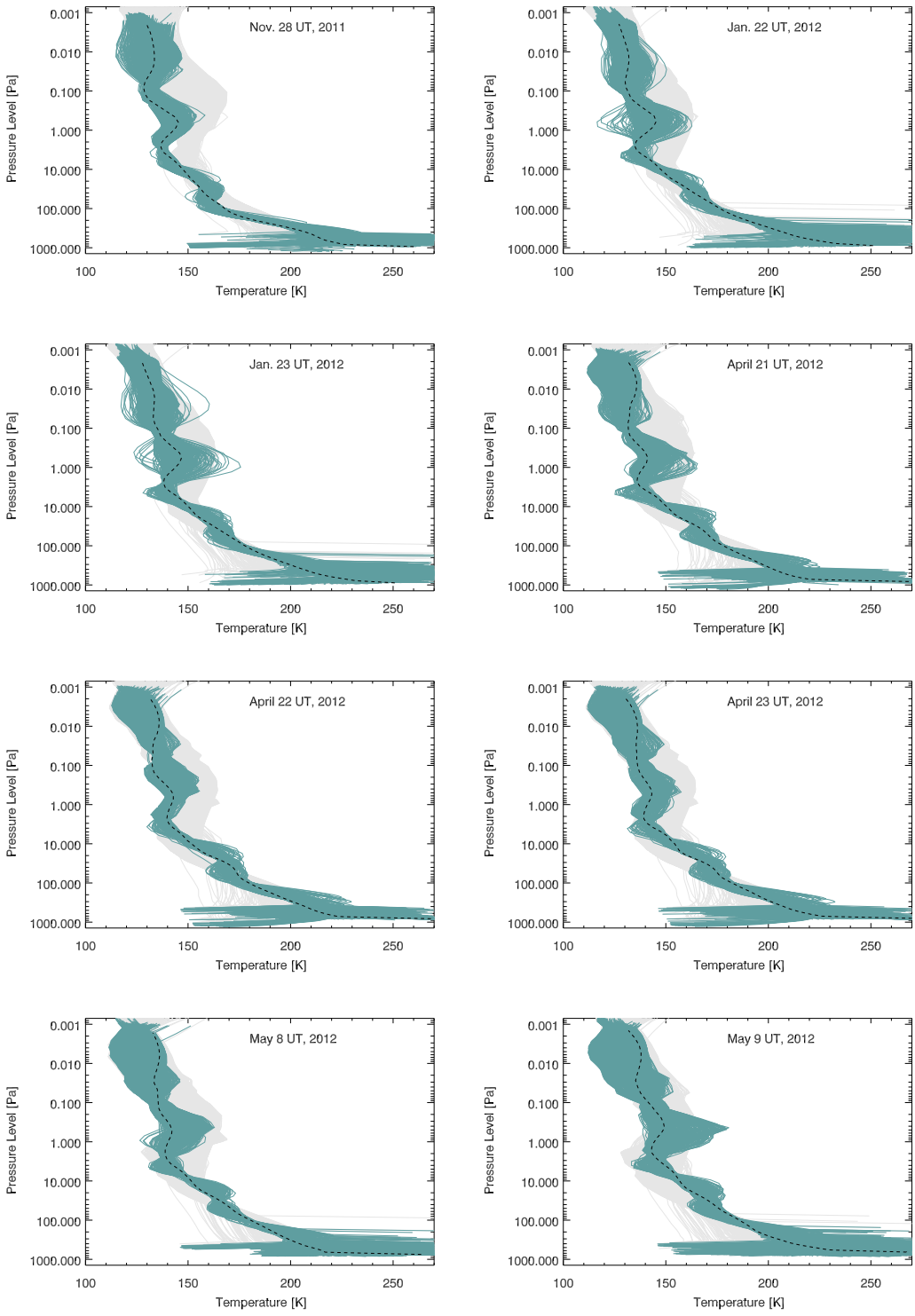

Figure 3.24 : For each night when CO is observed, we show 36×36 *a priori* MCD profiles (gray lines), the retrieved temperature profiles (turquoise lines), and the optimum extracted profile for calculating the abundance of the sulfur species (dashed black line) (Khayat et al. 2015).

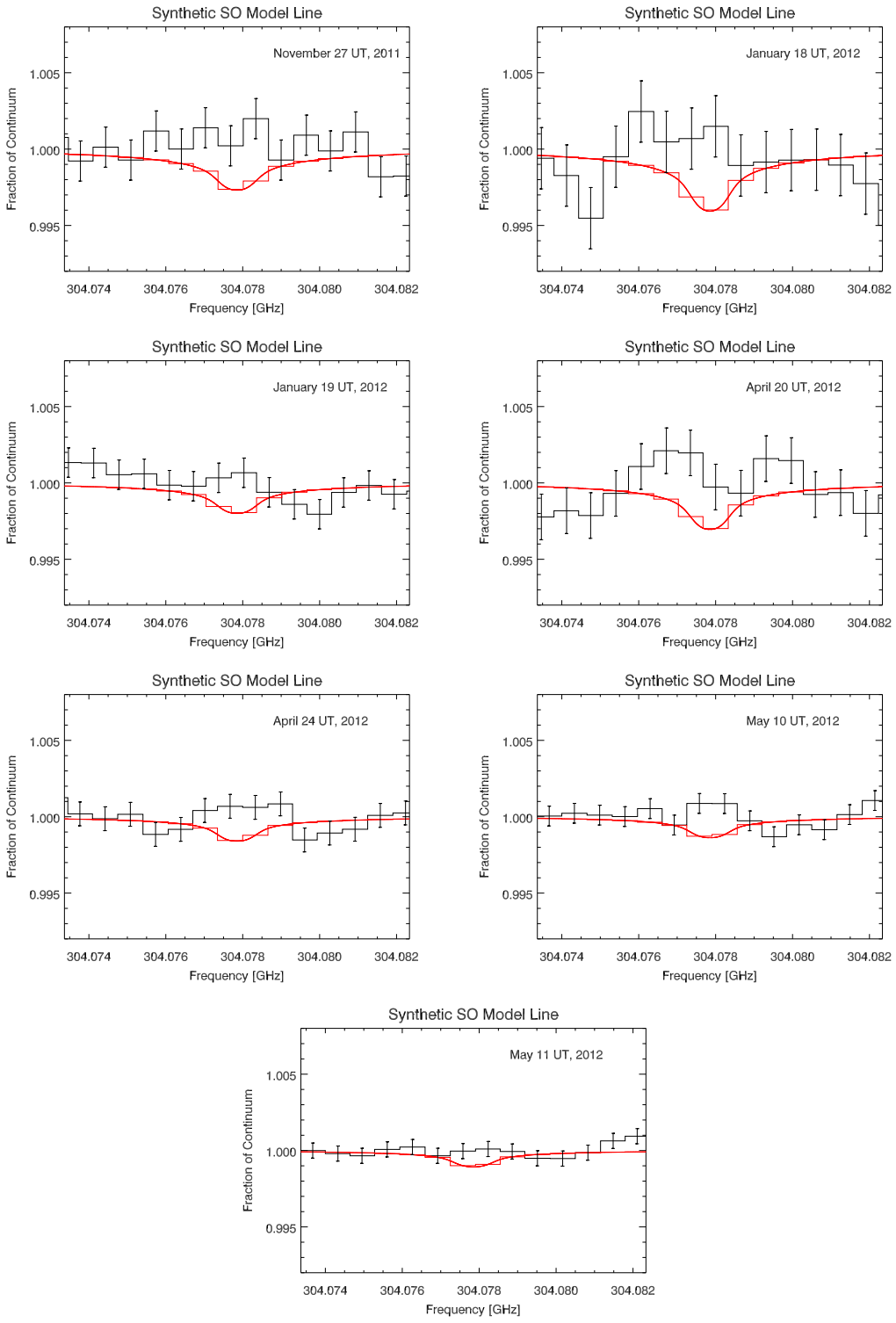

Figure 3.25 : The black solid line shows the spectrum of SO. The spectra are normalized to the continuum of Mars and shifted to the rest frequency. No SO absorption was found. The solid red lines show the expected absorption at 2σ.

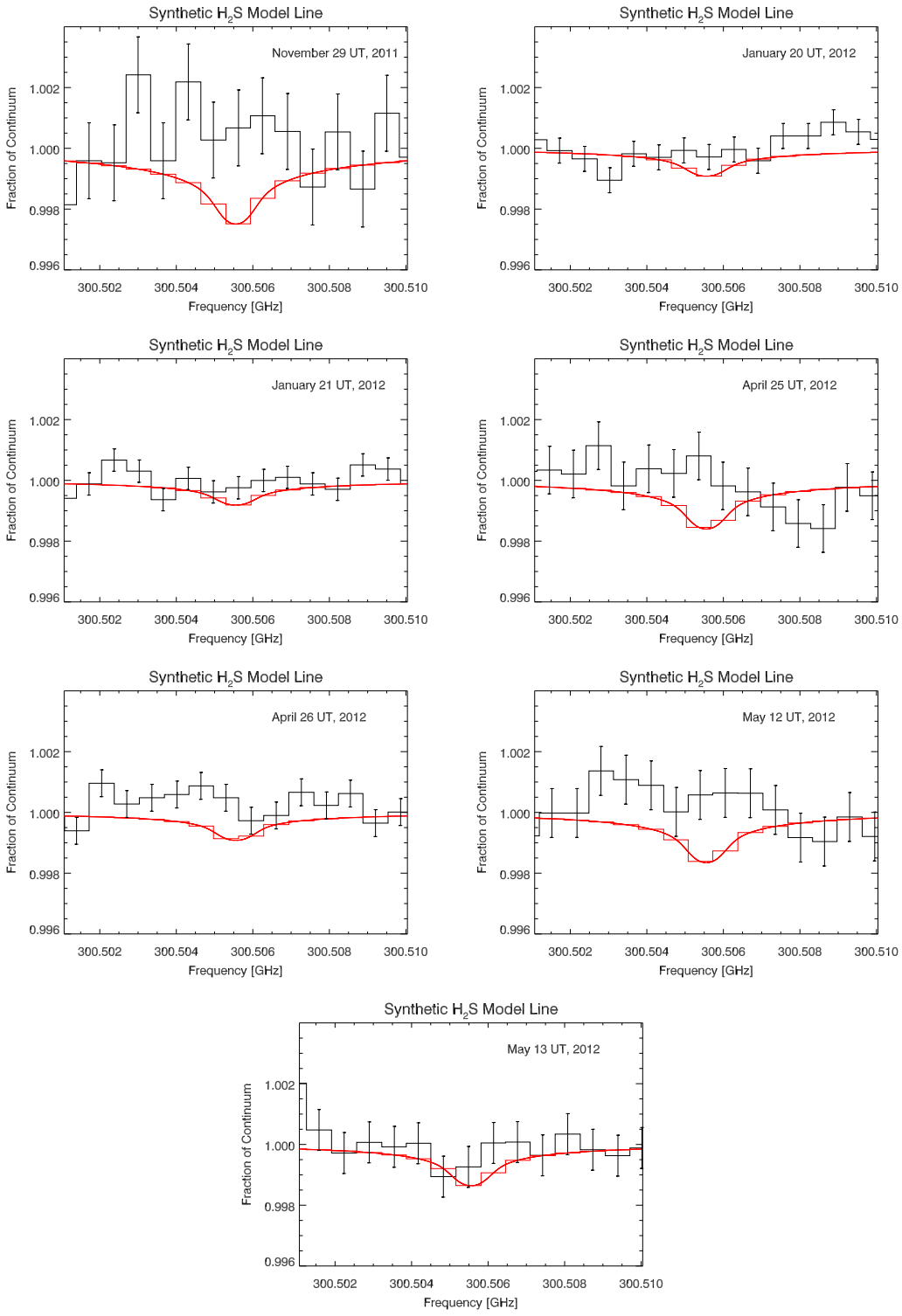

Figure 3.26 : The black solid line shows the spectrum of H_2S. The spectra are normalized to the continuum of Mars and shifted to the rest frequency. No H_2S absorption was found. The solid red lines show the expected absorption at 2σ.

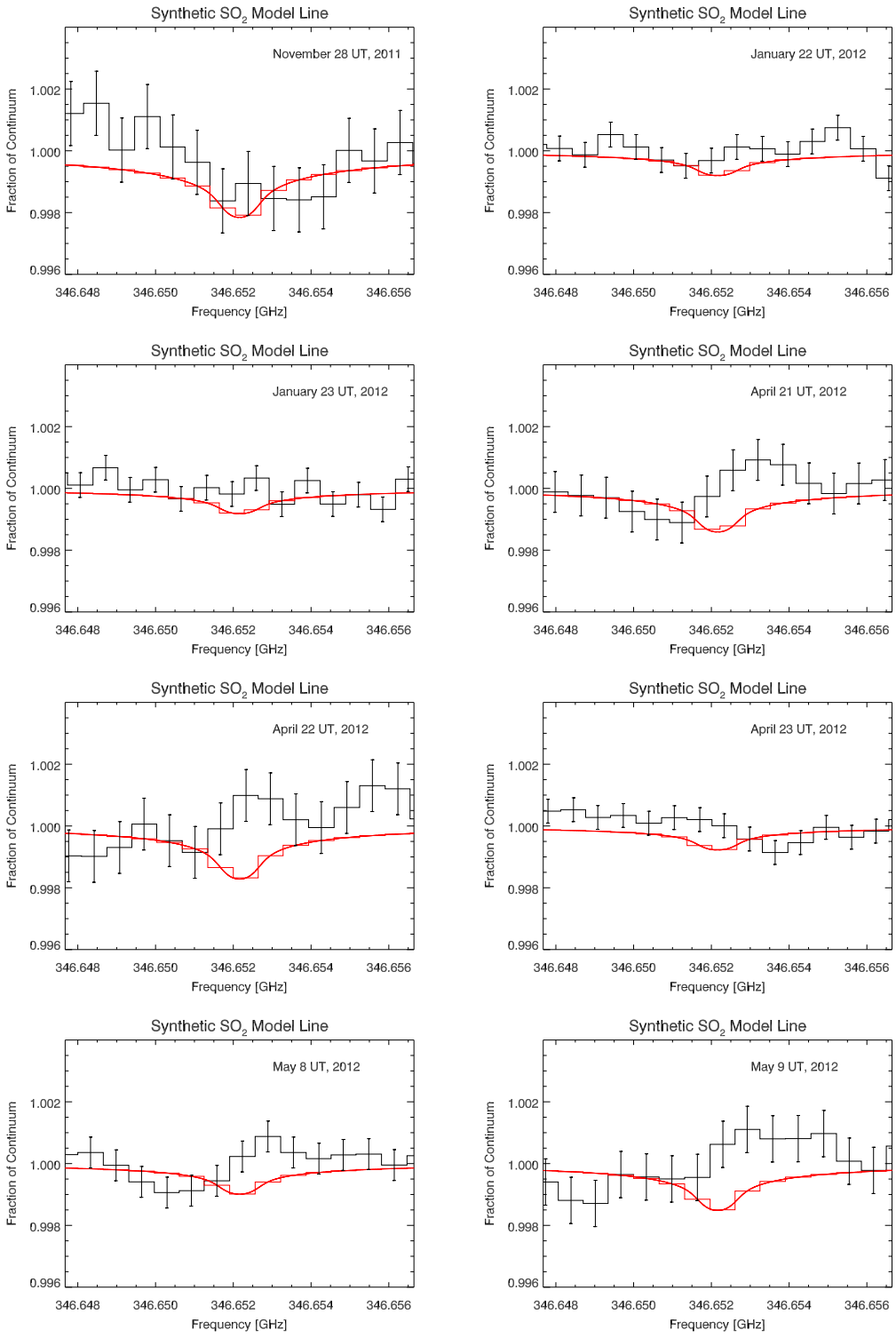

Figure 3.27 : The black solid line shows the spectrum of SO_2. The spectra are normalized to the continuum of Mars and shifted to the rest frequency. No SO_2 absorption was found. The solid red lines show the expected absorption at 2σ.

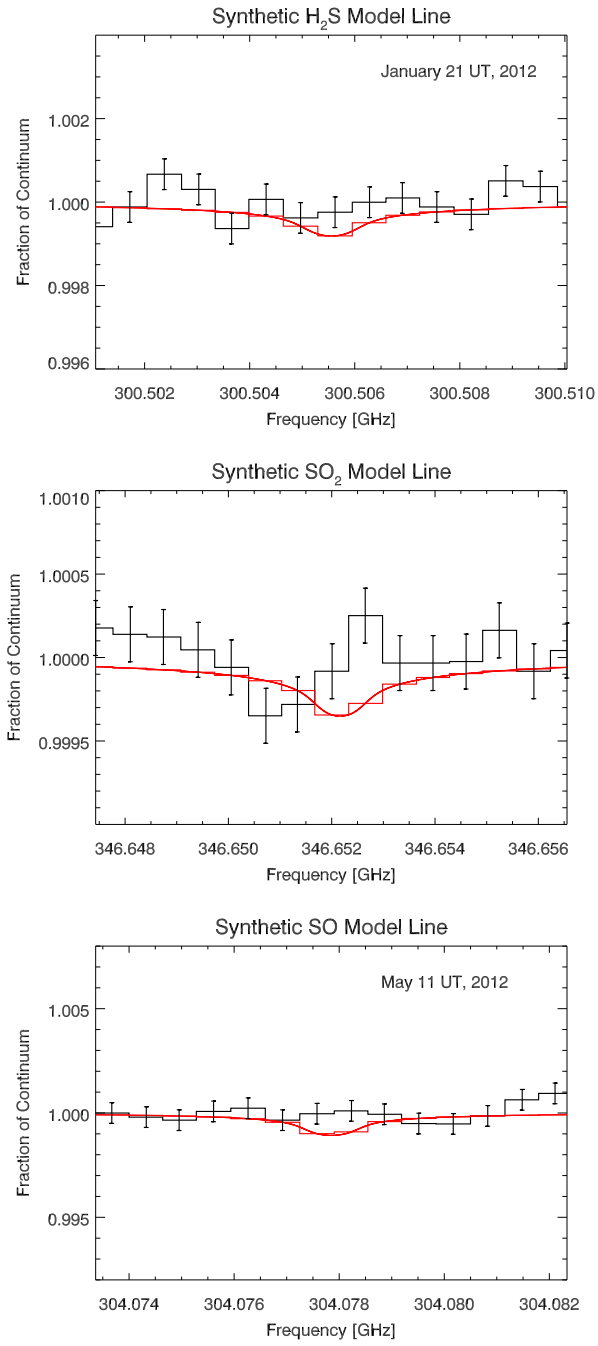

Figure 3.28 : The black solid line shows the spectrum for SO_2, SO and H_2S. For SO_2, it is the co-added spectrum for all the observing nights, while for SO and H_2S, it is the spectrum on the best night. The spectra are normalized to the continuum of Mars and shifted to the rest frequency. The red solid line and the dashed blue lines show the expected absorption at 2σ.

3.4 Observations at the James Clerk Maxwell Telescope

We used the single sideband high resolution heterodyne receiver "Heterodyne Array Receiver Program" (HARP) (Buckle et al. 2009), located in the right Nasmyth focus of the 15 m single dish antenna of the James Clerk Maxwell Telescope (JCMT) on Maunakea, Hawaii, to look for SO_2 ($J_{n,k} = 19_{1,19} - 18_{0,18}$) at 346.652 GHz. The targeted volcanic area, Tharsis, was observed on 23, 24 and 25 May 2014 at the mid-Northern Summer season, at Ls= 135° in Mars year 32 (MY 32). We observed Tharsis at longitudes ranging from 100°W to 159°W, at the respective sub-Earth point (Figure 3.29). The angular size of Mars was 12.5 arcsec in the middle of the run. The observing parameters are given in Table 3.4 (Khayat et al. 2015).

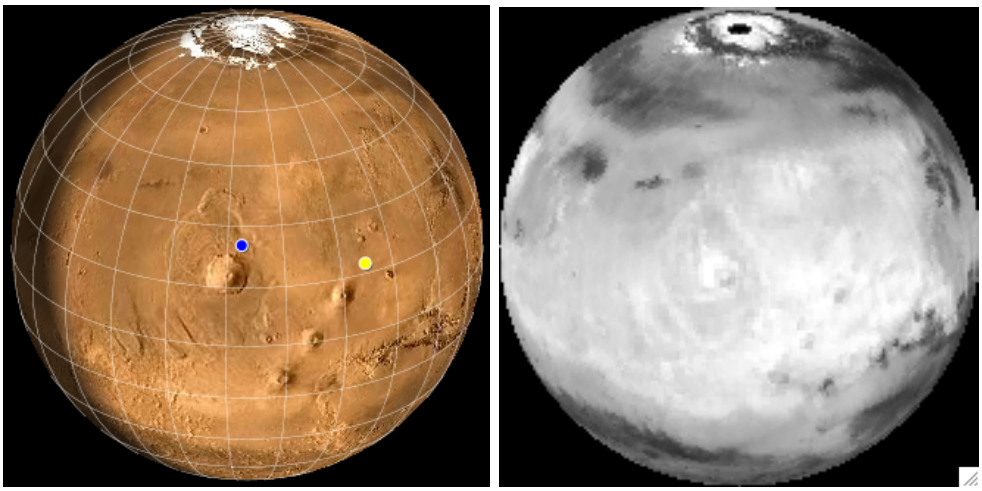

Figure 3.29 : Tharsis region on Mars as it appears on May 25, 2015, at 07:25 UT. Left panel: The map of Mars as rendered using Mars24 (Allison 1997; Allison & McEwen 2000). The yellow dot represents the sub-solar point (noon on Mars), where one would expect this to be near the highest surface temperature. Right panel: Using the albedo map obtained by the Mars Global Surveyor's Thermal Emission Spectrometer (Christensen et al. 2001), we were able to create a 2D orthographic projection of Mars, which was later used to extract the representative brightness temperature over the martian disk. Note that the images do not represent the real amount of residual ice on the Northern polar at the observing season ($L_s = 135°$).

The beam of the JCMT at 346.5 GHz has a FWHM of 14.5 arcsec. Chopping between Mars and the sky at 60 arcsec from the planet, the resulting estimated systematic

Table 3.4 : Parameters for Mars at the JCMT during the observing dates.

Target line	Frequency (GHz)	Date (UT)	Longitude on Mars	Heliocentric velocity (km/s)	Geocentric velocity (km/s)	Angular size (arcsec)	L_s (°)	Tau 225 GHz	Integration time (min)
SO_2	346.652	23 May 2014	123 W - 159 W	-2.03	+9.62	12.6	135	0.12	60
SO_2	346.652	24 May 2014	112 W - 158 W	-2.04	+9.75	12.5	135	0.10	60
SO_2	346.652	25 May 2014	100 W - 156 W	-2.04	+9.88	12.4	136	0.13	80

uncertainty for these nights was $\sim 4\%$ of the continuum level after checking the changes in the continuum around the SO_2 rest frequency. An example of the observed spectrum at the SO_2 setting for May 23, UT, 2014, is displayed in Figure 3.30.

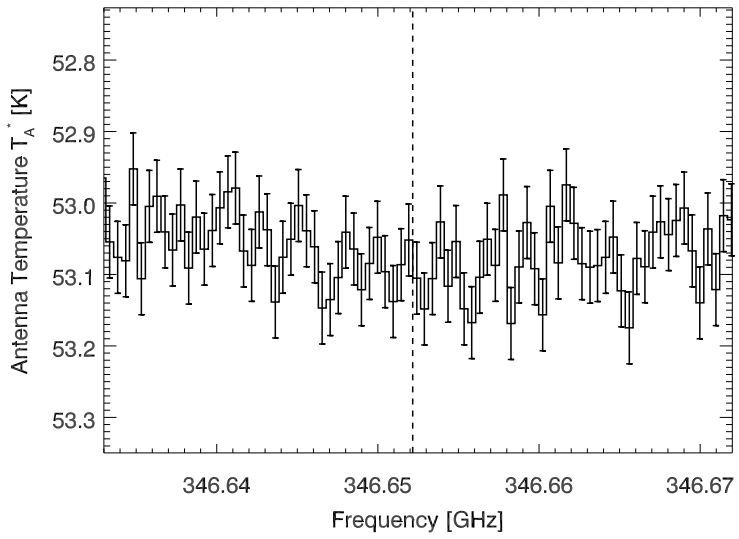

Figure 3.30 : Example of the summed single side band spectrum of SO_2 on May 23 UT, 2014. The spectrum is presented near rest frequencies (dashed line) of the line at 346.652 GHz. The error bars are the RMS uncertainty of the continuum.

We applied the same techniques we developed in section 3.2 for handling and processing the data collected at the CSO between 2011 and 2012. On May 25, 2014, we calculated an *a-priori* Mars brightness temperature T_b = 221.16 K, and observed the ^{12}CO (3-2) (rest frequency at 345.796 GHz) on Mars. The retrieved temperature-pressure profile was subsequently used for all the three consecutive nights of May 23, 24 and 25. The retrieved Mars brightness temperature T_b (= 206.13 K), the observed and synthetic CO lines,

the retrieved temperature profile, the corresponding contribution functions, the residuals between the observed and synthetic CO lines, and the extracted profiles for Mars on May 25 UT, 2014 are presented in Figures 3.32, 3.33, 3.34, 3.35 and 3.36, respectively.

3.4.1 Extracting the upper limits on SO_2

We applied our developed radiative transfer model to synthesize each spectral line, with the appropriate line shape parameters just like in section 3.3.2. At the back end of the receiver HARP, the digital autocorrelation spectrometer ACSIS is used at the band-width and channel spacing mode (1000 MHz × 2048). The spectral lines are modeled at a spectral resolution of $\sim 5{\times}10^{-3}$ MHz, then convolved with a boxcar kernel of 0.59 MHz width, the spectral resolution of the spectrometer (R = $\nu/\Delta\nu \sim$ 580,000). We later interpolated these values with the channel spacing of 0.49 MHz (Buckle et al. 2009) in order to compare our synthetic line shapes with the combined measured spectrum. Figure 3.31 shows no absorption of SO_2 on any of the dates, and therefore we co-added the 3 nights and presented the spectrum and the synthetic SO_2 model at 2σ in the same figure (lower panel). Our upper limits are presented in table 3.5.

Table 3.5 : Abundance limits (2σ) for the sulphuretted species on Mars using the JCMT on May 23, 24 and 25 UT, 2014.

Molecule	Date (UT)	RMS at the normalized continuum (K)	This Work (ppbv)	Previous (ppbv)
SO_2	co-added over 3 nights	4.49×10^{-4}	<3.1	<0.3 (in the IR) Krasnopolsky (2012) and Encrenaz et al. (2011)
		4.49×10^{-4}	<3.1	<2.0 (in the submm) Nakagawa et al. (2009)
SO_2	23 May 2014	7.35×10^{-4}	<5.1	
SO_2	24 May 2014	8.29×10^{-4}	<5.2	
SO_2	25 May 2014	10.3×10^{-4}	<6.4	

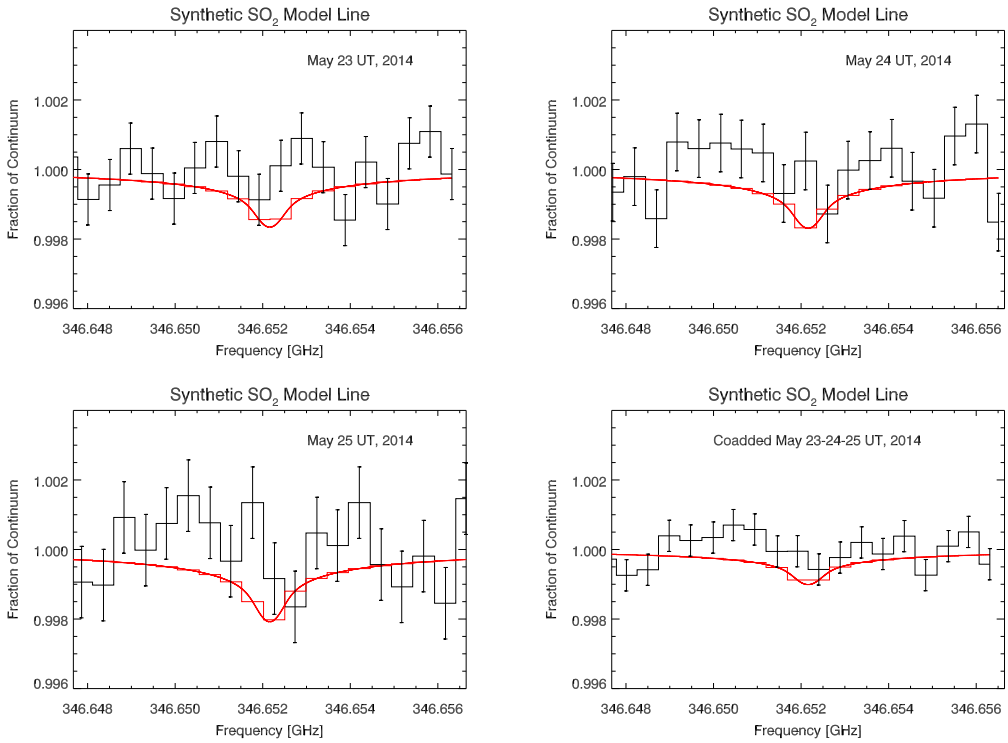

Figure 3.31 : The black solid line shows the spectrum of SO_2. The spectra are normalized to the continuum of Mars and shifted to the rest frequency. The solid red lines show the expected absorption at 2σ. The bottom panel represents the spectrum of the co-added data for May 23, 24 and 25 UT, 2014.

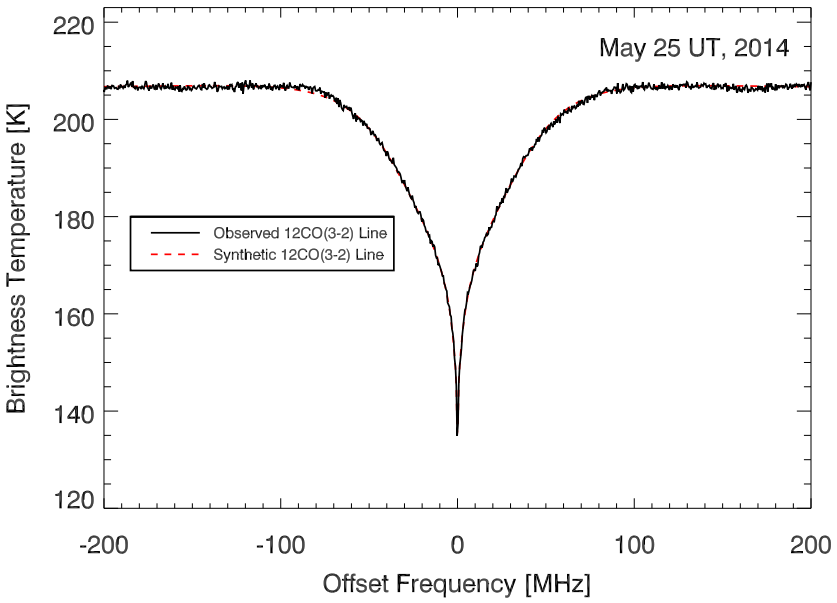

Figure 3.32 : Observed ^{12}CO (3-2) spectrum of Mars shifted to the rest frequency at 345.796 GHz (solid line) at the retrieved Mars brightness temperature on May 25 UT, 2014. The dashed red lines show the synthetic ^{12}CO(3-2) spectrum using the retrieved temperature profile and brightness temperature for Mars at the time of the observation.

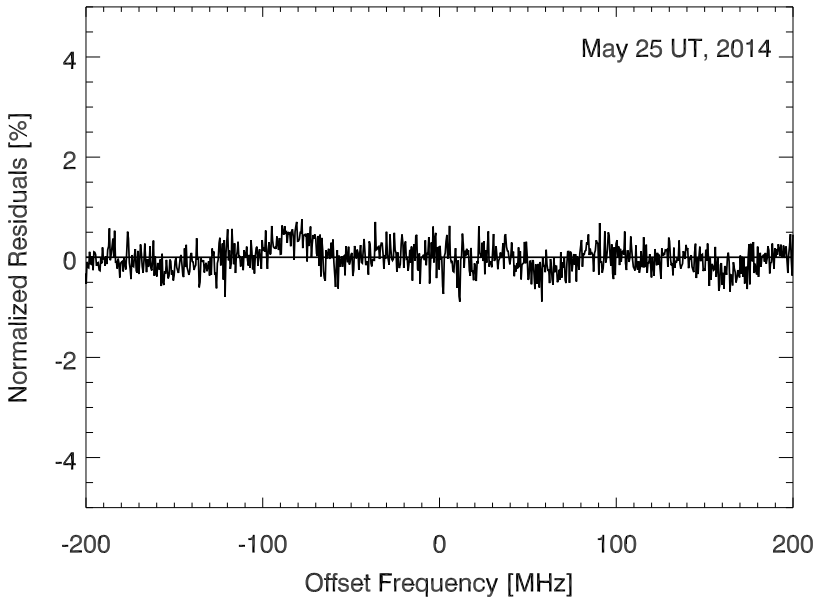

Figure 3.33 : Residual spectrum showing the difference between the observed and synthetic ^{12}CO(3-2) in Figure 3.32, normalized to the continuum of Mars on May 25, 2015.

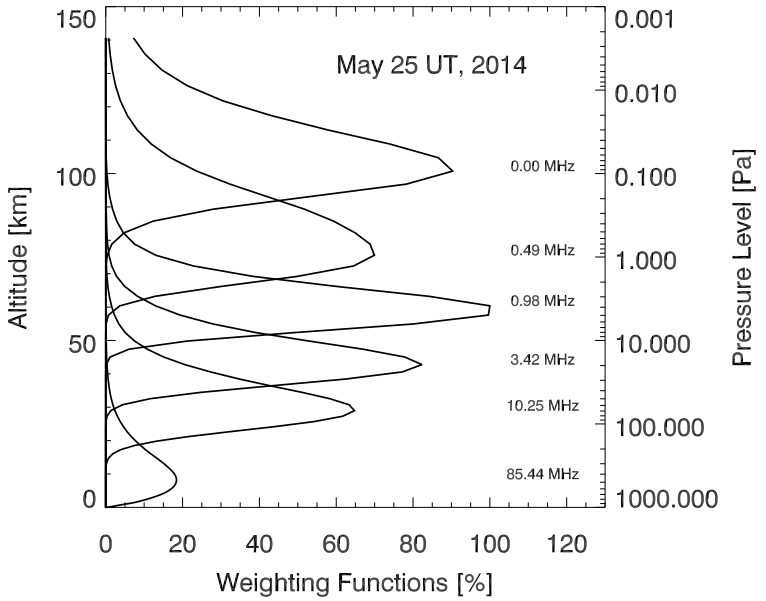

Figure 3.34 : Contribution functions for the ^{12}CO (3-2) line on May 25 UT, 2014. The frequency offsets where the contribution functions peak from the highest to lowest altitude level are 0.00, 0.49, 0.98, 3.42, 10.25 and 85.44 MHz.

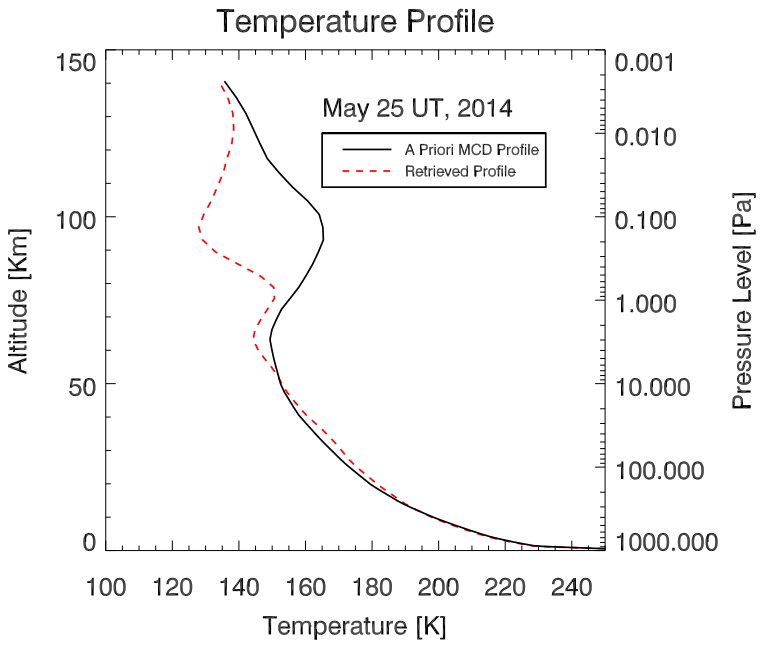

Figure 3.35 : One of the 36×36 *a priori* MCD profiles (solid line) that are used to invert the ^{12}CO (3-2) line. The retrieved temperature profile (dashed red lines) leads to the best fit between the observed and synthetic ^{12}CO (3-2) on May 25 UT, 2014, shown in Fig. 3.32

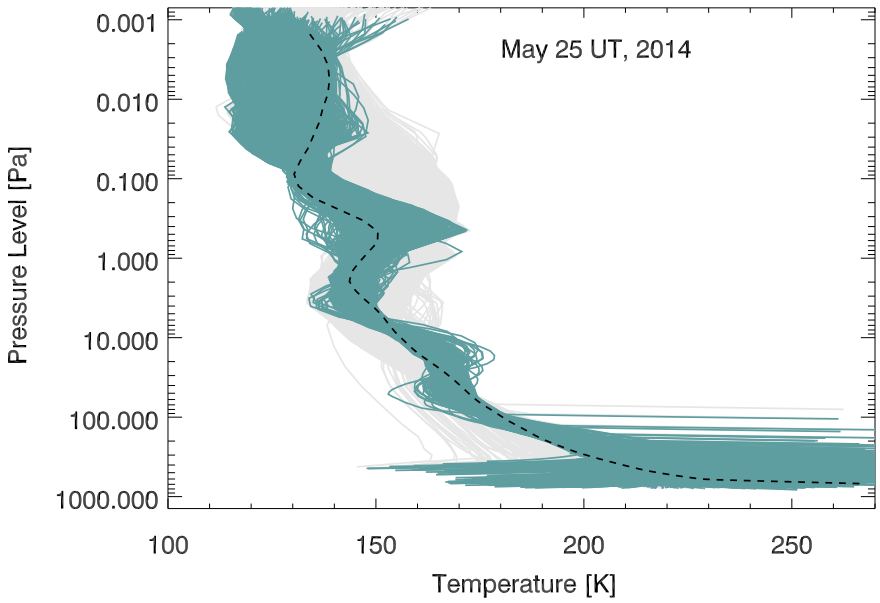

Figure 3.36 : For May 25, 2014, we show 36×36 *a priori* MCD profiles (gray lines), the retrieved temperature profiles (turquoise lines), and the optimum extracted profile for calculating the abundance on SO_2 (dashed black line)

References

Allison, M. 1997, Geophys. Res. Lett., 24, 1967

Allison, M. & McEwen, M. 2000, Planet. Space Sci., 48, 215

Belov, S. P., Tretiakov, M. I., & Suenram, R. D. 1992, Astrophys. J., 393, 848

Buckle, J. V., Hills, R. E., Smith, H., Dent, W. R. F., Bell, G., Curtis, E. I., Dace, R., Gibson, H., Graves, S. F., Leech, J., Richer, J. S., Williamson, R., Withington, S., Yassin, G., Bennett, R., Hastings, P., Laidlaw, I., Lightfoot, J. F., Burgess, T., Dewdney, P. E., Hovey, G., Willis, A. G., Redman, R., Wooff, B., Berry, D. S., Cavanagh, B., Davis, G. R., Dempsey, J., Friberg, P., Jenness, T., Kackley, R., Rees, N. P., Tilanus, R., Walther, C., Zwart, W., Klapwijk, T. M., Kroug, M., & Zijlstra, T. 2009, Monthly Notices of the Royal Astronomical Society, 399, 1026

Christensen, P. R., Bandfield, J. L., Hamilton, V. E., Ruff, S. W., Kieffer, H. H., Titus, T. N., Malin, M. C., Morris, R. V., Lane, M. D., Clark, R. L., Jakosky, B. M., Mellon, M. T., Pearl, J. C., Conrath, B. J., Smith, M. D., Clancy, R. T., Kuzmin, R. O., Roush, T., Mehall, G. L., Gorelick, N., Bender, K., Murray, K., Dason, S., Greene, E., Silverman, S., & Greenfield, M. 2001, J. Geophys. Res., 106, 23823

Clancy, R. T., Muhleman, D. O., & Jakosky, B. M. 1983, Icarus, 55, 282

Clancy, R. T., Sandor, B. J., Wolff, M. J., Christensen, P. R., Smith, M. D., Pearl, J. C., Conrath, B. J., & Wilson, R. J. 2000, J. Geophys. Res., 105, 9553

de Val-Borro, M., Rezac, L., Hartogh, P., Biver, N., Bockelée-Morvan, D., Crovisier, J., Küppers, M., Lis, D. C., Szutowicz, S., Blake, G. A., Emprechtinger, M., Jarchow, C., Jehin, E., Kidger, M., Lara, L.-M., Lellouch, E., Moreno, R., & Rengel, M. 2012, Astron. & Astrophys., 546, L4

Encrenaz, T., Bézard, B., Crovisier, J., Coustenis, A., Lellouch, E., Gulkis, S., & Atreya, S. K. 1995, Planet. Space Sci., 43, 1485

Encrenaz, T., Greathouse, T. K., Richter, M. J., Lacy, J. H., Fouchet, T., Bézard, B., Lefèvre, F., Forget, F., & Atreya, S. K. 2011, Astron. & Astrophys., 530, A37

Encrenaz, T., Lellouch, E., Atreya, S. K., & Wong, A. S. 2004, Planet. Space Sci., 52, 1023

Encrenaz, T., Lellouch, E., Rosenqvist, J., Drossart, P., Combes, M., Billebaud, F., de Pater, I., Gulkis, S., Maillard, J. P., & Paubert, G. 1991, Ann. Geophys., 9, 797

Forget, F., Hourdin, F., Fournier, R., Hourdin, C., Talagrand, O., Collins, M., Lewis, S. R., Read, P. L., & Huot, J.-P. 1999, J. Geophys. Res., 104, 24155

Golombek, M. P., Haldemann, A. F. C., Simpson, R. A., Fergason, R. L., Putzig, N. E., Arvidson, R. E., Bell, III, J. F., & Mellon, M. T. 2008, in The Martian Surface - Composition, Mineralogy, and Physical Properties, ed. J. Bell, III (Cambridge University Press), 468

Horn, J., Siebertz, O., Schmülling, F., Kunz, C., Schieder, R., & Winnewisser, G. 1999, Exp. Astron., 9, 17

Ke, Q. & Feldman, M. J. 1993, in Fourth International Symposium on Space Terahertz Technology, 33

Khayat, A. S., Villanueva, G. L., Mumma, M. J., & Tokunaga, A. T. 2015, Icarus, 253, 130

Kissel, A., Sumpf, B., Kronfeldt, H.-D., Tikhomirov, B. A., & Ponomarev, Y. N. 2002, J. Mol. Spectrosc., 216, 345

Kooi, J. W., Kovacs, A., Sumner, M. C., Chattopadhyay, G., Ceria, R., Miller, D., Bumble, B., Leduc, H. G., Stern, J. A., & Phillips, T. G. 2007, IEEE Transactions on Microwave Theory Techniques, 55, 2086

Krasnopolsky, V. A. 1995, J. Geophys. Res., 100, 3263

—. 2012, Icarus, 217, 144

Krasnopolsky, V. A., Maillard, J. P., & Owen, T. C. 2004, Icarus, 172, 537

Lellouch, E., Rosenqvist, J., Goldstein, J. J., Bougher, S. W., & Paubert, G. 1991, Astrophys. J., 383, 401

Leovy, C. 1966, Icarus, 5, 1

Lewis, S. R., Collins, M., Read, P. L., Forget, F., Hourdin, F., Fournier, R., Hourdin, C., Talagrand, O., & Huot, J.-P. 1999, J. Geophys. Res., 104, 24177

Mahaffy, P. R., Webster, C. R., Atreya, S. K., Franz, H., Wong, M., Conrad, P. G., Harpold, D., Jones, J. J., Leshin, L. A., Manning, H., Owen, T., Pepin, R. O., Squyres, S., Trainer, M., & MSL Science Team. 2013, Science, 341, 263

Mangum, J. G. 1993, Publications of the Astronomical Society of the Pacific, 105, 117

Markwardt, C. B. 2009, in Astronomical Society of the Pacific Conference Series, Vol. 411, Astron. Data Anal. Softw. Syst. XVIII, ed. D. A. Bohlender, D. Durand, & P. Dowler, 251

Matthews, H. E., Leech, J., & Friberg, P. 2004, http://cso.caltech.edu/wiki/cso/instruments/heterodyne/pointing

Muhleman, D. O. & Clancy, R. T. 1995, Appl. Opt., 34, 6067

Nair, H., Allen, M., Anbar, A. D., Yung, Y. L., & Clancy, R. T. 1994, Icarus, 111, 124

Nakagawa, H., Kasaba, Y., Maezawa, H., Hashimoto, A., Sagawa, H., Murata, I., Okano, S., Aoki, S., Moribe, N., Mizuno, A., Momose, M., Ohnishi, T., Mizuno, N., & Nagahama, T. 2009, Planet. Space Sci., 57, 2123

Penzias, A. A. & Burrus, C. A. 1973, Ann. Rev. Astron. Astrophys., 11, 51

Pickett, H. M., Poynter, R. L., Cohen, E. A., Delitsky, M. L., Pearson, J. C., & Müller, H. S. P. 1998, J. Quant. Spectrosc. Radiat. Trans., 60, 883

Rothman, L. S., Gordon, I. E., Barbe, A., Benner, D. C., Bernath, P. F., Birk, M., Boudon, V., Brown, L. R., Campargue, A., Champion, J.-P., Chance, K., Coudert, L. H., Dana, V., Devi, V. M., Fally, S., Flaud, J.-M., Gamache, R. R., Goldman, A., Jacquemart, D., Kleiner, I., Lacome, N., Lafferty, W. J., Mandin, J.-Y., Massie, S. T., Mikhailenko, S. N., Miller, C. E., Moazzen-Ahmadi, N., Naumenko, O. V., Nikitin, A. V., Orphal, J., Perevalov, V. I., Perrin, A., Predoi-Cross, A., Rinsland, C. P., Rotger, M., Šimečková, M., Smith, M. A. H., Sung, K., Tashkun, S. A., Tennyson, J., Toth, R. A., Vandaele, A. C., & Vander Auwera, J. 2009, J. Quant. Spectrosc. Radiat. Trans., 110, 533

Schilke, P., Groesbeck, T. D., Blake, G. A., & Phillips, T. G. 1997, Astrophys. J., Suppl. Ser., 108, 301

Simpson, R. A., Harmon, J. K., Zisk, S. H., Thompson, T. W., & Muhleman, D. O. 1992, in Mars, ed. H. H. Kieffer, B. M. Jakosky, C. W. Snyder, & M. S. Matthews (University of Arizona Press), 652–685

Snyder, J. P. 1987, US Geologic Survey Professional Paper 1395, 145153

Spera, F. J. 2000, in Encyclopedia of Volcanoes (Academic Press), 171–190

Suleiman, S. H., Kolodner, M. A., & Steffes, P. G. 1996, J. Geophys. Res., 101, 4623

Varanasi, P. 1975, J. Quant. Spectrosc. Radiat. Trans., 15, 191

Villanueva, G. L. 2004, PhD thesis, Max-Planck-Institut für Sonnensystemforschung

Chapter 4

Infrared Observations and Data Processing

This chapter describes new and extensive infrared searches for OCS at the R branch of its combination band ($\nu_1+\nu_3$) at 3.42 μm (2924 cm^{-1}) above the Tharsis and Syrtis volcanic regions. These searches span a range of 31 months, from December 2011 to June 2014. This work is part of a multi-band search for current volcanic outgassing on Mars that places sensitive limits of sulfur species in the atmosphere of the planet. In section 4.1, observations using the NASA Infrared Telescope Facility are presented. In section 4.2, the methodology in handling and processing the IR data by correcting for the anamorphic optics, and straightening the spectra (both spatially and spectrally), is explained. The removal of telluric and solar contamination in the Mars spectrum, in order to reveal information about trace gases in the atmosphere of the planet, is described. (2σ) upper limits for OCS are reported in section 4.3 after combining the data in 4 key dimensions: latitude, longitude, frequency and time. A newly-developed radiative transfer model for the atmosphere of Mars (IRRTM) that models Mars' two-way atmospheric transmittance, is also described. The implications of the OCS results and the conclusions are discussed in Chapter 5.

4.1 Observations using the NASA Infrared Telescope Facility

We observed Mars for more than two Earth years, looking for active release of OCS above Tharsis and Syrtis Major volcanic districts. The observations extended between December 15, 2011 and January 6, 2012 on the first Mars year (MY31) and May 30 to June 13, 2014 on the second one (MY32), covering different seasons on Mars: mid Northern Spring at L_s= 43°- 53°, and mid Northern Summer at L_s= 138°- 145°, respectively. The angular size of Mars varied between 7.9 and 12 arcseconds (arcsec), and the geocentric Doppler velocity ranged between -15.9 km/s and +11.2 km/s on the first and last run, respectively. The observing parameters for Mars and the mapped regions are listed in Table 4.1.

Table 4.1 : Parameters for Mars and the mapped volcanic regions during the observing dates.

Date (UT)	Volcanic Region	Doppler shift (km/s)	L_s (°)	Angular size (arsec)	Longitude range	Integration time (min)
15 December 2011	Tharsis	-15.9	43	7.9	105W - 120W	100
18 December 2011	Tharsis	-15.9	45	8.0	77W - 91W	62
3 January 2012	Syrtis Major	-15.3	52	9.2	276W - 300W	142
5 January 2012	Syrtis Major	-15.1	53	9.3	244W - 281W	152
6 January 2012	Syrtis Major	-15.0	53	9.5	229W - 272W	160
30 May 2014	Tharsis	+10.4	138	12.0	78W - 120W	92
12 June 2014	Syrtis Major	+11.2	144	10.8	302W - 344W	76
13 June 2014	Syrtis Major	+11.2	145	10.7	286W - 331W	104

The observations were carried out using CSHELL (Tokunaga et al. 1990; Greene et al. 1993), a high-resolution infrared spectrometer at the 3 m NASA Infrared Telescope Facility (IRTF) on top of Maunakea, Hawaii. We targeted OCS at its combination band (ν_1+ν_3) at 3.42 μm (2924 cm^{-1}). The spectral range covered during the observing runs is 2922.12 - 2927.64 cm^{-1} (3.4222 - 3.4257 μm). This frequency setting is characterized by strong methane lines that are present in Earth's atmosphere, and Maunakea's altitude of 4.2 km (60 % of the surface pressure) reduces their column abundance, and therefore their absorption, making it possible to look for trace gases in the martian atmosphere (Krasnopolsky 2005).

Cryogenic high-resolution echelle spectrometers such as CSHELL are excellent for probing minor constituents in planetary atmospheres. At near-infrared wavelengths, the intrinsic width of the martian spectral lines is ~ 0.001 cm^{-1}, and a resolving power exceeding one million is needed to measure their true line shapes. In its high resolution mode, CSHELL offers a resolving power of R = 43,000, corresponding to a spectral resolution of $\Delta\nu = 0.068$ cm^{-1} and a Doppler velocity resolution of Δv = 7 km/s. Using this, we were able to distinguish martian lines from their telluric (belonging to Earth's atmosphere) counterparts at Doppler shifts of Mars > 10 km/s during our observations. At R = 43,000 (0.5 arcsec slit width), there are 2.5 pixels/resolution on CSHELL's detector [a].

At each time we observed the planet, we positioned CSHELL's entrance slit (0.5×30 arcsec^2) on the North-South central meridian of Mars, and took individual scans while the planet rotated under the slit, therefore scanning the targeted volcanic regions on Mars under the sub-Earth point (Figure 4.1). We observed Syrtis at longitudes ranging from 229°W to 344°W, and Tharsis from longitude 77°W to 120°W.

The guiding was conducted "on-Mars" by frequently updating the tracking rates of the planet during these observations. Later on at the data reduction stage, we corrected for guiding inaccuracies by modeling the emergent flux received from Mars, a combination of thermal emission from the planet and solar reflected radiation, and comparing the modeled flux across the slit against the measured one hitting the detector. By doing so we were able to find the exact location of the slit on Mars for each scan. Even though the slit width is 0.5 arsec, our spatial resolution on the planet is limited by the seeing; we measured its full-width-at-half-maximum (FWHM) from the point-spread-function of a standard star that we used when focussing the telescope. The measured FWHM of the seeing ranged between 0.53 and 1.23 arcsec throughout the observing runs, reaching the best spatial resolution of 280 km on the planet on June 12, 2014.

The 30 arsec slit length of CSHELL is over 2 times the angular diameter of Mars, and therefore Mars and the Sky were included in each exposure. We nodded the telescope in

[a] http://irtfweb.ifa.hawaii.edu/ cshell/info.html

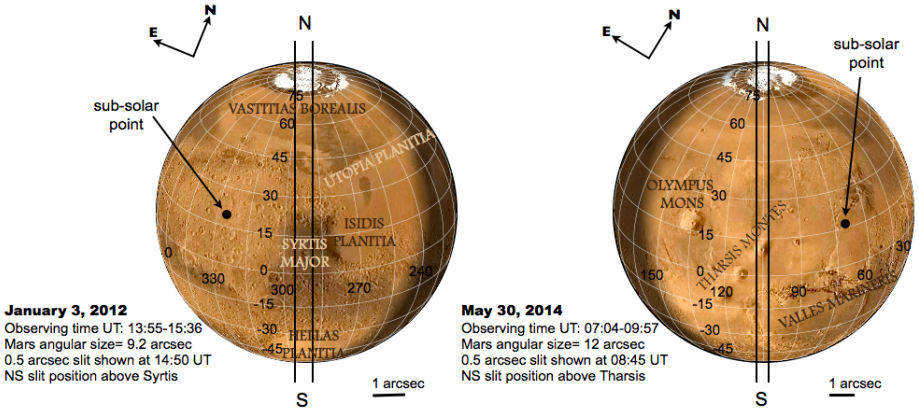

Figure 4.1 : The left panel shows the orientation of CSHELL's slit covering the N-S central meridian of Mars on January 3, 2012 when Mars' angular size was 9.2 arcsec. The two parallel lines represent the entrance slit that is shown to scale, with a 0.5 arcsec width. The sub-Earth point at 14:50 UT was right above Syrtis Major. The right panel shows the same slit configuration on Mars, but on May 30, 2014 when Mars' angular size was 12 arcsec. The sub-Earth point at 08:45 UT was above Tharsis Montes. We scanned Syrtis and Tharsis while Mars rotated under the spectrometer's slit. The perpendicular arrows on the top left of each panel represent the directions of the celestial North and East. The North pole position angle of Mars was oriented 22° and 31° East of the celestial North on January 3, 2012 and May 30, 2014, respectively. Longitudes on Mars are positive to the West. The map of Mars is rendered using Mars24 (Allison 1997; Allison & McEwen 2000).

two Mars positions along the slit (labeled "A" and "B"), separated by 15 arcsec, and took a series of 4 exposures (ABBA), with 1 minute on-source integration time per position. The (A1-B1-B2+A2) cancels the telluric and telescope emissions to first order in a Taylor series expansion about the mean airmass (Novak et al. 2002; Villanueva et al. 2008; Villanueva et al. 2013). After forming this sum, the residuals at the A and B positions in the spectral frame are the spectra of Mars (emission and absorption) multiplied by Earth's atmospheric transmittance, and higher order terms of the atmospheric emission (second order, etc.).

The top panel in Figure 4.2 represents the normalized-spectrum of Mars at the A beam position. It is contaminated with telluric absorption lines due to mainly methane (CH_4), hydrogen chloride (HCl) and water vapor (H_2O), as well as solar Fraunhofer lines with positions indicated by red circles. The panel in the middle represents the line strengths and positions of the Doppler shifted OCS lines, if they were to originate from Mars. The lower

panel represents the telluric transmittance model, with strengths and positions of telluric CH_4, HCl and H_2O. The highlighted region in blue indicates the frequency range where we looked for martian OCS. The telluric absorption in the spectrum against Mars was treated at a later stage.

We collected a total of 900 Mars scans (900 minutes of integration time) at the OCS setting, with each scan covering an area of 0.5 × Mars' angular size (arcsec^2) under the spectrometer's slit. Each scan is later divided spatially into different spectra across the geometric latitudes on Mars, in order to look for localized release of OCS on the planet.

4.2 Method

On every night, we collected "flat" and "dark" frames at the OCS frequency setting for data calibration purposes, either at the end of the night right after finishing up with observing Mars (on December 15, 2011 to January 6, 2012) or at the beginning of the night right before observing the planet (on May 30 to June 13, 2014). The goal is to get the SNR of flats to exceed that of stacked Mars spectra for the setting (per night), by at least a factor of 2. We managed to obtain on average a signal-to-noise ratio (SNR) of 1,000 per pixel in the combined flats per night.

We applied the same techniques in handling and processing the data over all the nights. In the following sections, we describe in full detail how the processing of the night of June 13 UT, 2014 has been conducted, before we present the results for the rest of the nights, at the end of this chapter.

4.2.1 Signal-to-noise Ratio from the Flats

On June 13 UT, 2014, we measured an average of 525 counts/coadd per pixel at 60 seconds in each flat scan, and collected a total of 42 flat scans. For photon-noise limited detection, we expect a total signal-to-noise ratio per pixel of:

$$SNR = \sqrt{N_{counts} \times N_{coadd} \times N_{flat} \times Gain} \tag{4.1}$$

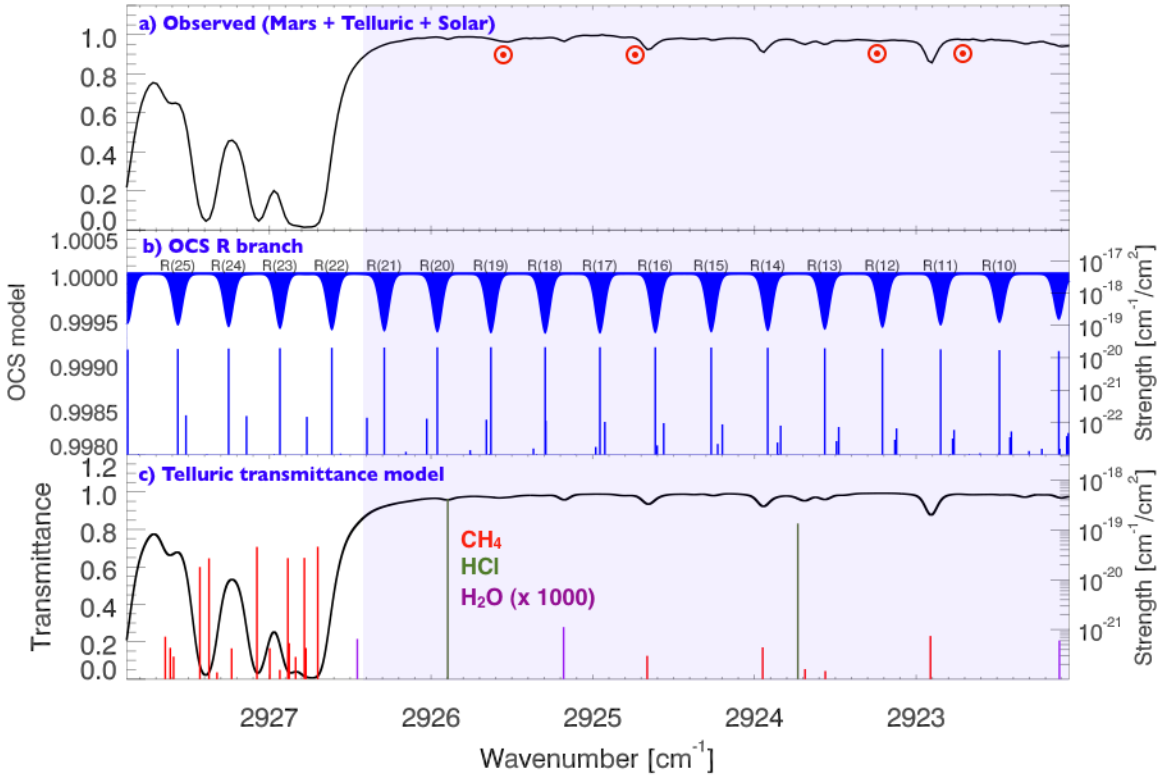

Figure 4.2 : Top panel: normalized-spectrum of Mars at the A beam position. It is contaminated with telluric absorption lines due to mainly methane (CH_4), hydrogen chloride (HCl) and water vapor (H_2O), as well as weak solar Fraunhofer lines (positions indicated by red circles). Middle panel: Doppler-shifted (-15.4 km/s) OCS R branch model at 3 ppbv, accounting for a two-way-airmass on Mars on January 03, 2012. The OCS is modeled using our own radiative transfer model. Vertical lines in blue are the strengths of the OCS transitions at the first scale height on Mars (H =11.8 km, T= 200 K). Lower panel: telluric transmittance model (black), with strengths and positions of telluric CH_4, HCl and H_2O. The transmission spectrum is modeled using the Line-By-Line Radiative Transfer Model (LBRTM) (Clough et al. 2005).

where $N_{counts} = 525$ is the number of counts per coadd per pixel, $N_{coadd} = 4$ is the number of coadds, $N_{flat} = 42$ is the total number of flat scans, and Gain[b] is the number of electrons per ADU = $11e^-$/ADU. The expected total SNR per pixel is then 985. We collected 7 dark frames, each having 4 coadds $\times$ 60 seconds. Mars' angular diameter is 10.74 arcsec, and CSHELL's slit length is 30 arcsec. Therefore, for each time we took scans of Mars,

[b]http://irtfweb.ifa.hawaii.edu/ cshell/manual_v2.pdf

we nodded the planet 15 arcsec on slit, and took 1 ABBA (4 × 60 seconds). We have the two beams (A and B) on the detector. We have collected a total of 104 "object" (Mars) frames, making 52 sets of AB pairs, or 26 sets of ABBA, starting at 05:34 UT and ending at 08:39 UT. Mars' North pole position angle in the sky NP= 32.42° East of North on the sky, and is defined "JPL Horizons" [c] as: " Target's North pole position angle (CCW, or east, with respect to direction of true-of-date Celestial North Pole)".

4.2.2 Defining the Different Regions on the Detector

At the "Sky" position on the detector, in Figures 4.3 and 4.4, there are: telluric emission lines, sky and telescope continuum emission, telluric absorption lines against the sky continuum, and a contribution from the dark current of the detector.

At the individual "A" and "B" beam positions in the same figures, there are: the spectrum of Mars (thermal emission and reflected sunlight with Mars absorption lines superposed) multiplied by Earth's atmospheric transmission, telluric emission lines, sky and telescope continuum emission, telluric absorption lines against Mars and sky continuum, and a contribution from the dark current of the detector.

At the beam positions on the detector, when nodding the telescope in two Mars positions along the slit and applying A minus B (A-B), we are removing the dark current, telluric sky emission lines, sky continuum emission, and its absorption features imposed by telluric gases. The latter three terms are removed to zeroth order only. First and higher order terms remain in the A-B difference frame, along with the spectrum of Mars (emission and absorption) multiplied by the telluric transmission.

In the space between the A and B position, at the "Sky" position, when we do A-B, the sky and telescope emission is removed, the dark current is removed, and there is no telluric absorption against any continuum remaining. Therefore, the number of counts in this region on the detector is small, containing only the first and higher order terms in the

[c] http://ssd.jpl.nasa.gov/horizons.cgi

Taylor series expansion of sky emissions, and the stochastic noise of all photons collected in the two frames (A, B).

The combined spectrum is using the average airmass of 2 scans, whereas for A1-B1-B2+A2, it is the average airmass of the 4 individual scans. Forming the sum of four successive frames (A1-B1-B2+A2) removes the first order term as well, but the second order terms and higher remain, albeit smaller.

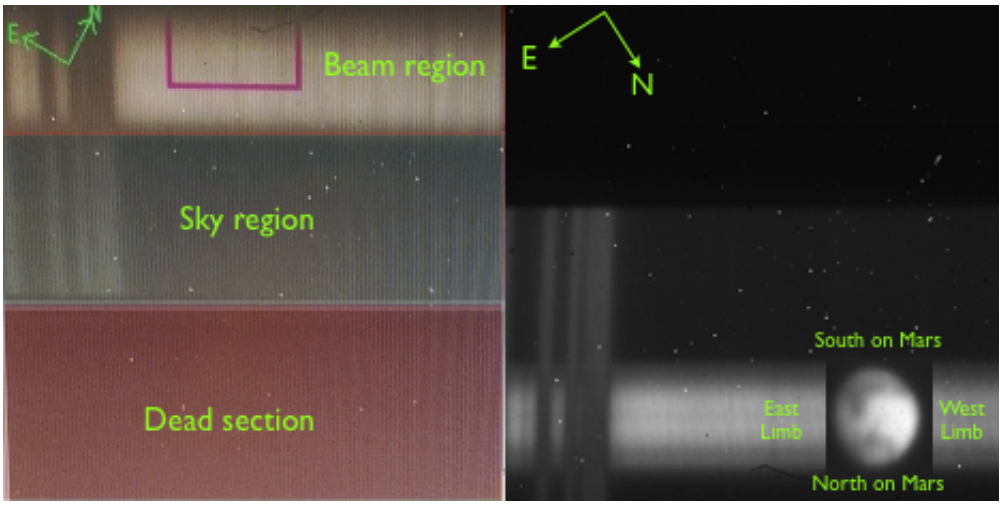

Figure 4.3 : The spectrum of Mars at the A position as seen on CSHELL's GUI (left), and on the detector (right) where the GUI's image is mirrored about the central horizontal axis. Bottom right: Mars image at 1 μm on June 17 UT, 2014, inserted on the image of the spectrum with the same slit orientation on the sky as on June 13UT, 2014. Syrtis Major can be seen in the image of Mars. The image is flipped, and therefore the North on Mars points downward on the detector.

4.2.3 Data Handling

The data were processed using the data reduction and analysis pipeline, coded in IDL (Interactive Data Language, Exelis Visual Information Solutions, Boulder, Colorado), and based on algorithms developed by Geronimo Villanueva, Michael Mumma and Mike DiSanti of the NASA Goddard Spaceflight Center (Villanueva et al. 2008; Mumma et al. 2009; Villanueva et al. 2011, 2013).

We first organize the data into different directories for the Mars' raw files, flats, darks and the standard star raw files. Next, we visually checked the Mars frames. The A and B beams are where they are supposed to be on the detector: A is at the lower part between vertical pixel 0 and 50, and B is at the upper part between pixel 100 and 150 (Figure 4.4). Both of the beams are on the detector because we nodded Mars "on" slit. The dead section on the detector is where no light from the sky (or flat lamp) hits the detector.

The average number of counts per frame is shown in Figure 4.5. The spectra of Mars at the A and B position are raw, and no flattening had been applied yet, showing different number of counts at the peak of the A and B beams.

After setting the cropping parameters, the data were stacked into 2 AB pairs (1 ABBA), and then cleaned as following. For each frame A1, A2, B1, B2, (A1-A2= dA) and (B1-B2= dB) we applied a cleaning process by first creating a mask identifying the "bad" pixels that have values higher than 5 standard deviations of their surrounding pixel values. After the masks were created, the bad pixels were then replaced with nearby averages.

At this stage the data had been read, cropped, flattened and cleaned. The next step is to correct for the distortion in the optics and the mechanical alignment of the array to the spectrum (Tokunaga, private communication), we wanted to re-sample the data into straight spatial rows and spectral columns.

4.2.4 Straightening and Linearizing the Spectrum, and Frequency Calibration

The original spectra are subjected to a two-dimensional distortion caused by the optical properties of a spectrometer like CSHELL, before being registered onto the detector. Therefore, there is a need for spatially (vertical direction on the detector) and spectrally (horizontal direction on the detector) straightening the data for further analysis (Villanueva et al. 2008; Villanueva et al. 2013).

Two early-type standard stars with clean spectra at the OCS grating setting have been observed during the Mars runs: BS 3665 and HIP 66249 (Wenger et al. 2000), on the first

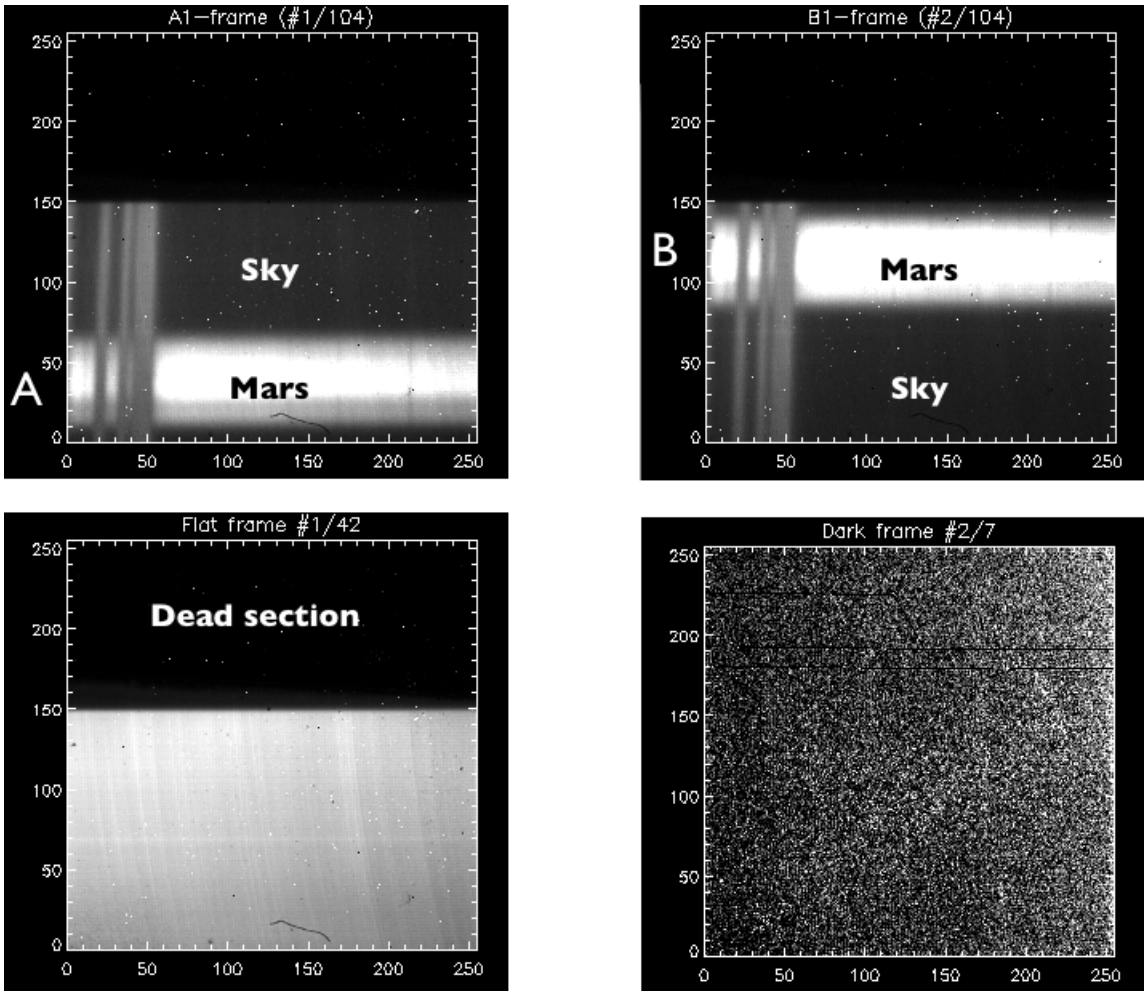

Figure 4.4 : Top left: Raw spectrum of Mars and the sky at the A position. Top right: Raw spectrum of Mars and the sky at the B position on the detector. The vertical heavy lines are the telluric lines belonging to methane. The spectrum is along the horizontal axis. Bottom left: Flat frame. Bottom right: Dark frame. The numbers on the vertical and horizontal axes are the pixel numbers on the detector.

(2011-2012) and second run (2014), respectively. The stars' beam sizes at the same A and B beam positions of Mars on the detector are narrow compared to Mars' continuum size. As a result, the star's continuum shows the position of the spectrum on the detector. By applying a polynomial fitting of degree 2 to the position of the standard star's continuum, we were able to spatially straighten the spectra to a milli-pixel accuracy.

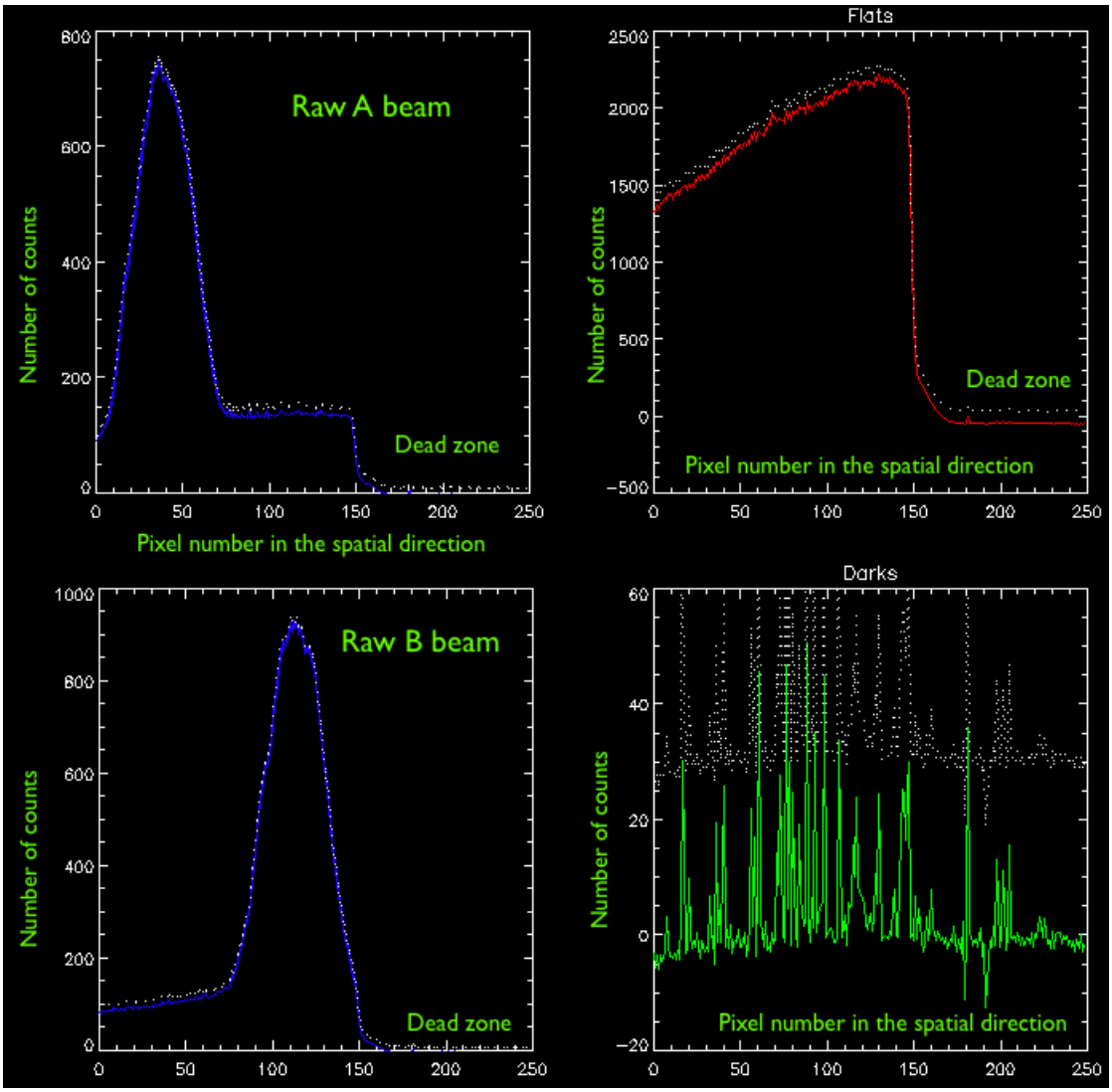

Figure 4.5 : Top left: Average number of counts in the A position of the raw frames, as a function of pixel number in the spatial direction. Top right: Average number of counts in the flat frames. Bottom left: Average number of counts at the B position of the raw Mars frames. Bottom right: Average number of counts in the Dark frames.

In order to correct for the tilt of the spectral lines, we relied on a Line-By-Line Radiative Transfer Model (Clough et al. 2005) in synthesizing Earth atmospheric transmittance spectra. The model spectra have been compared row-by-row, line-by-line to the observed telluric absorption, and therefore adjusting for the tilt of the spectral lines. Frequency calibration was later conducted using the positions of the telluric absorption lines.

4.2.5 Spatial Straightening

Since Mars is an extended object (10.74 arcsec), the planet's image extends over $\sim$ 54 pixels (plate scale= 0.2 arcsec/pixel) when the telescope is at focus. We need a very narrow target in the sky to be able to quantify and correct the tilt in the spatial direction.

We used the spectrum of the standard star HIP 66249 (or Zeta Vir) in order to determine a spatial solution and straighten the data spatially. The star's spectral type is A2 and the V magnitude = 3.38 (Wenger et al. 2000).

We took 4 ABBAs, 2 coadds $\times$ 60 seconds at each beam position. We counted an average of 288 and 262 counts/coadd at the A and B beam positions respectively (Figure 4.6).

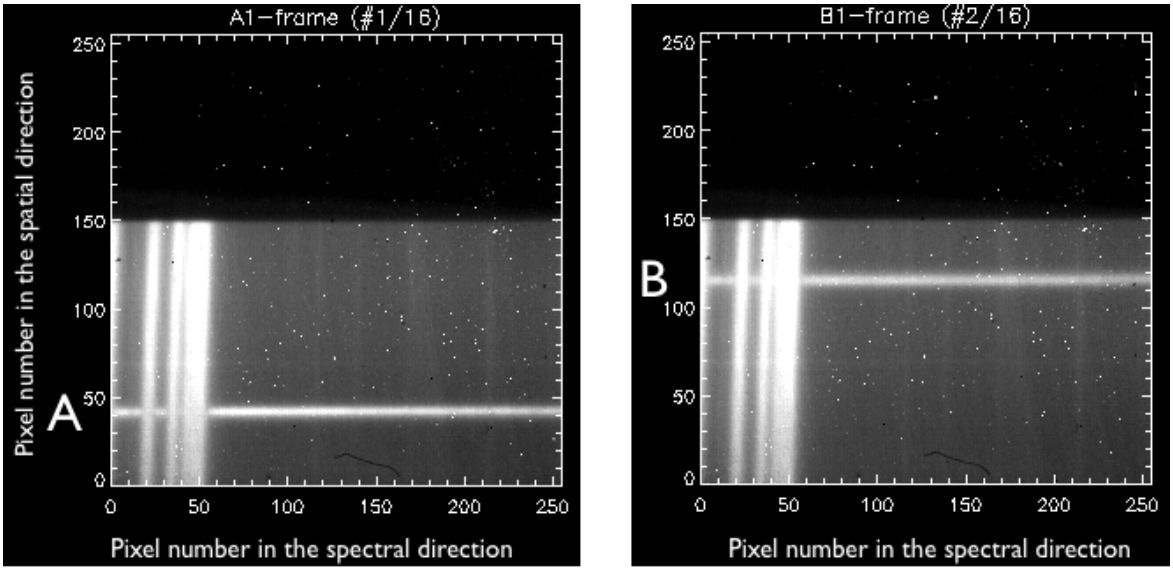

Figure 4.6 : The left and right panels show the A and B beam (horizontal continuum) positions of the standard star's spectrum on the detector, respectively. The positions of the star's spectrum will be used to spatially correct the Mars' spectra.

At each beam position of the star in Figure 4.6, we measured the center of the stellar image (maximum intensity) in the spatial direction, and plotted the data as a function of the pixel number in the spectral direction, in Figure 4.7 .

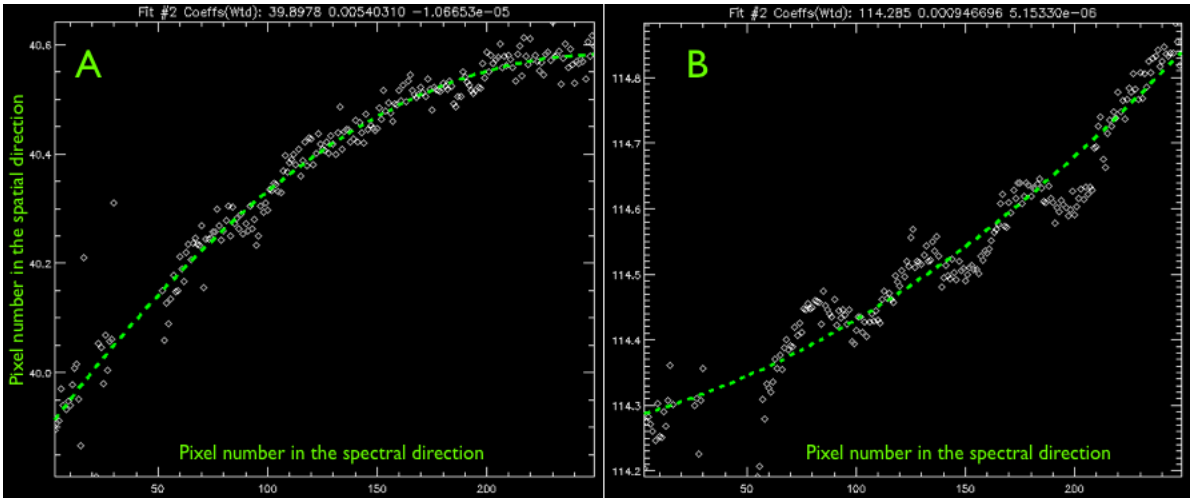

Figure 4.7 : Polynomial fitting for the data at the A and B positions of the standard star HIP 66249.

A polynomial fit of degree 2 gives the spatial solutions at the A and B beam in order to spatially straighten the data, i.e. remove the curvature in the spectrum. The solution for the A beam is: $39.89807 + 5.3910\times10^{-3}x - 1.0615\times10^{-5}x^2$. The solution for the B beam is: $114.28070 + 9.9101\times10^{-4}x + 4.8931\times10^{-6}x^2$, where x is the pixel number in the spectral direction.

In Figure 4.6, between x=10 and 60 the telluric absorption of methane at the A and B beam positions of the star (and Mars) results in some imperfections in the spatial solution, and that has an effect when later conducting the spectral straightening.

In Figure 4.8, in order to check how good the spatial straightening is, we stacked the star's straightened spectra and over-plotted cross sections along the beams in the spatial direction on the detector. If the straightening were bad, smearing should appear (in the form of rainbows) in the spatial direction. The rainbow at the B position in the spectral direction is a result of misalignment in the spectral direction, which we later corrected for. At about pixel $x \sim 55$, the telluric methane lines are tilted to the right (at the B beam position) as one moves upwards along the detector (the blue colored cross sections). These methane lines leave the "gray" rectangle in the bottom figure at $x \sim 55$, $y \sim 114$, and start

to show up in the B beam position. Since methane lines are in absorption (less flux) against the spectrum of the star, they are shallower at the minus B position.

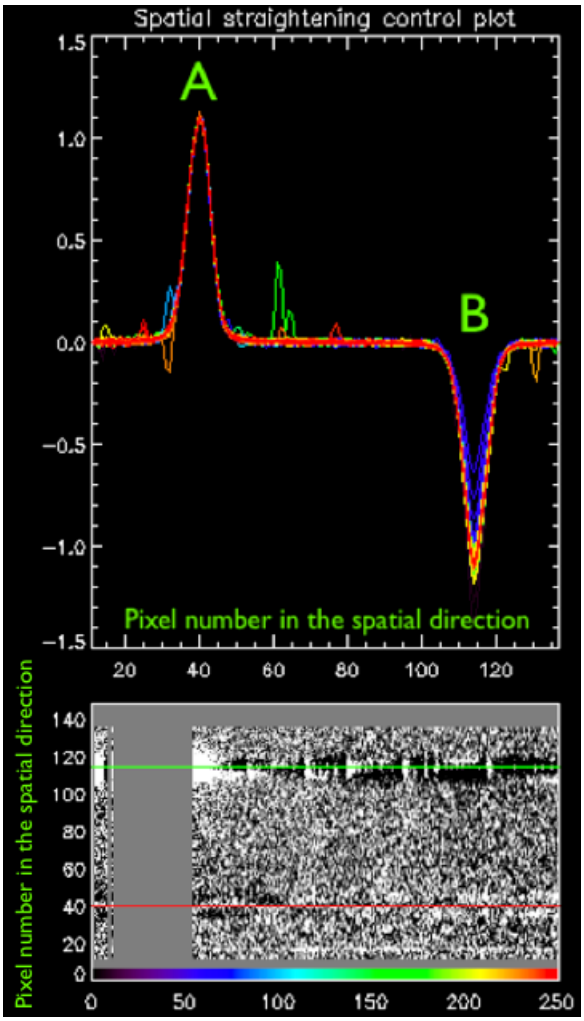

Figure 4.8 : Results of the spatial straightening on the stacked standard star spectra. The bottom panel shows the positions of the A (the horizontal red line around vertical pixel 40) and B (the horizontal green line around vertical pixel 115) beams. The vertical rectangle (gray) is the area excluded from the search; it is contaminated by telluric methane. The top panel represents the over-plotted vertical cross sections across the detector in the lower panel. The colors of the cross sections represent the colors of their corresponding spectral pixels in the lower panel, at which positions the cross sections had been taken.

4.2.6 Spectral Straightening and Frequency Calibration

After spatial straightening, the next step is spectral straightening and calibration. To start with, we used the following equation for CSHELL[d]:

$$\Delta\lambda \sim 2.4 \times 10^{-3} \times \lambda_{blaze} \tag{4.2}$$

where $\Delta\lambda$ is the spectral range, and λ is the wavelength at blaze angle. The grating's wavelength is 3.4188 μm (2925.0 cm^{-1}), and so the a-priori spectral range is 3.414 - 3.42 μm (2928.517 - 2921.499 cm^{-1}).

In order to achieve spectral straightening, we needed to rely on telluric spectral line positions at each row of the detector. Sky emission lines appear in the space between the two stellar beam positions (A and B) on the detector. If we model the Earth's atmospheric radiance at this frequency range, and manually change the frequency parameters for the model to fit the data row-by-row on the detector, we can spectrally straighten the data (Figure 4.9).

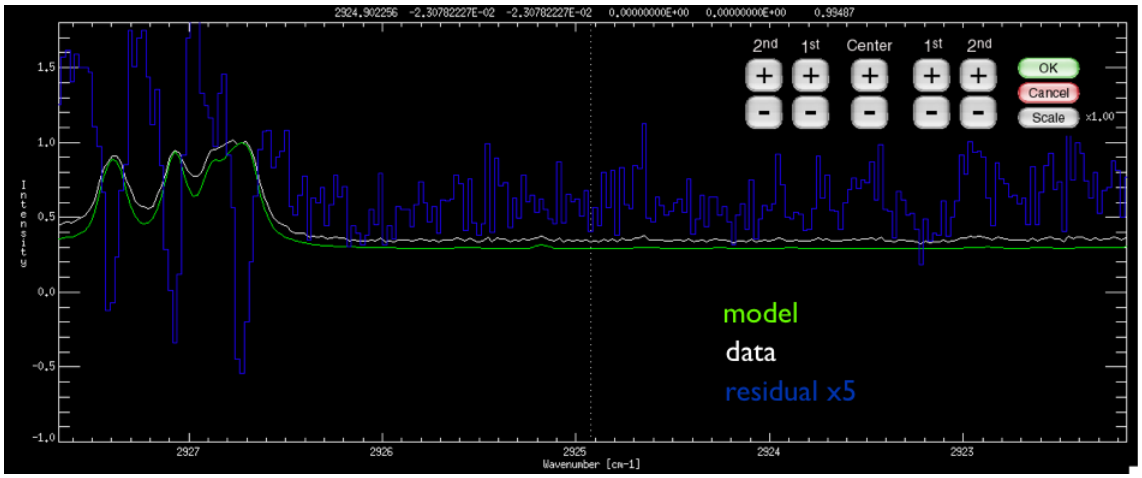

Figure 4.9 : Telluric sky emission model (in green) vs. the data in white. The residuals are in blue. The central wavenumber is adjusted with the "Center" button, the first and second, left and right dispersion coefficients are adjusted with the remaining buttons.

[d]http://irtfweb.ifa.hawaii.edu/ cshell/info.html

The frequency space is divided into a left and right section, with the central wavenumber dividing the two regions. For this setting, the a-priori central wavenumber (CWN) is manually set up to 2924.90 cm^{-1}. Two dispersion coefficients are considered: one to the left (DL) and the other to the right (DR). The dispersion solution to the left is CWN + DL1 x + DL2 x^2, where x is the horizontal distance in units of pixels from the center of the frequency scale. The same equation applies to the right side of the frame. Figure 4.10 shows the results of the dispersion fit, and Figure 4.11 shows the over-plotted residuals in the spatial direction after applying the spectral straightening solution.

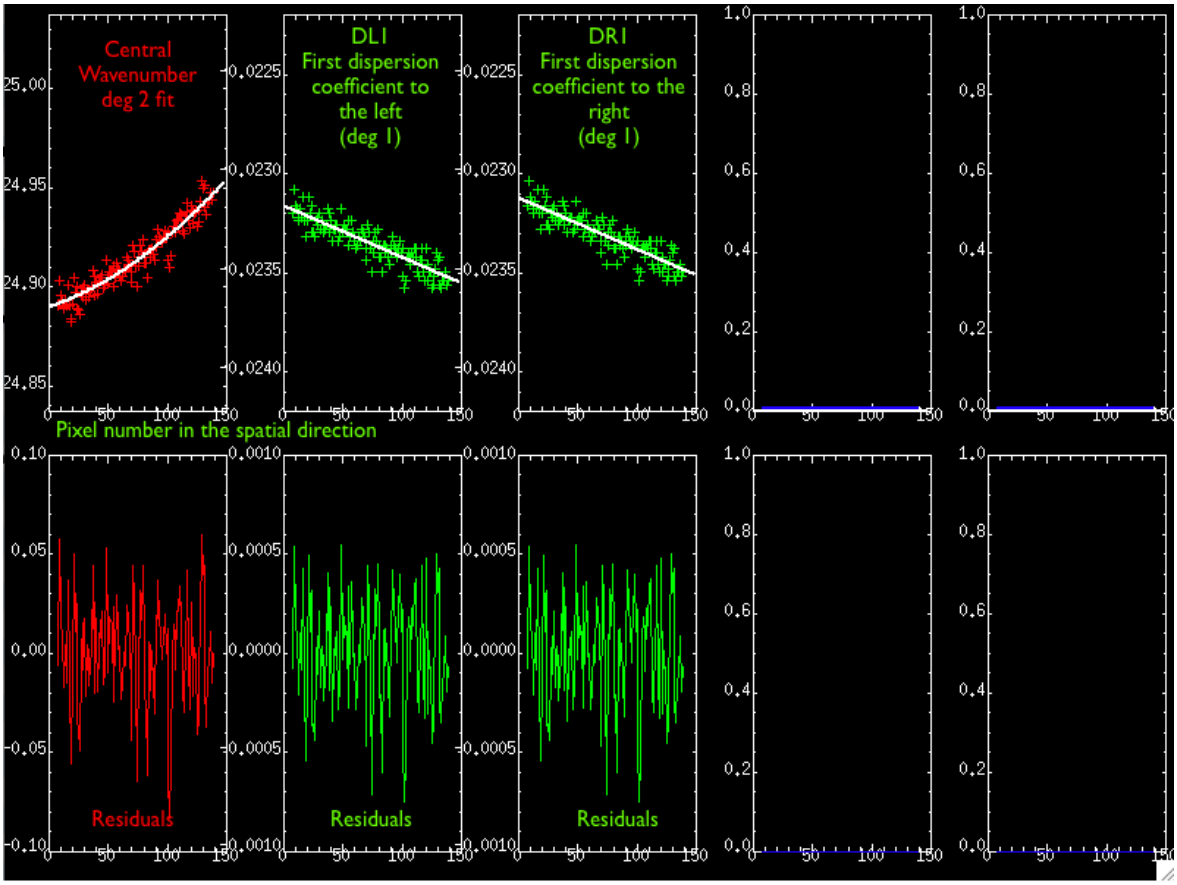

Figure 4.10 : Upper panels: Fitting results for the central wavenumber (CWN)(red), the first dispersion coefficients to the left (DL1) and right side (DR1). Lower panels: Residuals between the data and the polynomial fitting models for the corresponding CWN, DL1 and DR1.

At this stage, the data have been straightened in both spatial and spectral directions; the next step is the spectral calibration. We relied on a Line-by-line Radiative Transfer Model (LBLRTM) in order to model the radiance and the transmission of the Earth's atmosphere. For Maunakea, "standard tropical" profiles for temperature and pressure were used, as well as abundance profiles for telluric CO_2, H_2O, O_3, CO, N_2O, CH_4, O_2, NH_3, C_2H_6 and HCl (Anderson et al. 1986). The spectral resolving power, the altitude at the observing site, and the average airmass are also required for the LBLRTM. The water abundance factor is adjustable, and can be retrieved from the data if a prominent water line is available. The a-priori water factor is picked up using the approximate equation relating the measured opacity at 225 GHz to the measured precipitable water vapor (PWV)[e]:

$$\tau_{225GHz} = 0.033 \times PWV + 0.006 \tag{4.3}$$

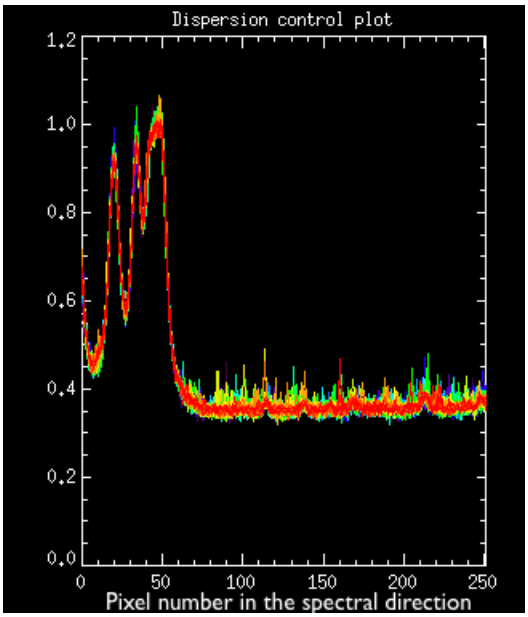

Figure 4.11 : The over-plotted residuals along the slit at each row on the detector after applying the spectral straightening solution.

[e]http://legacy.nrao.edu/alma/memos/html-memos/alma152/memo152.html

Figure 4.12 shows the calibrated data in white, when fitting it to the telluric model in green by the LBLRTM. The frequency solution was then applied to all the scans, and the data were later combined into 6 sets of equal numbers of AB pairs. The rule of thumb applied when combining the different AB pairs is the following: Not more than 10 sets per night, and not more than half an hour per set. An example of a "beam" file for one set is shown in Figure 4.13.

Now that the data have been straightened and frequency calibrated, it is crucial to know the location of CSHELL's slit on Mars.

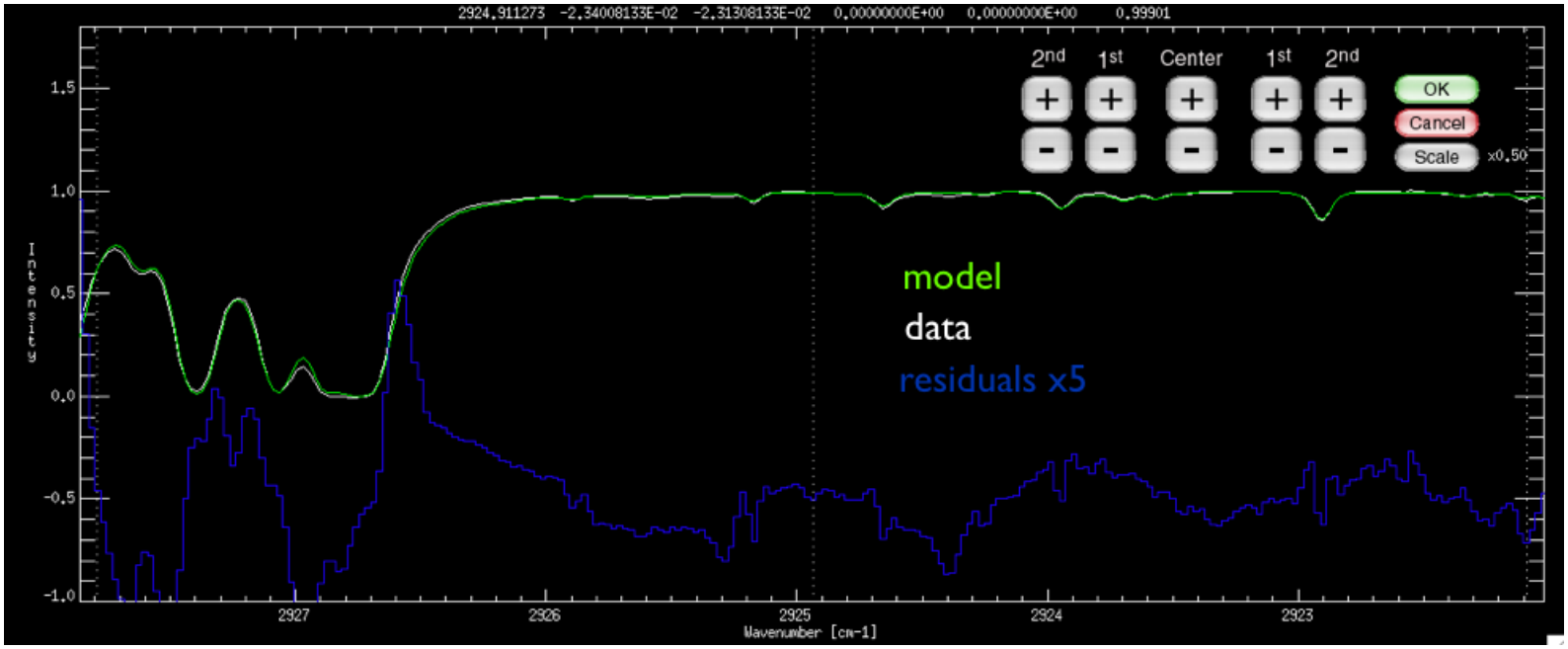

Figure 4.12 : Telluric absorption model (in green) vs. the data in white. The residuals are in blue. The central wavenumber is adjusted with the "Center" (±) button at the top right; the first and second, left and right dispersion coefficients are also adjusted with the remaining (±) buttons.

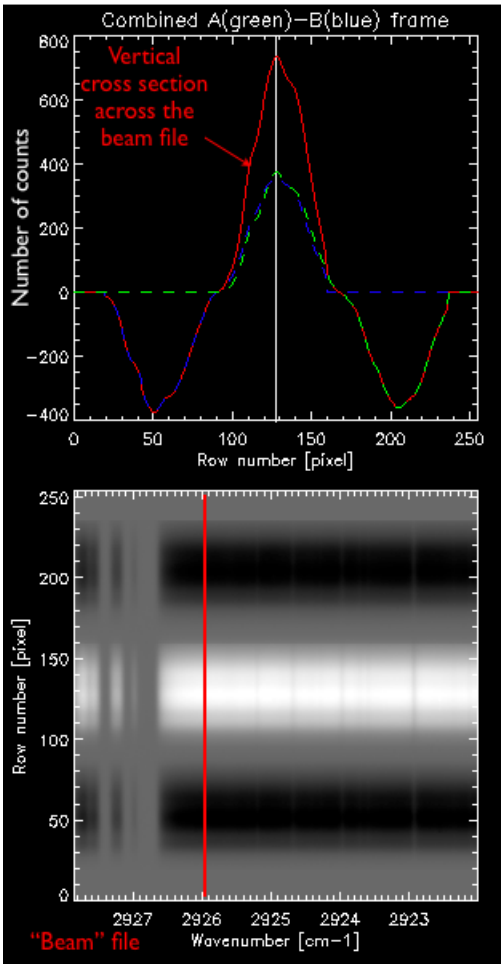

Figure 4.13 : Final result of the calibration where the data have been flattened, cleaned, spatially and spectrally straightened. The vertical cross section in the beam file is in the upper panel, whereas the beam file is in the lower panel. Note that this is no longer an image of the detector, but is a constructed image.

4.2.7 Identifying the Position of CSHELL's Slit on Mars

Tracking inaccuracies result in a shift in the footprint on Mars covered by the spectrometer's slit, therefore probing different regions on the planet than the targeted ones. This shift leads to wrong results, especially when targeting localized vents releasing, in our case, OCS on the planet, or when measuring abundance ratios of different molecular species across Mars. In order to find the exact location of the slit on Mars, we generated a Mars Climate Database, General Circulation Model (GCM, (Villanueva 2004; Millour et al. 2008)). The GCM relies on input parameters taken from the "JPL horizons"[f] including the time and date of the observation, the location of the sub-earth and sub-solar points, Mars' angular diameter, the season on Mars and the local times across the red planet. The GCM then extracts the surface temperature, the surface pressure, the pressure profile and the column temperature in the martian atmosphere at each position element across the disk of the red planet.

The emergent flux from Mars is a combination of thermal emission from the planet itself and the solar radiation reflected from its surface. The thermal emission from Mars, $\propto \epsilon \times {T_s}^4$, is calculated using the surface temperature from the GCM and the emissivity (Christensen et al. 2001) from the Mars Global Surveyor's Thermal Emission Spectrometer (MGS/TES). The reflected solar radiation transits Mars' atmosphere twice, and its intensity is proportional to the incidence angle on Mars, and the albedo of the surface (considered to be Lambertian) (Villanueva et al. 2008; Villanueva et al. 2013). The summation of the two components of the emergent flux at different slit positions from the center of Mars, affected by the seeing, are then compared against the measured flux from the planet, hitting the detector. For some settings, a solar Fraunhofer line appears, permitting estimation of the ratio of Mars thermal emission to reflected sunlight by comparing its measured equivalent width with the intrinsic value.

The highest correlation factor corresponds to the most accurate position of the slit on Mars at the time of the observation (Figure 4.14). For this specific dataset, the profile offset

[f] http://ssd.jpl.nasa.gov/horizons.cgil

at 0.2 planetary radius provided the highest correlation (0.99) of measured and synthetic intensities. Figure 4.15 shows the exact slit position found on Mars at the time of the

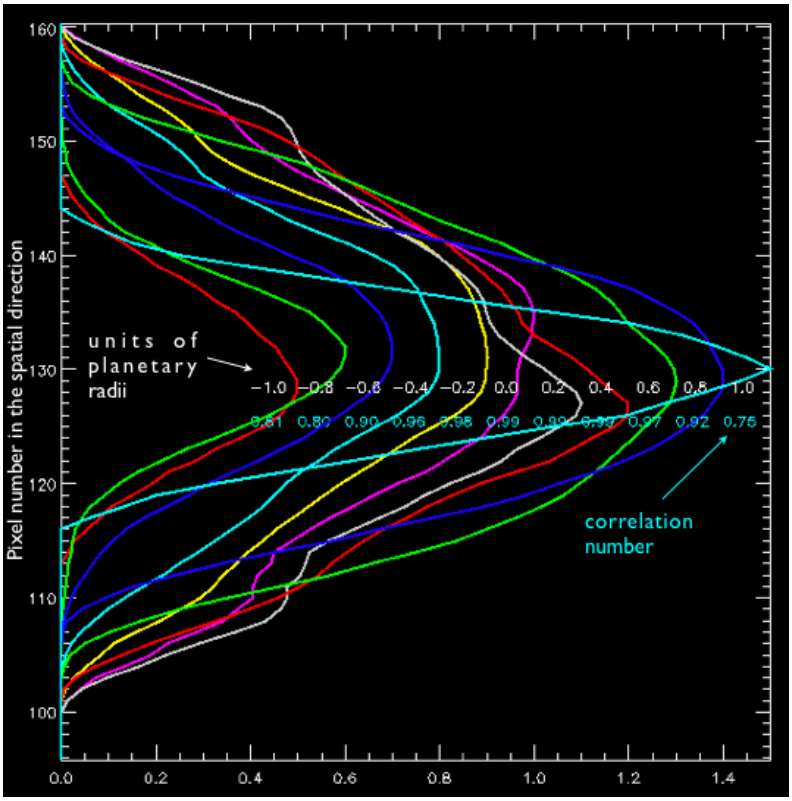

Figure 4.14 : Spatial flux profiles (model) by the GCM at different slit positions away from the center of Mars in the East/West directions. The total flux is a combination of the thermal emission from Mars and reflected sunlight off the planet. The numbers in white are the fraction of distances from the center of Mars in units of planetary radii. The blue numbers are the correlation factors of the match between the model and the data.

observation on June 13, 2014. The North pole of the red planet is pointed to the south in this image. The plots to the right in Figure 4.15 show the surface temperature (in red) extracted from the GCM, the surface pressure (thin white), the air (column) temperature, weighted by the atmospheric pressure, the expected solar radiation that is reflected off the surface of Mars (dash green), the expected thermal emission from the planet under the slit (dot dash green), and the model flux (solid green); the sum of the thermal emission from

the planet and the reflected sunlight. The flux from the data is in solid white. If the Mars atmosphere is clear and the location is correct, the data should match the model.

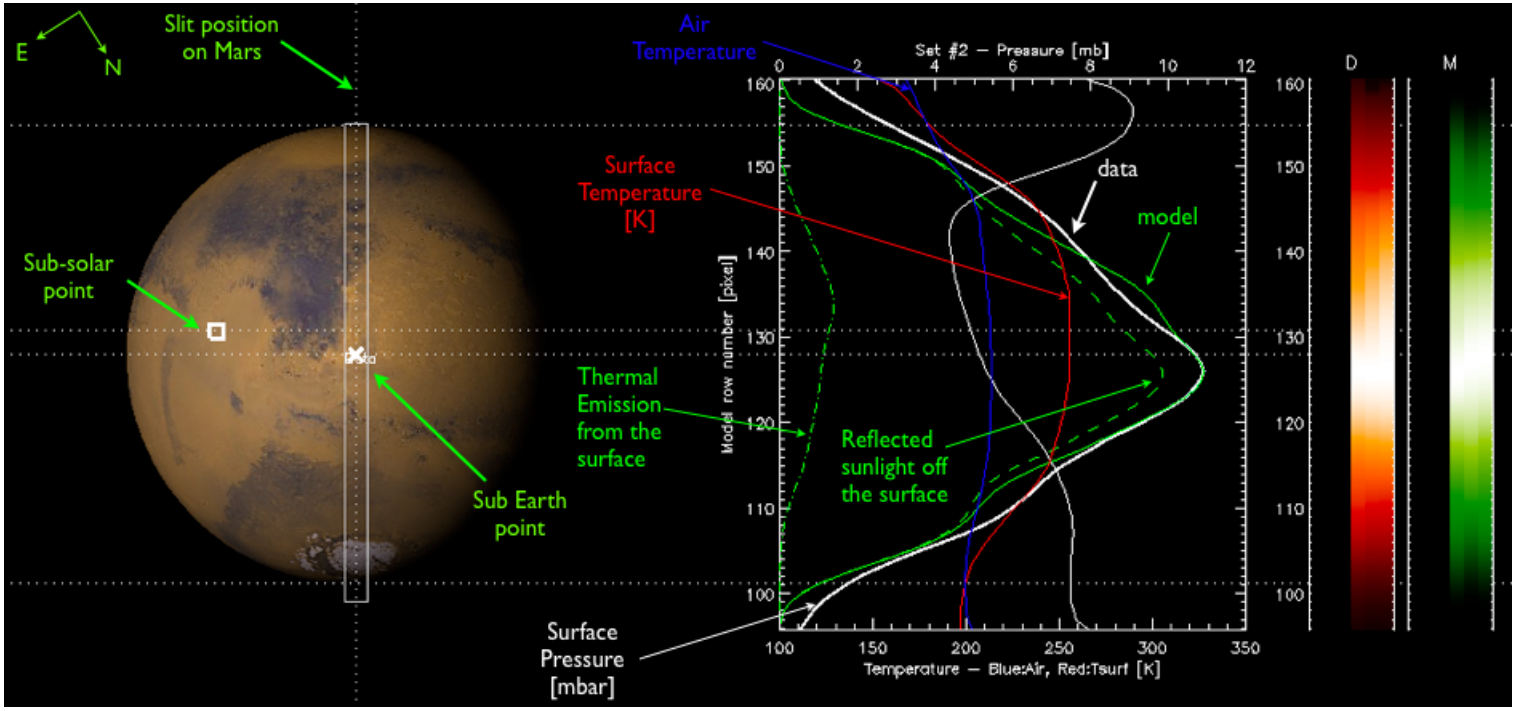

Figure 4.15 : The exact slit position on Mars, and the extracted profiles from the GCM that describe the physical conditions on Mars at the time of the observation.

4.2.8 Removal of Solar Fraunhofer Lines

The emergent flux from Mars is a combination of the thermal emission from the red planet and the solar radiation that includes Fraunhofer lines. The thermal emission is subjected to a one way airmass between Mars' surface and the observer, while the solar radiation goes through a two-way airmass (Sun-Mars'-surface and Mars'-surface-observer). Measuring the diminished equivalent width of the Fraunhofer line in the emergent flux from Mars indicates the contribution of the solar radiation to the total radiation received from the planet (Novak et al. 2002).

fsol is measured in the following way. In Figure 4.16, there are 6 solar lines (3 prominent), and 5 of them are blended with main atmospheric lines from Earth (i.e. CH_4). The best solar lines for measuring fsol should be free of terrestrial contamination. We chose the solar line encircled in red.

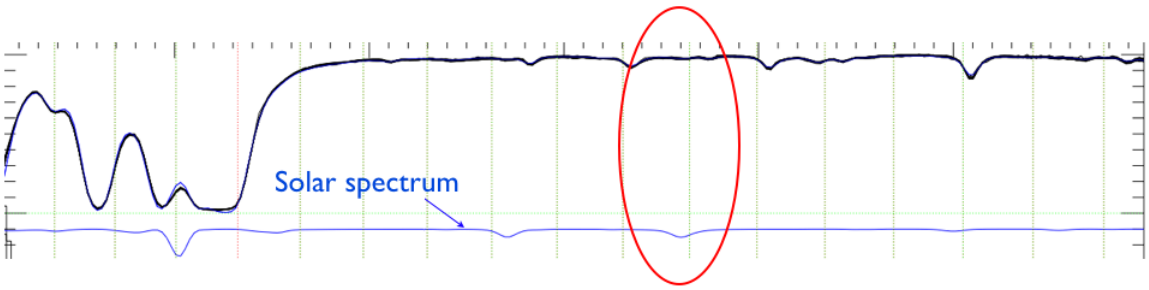

Figure 4.16 : Retrieving the solar factor from clear spectral regions in the data, indicated by the red ellipse, away from telluric contamination. The solar spectrum is in blue. We selected the solar line indicated in the red ellipse in order to measure the solar factor.

The thermal component from Mars is proportional to the surface temperature and emissivity of Mars. The row numbers on the detector where the thermal flux reaches a maximum, correspond to geographic regions under the slit where the surface emissivity, multiplied by the temperature, reaches a maximum. Considering the FWHM of ∼1 arcsec, and pixel size of 0.2 arcsec, we co-added 5 rows to improve the SNR. We ran the code with fsol=0 (no solar contribution) and looked up the residuals, and found that there is a prominent solar line in the residuals. This indicates that the solar contribution is not zero.

We then manually changed fsol until we got flat residual spectra for fsol ~ 0.99. The lowest value of fsol along the slit should be around where T_s is the highest, and so the measured fsol at the time of the observation and at this frequency range is ≥ 0.99. At 2925 cm^{-1} (3.42 μm), the measured equivalent width of the solar lines shows that the emergent intensity from Mars is mostly solar radiation (fsol = 1). Measuring the solar contribution is crucial in modeling the spectral lines from the martian atmosphere.

The "solar factor" (fsol) is equal to 1 when the total flux from Mars is reflected sunlight, and it is equal to 0 when the total flux is pure thermal emission from the red planet. At 3.42 μm, the measured equivalent width of the solar lines shows that the emergent intensity from Mars is mostly solar radiation (fsol =1), i.e. Mars is seen predominantly in reflected sunlight.

4.2.9 Removal of Telluric Lines

Observing Mars through the Earth's atmosphere introduces spectral features in the martian spectrum. The telluric absorption depends on the changing atmospheric conditions during the long observing sequence (day or night). To correct for them, we applied the technique developed by Villanueva et al. (2011, 2012b) by using the Line-By-Line Radiative Transfer Model (LBRTM) (Clough et al. 2005) to synthesize the Earth and Mars atmospheric transmittance spectra. Modeling the telluric absorption offers advantages over using Lunar or stellar spectra, because the data are acquired in every Mars scan. Using data acquired with Mars itself permits continuous atmospheric corrections over the entire observing period.

In Figure 4.12, there is strong telluric methane absorption (reaching zero transmission at some positions) between 2926.5 cm^{-1} and 2927.8 cm^{-1}. When there is a zero transmission in Earth's atmosphere, it is not possible to extract information about the spectrum of Mars. Therefore, as shown in Figures 4.17 and 4.18, the spectral region we analyzed extends between 2922.0 cm^{-1} and 2926.2 cm^{-1} (spectral pixel number between 67 and 251). We

started by working on the central row (vertical pixel # 141) on the detector and stacked it with two other adjacent rows (140 and 142).

In order to optimize the modeling of the telluric lines, further enhancements in the frequency calibration process were conducted, by searching for the frequency solution with a higher precision. In principle, one would start with the $a-priori$ frequency solution from the previous stage (Fig. 4.12), and move into a higher precision mode by reducing the step sizes when looking for a frequency solution until the parameters are well retrieved.

The sky conditions could change during one night, i.e. the amount of water vapor and ozone in Earth's atmosphere. When observing Mars at different airmasses, it is crucial to correct for such changes that lead into higher absorption in the telluric spectra when going to higher airmasses, and vice versa. In order to do that, one would consider several parameters that go into modeling the Earth's atmosphere, including the abundance profiles of its constituents and its thermal structure.

Abundance profile: We started with $a-priori$ abundance profiles from Anderson et al. (1986) for CO_2, H_2O, O_3, CO, N_2O, CH_4, O_2, NH_3, C_2H_6 and HCl, and then multiplied each one of them by a corresponding abundance factor. For each set of data, the airmass was taken into account in modeling the transmittance.

Thermal structure: Standard tropical temperature profiles were divided into two regions (lower atmosphere and stratosphere), and each one is multiplied by a "temperature factor" when fitting the model with the data (Villanueva et al. 2011). Other parameters were also retrieved from the data: the surface pressure and the resolving power. The retrieval of the fitted parameters occurs simultaneously or in stages, where a set of parameters is looked at first, then the other is looked at second.

A non-linear least square fitting algorithm, the Levenberg-Marquardt (Moré 1977; Markwardt 2009) was used to retrieve the above-mentioned parameters at the different retrieval stages. For one set of data at airmass=1.147, the retrieved abundances, temperature and pressure factors above Maunakea (4200 km) on June 13, 2014, are displayed here:

Table 4.2 : Retrieved abundance and thermal structure factors for one set of observations on June 13 UT, 2014.

CO_2	H_2O	O_3	CO	N_2O	CH_4	O_2
1.0000	0.6847	1.0000	1.0000	1.0000	1.0000	1.0000
NH_3	C_2H_6	HCl	T_1	T_2	$P_{surface}$	
1.0980	1.0000	1.0000	1.0007	1.0006	0.9943	

The different abundance factors were then used to model the Earth's telluric absorption model that is later removed from the data in Figure 4.18. Depending on the seeing and the pixel size of CSHELL's detector, we binned 3 rows of spectra in the spatial direction. The top of the figure represents the stacked spectrum (rows 140 to 142) along the detector. It contains spectral lines in absorption from the Earth's atmosphere, the solar reflected spectrum and martian lines. The data are in black and the model (telluric and solar) is in blue. In the middle of the figure are the model of the solar spectrum in blue ($\times$ 5), and the residual spectrum of Mars ($\times$ 5) after removing the telluric model spectrum and the solar spectrum. The numbers in red to the left of the figure indicate the row numbers that have been stacked, and the geographic latitude on Mars sampled by the slit. The numbers in blue on the wavenumber axis are the pixel numbers in the spectral direction on CSHELL's detector.

At this stage we have removed the solar spectrum and the Earth's telluric model from the data, and what is left is the spectrum of Mars. CSHELL's slit (Fig. 4.15) is sampling different geographic regions on the N-S central meridian of the red planet. The residual spectra of Mars across the slit are in Figure 4.19.

The signal-to-noise ratio at the residual spectra in each row ranged between the 185 at row # 0, and 435 at row # 10 (Fig. 4.19), whereas the average SNR/pixel from the flats is 1300. The low SNR at rows on the slit away from the center is caused by the higher airmass at the covered geographic regions, leading to more attenuation in the signal in the martian atmosphere. The opposite happens around the central rows on the slit, when there is less attenuation of the signal from Mars, hence a higher SNR. Airmass corrections were done at

the very end of the data processing stage, by considering an effective airmass " μ_e" for the night, discussed later in section 4.3.5

The vertical dashed lines in Figures 4.18 and 4.19 indicate the OCS line positions in the martian atmosphere if OCS were to be found. No prominent absorptions at these positions were detected. The stacked residual spectrum (shown at -4 on the vertical axis in Figure 4.19) has a SNR of 900, and at such high SNR, some residual features appear at the CH_4 and the HCl positions as a result of an imperfect fitting of the telluric model. The vertical red lines indicate the positions of the Doppler-shifted OCS transitions where we extracted the upper limits on the mixing ratio. Figures 4.26 to 4.32 show the residual spectra of Mars across the slit between December 15 UT, 2011 and June 12 UT, 2014.

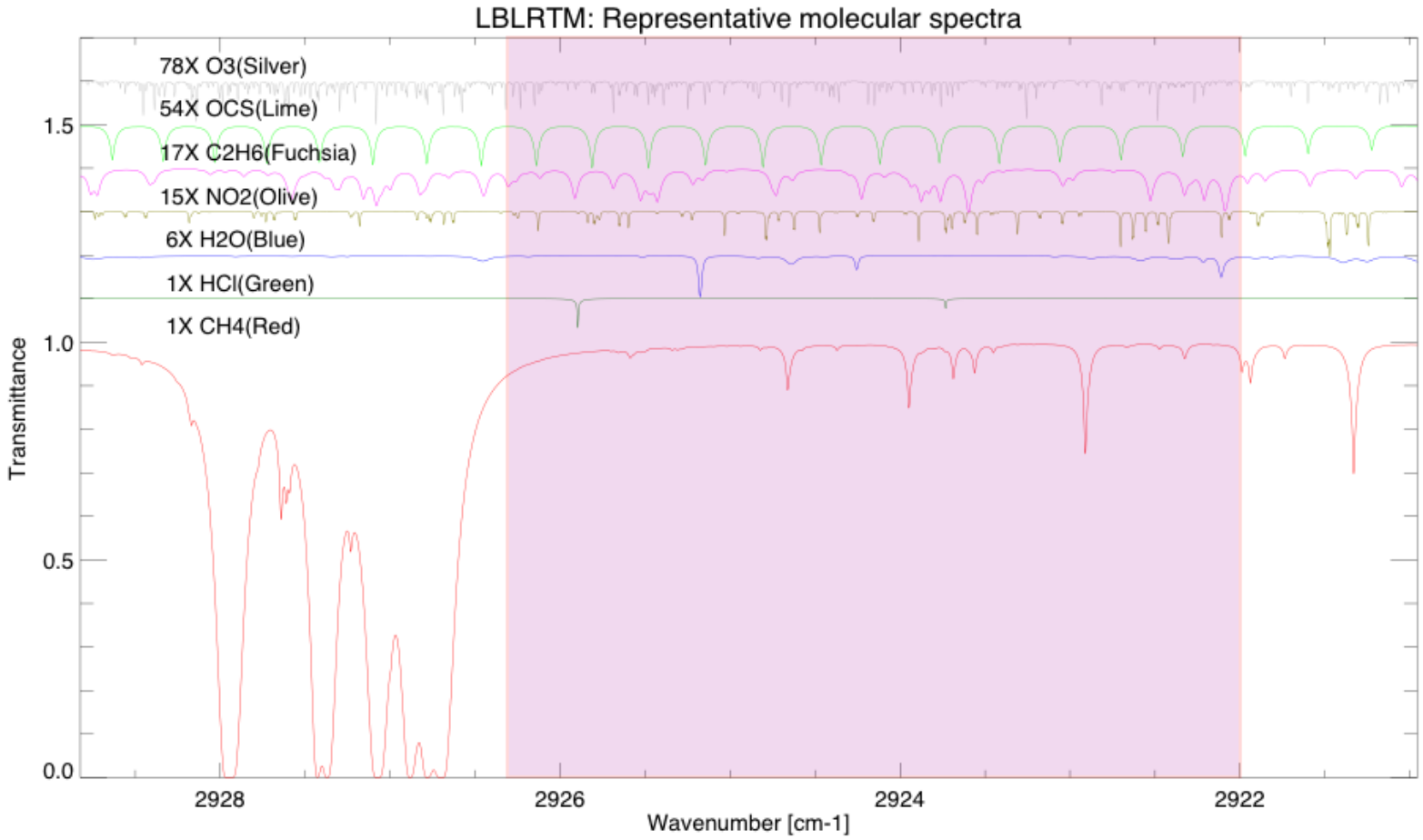

Figure 4.17 : LBLRTM model of the Earth's atmosphere using the retrieved abundances from the data. The area inside the purple region is where the results have been extracted from. The spectra for individual atmospheric components are plotted here.

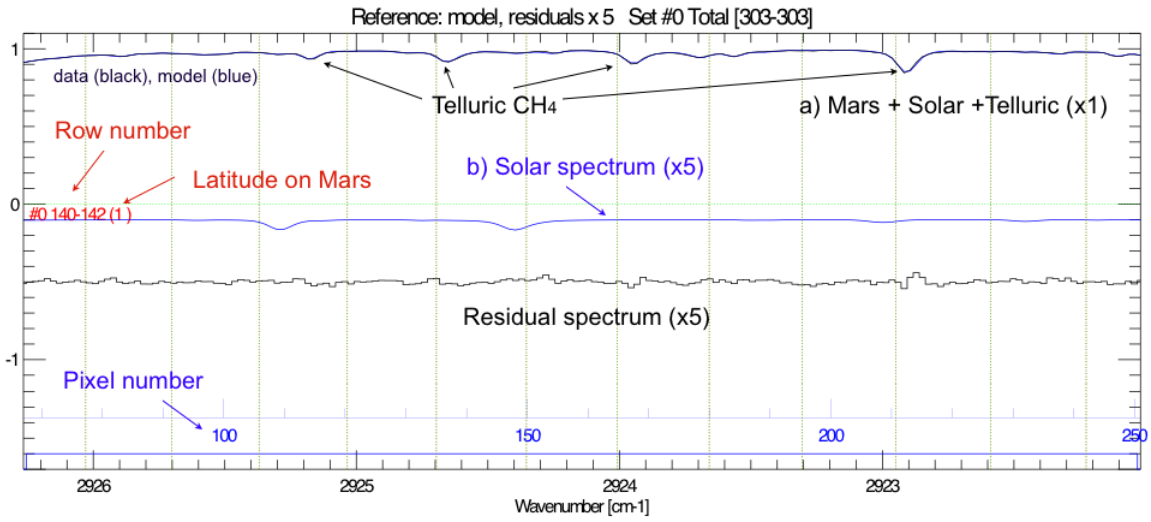

Figure 4.18 : At the top, the black spectrum represents the data from 3 stacked rows (140 to 142). The labels to the left are increments of 1 that encompass the normalized spectrum. The data include the spectrum of Mars, the solar spectrum and the telluric absorption. The solar spectrum ($\times$ 5) is in blue. In the middle there is the residual spectrum ($\times$ 5), where we expect to see martian lines. The vertical (green dotted) lines show the positions of the OCS lines if they were to be found in the atmosphere of Mars (compare with Fig. 4.2).

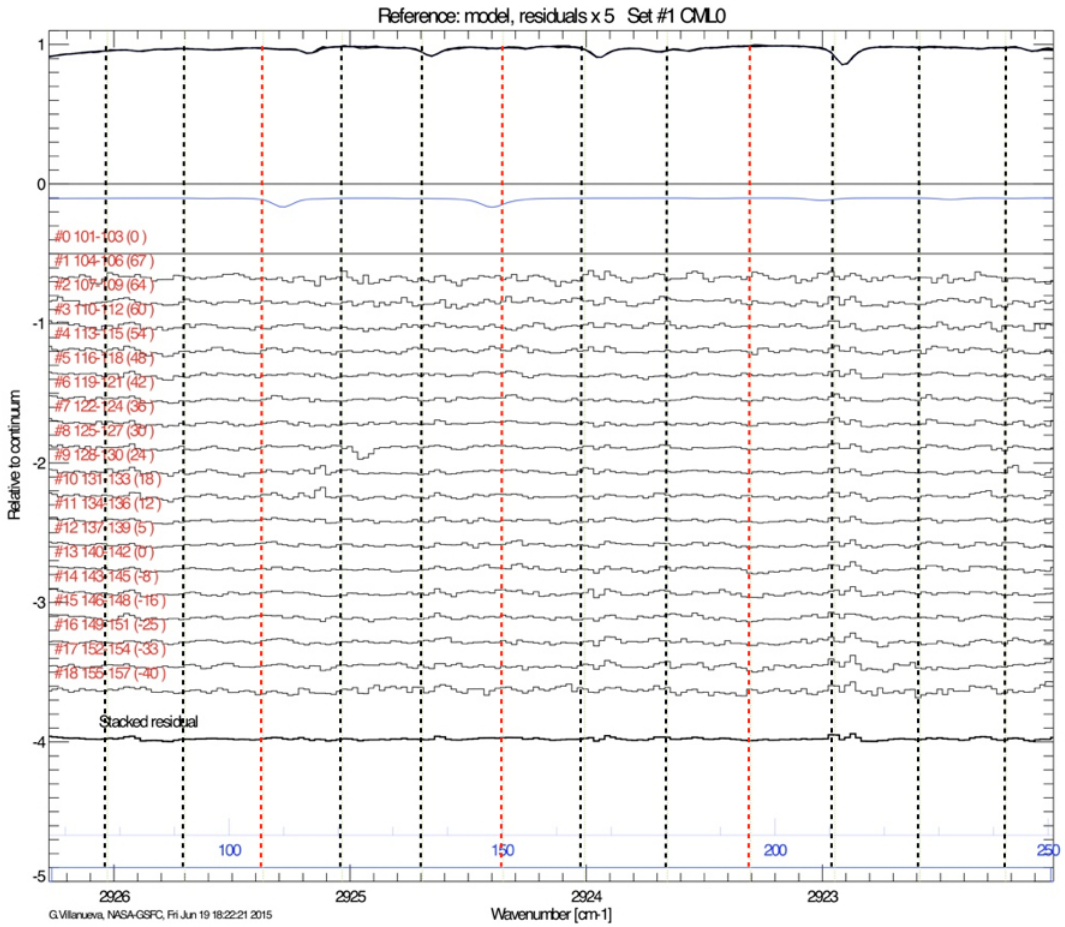

Figure 4.19 : The martian residual spectra along the slit when sampling the Syrtis region on June 13 UT, 2014, are shown here. Mars was at a topocentric Doppler shift of +11.2 km/s, and the spectra are presented in Earth's reference frame. The vertical dashed lines indicate the OCS line positions in the martian atmosphere if OCS were to be found. These lines are red-shifted by 0.109 cm^{-1} from their telluric counterparts. The vertical red lines indicate the positions we used when extracting the OCS upper limit on the mixing ratio.

4.3 Results: Measuring the OCS Upper Limit

4.3.1 Combining the Data in the Spatial Direction

In order to increase the SNR, we combined the residual spectra along the slit in the spatial direction using no weighting factors:

$$\overline{y} = \frac{\sum_{i=1}^{N} y_i}{N} \tag{4.4}$$

where $\overline{y}$ is the average value along the slit, at each pixel number. y_i is value of the normalized residual spectrum of Mars at the pixel in row "i", and N is the number of combined residual spectra (Fig. 4.19). Even-though the SNR in the residual spectra is not the same across the slit, with low values at high airmass and and vice versa, we haven't applied any weighting factor when stacking the data at this stage, because we later used an effective airmass throughout the night to compensate for airmass changes on Mars along the slit.

After combining the data in the spatial direction, we displayed the resulting residual spectrum across Mars around the OCS transition at 2925.48 cm^{-1} (Doppler shifted to 2925.37 cm^{-1}) in Figure 4.20. The red error bars indicate the standard deviations on the values at the pixels in the vertical direction, or the scatter of the values of the residual spectra around a mean value. If those error bars were small after the co-addition of the residual spectra, then the scatter is small, showing that the values at individual pixels have not changed by much. This indicates a systematic change in the residual flux value at the pixel, instead of a random scatter around a mean value. If those error bars were large, opposite conclusions could be reached; the values at the pixels are randomly changing. The blue error bars are the standard errors on each pixel, or the standard deviations on the mean (vertical) values. The purple error bars indicate the ± RMS value across the resulting spectrum in black. The SNR after stacking has increased from an average of 600 at each row into 1250. If the residual spectra were systematics free, then the expected SNR should reach 2000 (10 combined spectra).

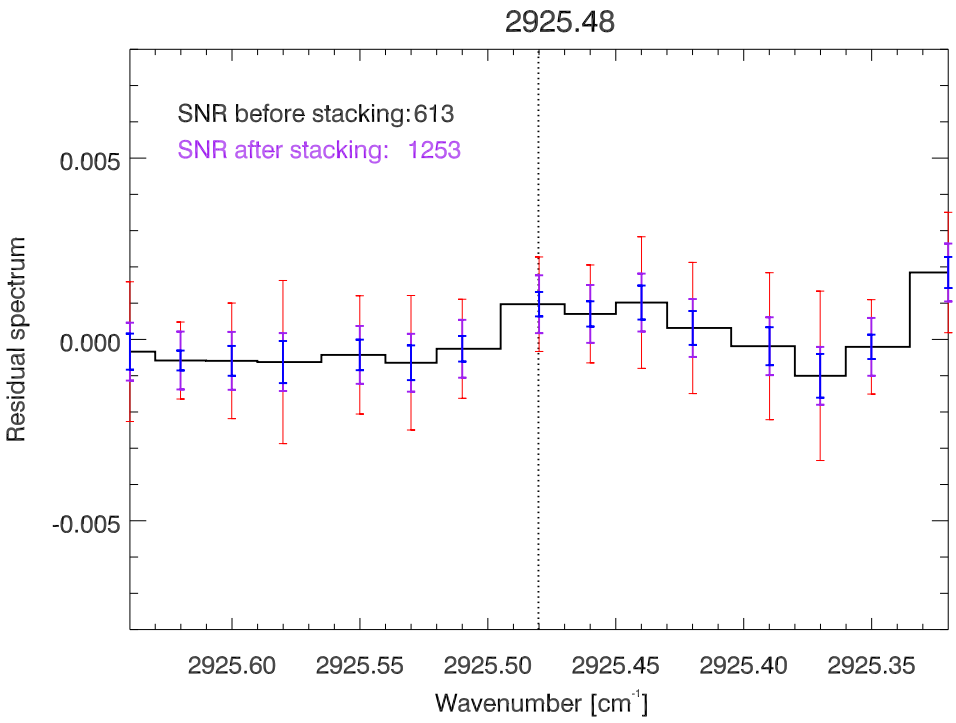

Figure 4.20 : A test case where data were combined in the spatial direction around 2925.48 cm^{-1} in order to check for the presence of systematics in the data. The red error bars indicate the standard deviations on the values of the residual spectra at each pixel in the spatial direction. The blue error bars are the standard errors on each pixel. The purple error bars indicate the ± RMS value across the resulting spectrum in black.

We combined the different sets during one night using the square root of the integration time as the weighting factor:

$$\overline{y} = \frac{\sum_{i=1}^{N} y_i \times \sqrt{t_i}}{\sum_{i=1}^{N} \sqrt{t_i}} \tag{4.5}$$

where $\overline{y}$ is the average value along the slit, at each pixel number. y_i is the residual flux value at each pixel at each residual spectrum for each set, t_i the integration time per set and N is the number of sets. In the majority of cases, we have chosen a combination of sets with equal integration times.

4.3.2 Combining the Data in the Spectral Direction

After combining the residual spectra in the spatial direction, we co-added them at 3 different OCS transitions in clear regions of the spectrum as indicated in Figure 4.19. The line strength at the first scale height in the martian atmosphere is used as the weighting factor using the following equation:

$$\overline{y} = \frac{\sum_{i=1}^{N} S_i \times y_i}{\sum_{i=1}^{N} S_i} \tag{4.6}$$

Where $\overline{y}$ is the average value at each pixel number, S_i is the line intensity at the first scale height for each transition, and N is the number of co-added transitions. At this stage, the systematics in the residual spectra are more prominent. Spectroscopic parameters using the HITRAN 2012 database (Rothman et al. 2013; Régalia-Jarlot et al. 2002) for the OCS transitions we used when co-adding the data are shown in Table 4.3. At each night, we have chosen to co-add the residual spectra at the appropriate OCS transitions where there are no systematic features in the residuals, leading to a combined spectrum with the highest SNR, hence the lowest upper limit.

After doing all the co-adding in the spatial and spectral directions on each night between December 15 UT, 2011 and June 13 UT, 2014, the final residual spectra are shown in Figures 4.23 and 4.24.

We evaluated the error bars using the standard deviation on the mean or standard error. In general, when w is the weighting factor in combining data, the standard deviation on the mean is:

$$\sigma_{\overline{y}} = \frac{\sqrt{\sum_{i=1}^{n} {w_i}^2}}{\sum_{i=1}^{n} (w_i/\sigma_y)} \tag{4.7}$$

where n is the number of data values and σ_y is the standard deviation of the data. When no weighting factor is considered, the equation becomes the usual equation showing that the standard deviation on the mean depends on the sample size.

$$\sigma_{\overline{y}} = \frac{\sigma_y}{\sqrt{n}} \tag{4.8}$$

Table 4.3 : Spectroscopic parameters for the OCS transitions used in co-adding the data. We selected a combination of transitions out of this list at different nights. The line strengths are calculated at the first scale height on Mars (H= 10.8 km, T= 200 K).

Wavenumber (cm^{-1})	Strength ($cm^{-1}/cm^2/atm$)	R branch number
2922.336	1.830×10^{-20}	R 10
2922.700	1.935×10^{-20}	R 11
2923.060	2.026×10^{-20}	R 12
2923.416	2.102×10^{-20}	R 13
2923.769	2.163×10^{-20}	R 14
2924.118	2.210×10^{-20}	R 15
2924.464	2.242×10^{-20}	R 16
2924.806	2.262×10^{-20}	R 17
2925.145	2.267×10^{-20}	R 18
2925.480	2.260×10^{-20}	R 19
2925.812	2.240×10^{-20}	R 20
2926.140	2.209×10^{-20}	R 21
2926.464	2.167×10^{-20}	R 22
2926.785	2.117×10^{-20}	R 23

The error bars (in blue) in Figures 4.23 and 4.24 represent the standard errors, and are calculated at **each pixel** using the equation:

$$\sigma_{\overline{y}} = \frac{\sqrt{\sum_{line=1}^{n} {S^2}_{line}}}{\sum_{line=1}^{n}(S_{line}/\sigma_y)} \tag{4.9}$$

where S_{line} is the line strength of the OCS transition, n is the number of transitions, and σ_y is the standard deviation of the value at each pixel (how much scatter does this value have between different residual spectra at this pixel).

4.3.3 Calculating the Total Column Density

The average surface pressure on Mars is calculated with the continuum contribution along the slit as a weighting factor. It is calculated to be P_S =6.65 mbar for one set on June 13 UT, 2014. The total column density in the martian atmosphere is calculated taking into account the main constituents of the atmosphere.

The mixing ratios for the main atmospheric constituents in the martian atmosphere are $q_{CO_2} = 0.9532$, $q_{N_2} = 2.7 \times 10^{-2}$, $q_{Ar} = 1.6 \times 10^{-2}$, $q_{O_2} = 1.3 \times 10^{-3}$ and $q_{CO} = 8 \times 10^{-4}$ (Lellouch et al. 1991).

$\overline{\mu} = 43.7 \times 10^{-3}$ kg/mol is the mean molecular weight of the martian atmosphere. g = 3.71 m/s^2 is the surface gravity on Mars and $N_A = 6.023 \times 10^{23}$ is the Avogadro number.

$$N_j[\frac{molecule}{cm^2}] = \frac{N_A \times P_s \times (q_{CO_2} + q_{N_2} + q_{Ar} + q_{O_2} + q_{CO})}{\overline{\mu} \times g \times 10^4} \tag{4.10}$$

The 10^4 is the unit change from m^2 to cm^2. Therefore, $N_j = 2.47 \times 10^{23}$ $\frac{\text{molecule}}{\text{cm}^2}$.

4.3.4 Measuring the Uncertainty in the Equivalent Width

By definition, the equivalent width is calculated using the equation:

$$EW = \int_{\lambda_1}^{\lambda_2} \frac{F_c - F_l}{F_c} d\lambda = \int_{\lambda_1}^{\lambda_2} (1 - \frac{F_l}{F_c}) d\lambda \tag{4.11}$$

F_l: Signal in the points that define the line profile.

F_c: Signal in the points that define the continuum.

When dealing with discrete values (pixels), the equation becomes:

$$EW = \sum_{\lambda_1}^{\lambda_2} (1 - \frac{F_{l_i}}{F_{c_i}}) \Delta\lambda = (n_l \times \Delta\lambda) - \Delta\lambda \sum_{\lambda_1}^{\lambda_2} \frac{F_{l_i}}{F_{c_i}} \tag{4.12}$$

where n_l is the number of data points across the line between λ_1 and λ_2 (Ebbets 1995), $\Delta\lambda$ is the pixel width, i is the pixel number across the line between λ_1 and λ_2, F_{l_i} is the signal value at pixel number i of the line, and F_{c_i} is the signal value at pixel number i of the continuum.

$$EW = (n_l \times \Delta\lambda) - \Delta\lambda \times (\frac{F_{l_1}}{F_{c_1}} + \frac{F_{l_2}}{F_{c_2}} + ... + \frac{F_{l_n}}{F_{c_n}}) \tag{4.13}$$

($n_l \times \Delta\lambda$) does not contribute to the uncertainty in the equivalent width.

The uncertainty in the equivalent width is calculated using the following equation:

$$\left\langle \delta EW^2 \right\rangle = \Delta\lambda^2 \times (\sigma^2(\frac{F_{l_1}}{F_{c_1}}) + \sigma^2(\frac{F_{l_2}}{F_{c_2}}) + ... + \sigma^2(\frac{F_{l_n}}{F_{c_n}})) + covariance \tag{4.14}$$

The data points are not correlated with the noise at other points, therefore the covariance term drops out.

Case 1:

Assuming that all the data points are independent and that the error bar (standard deviation over the spectrum, or RMS) is the same over all the pixels, we obtain:

$$\sigma(\frac{F_{l_1}}{F_{c_1}}) = \sigma(\frac{F_{l_2}}{F_{c_2}}) = ... = \sigma(\frac{F_{l_n}}{F_{c_n}}) = \sigma(\frac{F_l}{F_c}) \tag{4.15}$$

we then get the following equation:

$$\left\langle \delta EW^2 \right\rangle = n_l \times \Delta\lambda^2 \times \sigma^2(\frac{F_l}{F_c}) \tag{4.16}$$

The number of pixels across the line between λ_1 and λ_2 is approximated as:

$$n_l \times \Delta\lambda \simeq 2 \times FWHM \tag{4.17}$$

where FWHM is the full-width at half maximum of the synthetic spectral line. When there is no detected line and the data (F_l) are fluctuating around the continuum $F_c = 1$, the variance is:

$$\sigma^2(\frac{F_l}{F_c}) = \sigma^2(F_l) = \epsilon^2{}_{rms} \tag{4.18}$$

where $\epsilon_{\rm rms}$ is equal to the standard deviation, or 1/SNR.

$$\left\langle \delta EW^2 \right\rangle \simeq 2 \times \frac{FWHM}{\Delta\lambda} \times \Delta\lambda^2 \times \epsilon^2{}_{rms} \tag{4.19}$$

$$\left\langle \delta EW^2 \right\rangle^{1/2} \simeq \sqrt{2} \times (FWHM \times \Delta\lambda)^{1/2} \times \epsilon_{rms} \tag{4.20}$$

By comparison, Cayrel (1988) found:

$$\left\langle \delta EW^2 \right\rangle^{1/2} \simeq 1.5 \times (FWHM \times \Delta\lambda)^{1/2} \times \epsilon_{rms} \tag{4.21}$$

Case 2:

The data points are independent and the uncertainty (error bar) is **not** the same over all the pixels; it is the standard deviation of the mean (or standard error):

$$\left\langle \delta EW^2 \right\rangle = \Delta\lambda^2 \times (\sigma^2(\frac{F_{l_1}}{F_{c_1}}) + \sigma^2(\frac{F_{l_2}}{F_{c_2}}) + ... + \sigma^2(\frac{F_{l_n}}{F_{c_n}})) \tag{4.22}$$

When there is no detected line and the data (F_l) are fluctuating around the continuum $F_c = 1$, therefore:

$$\sigma^2(\frac{F_{l_i}}{F_{c_i}}) = \sigma^2(F_{l_i}) \tag{4.23}$$

and the uncertainty in the equivalent width is:

$$\left\langle \delta EW^2 \right\rangle^{1/2} = \Delta\lambda \times \sqrt{(\sigma^2(F_{l_1}) + \sigma^2(F_{l_2}) + ... + \sigma^2(F_{l_n}))} \tag{4.24}$$

The further enhancements in the SNR caused by stacking the residual spectra in the spatial direction along the slit, followed by the co-addition of OCS transitions, did not reveal any OCS absorption feature. We then synthesized a Gaussian OCS line with a full-width at half maximum (FWHM) equal to the CSHELL spectral resolution. We extracted an upper limit for OCS based on the uncertainty in the equivalent width that we derived in equation 4.24.

4.3.5 Upper limits on OCS

In the optically thin case (opacity $\tau << 1$), the equivalent width of the spectral line is proportional to the column density (Spitzer 1968). The 1-sigma uncertainty in the mixing

ratio is given by the equation:

$$\delta q = \frac{\delta EW}{N_j \times \mu \times S} \tag{4.25}$$

where δEW is the uncertainty in the equivalent width, N_j is the total column density in the martian atmosphere, S is the average line strength of the different OCS transitions, and μ is the total airmass calculated using the following equation (Villanueva et al. 2008):

$$\mu = f_{sol}(\mu_{sm} + \mu_{mo}) + (1 - f_{sol})\mu_{mo} \tag{4.26}$$

where $\mu_{sm} \sim \sec(\theta_{sm})$ is the Sun-to-Mars surface airmass, $\mu_{mo} \sim \sec(\theta_{mo})$ is Mars' surface-to-observer airmass, and fsol is the solar factor. θ_{sm} is the zenith angle of the Sun as see from the surface of Mars, and θ_{mo} is the zenith angle of the observer as seen from the surface of Mars. In our case where fsol=1, the solar reflected radiation goes through a two-way airmass before leaving the planet. In order to compensate for all the airmass changes of the observed regions on Mars, we have calculated the total airmass across the slit using equation 4.26. Figure 4.21 represents the Mars' surface-to-observer airmass (solid black), Sun-to-Mars' surface airmass (dashed black), and the total airmass (solid red) on June 13 UT, 2014.

The upper limit of OCS across Mars requires a representative airmass for the regions we observed under CSHELL's slit, therefore we calculated an "effective" airmass μ_e using the equation:

$$\mu_e = \frac{\sum_{i=1}^{N} \mu(z_i) \times \Delta z_i}{\sum_{i=1}^{N} \Delta z_i} \tag{4.27}$$

where $\mu(z_i)$ is the total airmass at spatial pixel "i" on the detector and Δz_i is the width on CSHELL's detector, in units of pixels, between two latitudes on Mars.

Now that we have combined the data over 4 key dimensions: latitude, longitude, time and frequency, the 2σ upper limits on the mixing ratio of OCS for June 13 UT, 2014 is 3.6 ppbv (Fig. 4.24). The error bars (in blue) are the standard deviation on the mean in the residual spectrum. As a comparison with previous results, Maguire (1977) established an

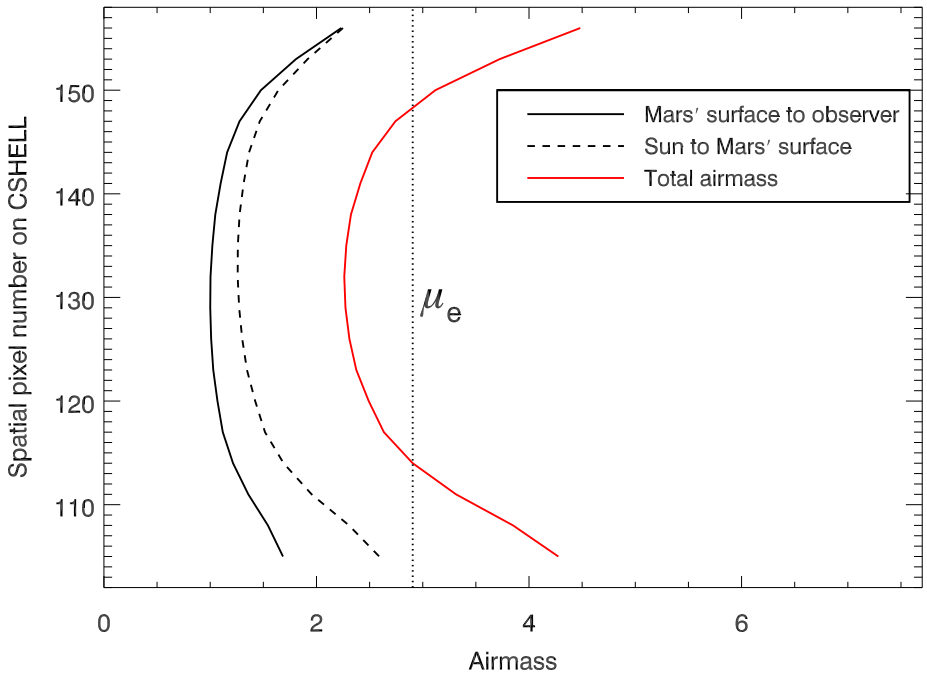

Figure 4.21 : Different airmass components for June 13 UT, 2014, are presented. They are divided into the Mars' surface-to-observer airmass (solid black), Sun-to-Mars' surface airmass (dashed black). The total airmass is in solid red. The effective airmass μ_e is represented with the dotted vertical line around 2.9.

upper limit of 14 ppbv (at 2 sigma) on OCS using Mariner 9's Infrared Spectrometer when combining 1747 spectra for almost a year!

The following table 4.4 presents the upper limits at 2σ on OCS, and Figures 4.23 and 4.24 show the residual spectra for all our observing nights between December 15 UT, 2011 and June 13 UT, 2014.

In order to increase the sensitivity in looking for OCS, the data have been co-added between 2011 and 2014. The residual spectra have been first co-added line-by-line throughout all the nights using the square root of the integration time at each night (from Table 4.1) as a weighting factor. At a second stage, the combination of the data has been done between the lines of different transitions of OCS, in the spectral direction, using the line strength and the square root of the number of nights when the corresponding OCS

Table 4.4 : Upper limits at 2σ on OCS.

Date (UT)	Volcanic Region	Number of transitions used	Upper limit at 2σ (ppbv)
15 December 2011	Tharsis	4	4.3
18 December 2011	Tharsis	4	4.4
3 January 2012	Syrtis Major	4	3.8
5 January 2012	Syrtis Major	4	3.8
6 January 2012	Syrtis Major	4	4.2
30 May 2014	Tharsis	5	3.5
12 June 2014	Syrtis Major	4	2.4
13 June 2014	Syrtis Major	3	3.6
Co-added over all nights			**0.8**

transition has been selected. The result (black spectrum) is shown in Figure 4.22, and the resulting upper limit over all the nights is 0.8 ppbv at 2σ. The error bars (in blue) represent the standard errors, and are calculated at each pixel using the equation:

$$\sigma_{\overline{y}} = \frac{\sqrt{\sum_{line=1}^{n} S^2{}_{line} \times t_{line}}}{\sum_{line=1}^{n} (S_{line} \times \sqrt{t_{line}}/\sigma_y)} \tag{4.28}$$

where S_{line} is the line strength of the OCS transition, n is the number of transitions, t_{line} is the number of nights where an OCS transition had been used, and σ_{y} is the standard deviation of the value at each pixel.

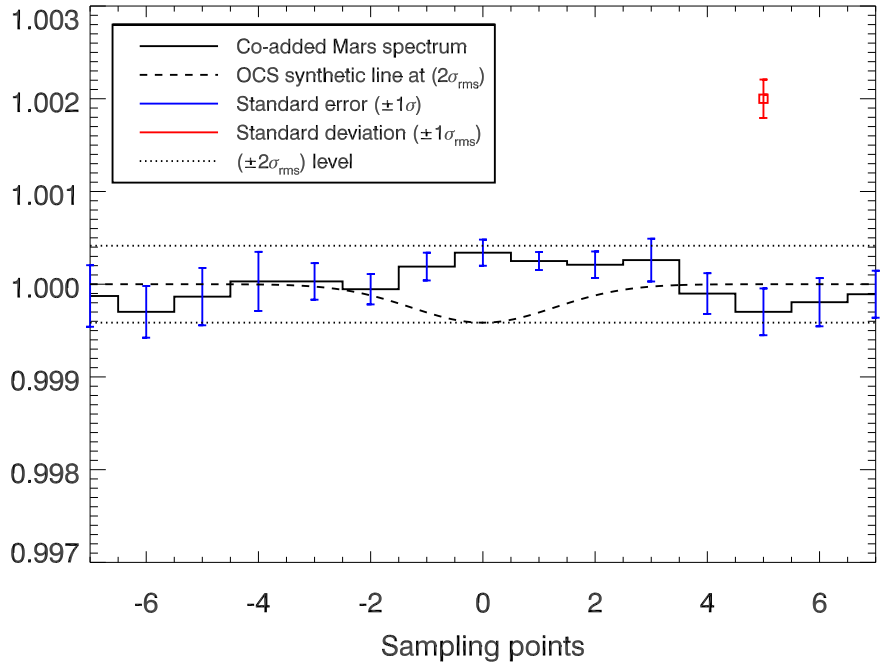

Figure 4.22 : After co-adding the data between December 15, 2011 and Jun 13, 2014, we reached a SNR of 4,800. The blue error bars are the standard errors, the red error bar is $\pm 1\sigma_{rms}$ over the spectrum (solid black), and the dashed black line is the synthetic OCS line at $2\sigma_{rms}$ level.

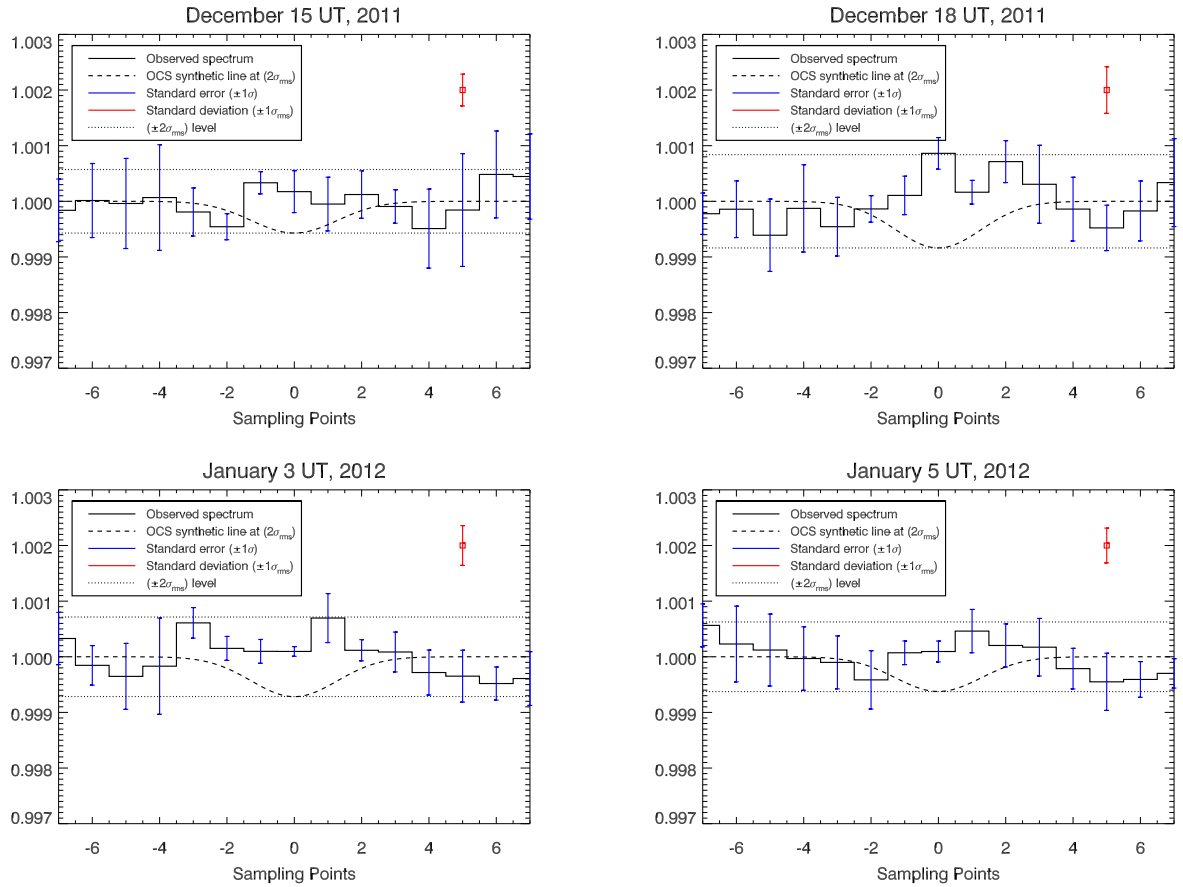

Figure 4.23 : After co-adding the data in the spectral and spatial directions on Mars, the residual spectra at each night for 15, 18 UT December, 2011, and 3, 5 UT January, 2012, are shown. The blue error bars are the standard errors, the red error bar is $\pm 1\sigma_{rms}$ over the residual spectrum (solid black), and the dashed black line is the synthetic OCS line at $2\sigma_{rms}$ level.

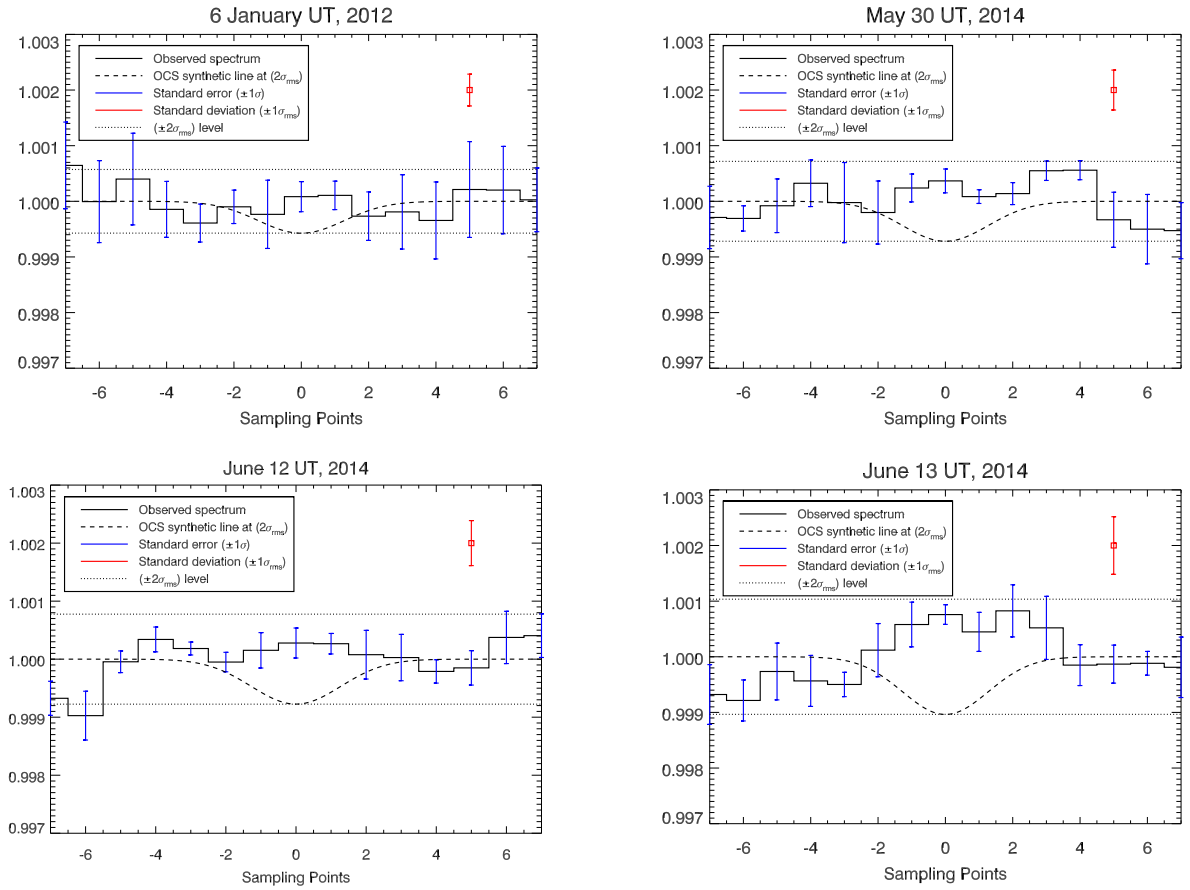

Figure 4.24 : After co-adding the data in the spectral and spatial directions on Mars, the residual spectra at each night for 6 UT January, 2012, 30 UT May, 12 and 13 UT June, 2014 are shown. The blue error bars are the standard errors, the red error bar is $\pm 1\sigma_{rms}$ over the residual spectrum (solid black), and the dashed black line is the synthetic OCS line at $2\sigma_{rms}$ level.

4.3.6 IR Radiative Transfer Model for Mars

We developed a radiative transfer code that computes the transmittance of the martian atmosphere. It is the IR Radiative Transfer Model (IRRTM). The code takes into account the two-way airmass, and considers a dust and scattering-free atmosphere. For OCS, we assume that it is well mixed, and that the temperature-pressure profile is uniform across Mars. We used the effective airmass defined in equation 4.27 to represent the airmass of the region covered by the spectrometer's slit. In our model, the mixing ratio for each targeted species is assumed to be uniform across the planet, as is the total surface pressure. The code then calculates the fully-resolved transmission (R = $\frac{\nu}{\Delta\nu} = 6{\times}10^6$), layer-by-layer in the atmosphere, wavelength-by-wavelength, line-by-line and convolves the transmission function with the spectrometer's slit function (Gaussian) at the specified resolving power. For a multi-layered, plane-parallel atmosphere, the spectral transmittance is given by the equation:

$$T_\nu = e^{-\tau_{0,\nu}} \tag{4.29}$$

where $\tau_{0,\nu}$ is the total optical depth of the atmosphere. The optical path increases with the incidence angle, and therefore the optical depth is multiplied by the factor $1/\mu$, where μ is the two-way-airmass in equation 4.26. The frequency-dependent optical depth above each layer at altitude z, $\tau_\nu(z)$, is given by:

$$\tau_\nu(z) = \int_z^\infty \alpha_\nu(z') \, \frac{\mathrm{dz}'}{\mu} \tag{4.30}$$

where $\alpha_\nu(\mathrm{z}')$ is the absorption coefficient at each layer at altitude z (z > z′), and dz′ is its corresponding thickness. The atmospheric layers are chosen to have an increasing thickness in the direction of altitude.

The absorption coefficient at each layer of the atmosphere, as a function of frequency is given by:

$$\alpha_\nu(z) = S_{\nu_0}(T) \times N(z) \times f_v(\nu - \nu_0). \tag{4.31}$$

where $S_{\nu_0}(T)$ is the strength of the transition of central frequency ν_0, and is given by:

$$S_{\nu_0}(T) = S_{\nu_0}(T_0)\frac{\exp(-hcE_L/k_BT)Q_T(T_0)[1-\exp(-hc\nu_0/k_BT)]}{\exp(-hcE_L/k_BT_0)Q_T(T)[1-\exp(-hc\nu_0/k_BT_0)]} \tag{4.32}$$

where S and Q are the spectral line strength and the partition function, respectively. These two parameters are calculated at temperature T of the atmospheric layer, and reference temperature $T_0 = 296$ K. E_L is the lower state energy. S, Q and E_L are extracted from the most recent HITRAN database of 2012 (Rothman et al. 2013). h, c and k_B are Planck constant, the speed of light, and Boltzmann constant, respectively.

$N(z)$ is the number density of the analyzed constituent in the atmosphere contained in each layer, and is expressed as:

$$N(z) = \frac{q \times P(z)}{k_B \times T(z)} \tag{4.33}$$

$P(z)$ is the pressure at altitude z of the atmospheric layer, q is the volume mixing ratio of the molecule analyzed. We consider a well mixed atmosphere where the mixing ratio is constant with altitude and k_B is the Boltzmann constant.
$f_v(\nu - \nu_0)$ is the frequency-dependent normalized Voigt function. In the pressure-broadened profile, γ, the half width of the Lorentzian should be calculated by:

$$\gamma = \gamma_f \times \frac{P}{P_0} \times (1-q) \times \left(\frac{T_0}{T}\right)^{n_f} + A \tag{4.34}$$

$$A = \gamma_s \times \frac{P}{P_0} \times q \times \left(\frac{T_0}{T}\right)^{n_s} \tag{4.35}$$

P_0 and T_0 are the pressure and temperature at the reference standard temperature and pressure (STP), P and T are the pressure and temperature at each atmospheric layer, γ_f and γ_s are the foreign and self broadened Lorentz half widths, whereas n_f and n_s

are the temperature dependent coefficients for the foreign and self broadening coefficients, respectively.

In the martian atmosphere, the molecules are considered under a CO_2 collisional regime. The HITRAN 2012 database (Rothman et al. 2013) provides γ_s, the broadened half-width of OCS in a CO_2 environment, γ_{OCS-CO_2} (Bouanich et al. 1988; Wilzewski et al. 2015a,b), and n_{OCS-CO_2} (Wilzewski et al. 2015c). Figure 4.25 shows part of the synthetic OCS R branch of the $(\nu_1 + \nu_3)$ band, between 2920 cm^{-1} and 2930 cm^{-1} using our developed IR radiative transfer model. The model is at an airmass of 3.0, a mixing ratio of 3.0 ppbv, and it is convolved to a resolving power R = 43,000.

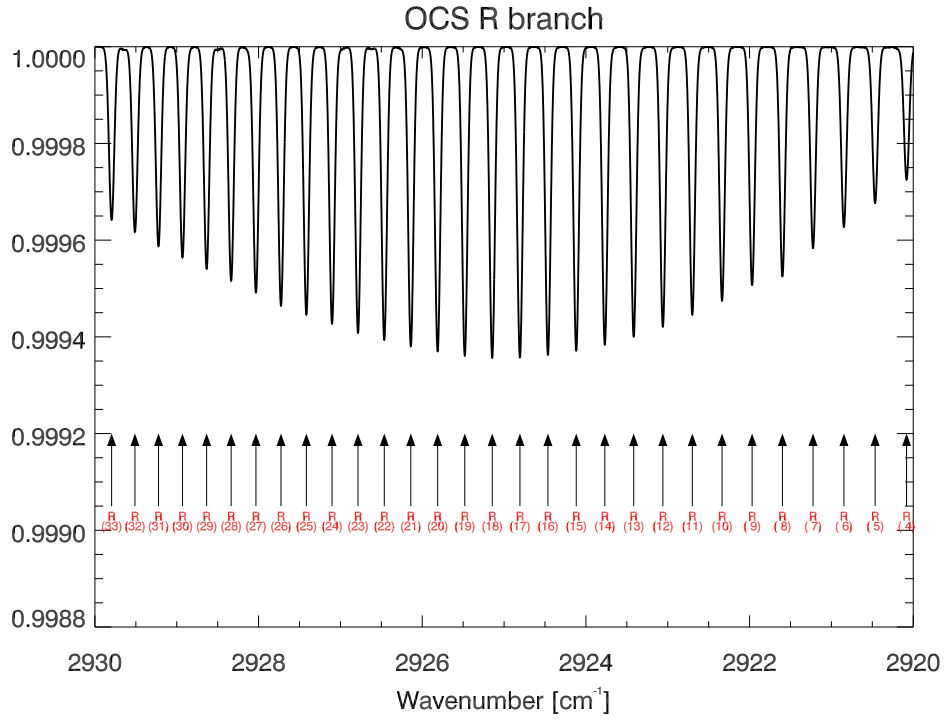

Figure 4.25 : Part of the synthetic OCS R branch of the $(\nu_1 + \nu_3)$ band, between 2920 cm^{-1} and 2930 cm^{-1} modeled using IRRTM, is presented here. The spectrum is obtained at an airmass of 3.0, a mixing ratio of 3.0 ppbv, and it is convolved to a resolving power R = 43,000.

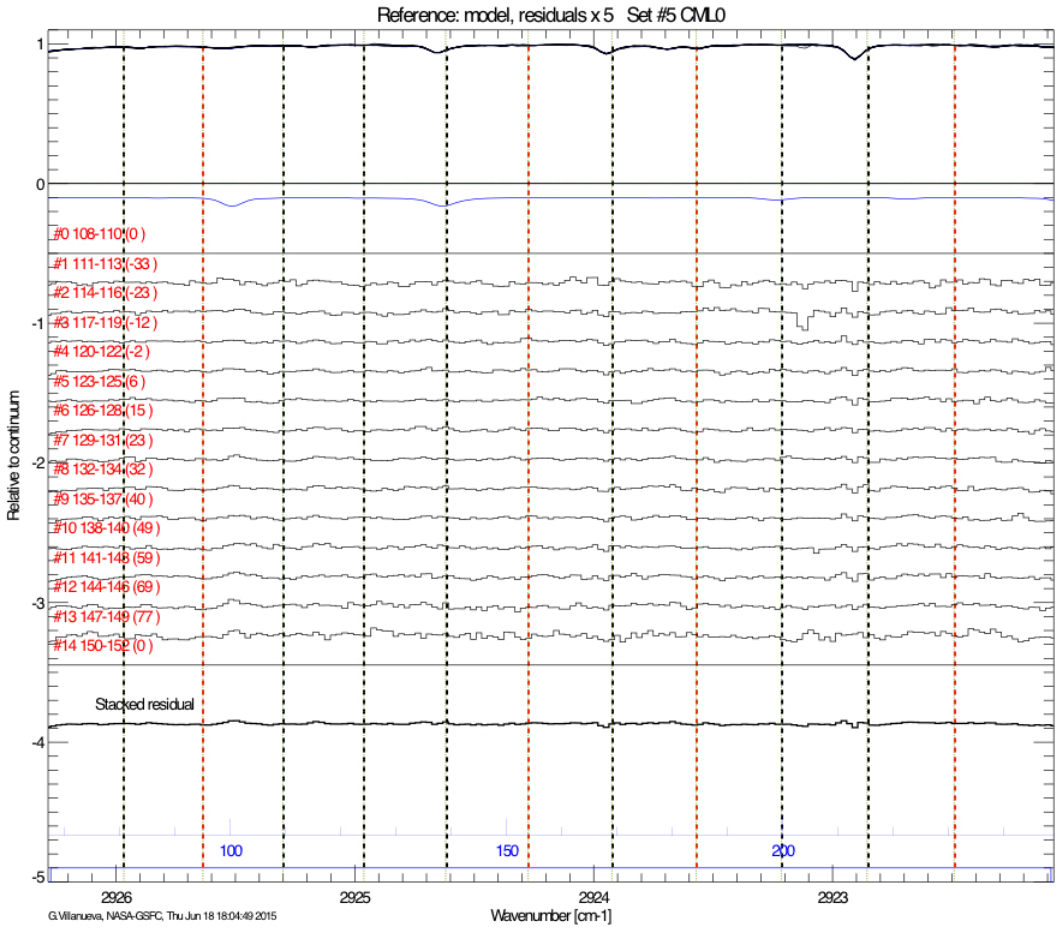

Figure 4.26 : The martian residual spectra along the slit when sampling the Tharsis region are shown here. Mars was at a topocentric Doppler shift of -16.1 km/s, and the spectra are shown in Earth's reference frame. The vertical dashed lines indicate the Doppler-shifted OCS line positions in the martian atmosphere if OCS were to be found on December 15 UT, 2011. These lines are blue-shifted by 0.157 cm^{-1} from their telluric counterparts. The vertical red lines indicate the positions we used when extracting the OCS upper limit on the mixing ratio.

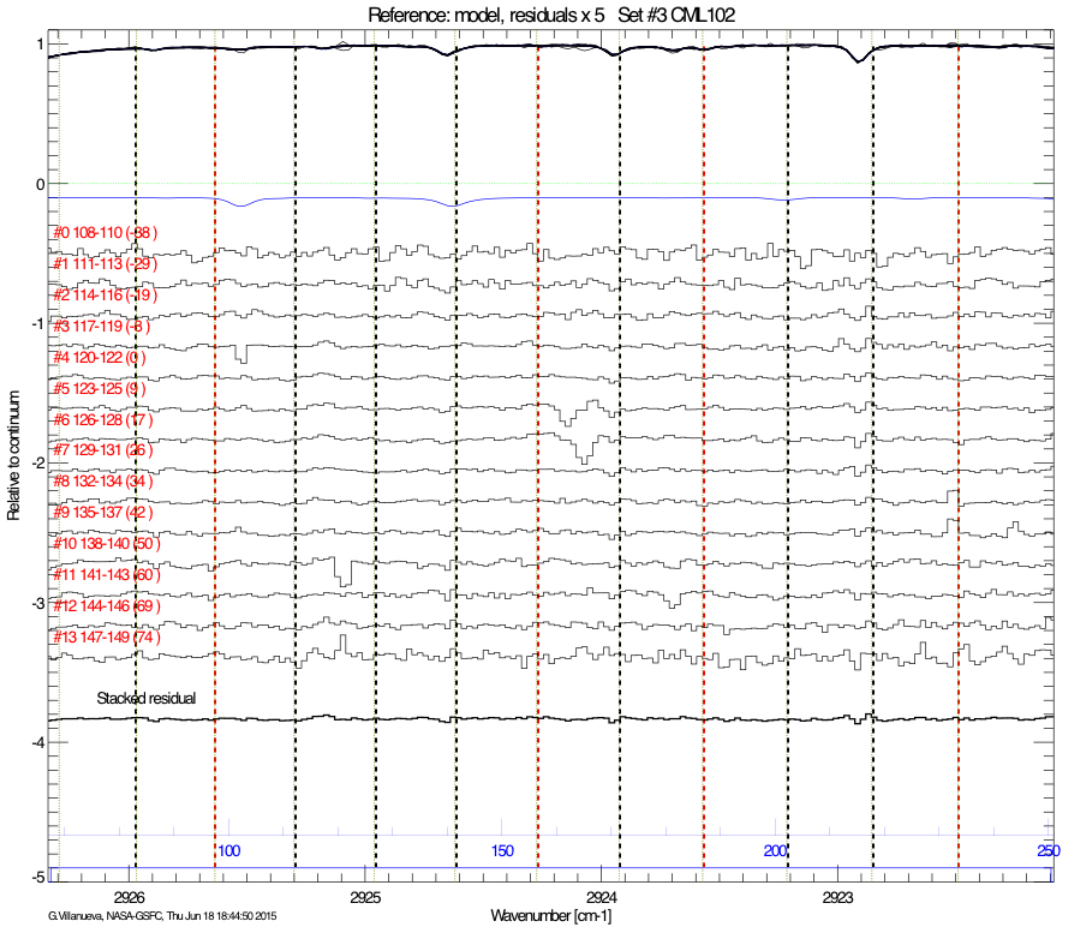

Figure 4.27 : The martian residual spectra along the slit when sampling the Tharsis region on December 18 UT, 2011, are shown here. Mars was at a topocentric Doppler shift of -16.0 km/s, and the spectra are presented in Earth's reference frame. The vertical dashed lines indicate the OCS line positions in the martian atmosphere if OCS were to be found. These lines are blue-shifted by 0.156 cm^{-1} from their telluric counterparts. The vertical red lines indicate the positions we used when extracting the OCS upper limit on the mixing ratio.

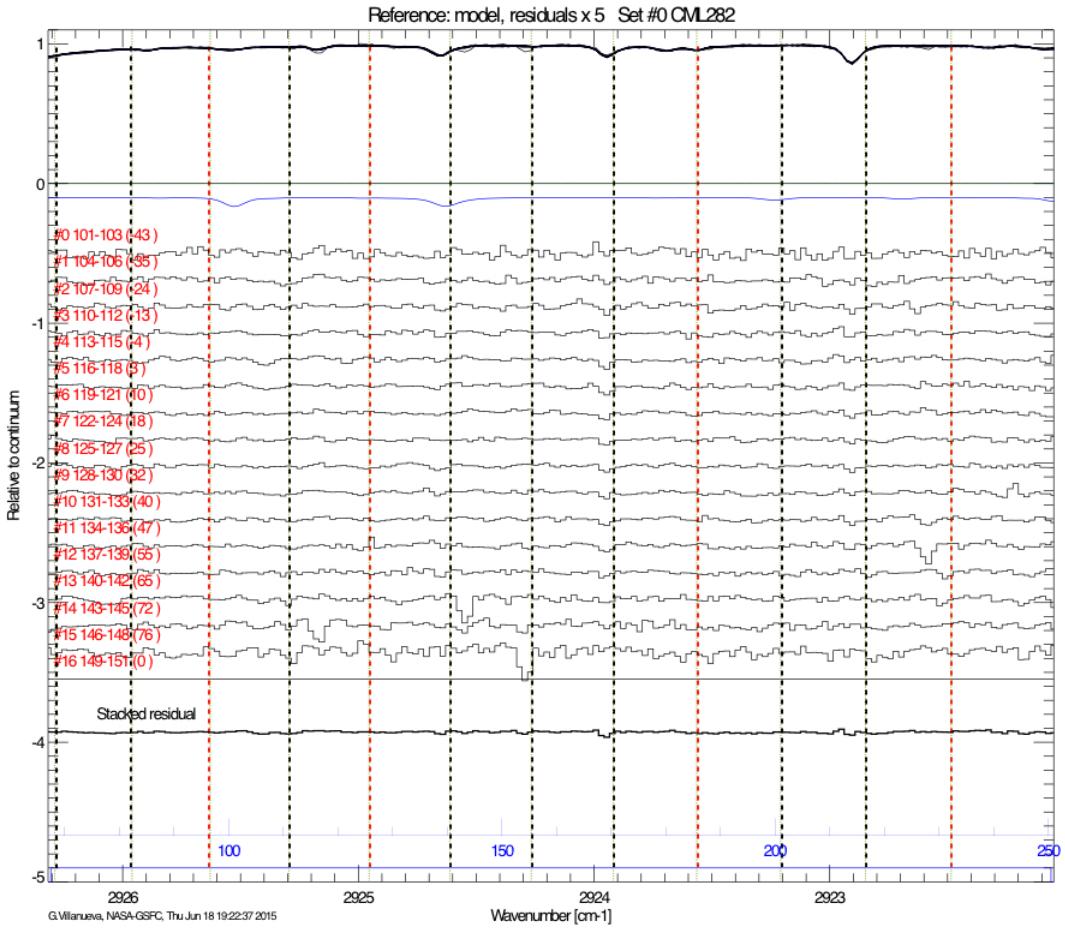

Figure 4.28 : The martian residual spectra along the slit when sampling the Syrtis region on January 03 UT, 2012, are shown here. Mars was at a topocentric Doppler shift of -15.5 km/s, and the spectra are presented in Earth's reference frame. The vertical dashed lines indicate the OCS line positions in the martian atmosphere if OCS were to be found. These lines are blue-shifted by 0.151 cm^{-1} from their telluric counterparts. The vertical red lines indicate the positions we used when extracting the OCS upper limit on the mixing ratio.

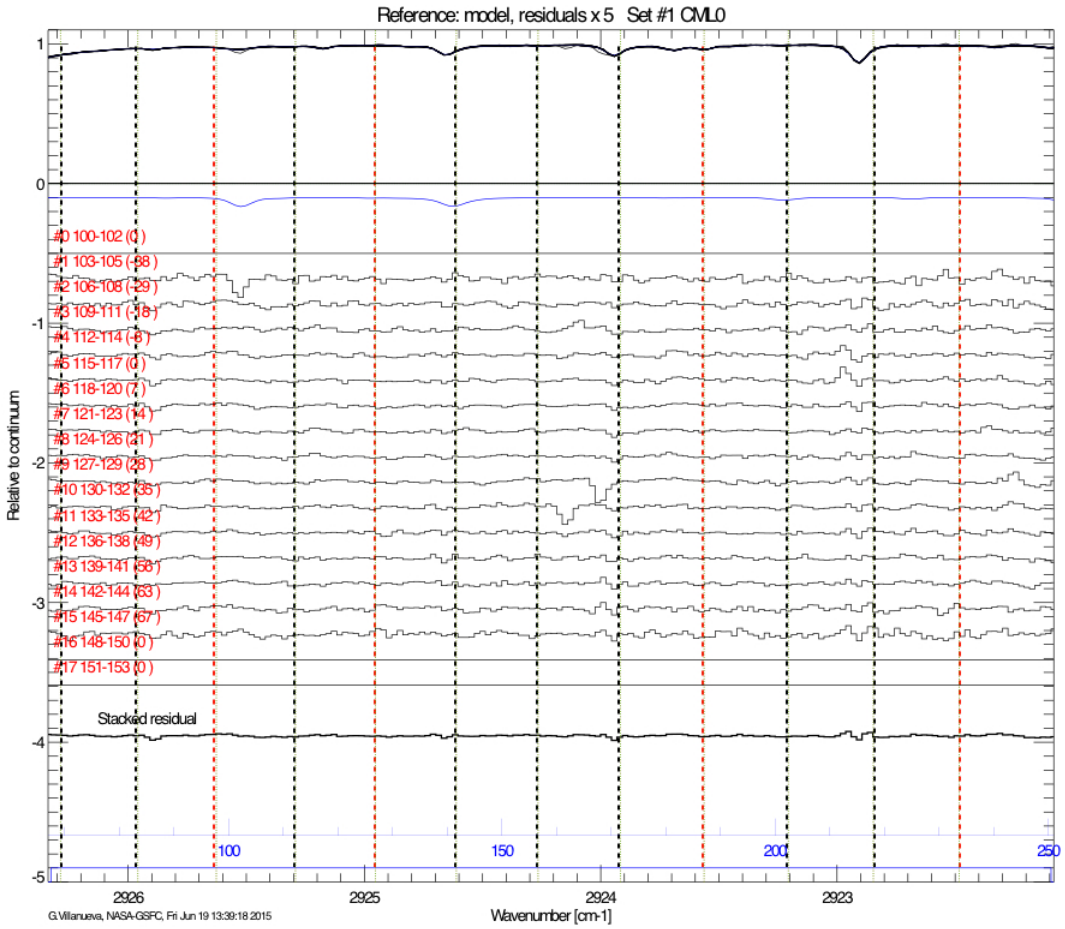

Figure 4.29 : The martian residual spectra along the slit when sampling the Syrtis region on January 05 UT, 2012, are shown here. Mars was at a topocentric Doppler shift of -15.3 km/s, and the spectra are presented in Earth's reference frame. The vertical dashed lines indicate the OCS line positions in the martian atmosphere if OCS were to be found. These lines are blue-shifted by 0.149 cm^{-1} from their telluric counterparts. The vertical red lines indicate the positions we used when extracting the OCS upper limit on the mixing ratio.

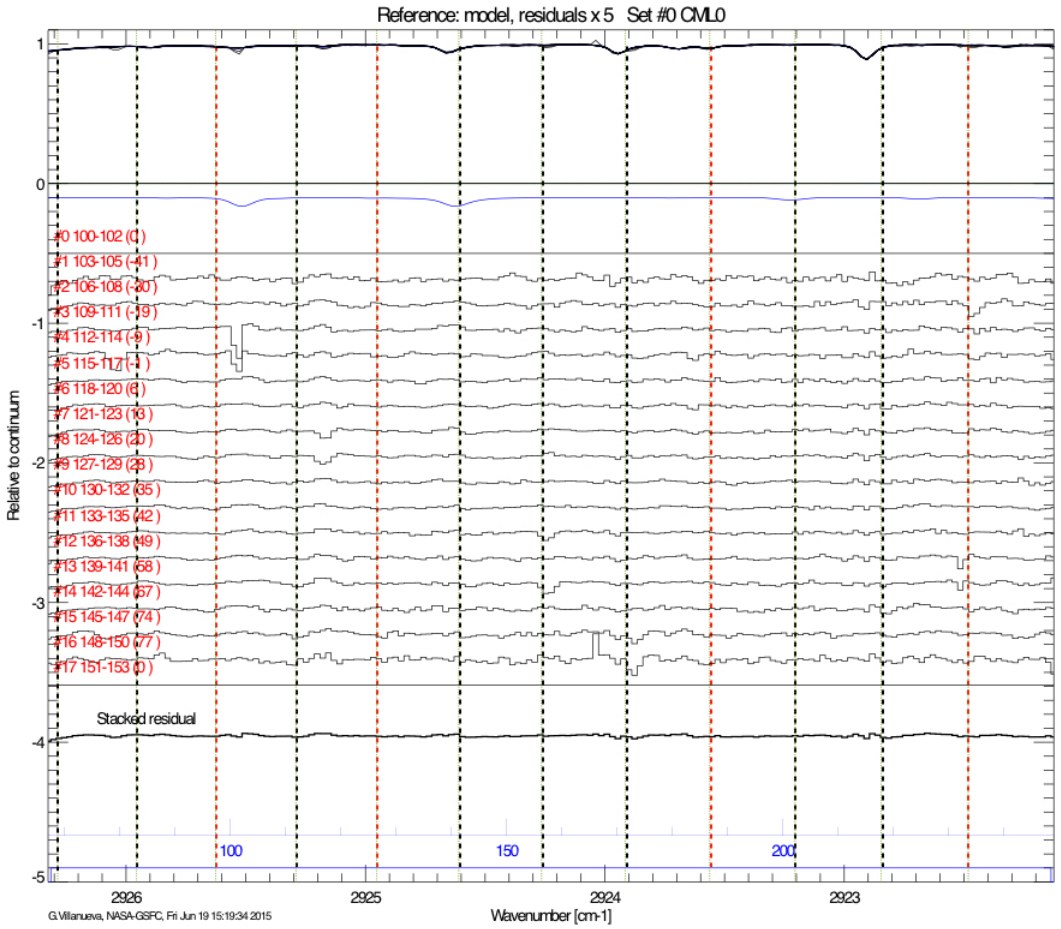

Figure 4.30 : The martian residual spectra along the slit when sampling the Syrtis region on January 06 UT, 2012, are shown here. Mars was at a topocentric Doppler shift of -15.3 km/s, and the spectra are presented in Earth's reference frame. The vertical dashed lines indicate the OCS line positions in the martian atmosphere if OCS were to be found. These lines are blue-shifted by 0.149 cm^{-1} from their telluric counterparts. The vertical red lines indicate the positions we used when extracting the OCS upper limit on the mixing ratio.

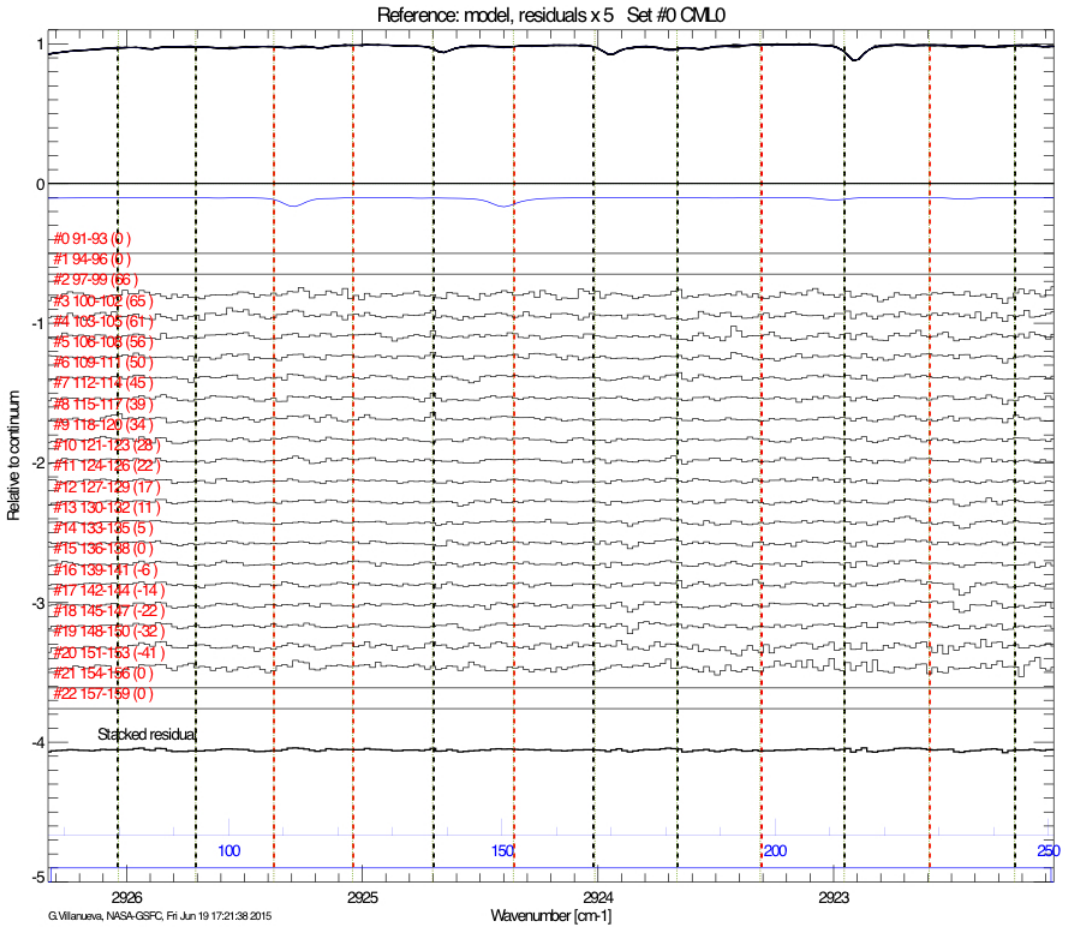

Figure 4.31 : The martian residual spectra along the slit when sampling the Tharsis region on May 30 UT, 2014, are shown here. Mars was at a topocentric Doppler shift of +10.5 km/s, and the spectra are presented in Earth's reference frame. The vertical dashed lines indicate the OCS line positions in the martian atmosphere if OCS were to be found. These lines are red-shifted by 0.102 cm^{-1} from their telluric counterparts. The vertical red lines indicate the positions we used when extracting the OCS upper limit on the mixing ratio.

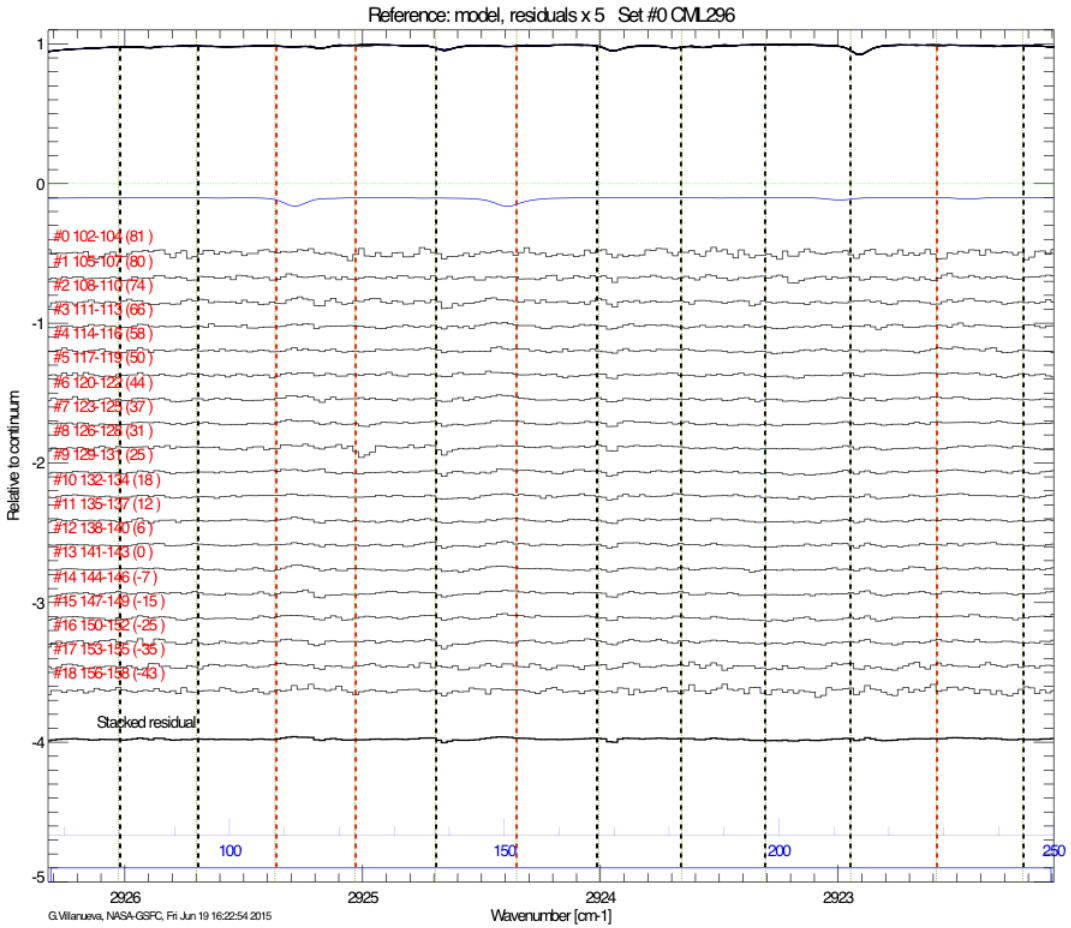

Figure 4.32 : The martian residual spectra along the slit when sampling the Syrtis region are shown here on June 12 UT, 2014. Mars was at a topocentric Doppler shift of +11.3 km/s, and the spectra are presented in Earth's reference frame. The vertical dashed lines indicate the OCS line positions in the martian atmosphere if OCS were to be found. These lines are red-shifted by 0.110 cm^{-1} from their telluric counterparts. The vertical red lines indicate the positions where we extracted the upper limit on the mixing ratio.

References

Allison, M. 1997, Geophys. Res. Lett., 24, 1967

Allison, M. & McEwen, M. 2000, Planet. Space Sci., 48, 215

Anderson, G. P., Clough, S., Kneizys, F., Chetwynd, J., & Shettle, E. P. 1986, AFGL atmospheric constituent profiles (0.120 km), Tech. rep., DTIC Document

Bouanich, J.-P., Campers, C., Blanquet, G., & Walrand, J. 1988, J. Quant. Spectrosc. Radiat. Trans., 39, 353

Cayrel, R. 1988, in IAU Symposium, Vol. 132, The Impact of Very High S/N Spectroscopy on Stellar Physics, ed. G. Cayrel de Strobel & M. Spite, 345

Christensen, P. R., Bandfield, J. L., Hamilton, V. E., Ruff, S. W., Kieffer, H. H., Titus, T. N., Malin, M. C., Morris, R. V., Lane, M. D., Clark, R. L., Jakosky, B. M., Mellon, M. T., Pearl, J. C., Conrath, B. J., Smith, M. D., Clancy, R. T., Kuzmin, R. O., Roush, T., Mehall, G. L., Gorelick, N., Bender, K., Murray, K., Dason, S., Greene, E., Silverman, S., & Greenfield, M. 2001, J. Geophys. Res., 106, 23823

Clough, S. A., Shephard, M. W., Mlawer, E. J., Delamere, J. S., Iacono, M. J., Cady-Pereira, K., Boukabara, S., & Brown, P. D. 2005, J. Quant. Spectrosc. Radiat. Trans., 91, 233

Ebbets, D. 1995, in Calibrating Hubble Space Telescope. Post Servicing Mission. Proceedings of a Workshop held at the Space Telescope Science Institute, 207

Encrenaz, T., Bezard, B., Greathouse, T. K., Richter, M. J., Lacy, J. H., Atreya, S. K., Wong, A. S., Lebonnois, S., Lefèvre, F., & Forget, F. 2004, Icarus, 170, 424

Greene, T. P., Tokunaga, A. T., Toomey, D. W., & Carr, J. B. 1993, in Society of Photo-Optical Instrumentation Engineers (SPIE) Conference Series, Vol. 1946, Infrared Detectors and Instrumentation, ed. A. M. Fowler, 313–324

Krasnopolsky, V. A. 2005, Icarus, 178, 487

Lellouch, E., Rosenqvist, J., Goldstein, J. J., Bougher, S. W., & Paubert, G. 1991, Astrophys. J., 383, 401

Maguire, W. C. 1977, Icarus, 32, 85

Markwardt, C. B. 2009, in Astronomical Society of the Pacific Conference Series, Vol. 411, Astron. Data Anal. Softw. Syst. XVIII, ed. D. A. Bohlender, D. Durand, & P. Dowler, 251

Millour, E., Forget, F., González-Galindo, F., Spiga, A., Lebonnois, S., Montabone, L., Lewis, S. R., Read, P. L., López-Valverde, M. A., Gilli, G., Lefèvre, F., Montmessin, F., Desjean, M.-C., Huot, J.-P., & McD/Gcm Development Team. 2008, LPI Contributions, 1447, 9029

Moré, J. J. 1977, in Numerical Analysis, ed. G. A. Watson (Berlin: Springer), 105–116

Mumma, M. J., Villanueva, G. L., Novak, R. E., Hewagama, T., Bonev, B. P., DiSanti, M. A., Mandell, A. M., & Smith, M. D. 2009, Science, 323, 1041

Novak, R. E., Mumma, M. J., DiSanti, M. A., Russo, N. D., & Magee-Sauer, K. 2002, Icarus, 158, 14

Régalia-Jarlot, L., Hamdouni, A., Thomas, X., der Heyden, P. V., & Barbe, A. 2002, J. Quant. Spectrosc. Radiat. Trans., 74, 455

Rothman, L., Gordon, I., Babikov, Y., Barbe, A., Benner, D. C., Bernath, P., Birk, M., Bizzocchi, L., Boudon, V., Brown, L., Campargue, A., Chance, K., Cohen, E., Coudert, L., Devi, V., Drouin, B., Fayt, A., Flaud, J.-M., Gamache, R., Harrison, J., Hartmann, J.-M., Hill, C., Hodges, J., Jacquemart, D., Jolly, A., Lamouroux, J., Roy, R. L., Li, G., Long, D., Lyulin, O., Mackie, C., Massie, S., Mikhailenko, S., Mller, H., Naumenko, O., Nikitin, A., Orphal, J., Perevalov, V., Perrin, A., Polovtseva, E., Richard, C., Smith, M., Starikova, E., Sung, K., Tashkun, S., Tennyson, J., Toon, G., Tyuterev, V., & Wagner, G. 2013, J. Quant. Spectrosc. Radiat. Trans., 130, 4 , hITRAN2012 special issue

Spitzer, Jr., L. 1968, Diffuse Matter in Space., Vol. 28 (Interscience Tracts on Physics and Astronomy)

Tokunaga, A. T., Toomey, D. W., Carr, J., Hall, D. N. B., & Epps, H. W. 1990, in Society of Photo-Optical Instrumentation Engineers (SPIE) Conference Series, Vol. 1235, Instrumentation in Astronomy VII, ed. D. L. Crawford, 131–143

Villanueva, G. L. 2004, PhD thesis, Max-Planck-Institut für Sonnensystemforschung

Villanueva, G. L., Mumma, M. J., & Magee-Sauer, K. 2011, J. Geophys. Res., 116, E08012

Villanueva, G. L., Mumma, M. J., Novak, R. E., & Hewagama, T. 2008, Icarus, 195, 34

Villanueva, G. L., Mumma, M. J., Novak, R. E., Radeva, Y. L., Käufl, H. U., Smette, A., Tokunaga, A., Khayat, A., Encrenaz, T., & Hartogh, P. 2013, Icarus, 223, 11

Wenger, M., Ochsenbein, F., Egret, D., Dubois, P., Bonnarel, F., Borde, S., Genova, F., Jasniewicz, G., Laloë, S., Lesteven, S., & Monier, R. 2000, Astron. & Astrophys. Suppl., 143, 9

Wilzewski, J. S., Gordon, I. E., Kochanov, R. V., Hill, C., & Rothman, L. S. 2015a, cO_2 broadening coefficients are experimental data from Ref. [944], supplemented by the smoothed values from the same source and supplemented with the results of a 2^{nd} order

polynomial fit (a+b×m+b×m^2) with uncertainty code 3. The fit parameters are a = 0.13825, b = 9.99809E-4, c = 7.803E-6

—. 2015b, oCS-CO_2 shift values for all transitions set to zero due to lack of data

—. 2015c, oCS-CO_2 temperature dependence values for all transitions set to 0.75 due to lack of data

Chapter 5

Implications, Conclusions and Future Directions

This chapter describes the mechanism of releasing volcanic gases from a magma body into the atmosphere of the planet. Using the results from previous chapters, the SO_2 outgassing rate is estimated, and compared with terrestrial analogs. The amount of magma that is able to degas similar amounts of SO_2 is estimated. The limits on the level of active release of volcanic gases on Mars are inferred. The implications of the results on the volcanic origin of the methane released on Mars in 2003 (Mumma et al. 2009) are later discussed. Future prospects with iSHELL, the next generation of high-resolution spectrometers on IRTF, and the corresponding sensitivity limits are presented. Future observing strategies with ALMA that will take advantage of its unprecedented sensitivity at sub arc-second spatial resolutions on Mars are also discussed. The chapter ends with a summary of the results and the conclusion.

5.1 Modeling SO_2 Outgassing and its Implications on the Current Outgassing from the Sub-surface of Mars

During an outgassing event, the production of molecules and their release into the atmosphere is followed by their destruction within a lifetime τ. If we consider an outgassing rate x (molecules/day), the number of molecules at the end of the first day is x (molecules).

On the next day, new molecules are being produced, and the number of molecules from the previous day has decayed exponentially, with a rate $k = 1/\tau$, inversely proportional to the lifetime τ (Figure 5.1).

day 0	x	**Expected number of molecules when the outgassing has started**
day 1	$x... + ..x \times e^{-kt}$	**Expected number of molecules after 1 day**
day 2	$x... + ..x \times e^{-kt} ... + ..x \times e^{-2kt}$	
day 3	$x... + ..x \times e^{-kt} ... + ..x \times e^{-2kt} + ...x \times e^{-3kt}$	
	.	
	.	
day n	$x \times \left(\sum_{i=0}^{n} e^{-kti} \right)$	**Expected number of molecules after n days**

Figure 5.1 : Model of the steady-state outgassing when molecules are being formed at a rate of x (molecules/day), and later destroyed at a rate $k = 1/\tau$, where τ is the lifetime, and t is the time unit. Each row represents the expected number of molecules to be present in the atmosphere, after time has elapsed.

The total mass of SO_2 in the martian atmosphere, as derived from the global mixing ratio across Mars, is given by the following equation:

$$M_{SO_2} = \mu_i \times M_{atmosphere} \tag{5.1}$$

where $\mu_i = \frac{m_i}{\overline{m}} \times q_{SO_2}$ is the mass mixing ratio, m_i (= 64 g/mol) is the molecular mass of SO_2, $\overline{m}$ is the mean molecular weight of the martian atmosphere (= 43.7 g/mol), q_{SO_2} is the global volume mixing ratio from our observations, and $M_{atmosphere}$ (= 2.5×10^{16} kg) is the total mass of the martian atmosphere. Our upper limits of 1.1 ppbv using the CSO and 3.1 ppbv using the JCMT correspond to 40 and 114 kilotons of SO_2, respectively.

During a constant outgassing event, the expected number of molecules N(t) as a function of time is:

$$N(t) = \frac{x}{k}(1 - e^{-kt}) \tag{5.2}$$

Asymptotically in equation 5.2, when time goes to a few lifetimes, the number of SO_2 molecules in the atmosphere becomes invariant and globally distributed, $N(t) = x/k$, and has a total mass corresponding to our upper limits of N= 40 and 114 kilotons (1.1 ppbv and 3.1 ppbv). Our current upper limit, combined with a lifetime τ= 1/k of SO_2 of 2 years, yields an outgassing rate (x) of SO_2 of less than 55 metric tons/day (t/d) between 23 Nov. 2011 and 13 May 2012, and less than 156 t/d between 23 and 25 May 2015, if a release is steady.

Kilauea (Hawaii) and Masaya (Nicaragua) volcanoes are considered as terrestrial analogs to the Tharsis volcanoes (Mouginis-Mark et al. 2007), with an average SO_2 emission rate of 1650 t/d for Kilauea (Elias & Sutton 2012), and 1100 t/d for Masaya (William-Jones et al. 2003). Average values for the measured SO_2 outgassing rates (t/d) for some Earth volcanoes compared to our derived upper limits on the rate for Mars are presented in Table 5.1.

Table 5.1 Average values for the measured SO_2 outgassing rates for some Earth volcanoes compared to our derived rate for Mars.

Volcano	Average SO_2 flux (metric tons/day)	Period over which the measurements were obtained	Reference
This work for Mars using the CSO	≤ 55	assuming constant outgassing 23 Nov. 2011-13 May 2012	Khayat et al. (2015)
This work for Mars using the JCMT	≤ 156	assuming constant outgassing 23 May 2014- 25 May 2014	
Kilauea (Hawaii)	1650	1979-2010	Elias & Sutton (2012)
Masaya (Nicaragua)	1100	1993-2001	William-Jones et al. (2003)
Nyamuragira (Congo)	≥ 2600	1979-2005	Bluth & Carn (2008)
Sierra Negra (Ecuador)	11	July 2006	Barrancos et al. (2008)
Erebus (Antarctica)	46	2h on 26 Dec. 2006	Boichu et al. (2010)
Erta 'Ale (Ethiopia)	60	1h on 15 Oct. 2005	Sawyer et al. (2008)

If we assume that perhaps there is still active volcanism within the crust, then measuring SO_2 fluxes is not only a good indicator for volcanic activity, but it also serves in estimating the amount of the magma that degassed the SO_2, if all the sulfur dioxide originates from

the magma (Andres et al. 1991; Kazahaya et al. 1994). The mechanism for releasing SO_2 is described by the *Poiseuille* flow model (Kazahaya et al. 1994), occurring at the upper part of the magma body, where the magma transport is driven by buoyancy. The difference in density between the non-degassed, lower density magma, and the degassed, higher density magma, drives the former to ascend in the inner part of the conduit, and the latter to descend in the outer part (Kazahaya et al. 1994). The non-degassed magma, when reaching the top of the magma body, releases the SO_2. The mass rate of magma degassing Q (kg/s) is related to the outgassed SO_2 flux by (Kazahaya et al. 1994):

$$Q = \frac{M_S Q_{SO_2}}{M_{SO_2} \Delta C_S} \tag{5.3}$$

where Q_{SO_2} is the outgassing rate of SO_2 (kg/s), M_S and M_{SO_2} are the molar weights for S and SO_2, respectively, and ΔC_S is the sulfur content of the degassing magma. Theoretical models by Gaillard & Scaillet (2009) denote values of 600-900 ppm (average 750 ppm) for the sulfur content in the mantle of Mars.

With our retrieved upper limit for SO_2 of 55 t/day (0.64 kg/s) at the CSO, and a density of 2600 kg/m^3 for the basalt magma (Spera 2000), the upper limit on the mass rate of magma that is able to degas SO_2 is 37 kilotons/day (425 kg/s), or 12,000 m^3/day (0.14 m^3/s). With our retrieved upper limit for SO_2 of 156 t/day (1.8 kg/s) at the JCMT, the upper limit on the mass rate of magma that is able to degas SO_2 is 104 kilotons/day (1,200 kg/s), or 40,000 m^3/day (0.46 m^3/s).

Wilson et al. (2001) estimated the mean amount of magma supply rate for Olympus, Ascraeus, Pavonis and Arsia Montes in Tharsis. By dividing the total volume of magma released onto the surface of Mars during several volcanic activities between $\sim$ 3.3 Gyr and 0.3 Gyr, by the lifetime of 1 Gyr of continuous activity (error by a factor up to 3), the mean magma supply rate is 0.05 m^3/s. As a comparison, this number is consistent with our derived upper limits for the magma supply rate of 0.14 m^3/s and 0.46 m^3/s.

Leshin et al. (2013) reported the presence of SO_2 and H_2S among the evolved gases when heating samples (up to ∼1108 K) of the Rocknest aeolian deposit at the site of the Mars Curiosity Rover. A possible origin of these sulfur species is the breakdown of S bearing minerals trapped in the solid phase. This suggests that the release of SO_2 and H_2S is possible at high temperatures, a characteristic of volcanic events.

Even more so, volcanic sulfate aerosols ($SO_4{}^{2-}$), when formed from the oxidation of SO_2, are globally dispersed across the atmosphere of Mars before being deposited over a global or hemispheric scale, could account for the surficial soil's sulfur content (3-4 wt%) at the Viking lander sites (Settle 1979; Mouginis-Mark et al. 1992).

Along with establishing an upper limit on SO, our current limits on H_2S and OCS are a significant improvement over previous limits. They limit the presence of major current outgassing events on Mars, and put constraints on the photochemistry in the martian atmosphere.

The best abundance limits (2σ) for the sulphuretted species on Mars in this work are presented in Table 5.2.

Table 5.2 : Best abundance limits (2σ) for the sulphuretted species on Mars in this work, compared to previous ones.

Molecule	This Work (ppbv)	Previous (ppbv)
SO_2	< 1.1	< 0.3 (in the IR) Krasnopolsky (2012) and Encrenaz et al. (2011) < 2.0 (in the submm), Nakagawa et al. (2009)
H_2S	< 1.3	< 20 (in the millimeter), Encrenaz et al. (1991)
SO	< 0.7	-
OCS	< 0.8	< 14 (in the IR), Maguire (1977) < 70 (in the millimeter), Encrenaz et al. (1991)

5.2 SO_2/CH_4 ratio and its Implication Regarding the Methane Release in 2003

Mumma et al. (2009) were able to determine the patch size on Mars over which the methane was released. The inferred total amount of methane, when spread uniformly across the planet, leads to a global upper limit on the mixing ratio of 6 ppbv.

CSO observations:

Our upper limit on SO_2 of 1.1 ppbv with the CSO in 2012 corresponds to a total mass of 40 kilotons of SO_2 uniformly distributed across the atmosphere of Mars. In Earth's volcanoes, the amount of SO_2 released is $1 - 10^5$ times that of CH_4 (Delmelle & Stix 2000).

In the case of a **one-time** outgassing event of SO_2 at the time when Mumma et al. (2009) detected methane, then the amount of SO_2 should decay exponentially with the lifetime of 2 years between 2003 and 2012. After 9 years, in 2012, only 1% of the original SO_2 should be left. This upper limit of 40 kilotons in 2012 corresponds to 3,600 kilotons of SO_2 back in 2003. Using the SO_2/CH_4 ratio in terrestrial volcanoes, the measured 42 kilotons of methane by Mumma et al. (2009) are within the expected range, therefore it is consistent with a volcanic origin, and we cannot rule out a non-volcanic origin of the observed methane in 2003.

In the case of a **steady-state** outgassing of SO_2 and an estimated lifetime of 2 years (Wong et al. 2003, 2004, 2005; Krasnopolsky 2005), the total abundance of SO_2 in the atmosphere should be invariant and globally distributed as shown in equation (5.2), between 2003 when Mumma et al. (2009) detected CH_4 and 2012 when we made the CSO observations.

With a constant outgassing of SO_2 below our detection limit of 1.1 ppbv, and when assuming volcanic SO_2/CH_4 ratios, one would expect 0.01 pptv (parts per trillion) to 1.1 ppbv of methane to be released in 2003, if outgassed solely from volcanoes. The expected methane abundance is then lower than what was measured (6 ppbv), and so the methane

released could not have a (mainly) volcanic origin, if it was released in a steady state.

JCMT observations:

Our results from the JCMT confirm the conclusions made by the CSO results in regards to the methane release in 2003.

In the case of a **one-time** outgassing event of SO_2 at the time when Mumma et al. (2009) detected methane, then after 11 years, only 0.4 % of the original SO_2 should be left. This upper limit of 114 kilotons in 2014 corresponds to 28,000 kilotons of SO_2 back in 2003. The detected 42 kilotons of methane are within the expected range, and therefore our SO_2 limit of 2014 does not allow to differentiate the origin of the observed CH_4 when considering sporadic release.

If we assume **steady-state** outgassing of SO_2 at the time when Mumma et al. (2009) detected CH_4, then we would expect 0.03 pptv - 3.1 ppbv of methane, if outgassed solely from volcanoes. The expected abundance is then lower than what was measured (6 ppbv), and thus the methane released could not have a mainly volcanic origin, if it was released in a steady state.

Earlier search for SO_2 by Krasnopolsky (2005, 2012), 3 months (June 2003) after the methane release (March 2003) came out unsuccessful, and a stringent limit of 0.3 ppbv (11 kilotons) was established. When considering either a **one-time** or a **steady-state** outgassing events of SO_2, the expected methane amount in March 2003 is smaller than the one observed by Mumma et al. (2009), and therefore the CH_4 could not be of (mainly) volcanic origin when assuming terrestrial SO_2/CH_4 outgassing ratios.

Webster et al. (2015) confirmed the presence of transient spikes of methane between mid and late Northern spring on the red planet, with a mean abundance value of 7.19 ± 2.06 ppbv ($\pm$95 % Cl) between 29 November 2013, and 28 January, 2014, but the methane spikes have not persisted.

They presented the methane abundance ratios around the Curiosity rover at Gale crater (4.5°S, 137.4°E). In contrast to Mumma et al. (2009), the geographic patch over which

the detected methane abundance is measured could not be specified. The global mixing ratio of methane would almost certainly be much smaller than the ∼7 ppbv. This is a disadvantage that localized observations from rovers on Mars present in terms of probing atmospheric constituents, when compared to orbiters or ground-based telescopes that could simultaneously map several extended regions on Mars. Furthermore, around the methane spikes, a mean background level of atmospheric methane of 0.69 ± 0.25 ppbv was found by Webster et al. (2015), and it is less than 7 ppbv.

Given how probable the outgassing from a local source is, the local abundance ratio of methane during the spikes (∼7 ppbv) by Webster et al. (2015) is not representative of the whole planet, and one could not draw conclusions on a volcanic origin of the methane released.

5.3 Future Observations with iSHELL on the NASA IRTF

The next generation of high-resolution spectrographs on the IRTF is iSHELL. The instrument is a 1.15 to 5.4 μm high-resolution immersion grating spectrograph, and is expected to have its first light by 2016. It is a replacement for CSHELL (described in Chapter 4). CSHELL, a single order spectrograph with a small simultaneous wavelength coverage of 0.006 μm at 2.2 μm, provides a spectral resolving power $\leq$ 43,000, and uses a single 256×256 InSb array (Tokunaga et al. 1990; Greene et al. 1993). In that regard iSHELL is a game changer. It is a cross-dispersed spectrograph, combined with a Teledyne 2048×2048 Hawaii 2RG (H2RG) array. It provides 20-100 times larger simultaneous wavelength coverage which allows the whole OCS band to be sampled simultaneously (Rayner et al. 2012). iSHELL offers a 70,000 resolving power that allows distinguishing narrower and weaker lines in the martian atmosphere, and separating them from their telluric counterparts.

Depending on the angular size of Mars at the time of the observations and iSHELL's slit length, represented as 5 arsec at the JHK modes, 15 arcsec at the LM modes, and 25

arcsec at 3.8-4.2 μm (Rayner 2015), one could make decisions on whether to nod "on" or "off" slit. Nodding "on" slit is conducted by having Mars' disk in both the A and B beam positions on the detector. This allows maximum efficiency in collecting data from the planet that is observed twice, instead of one time during "off" slit nodding. The same observing techniques described in Chapter 4 will be followed regarding positioning the spectrometer's slit on the N-S central meridian of Mars, and scanning the volcanic regions under the slit when the planet is rotating.

The right observing mode that samples OCS at its combination band (ν_1+ν_3) at 3.42 μm (2924 cm^{-1}) on iSHELL is L4 that simultaneously covers 3.28 to 3.67 μm. Figure 5.2 shows the L4 mode covering several wavelength orders (Rayner 2015). The rectangular box indicates the orders that are projected onto the detector's array. At L4, the slit length is 15 arcsec and therefore we recommend nodding Mars "off" slit when observing. Figure 5.3 shows the P and R branches of the OCS ν_1+ν_3 band at orders #149, 150 and 151 of the L4 setting with iSHELL. The OCS spectrum (blue) is modeled using our own radiative transfer code for Mars (IRRTM in Chapter 4). The spectrum is shown at rest frequency, for a mixing ratio of 10 ppbv for OCS in the martian atmosphere, and at a total airmass on Mars of 3.0. As a comparison, the area in pink is the spectral coverage by CSHELL at the setting centered at 3.418 μm that we used for looking for OCS on Mars in Chapter 4. The Earth's transmittance (in black) at 1.6 mm PWV and airmass 1.0 has been generated using ATRAN software (Lord 1992). The Earth's transmittance and the OCS spectrum are convolved to a resolving power R= 70,000 when considering a slit width of 0.375 arcsec for iSHELL.

5.3.1 Predicted Sensitivity Limits (ppbv)

Using equation 2.2 in Chapter 2 in order to calculate the minimum detectable mixing ratio for OCS, and by choosing the R22 transition at 3.4171 μm (2926.46 cm^{-1}) with $S_{R22} = 1.63 \times 10^{-20}$ cm^{-1}/cm^{-2} and at SNR= 300 (96 minutes integration time), an upper limit of 38 ppbv (1σ) for OCS could be achieved, with a corresponding equivalent

width of 13.9 $\times 10^{-5}$ cm^{-1}. The crucial advantage that iSHELL provides over CSHELL is that it allows a simultaneous coverage for the OCS band (Figures 5.2 and 5.3), allowing unprecedented sensitivities as compared to CSHELL that has a smaller spectral coverage shown in pink in Figure 5.3. The slicing of the residual spectra, after removing the solar and telluric contributions to the spectrum of Mars, around each line transition of OCS, then their co-addition increases the sensitivity of the mixing ratio by a square-root factor of the number of transitions. On average, just by eyeballing the clean spectral regions in orders 150 and 151 in Figure 5.3, the number of transitions that could be co-added is $\sim$ 40.

The signal-to-noise ratio (SNR) per pixel is given by the fundamental equation:

$$SNR = \frac{Sgt}{\sqrt{Sgt + Bgt + Dt + r^2}} \tag{5.4}$$

where S is the source counts (ADU/s), g is the gain of the detector array (2 e$^-$/ADU), t is the integration time (s), B is the background counts (ADU/S), D is the read noise (5 e$^-$ RMS), and r is the dark current (= 0.1 e$^-$/s). At 3.6 μm, the sky and telescope background are estimated to 1 e$^-$/s/pixel (Rayner et al. 2012).

When using a slit width of 0.375 arcsec, the resolving power is 70,000. The corresponding spectral resolution of 0.042 cm^{-1} covers 3 pixels on the detector, with 0.125 arcsec each. For a one-hour integration time, and a total spectral radiance from Mars (including solar reflected radiation) of 8.59 $\times 10^{-14}$ erg/s/cm^2/arcsec^2, the SNR per pixel is 240. The expected (1σ) detection limit for one hour integration time, when co-adding 40 transitions (Figure 5.3) of OCS is 7 ppbv.

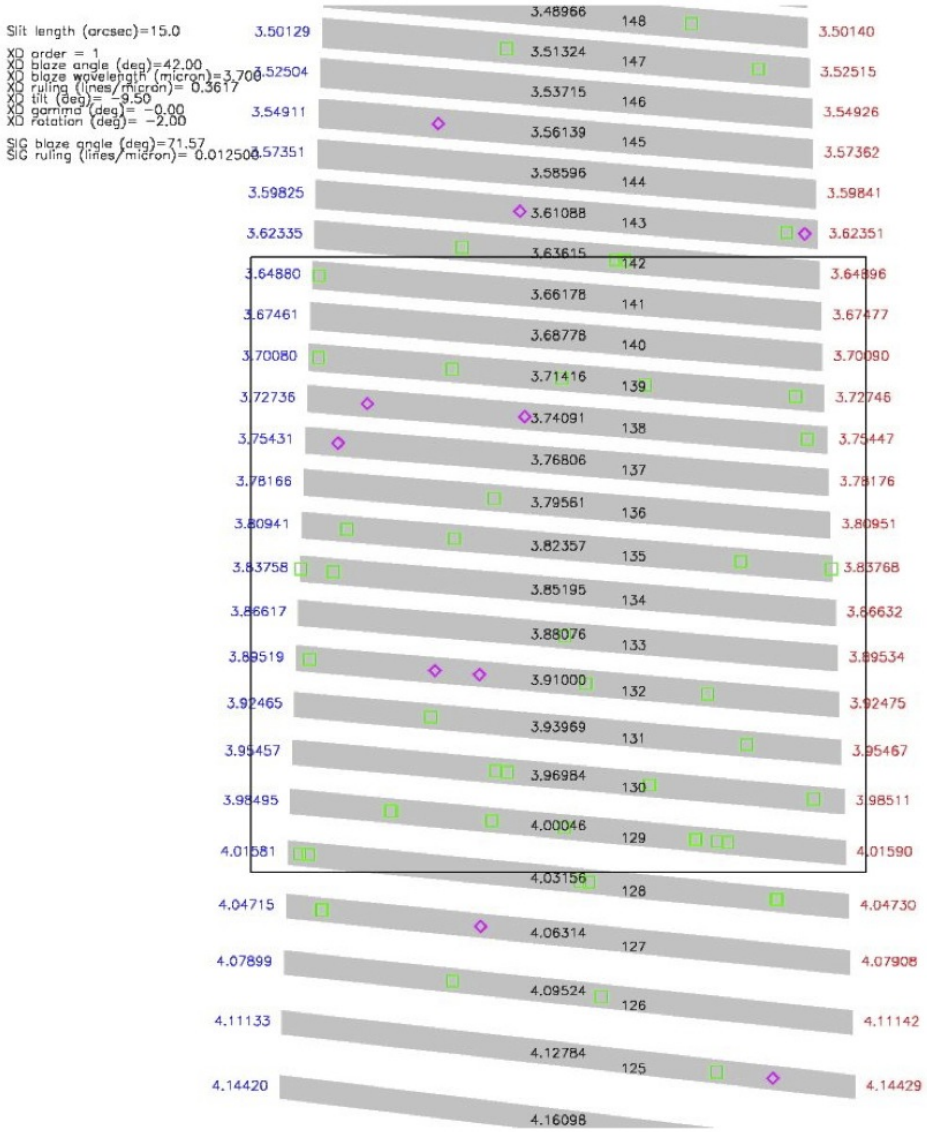

Figure 5.2 : This figure shows the L4 setting covering several wavelength orders (Rayner 2015). The rectangular box indicates the orders that are projected onto the detector's array. Image credit: IRTF.

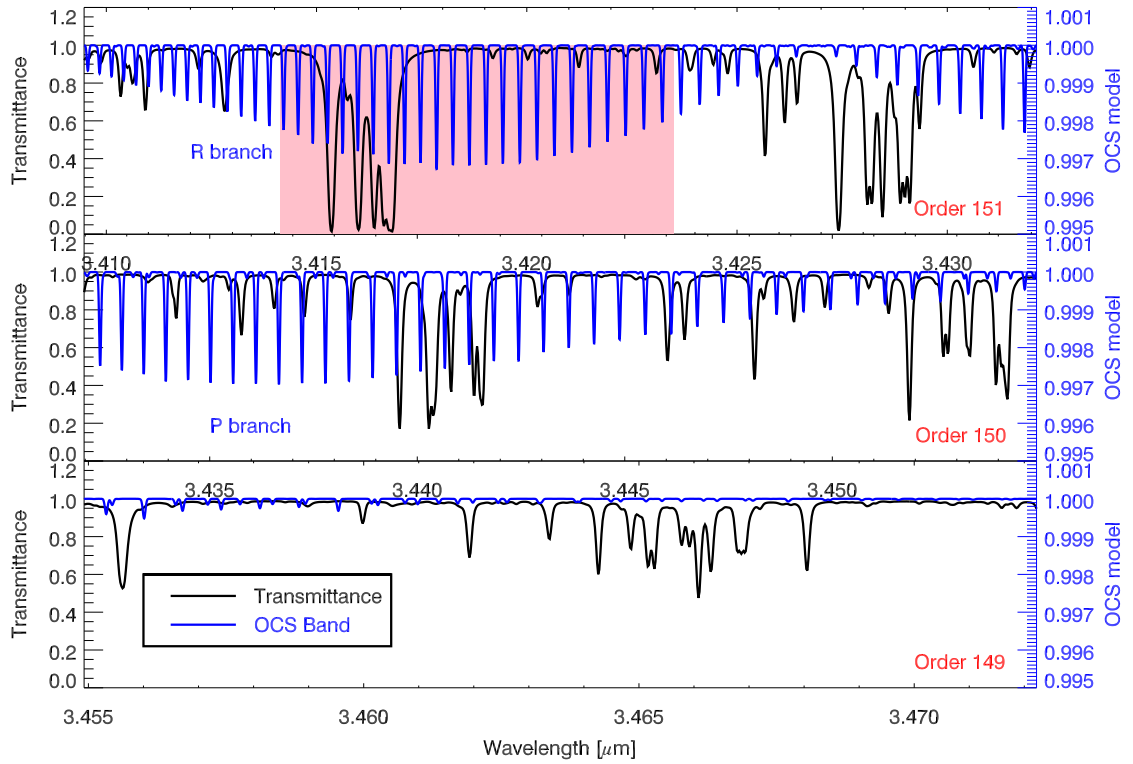

Figure 5.3 : This figure shows the P and R branches of the OCS $\nu_1+\nu_3$ band at orders #149, 150 and 151 of the L4 setting with iSHELL. The OCS spectrum (blue) is modeled using our own radiative transfer code for Mars (IRRTM). The spectrum is shown at rest frequency, a mixing ratio of 10 ppbv for OCS in the martian atmosphere, and at a total airmass on Mars of 3.0. The Earth's transmittance is shown in black. The Earth's transmittance and the OCS spectrum are convolved to a resolving power R= 70,000. For comparison, the box in pink shows the wavelength coverage of CSHELL at the same frequency setting.

5.4 Future Observing Strategies with the Atacama Large Millimeter Array (ALMA)

Our multi-species survey at two different seasons on Mars took advantage of a high spectral resolving power to look for major outgassing across the disk of the planet, but there are limitations to what single dish antennae could offer in terms of spatial resolution. The next step would be to spatially resolve the planet using the Atacama Large Millimeter Array (ALMA) and be able to search for localized and temporal outgassing events. Since SO_2 is the strongest indicator for volcanic outgassing as it is the most abundant among the other sulfur species in terrestrial analog volcanoes (Symonds et al. 1994), a good strategy would be to only target SO_2 at the sub-millimeter at different locations and seasons on Mars. The detection of atmospheric SO_2 would be a powerful indicator to trigger the search for H_2S, OCS and SO.

ALMA is an interferometer system consisting of an array of 12 and 7-m antennae located on the Chajnantor Plateau in the Chilean Andes. It samples the sky at different observing windows between 3 mm to 400 μm (84 to 720 GHz). With its most extended configuration, using the 12-m antennae at a 16 km baseline, it could reach spatial resolutions in the sky ranging between 6 milli-arsec at 675 GHz and 37 milli-arsec at 110 GHz [a]. For an extended source like Mars, the minimum achievable spatial resolution (in arcsec and km on Mars) when using a certain array configuration, is discussed in section 5.4.3.

5.4.1 Achievable Sensitivities

For an interferometer system, the achievable RMS fluctuation in the flux density per synthesized beam [Jy/beam] is given by the standard equation (Wilson et al. 2009):

$$S_{rms} = \frac{2k_B T_{sys}}{\eta_q \eta_c A_{eff} \sqrt{N(N-1) n_p \Delta_\nu t_{int}}} \tag{5.5}$$

[a] https://almascience.nrao.edu/about-alma/alma-basics

where k_b is the Boltzmann constant, T_{sys} is the system temperature, η_q (= 0.96) is the quantization efficiency, η_c (= 0.88) is the correlator efficiency, A_{eff} is the effective area of the antenna, N is the number of antennae in the array (N= 36 for the 12-m array), n_p is the number of polarizations (1 or 2 for single and dual, respectively), $\Delta\nu$ is the spectral resolution and t_{int} is the total integration time on source.

For observations during the ALMA Cycle 3 (October 2015 to September 2016.)[b], the different values for the parameters that go into the sensitivity calculations are explained in the document "ALMA Technical Handbook" [c]. The targeted SO_2, H_2S, SO and OCS transitions are covered under the "Band 7" as specified by ALMA, between 275 and 373 GHz (0.80 - 1.09 mm), and therefore throughout this section, all the sensitivities are estimated at the same band.

A_{eff}, the effective area of the antenna depends on the geometric area A and the aperture efficiency η_{ap} ($\mathrm{A_{eff}} = \eta_{\mathrm{ap}} \times \mathrm{A}$). The Ruze formula (Kiedron et al. 1986) for the aperture efficiency is $\eta_{\mathrm{ap}} = \mathrm{R_0} \exp(-16\pi^2\sigma^2/\lambda^2)$, where λ is the observing wavelength, σ is the rms surface accuracy of the antenna, and $\mathrm{R_0}$=0.72. At band 7 (345 GHz) and surface rms σ= 25 μm for the 12-m antenna, η_{ap}= 0.63.

At the 345 GHz range, the receiver at ALMA is a dual side band receiver (2SB), enabling the separation of the signals from the side bands simultaneously. Therefore, the system temperature is given by the equation[c]:

$$T_{sys} = \frac{T_{rx} + \eta_{eff} T_{sky} + (1 - \eta_{eff}) \times T_{amb}}{\eta_{eff} e^{-\tau_0 sec(z)}} \tag{5.6}$$

where T_{rx}(= 75 K) is the receiver noise temperature, η_{eff} (= 0.95) is the forward efficiency, $T_{sky} = T_{atm}(1 - e^{-\tau_0 sec(z)})$ is the sky temperature at atmospheric opacity $\tau = \tau_0 sec(z)$ at zenith angle (z). The expected atmospheric opacity at zenith is based on years of sky monitoring at the ALMA site[c], and is divided into 7 octiles, with 0.472 mm of PWV for 12.5% of the time for octile 1, 0.658 mm for 25% of the time for octile 2, and 0.913 mm on

[b]https://almascience.nrao.edu/proposing/call-for-proposals
[c]https://almascience.nrao.edu/documents-and-tools/cycle3/alma-technical-handbook

37.5% of the time for octile 3. T_{atm} is the physical temperature of the atmosphere. T_{amb} is the ambient noise temperature from the physical ambient temperature (270 K) caused by the emission from the ground and the telescopes themselves. For example, at 345 GHz and sky conditions of octile 3, τ_0= 0.158, and the system temperature towards zenith is T_{sys}= 155 K.

At Rayleigh-Jeans limit, the flux density, integrated over the solid angle Ω, is related to the brightness temperature using the following fundamental equation:

$$S_\lambda = \frac{2k_B T_B \Omega}{\lambda^2} \tag{5.7}$$

where the synthesized beam's solid angle $\Omega = \frac{\pi {\theta_{res}}^2}{4\ln 2}$, and θ_{res} is the spatial resolution. The conversion from the RMS fluctuation in flux density into brightness temperature T_{rms} is arranged in the following equation[c]:

$$\left(\frac{T_{rms}}{1K}\right) = \left(\frac{S_{rms}}{1Jy}\right)\left[13.6\left(\frac{300GHz}{\nu}\right)^2\left(\frac{1''}{\theta_{max}}\right)\left(\frac{1''}{\theta_{min}}\right)\right] \tag{5.8}$$

5.4.2 Correlator Tuning (Spectral Setup)

In order to specify the tuning parameters for the spectroscopic transitions of the candidate molecules in the martian atmosphere, ALMA provides a spectral visual editor under the "ALMA Observing Tool"[d] (hereafter OT). When selecting different line transitions, OT automatically provides the best Local Oscillator (LO) frequency to include all the candidate transitions in the spectral window, and avoids regions of poor atmospheric transmission at either sidebands where the signal is coming from; lower and upper side bands (LSB/USB). Poor atmospheric transmission degrades the sensitivity by increasing the system temperature.

The correlator at the spectral setup #1 in Figure 5.4 indicates an LO frequency of 340.2 GHz, with the SO_2 and CO transitions falling in the USB. We have chosen a

[d]https://almascience.nrao.edu/proposing/observing-tool

spectral window with a bandwidth of 234.375 MHz (203 km/s) and a spectral resolution of 122.070 KHz (0.106 km/s) to look for SO_2 at 346.652 GHz. The velocity resolution v = 0.1 km/s is sufficient to resolve the martian lines. The CO line at 345.796 GHz is wide (see Figures 3.11 and 3.20 in Chapter 3), and we therefore chose a larger bandwidth 468.750 MHz (406 km/s) that covers the line, and a spectral resolution of 244.141 KHz (0.212 km/s). Inverting the CO spectral line is intended to extract the temperature profiles across the disk of Mars, when seen by ALMA's synthesized beam at sub-arcsecond spatial resolutions.

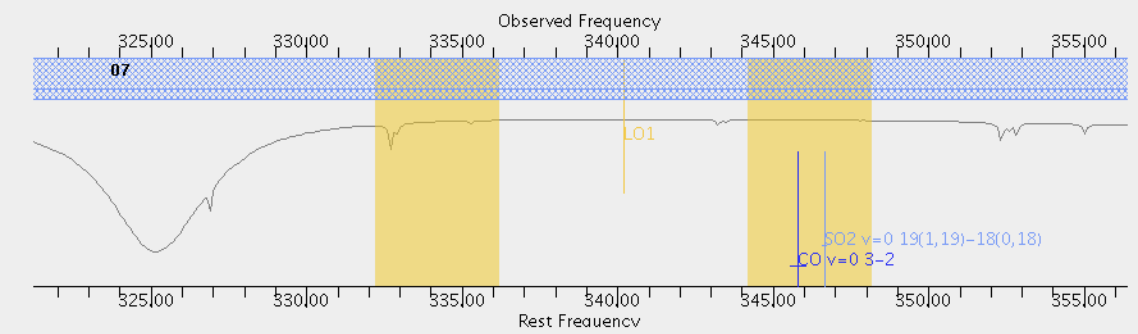

Figure 5.4 : Representative spectral windows (yellow) at the upper (right) and lower (left) side bands of the dual side band receiver at band 7, for spectral setup #1. The yellow vertical line shows the LO frequency at 340.2 GHz. The SO_2 and CO transitions lie in the USB. The Earth's atmospheric transmittance is represented by the curved purple line. The spectral windows and the tuning parameters have been simulated using the spectral visual editor, provided by ALMA's OT. Image credit: ALMA.

The correlator at the spectral setup #2 in Figure 5.5 indicates an LO frequency of 306.8 GHz, with the H_2S, OCS and SO transitions falling in the LSB. We have chosen a spectral window with a bandwidth of 234.375 MHz (234 km/s) and a spectral resolution of 122.070 KHz (0.122 km/s) to look for H_2S at 300.505 GHz. For the OCS and SO at 303.993 GHz and 304.077 GHz, respectively, we have chosen a bandwidth of 234.375 MHz (231 km/s) and a spectral resolution of 122.070 KHz (0.120 km/s) to look for them. The spatial resolution offered by ALMA has favored the search for OCS in the sub-millimeter over the near infrared at 3.42 μm, especially that we are now able to conduct a simultaneous search

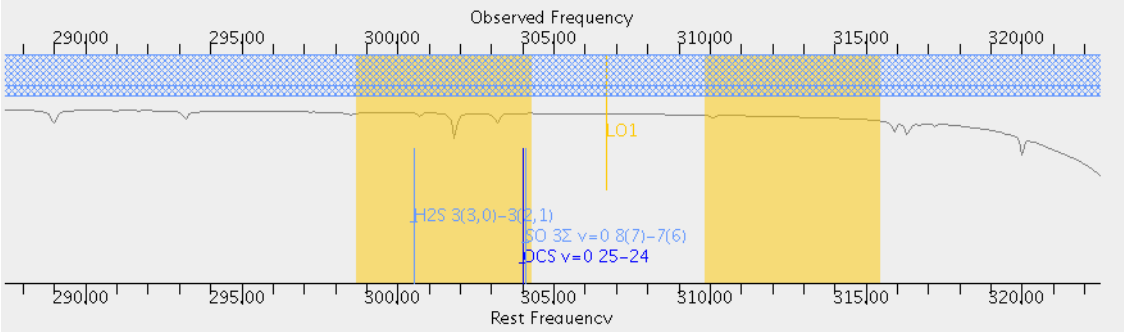

Figure 5.5 : Representative spectral windows (yellow) at the upper (right) and lower (left) side bands of the dual side band receiver at band 7, for spectral setup #2. The yellow vertical line shows the LO frequency at 306.8 GHz. The H_2S, OCS and SO transitions lie in the LSB. The Earth's atmospheric transmittance is represented by the curved purple line. The spectral windows and the tuning parameters have been simulated using the spectral visual editor, provided by ALMA's OT. Image credit: ALMA.

for H_2S, OCS and SO under one frequency setting with ALMA, and that's an additional major improvement over the CSO and the JCMT capabilities.

5.4.3 Array Configuration and Observing Strategy

For extended sources such as Mars, it is critical to define the correct baseline ranges, in order to gather between the spatial resolution and collecting enough flux from the planet. Interferometers display the components of the Fourier transform of the brightness distribution of celestial objects under a certain area in the $u - v$ plane as dictated by the baseline of the array[c]. When a large-scale source with a uniform brightness temperature is observed with an interferometer, it will have large amplitudes only up to a certain baseline range. If we increase the baseline, then the array will not be sensitive to emissions from such an extended source and it will filter the information out. This phenomenon is known as the spatial scale filtering.

The maximum recoverable scale $\theta_{\rm MRS}$ as adopted by ALMA is given by the following equation:

$$\theta_{MRS} \approx \frac{37100}{L_{min}\nu}[arcseconds] \tag{5.9}$$

where L_{min}[m] is the shortest baseline at a specified array configuration, and ν is the frequency in GHz.

For the same beam configuration, the angular resolution achieved $\theta_{\rm res}$ is given by the following equation adopted for ALMA:

$$\theta_{res} \approx \frac{61800}{L_{min}\nu}[arcseconds] \tag{5.10}$$

where L_{max}[m] is the longest baseline in the array configuration, and ν is the frequency in GHz.

The best array configurations to choose for Mars are the ones that will take advantage of a small angular resolution while conserving the brightness from Mars. The all 12-m array configurations C36-1 and C36-2 from cycle 3 are considered. For C36-1, L_{min} and L_{max} provided by ALMA are 14.7 m and 160.7 m, respectively, and they correspond to $\theta_{\rm MRS}$= 7.3 arccsec and $\theta_{\rm res}$= 1.0 arccsec, at band 7. For C36-2, L_{min} and L_{max} provided by ALMA are 14.7 m and 376.9 m, respectively, and they correspond to $\theta_{\rm MRS}$= 7.3 arccsec and $\theta_{\rm res}$= 0.5 arccsec, at band 7.

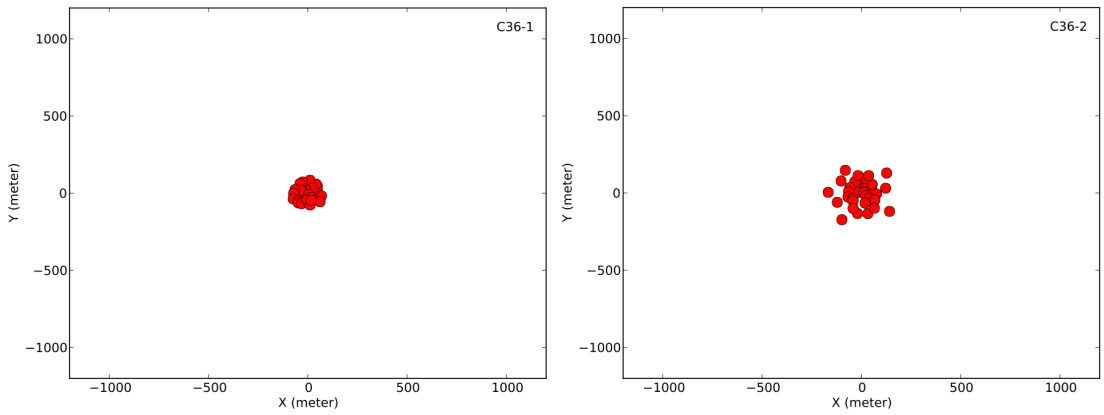

Figure 5.6 : The C36-1 and C36-2 array configurations of the 12-m antennae for sampling Mars with spatial resolutions of 1.0 and 0.5 arcsec, respectively. The array configurations have been simulated by ALMA, and the two images were provided by the "ALMA Technical Handbook"[c] (page 84). Image credit: ALMA.

The maximum recoverable scale for both array configurations is 7.3 arcsec, and therefore we pick a date when Mars' angular size is $\leq \theta_{\rm MRS}$. For example, on November 15 UT, 2016, the angular diameter of Mars is 7 arcsec. At the frequency of the SO_2 transition at 346.652 GHz, the 12-m antenna beam size (HPBW) is 16.75 arsec, 2.4 times the size of Mars.

The sensitivity is not uniform across the primary beam; it decreases away from the beam center all the way to the edges. In order to compensate for that, ALMA offers the capability of mosaic pointing. By setting up several pointing configurations within a rectangular field, a more-or-less uniform sensitivity across the target is obtained. In Figure 5.7 we present two pointing scenarios: individual and mosaic. The left panel shows the individual pointing setting where the disk of Mars (inside the dashed-green circle) is completely covered by the 12-m primary antenna beam (circle in red). The right panel shows a rectangular field around the disk of Mars for mosaic pointing, where the "spatial editor" [e] from ALMA suggests one mosaic pointing. The spacing between two pointings is set to Nyquist sampling, with spacing = 0.48113 time the antenna beam size. The spacing is 8.08 arcsec, larger than the rectangular field (or the size of Mars), thus the reason why ALMA has picked up one mosaic pointing. In the case of Mars, single pointing is enough, since the source is about within 1/3 of the primary beam as specified by ALMA[e], therefore preserving a more-or-less uniform sensitivity across the disk of Mars.

Returning back to sensitivities, we have chosen two spectral setups, # 1 and # 2, as presented in Figures 5.4 and 5.5. SO_2 is covered under the first setup, whereas H_2S, OCS and SO are covered under the second one. In order to check the total time for science goal by ALMA, we tested two spatial resolutions $\theta_{\rm res} = 0.5$ ($\sim$500 km on Mars) and 1.0 arcsec ($\sim$1000 km). At the 3^{rd} octile (0.913 mm PWV), Table 5.3 presents the achievable sensitivities and 1σ upper limits (in ppbv) on the sulfur-bearing species per synthesized beam, and integrated over the disk of Mars (in pptv). The total integration times on-source

[e]https://almascience.nrao.edu/documents-and-tools/cycle3/alma-ot-quickstart

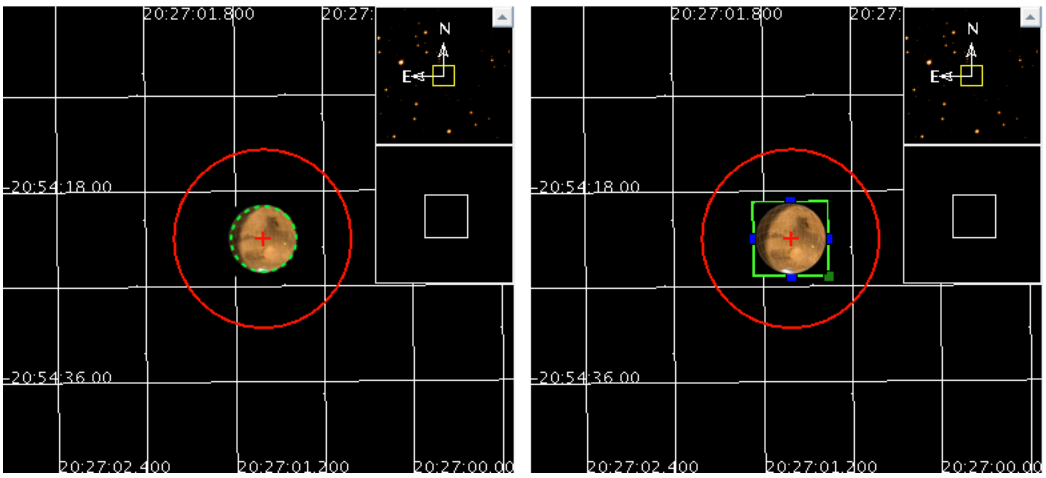

Figure 5.7 : The left panel shows the individual pointing setting where the disk of Mars (inside the dashed-green circle) is completely covered by the 12-m primary antenna beam (circle in red). The right panel shows a rectangular field around the disk of Mars for mosaic pointing, the "spatial editor"[e] from ALMA suggests one mosaic pointing. The spacing between two pointings is set to Nyquist sampling, with spacing = 0.48113 × of the antenna beam size. The spacing is 8.08 arcsec, larger than the rectangular field (or the size of Mars), thus the reason why ALMA has picked up one mosaic pointing. Image credit: ALMA.

were calculated using equation 5.5, and checked against the "ALMA sensitivity Calculator" [f]. The calibration time and other overhead times are provided by ALMA.

In spectral setup # 2 we are targeting 3 molecules at one time, and therefore the total time is the time to observe the 3 transitions altogether, unlike in setup # 1, where we are looking for one molecule (SO_2). Within few hours, ALMA could achieve at least one order of magnitude better sensitivities over the disk of Mars, when compared to single dish antennae the size of the CSO and JCMT.

For example, for a 1 hour on-source integration time with Mars' angular size of 7 arcsec, the CSO could achieve disk-averaged upper limits at 1σ of 4.7 ppbv, 4.0 ppbv and 1.0 ppbv, for SO_2, H_2S and SO, respectively. ALMA could achieve the same sensitivities, integrated over the whole disk of Mars, in 1.63 s, 1.1 s and 1.13 s on-source integration times, for SO_2, H_2S and SO, respectively. This is at least one order of magnitude enhancement in the on-source integration time. The down side with ALMA is the overhead time. Even though

[f] https://almascience.eso.org/proposing/sensitivity-calculator

Table 5.3 Sensitive upper limits at 1σ on the sulfur-bearing species, as achieved by ALMA.

Spectral setup	Molecule	θ_{res} [$''$]	On-source Time	Calibration Time	Remaining overhead Time	Total Time	S_{rms} [mJy]	T_{rms} [mK]	Upper limit [ppbv] per synthesized beam	Upper limit [pptv] Disk integrated
#1	SO_2	1.0	2.04 hr	1.67 hr	0.36 hr	4.07 hr	4.65	47.33	0.5	71
#2	H_2S	1.0	1.00 hr	1.04 hr	0.23 hr	2.27 hr	5.55	75.18	0.5	71
	OCS								1.0	144
	SO								0.13	19
#1	SO_2	0.5	1.37 d	1.1 d	5.04 hr	2.68 d	1.16	47.33	0.5	35
#2	H_2S	0.5	15.7 hr	11.5 hr	2.57 hr	1.25 d	1.39	75.18	0.5	35
	OCS								1.0	72
	SO								0.13	9

the on-source integration times are extremely short, the overhead time is 32 minutes on each of these molecules, if observed independently. A good strategy when observing with ALMA is including as many lines as nature could provide for the science goal under one spectral window, and get a single overhead time at once for the group of all lines.

The total time to look for all the suggested sulfur species above with array configuration C36-2 ($\theta_{\rm res}$= 0.5 arcsec) is about 4 days, and that is a very long time. In contrast, using the compact array configuration C36-1 ($\theta_{\rm res}$= 1.0 arcsec), the total is a little bit over 6 hours. It is recommended to use array configuration C36-1.

Since SO_2 is the strongest indicator for volcanic outgassing, a good strategy is to spend the time only searching for it first. If detected, it would trigger observations with finer spatial resolutions, with ALMA pointed at the suspected regions of the SO_2 plumes, and targeting the other species as well.

5.5 Summary and Conclusion

We carried out the most comprehensive to date (2015), ground-based, semi-simultaneous, multi-band and multi-species search for sulphuretted gases (SO_2, H_2S, OCS and SO) above the Tharsis and Syrtis volcanic regions on Mars.

The submillimeter search extended between 23 November 2011 and 25 May 2014 which corresponded to Mars' mid Northern Spring and mid Northern Summer seasons (L_s = 34 - 135°) for Mars Years 31 & 32. The strong submillimeter rotational transitions of SO_2, H_2S and SO were targeted using the high-resolution (R $\sim$ 346,000) heterodyne receiver Barney on the 10.4-m single-dish antenna of the Caltech Submillimeter Observatory, and HARP at R $\sim$ 580,000 on the 15-m James Clerk Maxwell Telescope at Maunakea, Hawai'i.

Our submillimeter survey targeted SO_2, SO and H_2S at their rotational transitions at 346.652 GHz, 304.078 GHz and 300.505 GHz, respectively. No active release was detected, and we infer 2σ upper limits across the disk of the planet using the CSO of 1.1 ppbv,

0.7 ppbv and 1.3 ppbv for SO_2, SO and H_2S, respectively. Using the JCMT, we infer a 2σ upper limit of 3.1 ppbv on SO_2.

The infrared search covered OCS in its combination band ($\nu_1+\nu_3$) at 3.42 μm (2924 cm^{-1}) at similar Mars years, during Mars' late Northern Spring and mid Northern Summer seasons, spanning L_s= 43° and L_s= 145°. The targeted volcanic districts were observed during the two intervals, 15 Dec. 2011 to 6 Jan. 2012 in the first year, and 30 May 2014 to 13 June 2014 in the second year, using the high resolution infrared spectrometer CSHELL at R= 43,000 on the 3-m NASA Infrared Telescope Facility. The residual spectra of Mars show no absorption of atmospheric OCS. When co-adding the spectra over all the observing nights between Dec. 2011 and June 2014, we infer a 2σ upper limit of 0.8 ppbv on OCS.

By estimating methane abundances that could be released as a result of volcanic outgassing using the ratio of SO_2/CH_4 in terrestrial volcanoes, we conclude a non-volcanic origin for the methane released in 2003 if an ongoing outgassing of SO_2 occurred. In the case of a one-time outgassing event of SO_2 and CH_4 at the time when Mumma et al. (2009) detected methane, we cannot draw conclusions on the origin of the CH_4 released.

Our current upper limit using the CSO of 1.1 ppbv for SO_2 yields an outgassing rate of less than 55 tons/day. Compared to two terrestrial analogs, we would be able to detect any volcanic release that is more than 4% the size of Kilauea or one twentieth the size of the Masaya volcano. The mass rate of magma that is able to degas 55 tons of SO_2 per day is 37 kilotons of magma per day, or 12,000 m^3 per day (0.14 m^3/s). With our retrieved upper limit for SO_2 of 156 t/day at the JCMT, the upper limit on the mass rate of magma that is able to degas SO_2 is 104 kilotons/day, or 40,000 m^3 per day (0.46 m^3/s). As a comparison with our derived rates, the mean magma supply rate (uncertainty of a factor 3) that built Olympus, Ascraeus, Pavonis and Arsia Montes in Tharsis is 4320 m^3/day (0.05 m^3/s).

The non-detection of any of the sulfur compounds in the atmosphere of Mars indicates the absence of major volcanic outgassing, and our comprehensive search provides limits to the level of current volcanic activity in the crust of Mars.

Future observations with ALMA will take advantage of its unprecedented sensitivity at sub arc-second spatial resolutions on Mars. The interferometer's capabilities are outstanding. When compared to the CSO, it is able achieve the same disk-integrated sensitivity on the sulphuretted species, within at least an order of magnitude shorter integration time. Searching for temporal outgassing of these different species from localized sources on the planet will be then possible.

References

Andres, R. J., Rose, W. I., Kyle, P. R., de Silva, S., Francis, P., Gardeweg, M., & Moreno Roa, H. 1991, J. Volc. Geotherm. Res., 46, 323

Barrancos, J., Roselló, J., Calvo, D., Padrón, E., Melián, G., Hernández, P., Pérez, N., Millán, M., & Galle, B. 2008, in Terrestrial Fluids, Earthquakes and Volcanoes: The Hiroshi Wakita Volume III, ed. N. Pérez, S. Gurrieri, C.-Y. King, & Y. Taran, Pageoph Topical Volumes (Birkhäuser Basel), 115–133

Bluth, G. J. S. & Carn, S. A. 2008, Int. J. Remote Sens., 29, 6667

Boichu, M., Oppenheimer, C., Tsanev, V., & Kyle, P. R. 2010, J. Volc. Geotherm. Res., 190, 325

Delmelle, P. & Stix, J. 2000, in Encyclopedia of Volcanoes, ed. H. Sigurdsson (Academic Press, San Diego), 803–815

Elias, T. & Sutton, A. 2012, U.S. Geological Survey Open-File Report 2012-1107, Available online at http://pubs.usgs.gov/of/2012/1107/, 1

Encrenaz, T., Greathouse, T. K., Richter, M. J., Lacy, J. H., Fouchet, T., Bézard, B., Lefèvre, F., Forget, F., & Atreya, S. K. 2011, Astron. & Astrophys., 530, A37

Encrenaz, T., Lellouch, E., Rosenqvist, J., Drossart, P., Combes, M., Billebaud, F., de Pater, I., Gulkis, S., Maillard, J. P., & Paubert, G. 1991, Ann. Geophys., 9, 797

Gaillard, F. & Scaillet, B. 2009, Earth Planet. Sci. Lett., 279, 34

Greene, T. P., Tokunaga, A. T., Toomey, D. W., & Carr, J. B. 1993, in Society of Photo-Optical Instrumentation Engineers (SPIE) Conference Series, Vol. 1946, Infrared Detectors and Instrumentation, ed. A. M. Fowler, 313–324

Kazahaya, K., Shinohara, H., & Saito, G. 1994, B. Volcanol., 56, 207

Khayat, A. S., Villanueva, G. L., Mumma, M. J., & Tokunaga, A. T. 2015, Icarus, 253, 130

Kiedron, K., Chian, C. T., & Chuang, K. L. 1986, Telecommunications and Data Acquisition Progress Report, 88, 29

Krasnopolsky, V. A. 2005, Icarus, 178, 487

—. 2012, Icarus, 217, 144

Leshin, L. A., Mahaffy, P. R., Webster, C. R., Cabane, M., Coll, P., Conrad, P. G., Archer, P. D., Atreya, S. K., Brunner, A. E., Buch, A., Eigenbrode, J. L., Flesch, G. J., Franz, H. B., Freissinet, C., Glavin, D. P., McAdam, A. C., Miller, K. E., Ming, D. W., Morris, R. V., Navarro-Gonzalez, R., Niles, P. B., Owen, T., Pepin, R. O., Squyres, S., Steele, A., Stern, J. C., Summons, R. E., Sumner, D. Y., Sutter, B., Szopa, C., Teinturier, S., Trainer, M. G., Wray, J. J., Grotzinger, J. P., & MSL Science Team. 2013, Science, 341, 1238937

Lord, S. D. 1992, NASA Technical Memor., 103957

Maguire, W. C. 1977, Icarus, 32, 85

Mouginis-Mark, P. J., Harris, A. J., & Rowland, S. K. 2007, in The Geology of Mars (Cambridge University Press), 71–94

Mouginis-Mark, P. J., Wilson, L., & Zuber, M. T. 1992, The Physical Volcanology of Mars (Cambridge University Press), 424–452

Mumma, M. J., Villanueva, G. L., Novak, R. E., Hewagama, T., Bonev, B. P., DiSanti, M. A., Mandell, A. M., & Smith, M. D. 2009, Science, 323, 1041

Nakagawa, H., Kasaba, Y., Maezawa, H., Hashimoto, A., Sagawa, H., Murata, I., Okano, S., Aoki, S., Moribe, N., Mizuno, A., Momose, M., Ohnishi, T., Mizuno, N., & Nagahama, T. 2009, Planet. Space Sci., 57, 2123

Rayner, J. 2015, in Initial iSHELL Observing Summary, NASA Infrared Telescope Facility Documents, 22

Rayner, J., Bond, T., Bonnet, M., Jaffe, D., Muller, G., & Tokunaga, A. 2012, in Society of Photo-Optical Instrumentation Engineers (SPIE) Conference Series, Vol. 8446, Society of Photo-Optical Instrumentation Engineers (SPIE) Conference Series, 2

Sawyer, G. M., Oppenheimer, C., Tsanev, V. I., & Yirgu, G. 2008, J. Volc. Geotherm. Res., 178, 837

Settle, M. 1979, J. Geophys. Res., 84, 8343

Spera, F. J. 2000, in Encyclopedia of Volcanoes (Academic Press), 171–190

Symonds, R., Rose, W., Bluth, G., & Gerlach, T. 1994, Volatiles in Magmas: Miner. Soc. Am. Rev. Miner., 30, 1

Tokunaga, A. T., Toomey, D. W., Carr, J., Hall, D. N. B., & Epps, H. W. 1990, in Society of Photo-Optical Instrumentation Engineers (SPIE) Conference Series, Vol. 1235, Instrumentation in Astronomy VII, ed. D. L. Crawford, 131–143

Webster, C. R., Mahaffy, P. R., Atreya, S. K., Flesch, G. J., Mischna, M. A., Meslin, P.-Y., Farley, K. A., Conrad, P. G., Christensen, L. E., Pavlov, A. A., Martín-Torres, J., Zorzano, M.-P., McConnochie, T. H., Owen, T., Eigenbrode, J. L., Glavin, D. P., Steele, A., Malespin, C. A., Archer, P. D., Sutter, B., Coll, P., Freissinet, C., McKay, C. P., Moores, J. E., Schwenzer, S. P., Bridges, J. C., Navarro-Gonzalez, R., Gellert, R., Lemmon, M. T., & Team, M. 2015, Science, 347, 415

William-Jones, G., Rymer, H., & Rothery, D. A. 2003, J. Volc. Geotherm. Res., 123, 137

Wilson, L., Scott, E., & Head, J. 2001, J. Geophys. Res., 106, 1423

Wilson, T. L., Rohlfs, K., & Hüttemeister, S. 2009, Tools of Radio Astronomy (Springer-Verlag)

Wong, A.-S., Atreya, S. K., & Encrenaz, T. 2003, J. Geophys. Res., 108, 5026

—. 2004, J. Geophys. Res., 109, 1007

—. 2005, J. Geophys. Res., 110, 10002